University of California
Santa Barbara

Problems in condensed matter theory motivated by quantum computers

A dissertation submitted in partial satisfaction
of the requirements for the degree

Doctor of Philosophy
in
Physics

by

Aleksei Khindanov

Committee in charge:

Professor Chetan Nayak, Co-Chair
Dr. Andrey Antipov, Co-Chair
Professor Matthew Fisher
Professor Andrea Young

September 2023

The Dissertation of Aleksei Khindanov is approved.

Professor Matthew Fisher

Professor Andrea Young

Dr. Andrey Antipov, Committee Co-Chair

Professor Chetan Nayak, Committee Co-Chair

August 2023

Problems in condensed matter theory motivated by quantum computers

by

Aleksei Khindanov

To my mother, my father, my sister, my brother, and my late grandmother, for all their support and love.

Acknowledgements

Standing at the very end of my PhD studies and reflecting on the past six years of my life, I realize there are so many things that have happened to me that I am thankful for and so many people I am thankful to. That said, with an absolute certainty I can say that the thing I am grateful for the most is the opportunity that I have had during my PhD years to interact with and learn from so many brilliant people.

First and foremost, I would like to thank people who have advised me, formally and informally, throughout various parts of my PhD career – from the moment I have stepped upon the path of a researcher, and to this day. Those are Andrey Antipov, Dima Pikulin, Roman Lutchyn, and Igor Aleiner. This work would not have been possible without their mentorship.

I would also like to thank other members of my dissertation committee – Chetan Nayak, Matthew Fisher and Andrea Young – for their advise and numerous illuminating conversations.

I am tremendously thankful to members of the wonderful Microsoft Station Q team for various collaborations and fascinating discussions, in particular to Andrey Antipov, Dima Pikulin, Roman Lutchyn, Chetan Nayak, Torsten Karzig, William Cole, Christina Knapp, Ivan Sadovskyy, and Bela Bauer.

Another gratitude goes to members of the Google Quantum AI team that I have interacted with during my internship there, Igor Aleiner, Kostyantyn Kechedzhi and Vadim Smelyanski.

Additionally, I would like to thank all the exceptional researchers, both in theory and experiment, that I have ever collaborated with and that have not yet been mentioned. In particular, I would like to mention Jukka Väyrynen, Rafał Rechciński, Jason Alicea, Patrick Lee, Greg Mazur, Nick van Loo, Yong P. Chen, Leonid Rokhinson, and Jian Liao.

My immense gratitude goes to professors at the UCSB Physics department that I have learned from, in particular Matthew Fisher, Chetan Nayak, Andrea Young, Leon Balents, Andreas Ludwig, Sagar Vijay, Mark Srednicki, Mark Sherwin, Cenke Xu, and Tengiz Bibilashvili.

I would also like to thank various friends and colleagues from the UCSB Physics department and beyond, in particular Mia Nowotarski, Joe Costello, Sergio Hernandez Cuenca, Seamus O'Hara, Will Schultz, Sarah Steiger, Noah Swimmer, Josh Straub, Yaodong Li, Zhitao Chen, Aaron Kennon, Mark Turiansky, Wayne Weng, Brad Price, Antonín Sojka, Alex Meiburg, Chaitanya Murthy, Mark Arildsen, Kasra Hejazi, Alexey Milekhin, and Yuri Lensky.

Lastly, but perhaps most importantly, I would like to thank my family for supporting me in highs and lows throughout my PhD journey – my mom Agrippina, my dad Innokentii, my sister Alina, my brother Sasha, my late grandmother Pana, and my aunt Irina.

Curriculum Vitæ
Aleksei Khindanov

Education

2023	Ph.D. in Physics (Expected), University of California, Santa Barbara.
2020	M.A. in Physics, University of California, Santa Barbara.
2017	B.Sc. in Applied Mathematics and Physics, Moscow Institute of Physics and Technology.

Peer-reviewed Publications

G. P. Mazur, N. van Loo, J. Y. Wang, T. Dvir, G. Wang, **A. Khindanov**, S. Korneychuk, F. Borsoi, R. C. Dekker, G. Badawy, P. Vinke, S. Gazibegovic, E. P. A. M. Bakkers, M. Quintero-Perez, S. Heedt, and L. P. Kouwenhoven. *Spin-mixing enhanced proximity effect in aluminum-based superconductor-semiconductor hybrids.* Advanced Materials 34, 2202034 (2022).

A. Khindanov, J. Alicea, P. Lee, W. S. Cole, and A. E. Antipov. *Topological superconductivity in nanowires proximate to a diffusive superconductor–magnetic-insulator bilayer.* Physical Review B 103, 134506 (2021).

A. Khindanov, D. I. Pikulin, and T. Karzig. *Visibility of noisy quantum dot-based measurements of Majorana qubits.* SciPost Physics 10, 127 (2021).

Publications in Preparation

D. I. Pikulin, **A. Khindanov**, and Yu. V. Nazarov. *Weakly disordered wide Josephson junction.* In preparation.

R. Rechciński, **A. Khindanov**, D. I. Pikulin, R. M. Lutchyn, and J. I. Väyrynen. *Influence of disorder on antidot vortex Majorana states in 3D topological insulators.* In preparation.

A. Khindanov and I. L. Aleiner, *Random-Matrix Theory of a Dynamical Measurement-induced Phase Transition in Nonlocal Floquet Quantum Circuits.* In preparation.

A. Khindanov, T. Karzig, R. M. Lutchyn, and D. I. Pikulin. *Effects of coupling between quantum dot and quasiparticle continuum modes in topological superconductor-quantum dot-topological superconductor junctions.* In preparation.

Abstract

Problems in condensed matter theory motivated by quantum computers

by

Aleksei Khindanov

Quantum computers, once their fault-tolerant versions are built, are widely believed to revolutionize the world, bringing an exponential quantum advantage to problems in chemistry, physics and material science. In this thesis, we explore various problems in theoretical condensed matter physics that are in one way or another related to quantum computers. The first part of this thesis is devoted to Majorana zero-energy modes and topological quantum computing. We describe how Majorana modes can be synthesized in superconductor-semiconductor heterostructures, and emphasize vulnerabilities of the topological phase in such heterostructures to external magnetic fields. We further demonstrate how and to what degree the addition of a magnetic insulator or spin-orbit scattering to a heterostructure can help alleviating the negative effects of external magnetic fields. Additionally, we analyze quantum dot-based measurements of Majorana qubits. In particular, we identify the optimal regime for such measurements, and estimate to what degree external noise sources and coupling of the quantum dot to quasiparticle modes in superconductors affect the fidelity of the measurements. The other part of this thesis is devoted to the many-body physics in quantum circuits. We describe a Floquet circuit model in which projective measurements can drive a dynamical spectral phase transition in otherwise purely unitary dynamics of the circuit. Using random-matrix theory, we analytically calculate various properties of this transition, and analyze how the transition can be revealed in the long-time dynamics of the system.

Contents

Chapter 1

Introduction

This thesis presents the results of the research on various different topics in theoretical condensed matter physics, oftentimes quite different in the spirit and scope, but the unifying theme for all of them is their relation to the field of quantum computing.

Quantum computing is a computing paradigm that utilizes quantum-mechanical degrees of freedom (as opposed to classical bits in conventional, "classical" computers) to perform computations [1]. Fully operational quantum computer with a sufficient number of error-free qubits is expected to provide an exponential computational advantage for certain problems, when compared to existing classical algorithms [2]. The most notable application where such exponential speed-up is anticipated is the simulation of many-body quantum systems appearing in chemistry, physics, and material science [3]. Besides that, a few other algorithms with an exponential quantum advantage are known, such as the Shor's algorithm for integer factorization[4] and the algorithm for approximating Jones polynomial in knot theory[5]. Additionally, for certain problems a polynomial quantum speed-up (again, when comparing with *existing* classical algorithms) is known, for example for search problems[6] and combinatorial optimization[7].

Despite tremendous effort and significant progress in the field, it seems likely that

it will take a long time (perhaps, decades) until a fault-tolerant quantum computer with error corrected qubits can be built. Due to this fact, a lot of research has been concentrated on showcasing what can be done on existing quantum hardware with dozens or hundreds of noisy qubits. Such noisy intermediate-scale quantum (NISQ)[8] devices have been used to demonstrate quantum advantage[9] and investigate various models in the many-body physics.

A large part of this thesis is devoted to the field of topological quantum computing[10]. Topological quantum computing utilizes a special type of particles in two dimensions – non-Abelian anyons – to store and manipulate quantum information with a degree of intrinsic fault-tolerance. Due to this fact topological qubits are expected to be less susceptible to environmental noise than qubits in other physical platforms, and thus the aforementioned practical applications for quantum computing could be achievable with a smaller number of topological qubits than the non-topological ones. A certain type of non-Abelian anyons – Majorana particles – have been theorized to exist in various solid-state systems [11], and can potentially be utilized for a qubit implementation. Unambiguous experimental detection of such particles, not to mention further physical implementation of a Majorana qubit, however, is a difficult task and is an ongoing research effort. In this work I present approaches to improving hardware that can host the Majorana particles[12, 13], and further analyze optimal regimes for Majorana qubit measurements[14, 15].

Another part of this thesis is devoted to many-body physics applications for modern noisy intermediate-scale quantum (NISQ) devices. In this thesis we consider a particular problem of analyzing how qubit measurements can drive dynamical phase transitions in otherwise purely unitary dynamics of quantum circuits[16].

This thesis is organized as follows. In Chapter 2, we outline how Majorana particles can be synthesized in one-dimensional superconductor-semiconductor heterostructures and describe susceptibilities of such heterostructures to external magnetic fields. We

further introduce the Usadel equation formalism and describe how it can be utilized to study superconductor-semiconductor heterostructures with disordered superconductors. Then, we apply the Usadel formalism to study the effects of external magnetic fields, spin-orbit and magnetic scattering on the topological phase in the heterostructure, and further describe to what extent the coupling of a magnetic insulator or the addition of the spin-orbit scattering can alleviate the negative effects of external magnetic fields on the heterostructure. In Chapter 3, we analyze how quantum dots can be used to measure the state encoded by pairs and fours of Majorana zero modes. We also determine the best regime for such measurements, and estimate how various noise sources affect the fidelity of the measurements. In Chapter 4, we calculate how the coupling between quasiparticle continuum modes in superconductors and a quantum dot impact the quantum dot-based measurements of Majorana qubits. Furthermore, we study the physics of the $0-\pi$ transition in topological superconductor-quantum dot-topological superconductor junctions. Finally, in Chapter 5 we switch gears from the Majorana physics to the physics of quantum circuits. We introduce a Floquet circuit model with unitary operations and projective measurements that exhibits a measurement-induced dynamical phase transition in the spectrum of its non-unitary evolution operator. Using random-matrix theory, we analytically calculate properties of this transition and further describe how this transition is revealed in various physical quantities.

Chapter 2

Application of the Usadel equation to study diffusive superconductor-semiconductor heterostructures

2.1 Permissions and Attributions

1. The content of Chapter 2 and Appendix A is the result of a collaboration with Jason Alicea, Patrick Lee, William S. Cole, Andrey E. Antipov, G.P. Mazur, N. van Loo, J.-Y. Wang, T. Dvir, G. Wang, S. Korneychuk, F. Borsoi, R.C. Dekker, G. Badawy, P. Vinke, S. Gazibegovic, E.P.A.M. Bakkers, M. Quintero-Pérez, S. Heedt, and L.P. Kouwenhoven, and has previously appeared in Physical Review B 103, 134506 (2021)[12] and Advanced Materials 34, 2202034 (2022)[13]. It is reproduced here with the permission of the American Physical Society (`https://journals.aps.org/prb/`) and Wiley-VCH GmbH (`https://onlinelibrary.`

wiley.com/journal/15214095).

2.2 Introduction

A physical realization of spatially separated Majorana zero-energy modes (MZMs) in solid-state systems can lead to a practical implementation of a topological quantum computer – a type of quantum hardware with intrinsic degree of fault-tolerance [10, 11]. Despite numerous theoretical proposals for the realization of MZMs in a variety of hardware platforms, such as 2D[17] and 3D[18] topological insulators, semiconducting nanowires[19, 20], 2DEGs[21], atomic chains[22], and many others, the experimental detection of MZMs has been a formidable task.

Recently, Ref. [23] observed experimental signatures in local and non-local transport properties consistent[24] with the presence of MZMs. Devices used in the experiment were based on quasi-one-dimensional semiconducting nanowires created by gating out a 2DEGs and proximitized by a superconducting layer. In its simplest form, the model for a one-dimensional proximitized semiconducting wire has the following form:

$$H = \int_0^L dx \Psi^\dagger(x) \left(-\frac{\partial_x^2}{2m^*} - \mu + i\alpha\hat{\sigma}_y\partial_x + V_x\hat{\sigma}_x \right) \Psi(x) + \int_0^L dx \left(\Delta_{\text{ind}} \psi_\uparrow^\dagger(x)\psi_\downarrow^\dagger(x) + \text{h.c.} \right), \tag{2.1}$$

where $\Psi^T(x) = (\psi_\uparrow(x), \psi_\downarrow(x))$ is a two-dimensional spinor of electronic annihilation operators, m^* is the effective electronic mass, μ is the chemical potential inside the nanowire, α is the Rashba spin-orbit coupling, V_x is the Zeeman field directed along the direction of the wire, which is usually created by applying an external magnetic field, Δ_{ind} is the superconducting pairing potential in the nanowire induced by the proximity to a superconductor, L is the length of the wire, and $\hat{\sigma}_i$ are the Pauli operators in the spin space. For the purposes of the topological quantum information processing, there are two basic

ingredients that are necessary: first, the ability to tune the system into the topological phase where the MZMs would appear, and second, the gap in the topological phase has to be sufficiently large to protect the stored quantum information from environmental decoherence. In the simple formulation of the model (2.1), the topological superconductivity and MZMs emerge in the system for sufficiently large Zeeman fields, specifically when

$$V_x \geq \sqrt{\mu^2 + \Delta_{\text{ind}}^2}. \tag{2.2}$$

In this toy model picture, the stronger are the effective spin-orbit energy $E_{\text{so}} = m^*\alpha^2/2$, the Zeeman field V_x and the induced pairing Δ_{ind}, the larger is the gap in the topological phase, while sufficiently large values of the Zeeman field are also necessary to achieve the condition (2.2).

However, the situation in realistic samples is *much* more complicated than the one described by the model (2.1)-(2.2). First and foremost, disorder plays a crucial role in the physics of experimental devices, whether it is caused by charge impurities, potential inhomogeneities, or imperfections in the superconductor-semiconductor interface. While the topological phase is known to survive small-to-intermediate levels of non-magnetic disorder, strong disorder is detrimental for it and moreover can mimic the signatures of the MZMs in local transport properties in the trivial phase [25]. Semiconductors with high electronic mobility and clean superconductor-semiconductor interfaces are thus necessary to engineer the topological phase. Secondly, the parameter Δ_{ind} does not fully encapsulate the effects of the superconductor-semiconductor proximity. The effective coupling γ between the superconductor and the semiconductor, while governing the ratio of the induced pairing potential Δ_{ind} and the gap Δ_0 of the parent superconductor, also affects the degree to which the parameters of the unproximitized nanowire, primarily the effective Rashba energy E_{so} and the g-factor (and hence V_x), renormalize due to the

proximity to the superconductor, where these parameters are much smaller. Specifically, larger values of γ result in the larger values of Δ_{ind}, which leads to a better protection against the interface disorder and a larger maximal topological gap, but it also causes the decrease in the values of E_{so} and the g-factor, which is detrimental for the topological phase and the topological gap [26, 27].

All the above considerations put significant constraints on material choices for the superconductor-semiconductor hybrids and their fabrication techniques [28]. On the semiconductor side, the usual materials of choice are InAs or InSb, which boast large intrinsic values of the Rashba spin-orbit energy E_{so} and the g-factor, have a good susceptibility to external gate tuning, and can be fabricated to possess relatively large electronic mobility. On the superconductor side, Al has been the standard material of choice. Even though Al possess a relatively small superconducting gap (up to $\approx 300\mu$eV) when compared to many other common superconductors, it can be deposited *in situ* on the semiconducting nanowire without breaking the vacuum, thus preventing the oxide layer from forming at the interface and dramatically reducing the level of the interface disorder.

Another important aspect that has to be taken into account when designing superconductor-semiconductor heterostructures is the susceptibility of the parent superconductor to detrimental effects of the external magnetic field. While the external magnetic field is usually considered to be a necessary component to induce the Zeeman field in the nanowire and drive it into the topological phase, see Eq. (2.2), it can also reduce or collapse the gap in the parent superconductor if the g-factor in the nanowire is not sufficiently large, which is often the case in practice. There are two basic mechanisms via which the external magnetic field affects the parent gap. First, the orbital effect of the magnetic field, when coupled with the intrinsic non-magnetic disorder in the superconductor, acts as an effective magnetic disorder and thus continuously reduces the superconducting gap all the way to zero as the strength of the magnetic field increases

[29]. The magnitude of the orbital effect in a thin superconducting strip parallel to the magnetic field is proportional to the thickness of the strip (squared)[29], and thus to a certain extent the orbital effect can be mitigated by fabricating superconducting strips of sufficiently small thickness. However, the strips cannot be made too thin as for thicknesses fewer than a few nm the superconductivity is destroyed. (Another advantage of using thin Al films is the fact that the gap of such thin films is significantly enhanced when compared to the Al bulk gap value: the zero temperature bulk gap of the Al is 180μeV while, for example, recent experiments on the InAs-Al hybrids achieve the value of 300μeV for the parent Al gap.) The second mechanism by which the gap in thin superconducting strips is destroyed is the Zeeman field induced within the superconductor by the external magnetic field. Once this Zeeman field V_x^{SC} reaches the value of $V_x^{SC} = \Delta_0/\sqrt{2}$, where Δ_0 is the zero-temperature gap in the absence of the external magnetic field, the superconductor suffers the first-order phase transition into a normal metallic phase, and the superconductivity is destroyed. This limiting value of the Zeeman field is known as the Chandrasekhar-Clogston limit[30, 31].

There are various proposed ways in which the aforementioned detrimental effects of the external magnetic field can be alleviated. One of them is by coupling a magnetic insulator to the superconductor-semiconductor heterostructure, which was first proposed in Ref. [21], and later attempted experimentally in Refs. [32, 33, 34], where EuS was picked as a magnetic insulator of choice due to the ability to create a relatively clean interface between EuS and Al/InAs, followed by various theoretical studies [12, 35, 36, 37, 38, 39, 40]. In Ref. [32] the defect-free heterostructure between an InAs semiconductor wire and a EuS has been prepared and studied. However, negligible direct magnetization of InAs was reported. Nevertheless, while such direct coupling between EuS and InAs seems to be absent, EuS is known to induce the Zeeman spin splitting in Al [41, 42, 43, 44, 45], which by itself is not sufficient to achieve the zero-field topological superconductivity,

but might help in reducing the minimum field required to induce the topological phase.

Another potential approach to reducing detrimental effects of specifically Zeeman field in the parent superconductor is by introducing heavy-atom impurities to the superconductor, which induce strong spin-orbit scattering. Spin-orbit scattering is well-known to reduce the Zeeman splitting in superconductors [29], and thus can serve as a powerful tool to push the Chandrasekhar-Clogston limit further from its conventional (spin-orbit-scattering-free) value. Recently, Ref. [13] performed experiments with InSb-Al heterostructure, where Al strip was covered by a very thin layer of Pt atoms that are known to induce spin-orbit scattering. Ref. [13] showed that such Pt-covered heterostructures can sustain larger magnetic fields than their Pt-free counterparts.

In this chapter, we theoretically study the aforementioned ways to alleviate the detrimental effects of the magnetic field on superconductor-semiconductor hybrids and the topological phase. It is important to note that the superconductors that have been used in proximity heterostructure experiments, such as Al, NbTiN, Sn, and Pb are all diffusive either due to intrinsic disorder or oxidation on the surface. On the other hand, the optimal platform for Majorana nanowires should feature "clean" semiconductors with defects minimized [46]. Therefore, one needs to put forward a theoretical framework that includes self-consistent superconducting effects in different parts of the system, disorder scattering, as well as proximity effects. One such approach would be a self-consistent microscopic Bogoliubov-de Gennes treatment. However, in practice the need to include phenomena at disparate lengthscales — ranging between angstroms to hundreds of nanometers and governed by the Fermi wavelengths, superconducting and magnetic coherence lengths as well as disorder scattering mean free path — makes it prohibitive for numerical real-space calculations, thus necessitating an effective theory. Here we develop such effective theory based on the Usadel equation, which is an established tool to study disordered superconductors. The Usadel equation approach allows one to self-consistently account for

various effects in the superconductor, such as Zeeman field, orbital effect of the magnetic field, spin-orbit scattering and magnetic scattering, and then use the obtained results for the parent superconductor to study its effects on the nanowire.

2.3 The Usadel equation

The Usadel equation is a nonlinear second-order differential equation for the quasiclassical Green's function of a superconductor. Although it is a standard method for describing superconductors [47], for completeness of the presentation we introduce it in this section. The detailed derivation can be found in Ref. [48]. The Usadel equation is valid in the limit $\lambda_F \ll l_{MFP} \ll \xi$, where λ_F is the metallic Fermi velocity, l_{MFP} is the mean free path and ξ is the superconducting coherence length. For typical s-wave superconductors used in Majorana nanowires, such as Al, this approximation holds, as $\lambda_F \simeq 1\mathring{A}$, $l_{MFP} \simeq 20$nm [49], and $\xi \simeq 300$nm [50].

The starting point is the Gor'kov equation for the superconducting Green's function $\check{G}_{SC}(i\omega_n, \boldsymbol{r_1}, \boldsymbol{r_2})$ [51] describing an excitation in Nambu space between spatial coordinates r_1 and r_2 at the (imaginary) frequency $i\omega_n$. We will use the mixed real- and momentum-space representation $\check{G}_{SC}(\boldsymbol{r}, \boldsymbol{k})$ obtained by the Wigner transform to the center-of-mass coordinates $\boldsymbol{r} \equiv (\boldsymbol{r_1}+\boldsymbol{r_2})/2$ and a Fourier transform over the relative coordinate $\boldsymbol{r_1}-\boldsymbol{r_2} \to \boldsymbol{k}$. Taking advantage of the short Fermi wavelength in the superconductor, one can apply the quasiclassical approximation and integrate out the magnitude of the relative momenta on the Fermi surface, yielding a quasiclassical Green's function $\check{g}(i\omega_n, \boldsymbol{r}, \boldsymbol{k}_F) = \mathcal{P}\hat{\tau}_z \frac{i}{\pi} \int d\xi_k \check{G}_{SC}(\omega_n, \boldsymbol{r}, \boldsymbol{k})$ [52, 53], where $\boldsymbol{k}_F$ denotes the direction of momenta on the Fermi surface, ξ_k is the electronic dispersion relation, $\hat{\tau}_z$ is a Pauli matrix in Nambu space, and $\mathcal{P}$ indicates principal-value integration. The quasiclassical Green's function $\check{g}$ is subject to a normalization condition $\check{g}(i\omega_n, \boldsymbol{r}, \boldsymbol{k}_F)^2 = \check{1}$. Disorder averaging for

scattering off non-magnetic, magnetic and spin-orbit impurities [54, 55] is performed with the help of the self-consistent Born approximation and results in self-energy corrections to $\check{g}$.

Further simplification is possible in the dirty limit when the mean free path associated with the scattering off non-magnetic impurities is much smaller than the superconducting coherence length (but still much larger than the Fermi wavelength). In this case one can expand $\check{g}(i\omega_n, \boldsymbol{r}, \boldsymbol{k}_F)$ up to a linear order in $\boldsymbol{k}_F$ and arrive to the Usadel equation for the isotropic (independent of $\boldsymbol{k}_F$) part of the quasiclassical Green's function $\check{g}(i\omega_n, \boldsymbol{r})$. Throughout the chapter we make use of the Usadel equations in the form utilized in Refs. [47, 56]:

$$D\boldsymbol{\partial} \cdot (\check{g}\boldsymbol{\partial}\check{g}) - [\omega_n \hat{\tau}_z + i\boldsymbol{V}_Z^{SC} \cdot \hat{\boldsymbol{\sigma}}\hat{\tau}_z + \Delta\hat{\tau}_+ + \Delta^*\hat{\tau}_- + \check{\Sigma}, \check{g}] = 0, \tag{2.3}$$

where the covariant derivative is $\boldsymbol{\partial}\check{X} = \boldsymbol{\nabla} - i[\boldsymbol{A}\hat{\tau}_z, \check{X}]$, $\boldsymbol{A}$ is the vector potential, D is a diffusion constant associated with the electronic scattering off non-magnetic impurities and it is given by $D = v_{\mathrm{F}} l_{MFP}/3$, where v_{F} is the Fermi velocity in the superconductor and l_{MFP} is the mean-free path, $\boldsymbol{V}_Z^{SC}$ is the Zeeman field which may arise due to an external magnetic field or a proximity to a magnetic material, Δ is the pairing potential, $\hat{\boldsymbol{\sigma}}(\hat{\boldsymbol{\tau}})$ is a set of Pauli matrices in spin (Nambu) space and $\hat{\tau}_\pm = (\hat{\tau}_x \pm i\hat{\tau}_y)/2$. Equation (2.3) is written in the Nambu spinor basis $(\psi_\uparrow, \psi_\downarrow, -\psi_\downarrow^\dagger, \psi_\uparrow^\dagger)^T$.

The self-energy $\check{\Sigma} = \check{\Sigma}_{so} + \check{\Sigma}_{sf}$ incorporates elastic spin relaxation mechanisms that we consider throughout this work: spin-orbit scattering $\check{\Sigma}_{so} = \hat{\boldsymbol{\sigma}}\check{g}\hat{\boldsymbol{\sigma}}/(8\tau_{so})$ off heavy ions which preserves time-reversal symmetry and spin-flip scattering $\check{\Sigma}_{sf} = \hat{\boldsymbol{\sigma}}\hat{\tau}_z\check{g}\hat{\tau}_z\hat{\boldsymbol{\sigma}}/(8\tau_{sf})$ off magnetic impurities which breaks time-reversal symmetry. For convenience, we introduce energy scales $\Gamma_{so/sf} = 3/(2\tau_{so/sf})$ associated with these two types of scattering.

In general, the Usadel equation (2.3) has to be supplemented with boundary condi-

tions, and the corresponding boundary problem has to be solved. In the context of a SC-SM heterostructure in a parallel magnetic field, vacuum boundary conditions, $\boldsymbol{\partial}\check{g} = 0$, can be assumed at all boundaries, including the boundary between the SC and the SM. This is justified by the small effective transparency of the interface for quasiparticles traveling from the superconductor into the semiconductor: quasiparticles in the superconductor have a much larger Fermi momentum than in the semiconductor. Only quasiparticles moving with a small momentum parallel to the interface can tunnel from the superconductor to the semiconductor, but strong disorder in the superconductor randomizes the momentum direction, resulting in a low-probability of tunneling [57]. Note that electrons from the semiconductor have a high probability of tunneling into the superconductor and reflecting back as a hole, providing Andreev scattering. Additional corrections in the very strong tunneling regime involving coherent tunneling and disorder scattering in the superconductor can generate additional subgap states at finite magnetic fields [58]; we do not consider this regime.

Given the vacuum boundary conditions and assuming the uniformity of the spin relaxation and Zeeman effects in the SC, it has been shown that for very thin superconductors (with thickness $d_{\mathrm{SC}} \ll \xi, \lambda_{\mathrm{London}}$, where $\lambda_{\mathrm{London}}$ is the London penetration depth) in a parallel magnetic field the spatial dependencies of the Green's function and the order parameter can be neglected [59], $\check{g}(\omega_n, \boldsymbol{r}) \to \check{g}(\omega_n)$, and the order parameter can be chosen real, $\Delta \in \mathbb{R}$. In that case, the Usadel equation (2.3) becomes a non-linear algebraic equation [1]:

$$\left[\omega_n \hat{\tau}_z + i\boldsymbol{V}_{\mathrm{Z}}^{SC} \cdot \hat{\boldsymbol{\sigma}}\hat{\tau}_z + \Delta\hat{\tau}_x + \check{\Sigma}, \check{g}\right] = 0, \tag{2.4}$$

where orbital effects of the magnetic field lead to an additional contribution to the self-

[1] SC-MI bilayers with superconductors of thickness comparable or greater than the coherence length have been recently studied in Ref. [45]

energy:

$$\check{\Sigma} = \check{\Sigma}_{so} + \check{\Sigma}_{sf} + \check{\Sigma}_{orb}, \tag{2.5}$$

$$\check{\Sigma}_{orb} = \Gamma_{orb}\frac{\hat{\tau}_z\check{g}\hat{\tau}_z}{4}, \tag{2.6}$$

and the orbital depairing energy is given by

$$\Gamma_{orb} = \frac{De^2B^2d_{\mathrm{SC}}^2}{3\hbar c^2}. \tag{2.7}$$

Equation (2.7) is a familiar result for thin superconducting films subjected to a parallel magnetic field [60, 29].

Equation (2.4) can be solved by the following Green's function parametrization in terms of functions $\theta(\omega_n, \boldsymbol{r})$ and $\phi(\omega_n, \boldsymbol{r})$[47, 56]:

$$\check{g}(\omega_n, \boldsymbol{r}) = \hat{\tau}_z\cos\theta(\cosh\phi + i\hat{\sigma}_x\tan\theta\sinh\phi) + \hat{\tau}_x\sin\theta(\cosh\phi - i\hat{\sigma}_x\cot\theta\sinh\phi). \tag{2.8}$$

Note that the parametrization (2.8) automatically satisfies the normalization condition $\check{g}^2 = \check{1}$. The matrix Eq. (2.4) hence becomes a set of nonlinear equations

$$\cosh\phi(\Delta\cos\theta - \omega_n\sin\theta) - V_Z^{SC}\sinh\phi\cos\theta - \\ - \sin 2\theta\left[\frac{\Gamma_{sf}}{12}(2\cosh^2\phi + 1) + \frac{\Gamma_{orb}}{4}(2\cosh^2\phi - 1)\right] = 0, \tag{2.9a}$$

$$\sinh\phi(\Delta\sin\theta + \omega_n\cos\theta) - V_Z^{SC}\cosh\phi\sin\theta + \\ + \cosh\phi\sinh\phi\left[\frac{\Gamma_{so}}{3} + \left(\frac{\Gamma_{sf}}{6} + \frac{\Gamma_{orb}}{6}\right)\cos 2\theta\right] = 0. \tag{2.9b}$$

Once the quasiclassical Green's function $\check{g}$ is computed via Eqs. (2.8)-(2.9b), one can evaluate various physical properties of the superconductor, such as the pairing potential, free energy and the density of states. Reference [56] derives expressions for these physical quantities in terms of functions $\theta(\omega_n, \boldsymbol{r})$, $\phi(\omega_n, \boldsymbol{r})$, and here we present those expressions for the reader's convenience.

First, the pairing potential can be calculated by the means of the "gap equation"

$$\Delta \log(\frac{T}{T_{c0}}) = 2\pi T \sum_{\omega_n>0} \left(\frac{1}{4}\mathrm{Tr}(\hat{\tau}_x \check{g}) - \frac{\Delta}{\omega_n} \right) = 2\pi T \sum_{\omega_n>0} \left(\cosh\phi \sin\theta - \frac{\Delta}{\omega_n} \right), \tag{2.10}$$

with T being temperature and T_{c0} denoting critical temperature of the superconductor when no Zeeman field or spin relaxation processes are present. Importantly, Eq. (2.10) has to be paired with Eqs. (2.9a)-(2.9b) in order to achieve self-consistency of the calculations. Second, the free energy density difference between the superconducting and the normal state can be obtained as [56]

$$\begin{aligned} f_{sn} = \pi T \nu_0 \sum_{\omega_n>0} \big\{ & 4\omega_n - 2\cosh\phi(2\omega_n \cos\theta + \Delta \sin\theta) + 4V_Z^{SC} \sinh\phi \sin\theta + \\ & + \frac{1}{2}\left(\Gamma_{so} + \Gamma_{sf} + \Gamma_{orb}\right) - \frac{1}{2}(\Gamma_{so} + (\Gamma_{sf} + \Gamma_{orb})\cos 2\theta)\cosh^2\phi - \\ & - \frac{1}{2}\left(\frac{1}{3}\Gamma_{so} - \left(\frac{1}{3}\Gamma_{sf} - \Gamma_{orb}\right)\cos 2\theta\right)\sinh^2\phi \big\}, \end{aligned} \tag{2.11}$$

where ν_0 denotes the normal density of sates at the Fermi level. The condition $f_{sn} < 0$ is necessary to ensure thermodynamic stability of the superconducting phase. Third, the total density of states can be evaluated using quasiclassical Green's function:

$$\nu(E) = \frac{1}{8}\nu_0 \Re[\mathrm{Tr}(\hat{\tau}_z \check{g}|_{\omega_n \to -iE^+})] = \frac{1}{2}\nu_0 \Re[\cos\theta \cosh\phi|_{\omega_n \to -iE^+}]. \tag{2.12}$$

Experimentally, SIN junctions oftentimes used to measure the density of states. The

differential conductance in the SIN junction is related to the density of states through convolution [61],

$$\frac{dI}{dV}(V) \propto \int_{-\infty}^{\infty} \nu(E) K(E + eV) dE, \tag{2.13}$$

where V is a voltage bias and the convolution kernel is given by

$$K(x) = \frac{\beta e^{\beta x}}{(1 + e^{\beta x})^2} \tag{2.14}$$

with the inverse temperature $\beta = 1/k_{\mathrm{B}}T$.

Equations (2.9a)-(2.13) provide a sufficient apparatus to self-consistently calculate the quasiclassical Green's function of the parent SC and study the combined effect of Zeeman field, magnetic and spin-orbit scattering on the superconducting properties.

2.4 Properties of Al and Al/Pt thin films

In this section we apply the Usadel equation apparatus developed in the previous section to study properties of thin superconducting films within superconductor-semiconductor heterostructures. As discussed in the introduction to this chapter, Al has emerged as a superconductor of choice in the search for topological superconductivity in one-dimensional hybrids primarily due to the ability to create clean interfaces between thin Al shells and various semiconductors of choice, such as InAs and InSb. However, Al as a superconductor suffers from a relatively small gap (up to $\approx 300\mu$eV for thin films), which is further reduced by the presence of the magnetic field required to induce topological superconductivity, while potential topological quantum computing applications require large gap to protect quantum information from decoherence.

One way to mitigate the detrimental effects of the external magnetic field on the gap is by adding atoms of heavy elements (such as platinum) to the Al shells, which introduces

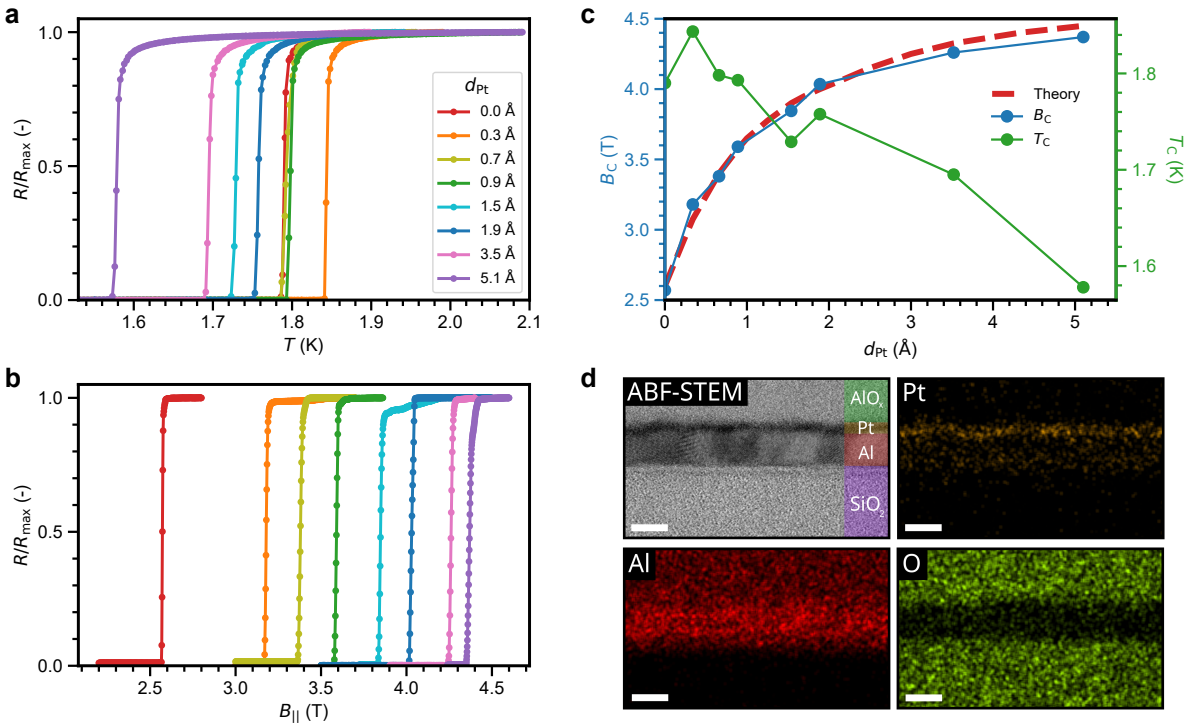

Figure 2.1: **Properties of Al/Pt thin films.** Four-point measurements of resistance R normalized to its value in the normal state R_N as a function of temperature (**A**) and magnetic field (**B**). Measurements have been performed for 6 nm thick aluminum films with varying amount of platinum d_{Pt}. (**C**) Critical magnetic field and temperature as a function of Pt thickness, together with the predicted critical field from theory calculations. (**D**) Annular bright field scanning-tunneling electron micrograph and energy-dispersive X-ray images of the Al film with 1.89 Å of Pt. Scale bars are 5 nm. Figure is from Ref. [13].

spin-orbit scattering into the system. Reference [13] measured critical temperatures and critical fields of Al thin films (thickness 6 nm) with added Pt layer as a function of Pt layer thickness. The results of these measurements are presented in Fig. 2.1, which depicts the superconducting transitions of Al/Pt films as a function of temperature (Fig. 2.1A) and parallel magnetic field (Fig. 2.1B). Importantly, the addition of Pt does not affect the shape and sharpness of the superconducting transitions, which indicates that the films do not become strongly disordered or inhomogeneous [62]. The bare aluminum film has a critical temperature $T_c = 1.79\,\mathrm{K}$ and a critical field $B_c = 2.6\,\mathrm{T}$. Upon the addition

Independent parameters				Extracted Parameters		
T (mK)	d_{SC} (nm)	g_{el}	v_{F} (m/s)	Δ_0 (meV)	l_{mfp} (nm)	Γ_{SO} (meV)
20	6	2	2×10^6	0.27	0.9	see Fig. 2.2a

Table 2.1: Values of parameters used in critical field simulations of Al and Al/Pt films, see Fig. 2.1. Extracted parameters were obtained by fitting experimental data.

of platinum, the critical field is increased above the bare aluminum's Chandrasekhar-Clogston limit already for platinum layer thickness $d_{\mathrm{Pt}} \approx 1$ Å, while leaving T_{c} unaffected. Fig. 2.1D presents the cross-section of an Al/Pt film with $d_{\mathrm{Pt}} \approx 1.9$ Å, which reveals the poly-crystalline structure of the Al.

In agreement with other studies on Al/Pt bilayers [63], the critical field starts to saturate for $d_{\mathrm{Pt}} \approx 2$ Å and increases only by an additional 300 mT for $d_{\mathrm{Pt}} \approx 5.1$ Å (see Fig. 2.1C). At these thicknesses, however, T_{c} starts to decrease as a result of the inverse proximity effect, as shown for Au/Be bilayers [64].

We use the Usadel equation, see Eqs. (2.4)-(2.10), to calculate the values of the pair potential and to simulate the critical fields of the Al and Al/Pt films considered in Fig. 2.1. We take the critical temperature to be $T_{c0} = 1.79$ K for all simulated samples. Using the critical field of the bare Al film (which we assume has a negligible amount of spin-orbit impurities) measured in the experiment, $B_c \approx 2.6$ T, we extract the value of the mean free path in the film by solving the Usadel equation (2.4)-(2.10) with $\Gamma_{\mathrm{SO}} = 0$ and obtain $l_{MFP} \approx 0.9$ nm. We further use this value to simulate the critical fields of the Pt-covered samples (see red dashed curve in Fig. 2.1 of the main text) and extract the respective values of the spin-orbit scattering rate (see Fig. 2.2a). Our theorety captures the increase of B_{c} as a direct result of including spin-orbit scattering (Fig. 2.1c). Values of the parameters used in these simulations, both independent and extracted by fitting experimental data, are given in Table 2.1.

Similarly to initial studies of the Al/Pt system, our theoretical model yields a linear

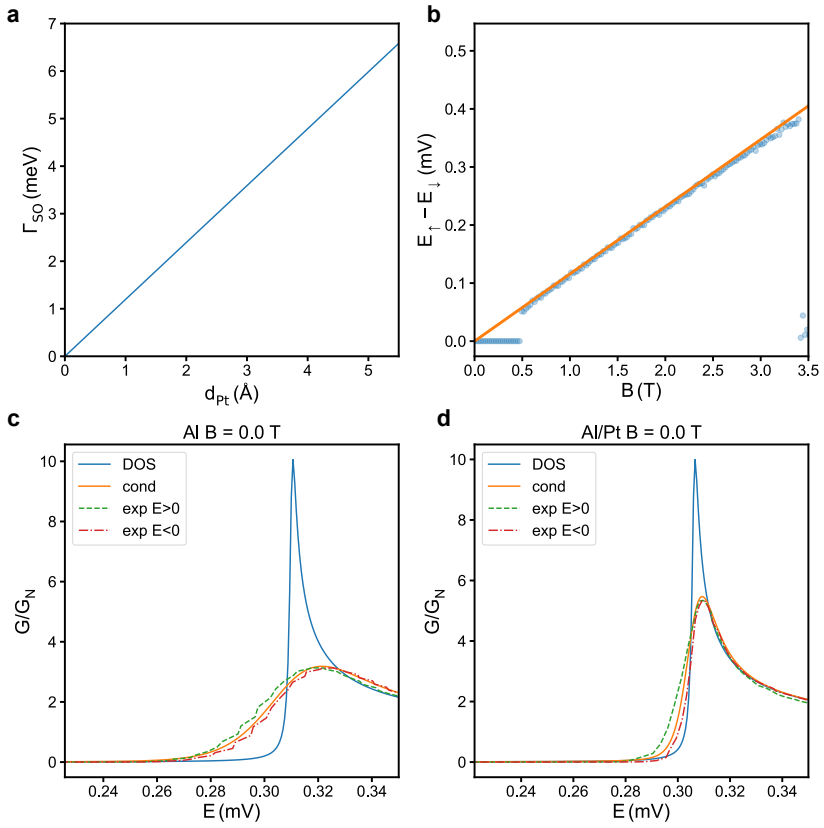

Figure 2.2: **a.** Spin-orbit scattering energy Γ_{SO} as a function of platinum thickness fitted to experimental film data presented in the main text. **b.** Experimentally extracted energy difference between Zeeman-split quasiparticle peaks (blue dots), and the corresponding Zeeman energy with $g = 2$. **c.** Calculated DOS (blue) and thermally broadened conductance (orange) for the Al tunnel junction. Green and red curves correspond to positive and negative bias respectively. **d.** Same curves for the Al/Pt tunnel junction.

dependence of Γ_{SO} on d_{Pt}, see Fig. 2.2(a). We note however that even for $d_{Pt} = 5.1\,\text{Å}$, the extracted value of Γ_{SO} is smaller than $\Gamma_{SO} = 7.5\,\text{meV}$, which was extracted from the tunneling measurements [13]. Initial studies of Al/Pt revealed unphysically large spin-orbit scattering rates [63]. In the case of the above mentioned experiment, the extracted spin-orbit scattering rate was higher than the momentum scattering rate, which indicated that the increase of critical field was not fully understood. It was pointed out later [65] that, due to Fermi liquid effects, the g-factor of such a thin Al films is being reduced [61].

	Independent parameters				Extracted Parameters		
	T (mK)	d_{SC} (nm)	g_{el}	v_{F} (m/s)	Δ_0 (meV)	l_{mfp} (nm)	Γ_{SO} (meV)
Al	110	4.5	2	2×10^6	0.31	0.68	0.0
Al/Pt	30	4.5	2	2×10^6	0.306	0.68	7.5

Table 2.2: Values of parameters used in conductance spectroscopy simulations of Al and Al/Pt tunnel junctions (see Fig. 2 of the main text). Extracted parameters were obtained by fitting experimental data.

We plot the energy difference between the spin-up and spin-down quasiparticle peaks in a 4.5-nm Al film as a function of magnetic field in Fig. 2.2(b). The analysis is made for fields larger then 1 T. In our case, we do not observe a clear deviation from a g-factor of 2 (indicated by the orange curve). The slight discrepancy observed near the transition can be a result of the peak broadening, rather than Fermi-liquid effects. We note, however, that the Fermi-liquid correction becomes more relevant at higher magnetic field values, and we cannot fully exclude the presence of these effects in Al/Pt devices.

Furthermore, Ref. [13] experimentally investigated the impact of Pt atoms on the Al quasiparticle density of states through normal-metal/insulator/superconductor (NIS) tunneling measurements. A schematic illustration and the used measurement circuit for these experiments are shown in Figure 2.3(c). Further details on the fabrication and measurement details can be found in the supplementary materials of Ref. [13]. Here we again utilize the Usadel equation approach, see Eqs. (2.9a)-(2.13) to theoretically simulate the measured conductance spectroscopy on the Al and Al/Pt films. Table 2.2 summarizes values of the parameters, both independent and extracted by fitting experimental data, used in the conductance simulations.

For the aluminum film, the experiments showed the presence of the Zeeman splitting of the quasiparticle coherence peaks (Fig. 2.3a). Furthermore, at a magnetic field of B = 3.45 T, the film underwnet a first-order phase transition to the normal state. Our theoretical model reproduces these two key features (Fig. 2.3d, see also Fig. 2.2c showing

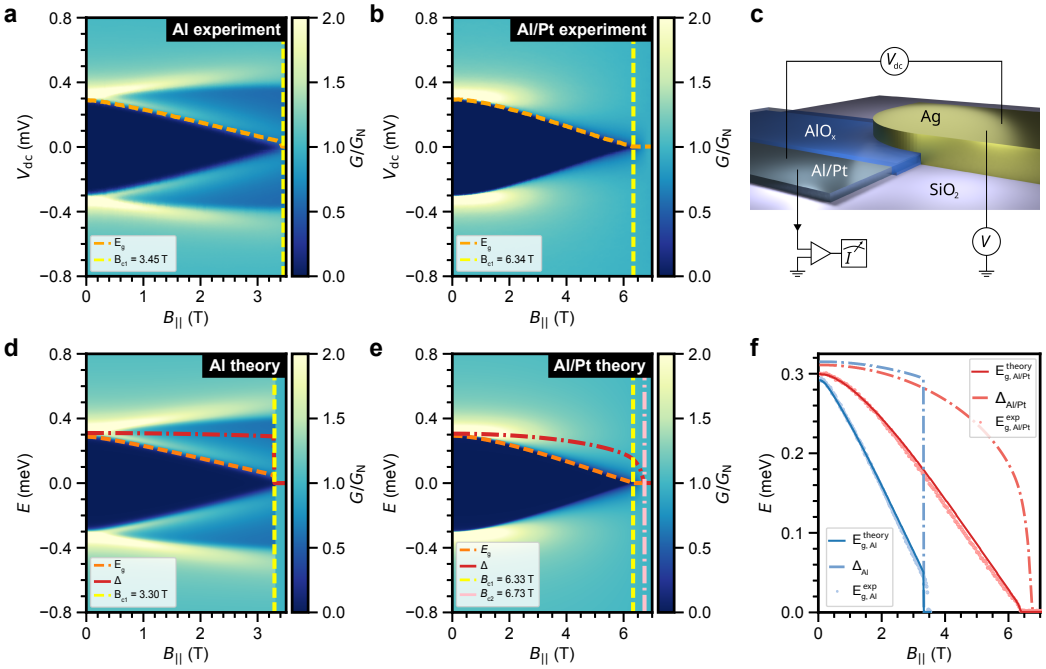

Figure 2.3: **Conductance spectroscopy on Al and Al/Pt NIS tunnel junctions.** (**A**) Experimental tunneling conductance of a $\sim$4.5 nm Al tunnel junction. (**B**) Experimental tunneling conductance of a $\sim$4.5 nm Al + 1.9 Å Pt tunnel junction. (**C**) False-color scanning-electron micrograph of a typical Al/AlOx/Ag tunnel junction. Scale bars are 1 μm. (**D**) Tunneling conductance from theory calculations of the Al tunnel junction. (**E**) Tunneling conductance from theory calculations of the Al/Pt tunnel junction. The dashed orange lines present the energy gap E_g. The order parameter Δ which is extracted from theory is presented by dashed red lines. Dashed yellow lines show the magnetic field B_{c1} for which the energy gap is closed, and the dashed pink lines indicate the magnetic field B_{c2} for which the order parameter is calculated to vanish. (**F**) Overview of the extracted energy gap from experiments, the predicted energy gap from theory and the corresponding order parameter of the films. Figure is from Ref. [13].

the density of states and the conductance at $B = 0$), where the first-order transition is reflected in an abrupt collapse of the order parameter. The critical field extracted from the model is 200 mT smaller than the experimentally measured value. This discrepancy between theory and experiment can be explained by the hysteretic behavior of the order parameter near the transition [66]. A metastable superconducting state can persist for magnetic fields slightly above the calculated critical value.

For the Al/Pt film with $d_{\mathrm{Pt}} = 1.9\,\text{Å}$, Zeeman splitting was not observed in the experiment. Instead, the film undergoes a second-order phase transition at $B = 6.34\,\mathrm{T}$ induced primarily by orbital effects (Fig. 2.3b). Importantly, the energy gap in the film remains free of quasiparticle states. Theoretical modelling of the film reveals a small magnetic field range with gapless superconductivity close to the transition (Fig. 2.3e, see also Fig. 2.2d showing the density of states and the conductance at $B = 0$), which is an expected feature when the transition from the superconducting into the normal state is of second order [29]. For both Al and Al/Pt films, the model yields diffusion constants which correspond to a mean free path of $l_{MFP} \approx 7\,\text{Å}$.

This value is consistent with reports on Al films grown under similar conditions [67, 61]. Since the addition of Pt does not seem to affect the mean free path, the increase in critical magnetic field cannot be attributed to increased disorder. The suppression of Zeeman splitting instead demonstrates that spin mixing is the dominant mechanism. From the model, the increased spin-orbit scattering energy of the Al/Pt film is extracted to be $\Gamma_{\mathrm{SO}} = 7.5\,\mathrm{meV}$, corresponding to a spin-orbit scattering time of $\tau_{\mathrm{SO}} = 1.3 \cdot 10^{-13}\,\mathrm{s}$. We note, however, that this extracted value of the spin-orbit scattering rate could be overestimated due to the presence of Fermi-liquid effects [65]. In Fig. 2.3(f), the measured energy gap is shown together with the energy gap extracted from theory, as well as the corresponding order parameter. We observe good quantitative agreement between the model and our experiment.

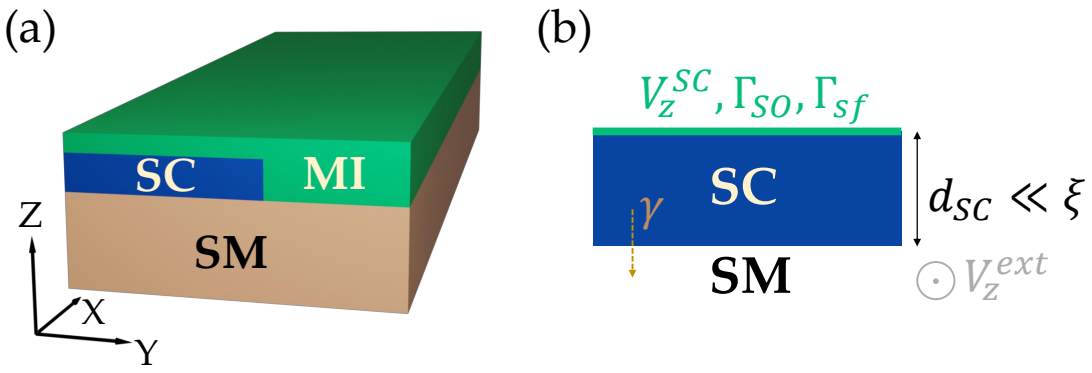

Figure 2.4: (a) Semiconductor (SM) nanowire proximitized by a superconductor–magnetic insulator (SC-MI) bilayer. (b) Effects of the magnetic insulator on the superconductor can be described by an appropriate boundary condition marked with green.

2.5 Topological superconductivity in nanowires proximate to a diffusive superconductor-magnetic insulator bilayer

As discussed in the introduction to this chapter, another potential way to mitigate detrimental effects of the external magnetic field on the parent superconductor is by introducing a magnetic insulators to the superconductor-semiconductor heterostructure. A typical setup of a combined heterostructure consists of semiconducting (SM), superconducting (SC) and magnetic insulator (MI) parts connected together as shown schematically in Fig. 3.1(a). Here the magnetic insulator such as EuS, induces a Zeeman spin splitting by virtual tunneling.

In this section we focus on the physics of MI/SC/SM stack. Instead of directly modeling the geometry shown in Fig. 3.1(a), we consider a variety of scattering mechanisms at the interface between the MI and the SC, as shown in Fig. 3.1(b). We assume that the effect of the interface between the MI and the SM, shown on the right side of Fig. 3.1(a), can be modeled by an effective bulk Zeeman field in the SM. To this end we de-

velop a two-step approach. First, utilizing the short mean free paths in superconductors, we calculate the properties of the MI-SC bilayer using the Usadel equation approach described in Section 2.3, and, second, we use this result as a boundary condition for the nanowire model. We apply the Usadel equation to compute the pair potential, critical temperature, and the density of states in the superconductor. Various physical processes such as applied magnetic field, exchange field from the magnetic insulator and scattering off magnetic and/or spin-orbit impurities in the SC are incorporated. Note that the magnetic and spin-orbit scattering is introduced phenomenologically to our model. Magnetic scattering can be either due to intrinsic magnetic impurities in the superconductor, or due to electron scattering off the magnetic insulator surface. Similarly, spin-orbit scattering can either be intrinsic to the superconductor, for example, as it happens in Pb, or result from scattering off heavy ions. The superconducting proximity effect is then readily described by the solution of the Usadel equation.

We will be focused on the experimentally relevant regime of a thin superconductor compared to its coherence length (see Fig. 3.1b). Furthermore, in this section we are interested in the regimes of small applied external magnetic fields, thus from now on we ignore the orbital contribution of the applied field, $\boldsymbol{A} = 0$.

To utilize the Usadel equation, the boundary between the superconductor and the magnetic insulator has to be supplemented with an appropriate boundary condition. General spin-dependent boundary conditions for the isotropic superconductor Green's function have been derived in Ref. [68]. In the case of a boundary between magnetic insulator and thin superconductor (with thickness much smaller than the coherence length $d_{SC} \ll \xi$), the authors of Ref. [68] showed that effects of the magnetic insulator on the superconductor can be described by a uniform effective Zeeman field $V_{eff}^{Z} \propto d_{SC}^{-1}$ and magnetic scattering induced in the superconductor.

It is worth mentioning here the crucial difference between clean and dirty supercon-

ductors. In the case of a clean SC, Ref. [69] showed that effects of the MI on the SC are distinct from those generated by the external Zeeman field. In particular, the transition of the clean SC adjacent to the MI into a normal state can be second order, as opposed to the strictly first order transition in the presence of the Zeeman field. However, an experiment from Ref. [42] demonstrated inadequacy of assuming clean Al when describing EuS-Al bilayers and indicated that dirty Al should be considered instead. Later on, Ref. [68] showed microscopically that, in the dirty limit, the impact of the MI on the SC is in fact equivalent to that of a Zeeman field and magnetic scattering.

2.5.1 Superconductor-semiconductor proximity effect

Once the quasiclassical Green's function of the parent SC is calculated using the Usadel equation, see Section 2.3, one can analyze the SC-SM proximity effect and investigate emergence of the topological phase in the heterostructure. The proximity effect arises due to electron tunneling between the superconductor and the semiconductor. Ignoring irreducible contributions in electron tunneling which can be shown to be much smaller than reducible ones [26, 70, 71], the proximity effect can be described by the disorder-averaged SC Green's function, and superconducting degrees of freedom in the system can be integrated out. As a result, effects of the parent SC on the SM can be fully incorporated into the interface self-energy $\check{\Sigma}(\omega)$[26]. Assuming spin-independent SC-SM electron tunneling [2], the interface self-energy reads

$$\check{\Sigma}(\omega) = |t|^2 \nu_0 \int d\xi_k \check{G}_{SC}(\xi_k, \omega) \tag{2.15}$$

with $|t|$ being the tunneling amplitude. Note that $\check{\Sigma}(\omega)$ in Eq. (2.15) does not depend on the Fermi momentum direction. Recalling the definition of the isotropic quasiclassical

[2]Spin-dependent tunneling between the SC and SM has been recently considered in Ref. [38]

Green's function, one can write

$$\check{\Sigma}(\omega) = -i\gamma\hat{\tau}_z\check{g}(\omega_n)|_{\omega_n\to -i\omega}, \tag{2.16}$$

where the SC-SM coupling $\gamma = \pi|t|^2\nu_0$ has been introduced.

The Green's function of the quasi-1D SM nanowire can be written as [26]

$$\check{G}^{-1}(k,\omega) = \omega - V_Z^{SM}\hat{\sigma}_x - [\xi_k + \alpha_R k\hat{\sigma}_y]\hat{\tau}_z - \check{\Sigma}(\omega). \tag{2.17}$$

Here V_Z^{SM} is the Zeeman field induced along the direction of the nanowire, for example due to magnetic proximity from the adjacent magnetic insulator and/or external magnetic field, $\xi_k = k^2/2m^* - \mu$ with m^* and μ being the SM effective electron mass and chemical potential, respectively, α_R is Rashba spin-orbit coupling, and $\check{\Sigma}(\omega)$ is given by Eq. (2.16). Writing $\check{g}(\omega_n)$ as in Eq. (2.8) gives

$$\begin{aligned}\check{G}^{-1}(k,\omega) = \omega + i\gamma\cosh\phi\cos\theta - (V_Z^{SM} + \gamma\sinh\phi\sin\theta)\hat{\sigma}_x - (\xi_k + \alpha_R k\hat{\sigma}_y)\hat{\tau}_z - \\ -\gamma\cosh\phi\sin\theta\hat{\tau}_y + i\gamma\sinh\phi\cos\theta\hat{\tau}_y\hat{\sigma}_x,\end{aligned} \tag{2.18}$$

where $\phi(\omega)$, $\theta(\omega)$ are analytically continued into the real time domain via $\omega_n \to -i\omega$. Equation (2.18) shows that proximity to the SC induces four extra terms in the nanowire Green's function: frequency shift $\propto \cosh\phi\cos\theta$, Zeeman energy $\propto \sinh\phi\cos\theta$, spin-singlet even-frequency pairing $\propto \cosh\phi\sin\theta$ and spin-triplet odd-frequency pairing $\propto \sinh\phi\cos\theta$. In the absence of spin-orbit and magnetic scattering in the SC, these proximity-induced terms can be calculated analytically. Appendix A.1 presents the corresponding expressions.

The low-energy spectrum of the system can be determined by computing poles of the

Green's function (2.18) from

$$\det[\check{G}^{-1}(k,\omega)] = 0. \tag{2.19}$$

To this end, one first calculates the self-consistent pair potential and determines the Clogston limit using Eqs. (2.9a)-(2.11). Next, the Usadel equations (2.9a)-(2.9b) are solved once again, this time in the real time domain using the self-consistent value of the pair potential. Then, the obtained real time quasiclassical Green's function parametrized through $\phi(\omega)$, $\theta(\omega)$ is plugged into Eq. (2.18), which produces expressions for the proximity-induced terms in the Green's function. Finally, the low energy spectrum of the system is inferred by solving Eq. (2.19).

The spectrum can be used to directly identify topological phase transitions (critical points are signified by gap closure and reopening) and the topological gap.

2.5.2 Results

In the following we first review the results of calculations for the parent SC in isolation. In particular, we analyze the dependence of the superconducting density of states, pair potential and critical temperature on Zeeman field and spin-orbit and magnetic scattering. Then we consider the SC-SM proximity effect and calculate the dependence of the topological phase transition on these parameters. Finally, the dependence of the topological gap on external magnetic field for various values of Zeeman field and/or spin-orbit and magnetic scattering in the SC is demonstrated.

Properties of the parent superconductor

We begin with an analysis of how Zeeman energy and spin-orbit scattering affect the SC. Although the results in this section are established [72, 73, 74, 75], we reproduce them here both as a validation of our methodology and to make the presentation self-contained.

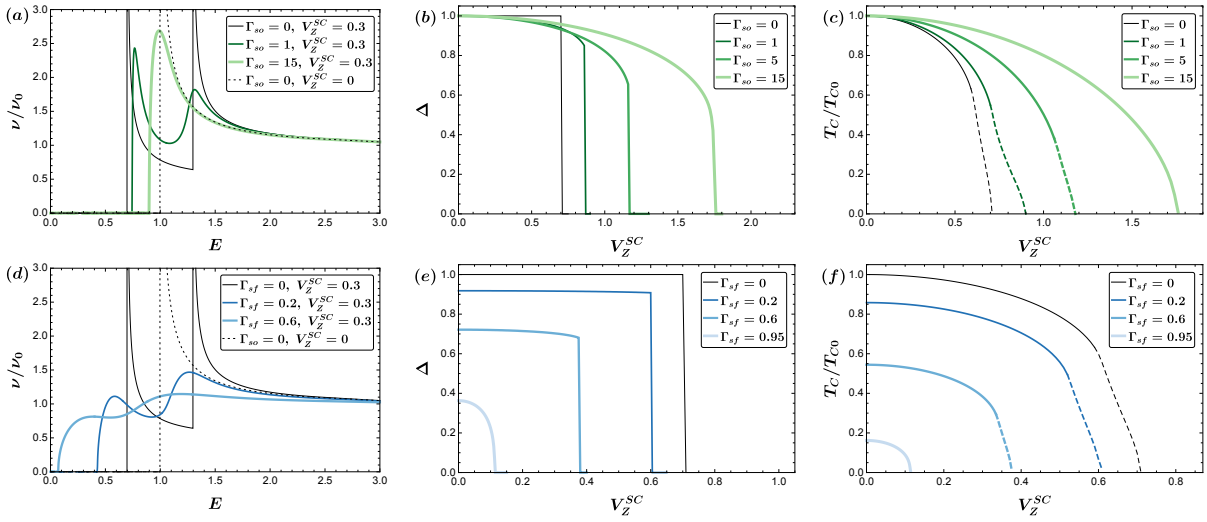

Figure 2.5: Dependence of density of states (left column), pairing potential (middle column) and critical temperature (right column) of the SC on Zeeman field V_Z^{SC} for various values of spin-orbit (upper row, Γ_{so}) and magnetic (lower row, Γ_{sf}) scattering energy. Magnetic scattering in (a)-(c) and spin-orbit scattering in (d)-(f) is set to zero. For (a)-(b) and (d)-(e), temperature is fixed to $T/T_{c0} = 0.01$. Solid (dashed) lines in (c) and (f) indicate second (first) order transition. All energies in (a)-(f) are measured in units of the bare superconducting gap Δ_{00}.

Figure 2.5(a) depicts the SC density of states of Eq. (2.12) plotted for a fixed value of Zeeman field and various values of spin-orbit scattering energies. Throughout energy is measured in units of the bare gap Δ_{00} of the SC when no Zeeman field or spin relaxation processes are present. Figure 2.5(a) demonstrates that the Zeeman energy splits the density of states in the superconductor into two spin bands. Spin-orbit scattering reduces the spin splitting in the SC formed by the Zeeman field and eventually merges the two spin-resolved peaks in the density of states into one; in the limit of infinite spin-orbit scattering a single-peak BCS density of states is recovered [73]. The pairing potential is likewise affected by spin-orbit scattering, as illustrated in Fig. 2.5(b) where we plot it as a function of Zeeman field for several values of Γ_{so}. In the absence of spin-orbit scattering, the pairing potential is constant as a function of V_Z^{SC} up to a value of $V_Z^{SC} = 1/\sqrt{2}$ where it vanishes and the system undergoes a first order transition into the normal state.

This critical value of Zeeman field is the Clogston limit [30, 31, 72] representing the maximum paramagnetic spin splitting that the SC can withstand. Adding spin-orbit scattering to the system pushes the Clogston limit to higher critical values of V_Z^{SC}; see Fig. 2.5(b). The pair potential in turn decreases as a function of V_Z^{SC} when $\Gamma_{so} \neq 0$ and for values of $\Gamma_{so} \gtrsim 15$ the transition to the normal state becomes second order. Lastly, we consider how the critical temperature T_c is impacted by both Zeeman field and spin-orbit scattering in Fig. 2.5(c). At finite Zeeman splitting spin-orbit scattering increases the critical temperature; just as in Fig. 2.5(b), spin-orbit scattering increases the Clogston limit, while values of spin-orbit scattering larger than a certain threshold result in the transition switching from first to second order.

Now we consider the combined effect of Zeeman energy and magnetic scattering on the SC in Fig. 2.5(d)-2.5(f). We present the density of states, plotted for a fixed value of Zeeman field and several values of magnetic scattering energies, in Fig. 2.5(d). Magnetic scattering smears out the density of states peaks and reduces the excitation gap. For sufficiently large values of Γ_{sf}, the SC becomes gapless [29]. Moving on to the analysis of the pairing potential, Fig. 2.5(e) depicts its dependence on Zeeman field and magnetic scattering. We observe that the presence of magnetic scattering in the SC reduces the pairing potential and, unlike spin-orbit scattering, decreases the Clogston limit. At the same time, similar to spin-orbit scattering, adding a sufficiently large Γ_{sf} switches the order of the transition from first to second. Figure 2.5(f), which presents the dependence of the critical temperature on Zeeman field and magnetic scattering, supports the above conclusions. The opposite behavior compared to spin-orbit scattering is observed, i.e., increasing the magnitude of magnetic scattering that breaks time-reversal symmetry reduces the critical temperature at all values of induced Zeeman splitting.

Topological phase transition

Having calculated self-consistent values of the pair potential in the parent SC, we now analyze the emergence of the topological phase in the proximitized nanowire. Importantly, the frequency dependence of the Green's function in Eq. (2.18) is irrelevant to the topological phase transition: at the critical point the energy gap at $k = 0$ closes, which enables one to identify the transition by setting $\omega_n = 0$ in Eqs. (2.9a)-(2.9b) and $k = \omega = 0$ in Eq. (2.18) as long as the correct self-consistent value of the pair potential $\Delta = \Delta(V_Z^{SC}, \Gamma_{so}, \Gamma_{sf})$ is given. In this case, Eq. (2.9a) gives $\theta = \pi/2$ while Eq. (2.9b) reads

$$\Delta \sinh\phi - V_Z^{SC}\cosh\phi + \frac{1}{3}\left(\Gamma_{so} - \frac{\Gamma_{sf}}{2}\right)\cosh\phi\sinh\phi = 0. \tag{2.20}$$

At the same time, the Green's function (2.18) becomes

$$\check{G}^{-1}(k=0,\omega=0) = -(V_Z^{SM} + \gamma\sinh\phi)\hat{\sigma}_x - \gamma\cosh\phi\hat{\tau}_y, \tag{2.21}$$

where for simplicity we set chemical potential in the nanowire to zero, $\mu = 0$. Note that the induced Zeeman energy (spin-singlet pairing) in the nanowire is equal to $\gamma\sinh\phi$ ($\gamma\cosh\phi$) while odd-frequency spin-triplet pairing vanishes. From Eq. (2.21) we identify the minimum Zeeman field in the SM necessary to create the topological phase, $V_{Z,c}^{SM}$, as

$$V_{Z,c}^{SM} = \gamma(\cosh\phi - \sinh\phi). \tag{2.22}$$

Rewriting Eq. (2.20) in terms of this quantity gives

$$\left(\Delta - V_Z^{SC}\right)\left(V_{Z,c}^{SM}/\gamma\right) - \left(\Delta + V_Z^{SC}\right)\left(V_{Z,c}^{SM}/\gamma\right)^3 + \frac{\Gamma}{6}\left[1 - \left(V_{Z,c}^{SM}/\gamma\right)^4\right] = 0, \tag{2.23}$$

where we denoted $\Gamma \equiv \Gamma_{so} - \Gamma_{sf}/2$. Note that Γ in general does not fully incorporate effects of spin relaxation processes on the topological critical point because the value of the self-consistent pair potential $\Delta = \Delta(V_Z^{SC}, \Gamma_{so}, \Gamma_{sf})$ depends on these processes as well. Although an analytic solution to the quartic equation (2.23) exists, in general it is cumbersome and we do not present it here. Instead, we build intuition by considering limiting behavior of Eq. (2.23). First, in the limit of $\Gamma = 0$, which corresponds either to the absence of spin relaxation processes $\Gamma_{so} = \Gamma_{sf} = 0$ or to the case when $\Gamma_{so} = \Gamma_{sf}/2$, we find that a minimum Zeeman field of

$$\frac{V_{Z,c}^{SM}}{\gamma} = \sqrt{\frac{\Delta - V_Z^{SC}}{\Delta + V_Z^{SC}}} \tag{2.24}$$

is required in the SM in order to induce topological superconductivity. For small but non-zero values of Γ, $|\Gamma| \ll \left(\Delta^2 - \left(V_Z^{SC}\right)^2\right)^{3/2} / \left(V_Z^{SC}\Delta\right)$, perturbative corrections to $V_{Z,c}^{SM}$ of Eq. (2.24) can be calculated. Up to first order in Γ we obtain

$$\frac{V_{Z,c}^{SM}}{\gamma} = \sqrt{\frac{\Delta - V_Z^{SC}}{\Delta + V_Z^{SC}}} + \frac{\Delta V_Z^{SC}}{3(\Delta - V_Z^{SC})(\Delta + V_Z^{SC})^2}\Gamma + O(\Gamma^2). \tag{2.25}$$

In the absence of spin-orbit and magnetic scattering, Eq. (2.24) demonstrates that it is impossible to close the gap without an additional Zeeman field in the SM: in this case the topological phase requires $V_Z^{SC} > \Delta$ which is prohibited by the Clogston limit. Adding a small spin-orbit scattering, which leads to a small positive Γ, does not improve the situation. On the contrary, the corresponding correction in Eq. (2.25) increases value of the critical Zeeman field. This behavior is a manifestation of the fact that spin-orbit scattering quenches spin splitting in the SC; see Fig. 2.5(a) and the corresponding discussion in Section 2.5.2. Due to this fact, the effective Zeeman energy transferred from the SC to the SM is decreased by the presence of spin-orbit scattering in the superconductor. On

the other hand, adding purely magnetic scattering, which leads to negative Γ, reduces the critical SM Zeeman field for a fixed value of V_Z^{SC}. However, magnetic scattering also suppresses the Clogston limit as has been discussed in Section 2.5.2, so that the maximum V_Z^{SC} that the parent SC can sustain is smaller. For this reason, adding magnetic scattering does not assist in reducing $V_{Z,c}^{SM}$. We show this below when we solve Eq. (2.23) numerically for self-consistent Δ and general values of $V_Z^{SC}, \Gamma_{so}, \Gamma_{sf}$.

Next, we consider the opposite limit of infinite spin-orbit scattering, $\Gamma_{so} \approx \Gamma \to \infty$, or no Zeeman splitting in the SC, $V_Z^{SC} = 0$. In both of these limits, Eq. (2.23) yields $V_{Z,c}^{SM} = \gamma$ regardless of the values of other parameters. Note that $V_{Z,c}^{SM} = \gamma$ is a familiar result for the topological criterion at zero chemical potential [26]. Expanding the solution of Eq. (2.23) near $V_{Z,c}^{SM} = \gamma$, we can find corrections for finite but large Γ_{so} or nonzero V_Z^{SC}:

$$\frac{V_{Z,c}^{SM}}{\gamma} = 1 - \frac{3V_Z^{SC}}{3\Delta + 6V_Z^{SC} + \Gamma_{so}} + \cdots , \tag{2.26}$$

which is valid as long as $3V_Z^{SC} \ll 3\Delta + 6V_Z^{SC} + \Gamma_{so}$. Further expanding Eq. (2.26) in the limit of large spin-orbit scattering $\Gamma_{so} \gg V_Z^{SC}, \Delta$ leads to

$$\frac{V_{Z,c}^{SM}}{\gamma} = 1 - \frac{3V_Z^{SC}}{\Gamma_{so}} + O\left(\frac{1}{\Gamma_{so}^2}\right). \tag{2.27}$$

Equation (2.27) shows once again that spin-orbit scattering suppresses Zeeman splitting in the SC. On the other hand, expanding Eq. (2.26) in the limit of small SC Zeeman energy $V_Z^{SC} \ll \Gamma_{so}, \Delta$ gives

$$\frac{V_{Z,c}^{SM}}{\gamma} = 1 - \frac{3V_Z^{SC}}{3\Delta + \Gamma_{so}} + O\left(\left(V_Z^{SC}\right)^2\right). \tag{2.28}$$

Figure 2.6 presents the solution of Eq. (2.23) for general values of V_Z^{SC} and Γ_{so}, Γ_{sf}. Self-consistent values of the pair potential $\Delta(V_Z^{SC}, \Gamma_{so}, \Gamma_{sf})$ cannot be in general obtained

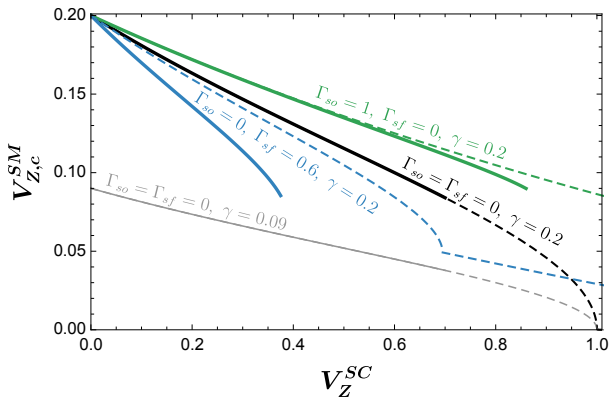

Figure 2.6: Critical Zeeman energy $V_{Z,c}^{SM}$ required to be added to the nanowire in order to induce topological phase versus Zeeman energy in the parent superconductor V_Z^{SC} for various values of spin-orbit and magnetic scattering and superconductor-semiconductor coupling γ. Solid lines are calculated self-consistently and terminate at the Clogston limit, while dashed lines are calculated non-self-consistently. Chemical potential in the nanowire is set to zero. All energies are measured in units of the bare superconducting gap Δ_{00}.

analytically, so in Fig. 2.6 we depict the curves $V_{Z,c}^{SM}(V_Z^{SC})$ for two different settings: (1) solid curves represent the situation when numerically calculated values of the self-consistent pair potential $\Delta = \Delta(V_Z^{SC}, \Gamma_{so}, \Gamma_{sf})$ [Fig. 2.5(b),(e)] are used in Eq. (2.23), while (2) dashed curves illustrate the case when Eq. (2.23) is solved with the non-self-consistent pair potential $\Delta = \Delta_{00}$. Each solid curve in Fig. 2.6 terminates at its respective Clogston limit when the parent superconductor transitions into the normal state. Even though spin-orbit scattering, if present in the SC, can push Clogston limit further — see Fig. 2.5(b)-2.5(c) and discussion in Section 2.5.2 — it also quenches spin splitting in the SC and, correspondingly, Zeeman energy transferred to the SM. At the same time, magnetic scattering suppresses the Clogston limit as can be seen in Figs. 2.5(e)-2.5(f). On top of that, magnetic scattering quenches the pair potential in the parent SC and thus has a detrimental effect on the topological gap; see Section 2.5.2. For this reason, spin-orbit and magnetic scattering do not assist in creating topological superconductivity in the nanowire.

Therefore, we emphasize again that the topological phase *cannot* be achieved in hybrid heterostructures when the Zeeman field is only induced in the parent superconductor, regardless of whether spin-orbit or magnetic scattering is present in the superconductor. This conclusion has been stated in recent works by other authors as well [35, 38], although they did not explicitly consider spin relaxation processes in the SC.

Reduction of the critical field $V_{Z,c}^{SM}$ can be achieved by weakening the SC-SM coupling γ, see Eq. (2.22) and the grey line in Fig. 2.6. However, in the weak coupling regime a smaller coupling leads to a smaller topological gap, see Section 2.5.2.

Dashed curves in Fig. 2.6 represent the results of non-self-consistent calculations. For $\Gamma_{sf} = 0$ these curves closely follow the solid self-consistent lines. However, in the presence of magnetic scattering (blue curve in Fig. 2.6) the dashed and the solid curves are positioned considerably off from each other because magnetic scattering substantially reduces the pairing potential; see Fig. 2.5(e). This reduction cannot be captured by the non-self-consistent pair potential. Another drawback of the non-self-consistent calculation is that it does not enforce the Clogston limit, and therefore the dashed curves in Fig. 2.6 do not terminate. This pathology could lead to incorrect conclusions about the topological phase diagram. For this reason, we emphasize the importance of self-consistency in the SC Green's function (and subsequent topological phase diagram) calculation if Zeeman energy and spin relaxation mechanisms are present in the superconductor.

Topological gap

Beyond the critical point, a crucial property of the topological phase is the spectral gap. A larger gap enhances the protection of the topological phase against quasiparticle poisoning and disorder. In this subsection, we calculate the gap in the nanowire and analyze its dependence on Zeeman splitting and spin-orbit and magnetic scattering in the parent SC. In general, because of the nontrivial frequency dependence of the Green's

function (2.18), the energy spectrum of the nanowire has to be computed numerically. Moreover, in case of spin relaxation processes present in the SC, the Usadel equations (2.9a)-(2.9b) are solved numerically as well. For this reason, we perform a numerical analysis of Eqs. (2.9a)-(2.9b), (2.18). Throughout the calculations we set the Rashba coupling in the nanowire to $\alpha = 0.2$ eV·Å and the effective electron mass to $m^* = 0.02m_0$, where m_0 is the electron rest mass. We continue using the bare gap of the parent SC $\Delta_{00} = 0.23$ meV as a unit of energy.

As discussed in Section 2.5.2, a certain Zeeman field $V_{Z,c}^{SM}$ has to be introduced directly to the semiconductor to achieve the topological phase. Here we consider the case when $V_{Z,c}^{SM}$ is created by applying an external Zeeman field V_Z^{ext} to the entire system. As stated in Section **??**, we ignore orbital effects of the magnetic field. We assume that there is no coupling between the SM and the MI, although this assertion can be easily adjusted in our framework by using a different parametrization of V_Z^{ext}. The total Zeeman energies of the SC and the SM are $V_Z^{SC} = g_{SC}V_Z^{ext} + V_{Z,0}^{SC}$ and $V_Z^{SM} = g_{SM}V_Z^{ext}$, respectively, where $V_{Z,0}^{SC}$ is the MI-induced Zeeman splitting in the SC and we take $g_{SC} = 2$ and $g_{SM} = -15$.

Figure 2.7 shows the computed spectral gap as a function of the chemical potential μ in the nanowire and the external Zeeman field V_Z^{ext} for $V_{Z,0}^{SC} = 0.55$ in the absence of the magnetic and spin-orbit scattering in the SC. The topological part of the phase diagram is marked red, solid black lines represent its boundary. If the MI does not couple to the SC — i.e., $V_{Z,0}^{SC} = 0$, — the phase boundary is depicted by dashed black lines. In this case the orientation of the external field does not play any role which is exhibited by the symmetry of the two dashed curves with respect to the $V_Z^{ext} = 0$ line. However, if the MI induces Zeeman splitting in the SC, the relative orientation of the two fields — V_Z^{ext} and $V_{Z,0}^{SC}$ — is important. In the antiparallel configuration, which corresponds to the case of $V_Z^{ext} < 0$ in Fig. 2.7, the Zeeman splittings created by the MI and the applied field have opposite signs in the SC and the same sign in the SM. As a result, the topological

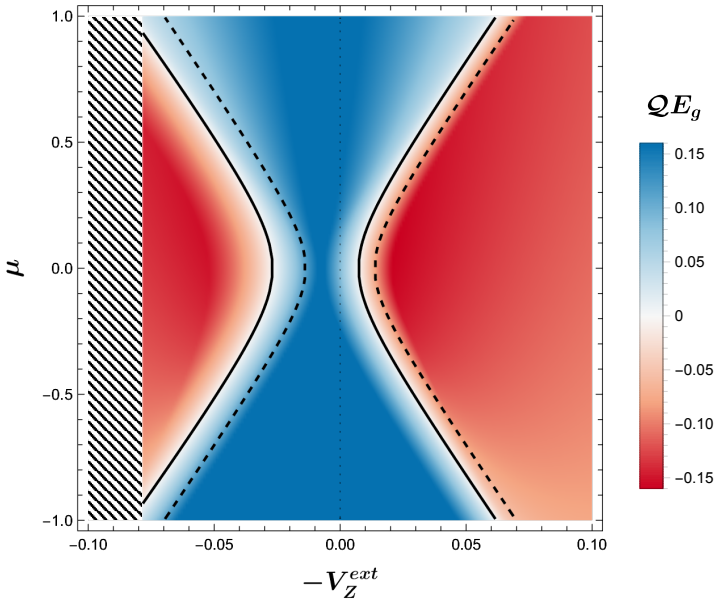

Figure 2.7: Spectral gap E_g (color) multiplied by the topological invariant $\mathcal{Q} = \pm 1$ as a function of the chemical potential μ in the semiconductor and the external Zeeman field V_Z^{ext} for $\Gamma_{so} = \Gamma_{sf} = 0$, $V_{Z,0}^{SC} = 0.55$. The phase boundary is marked by solid black lines. Dashed black lines represent the phase boundary when $V_{Z,0}^{SC} = 0$. The hatched region depicts the part of the phase diagram beyond the Clogston limit when superconductivity in the parent SC is destroyed. All energies are measured in units of the parent superconductor's bare gap Δ_{00}.

phase is achieved at smaller values of $|V_Z^{ext}|$ compared to the case when $V_{Z,0}^{SC} = 0$. On the other hand, when the direction of V_Z^{ext} is parallel to the magnetization of the MI — $V_Z^{ext} > 0$ in Fig. 2.7 — the Zeeman splittings have the same sign in the SC but the opposite signs in the SM. This is an unfavorable configuration for the topological phase: the Clogston limit in this case is reached at smaller values of the applied field, while the phase transition to the p-wave superconductivity requires a larger applied field compared to the case with no MI.

We now proceed to studying individual effects of the Zeeman splitting, spin-orbit and magnetic scattering on the topological gap. To this end, we fix the chemical potential in the nanowire to zero and plot the dependence of the gap on V_Z^{ext} in Fig. 2.8 for the antiparallel configuration of the applied field and the MI magnetization, which is

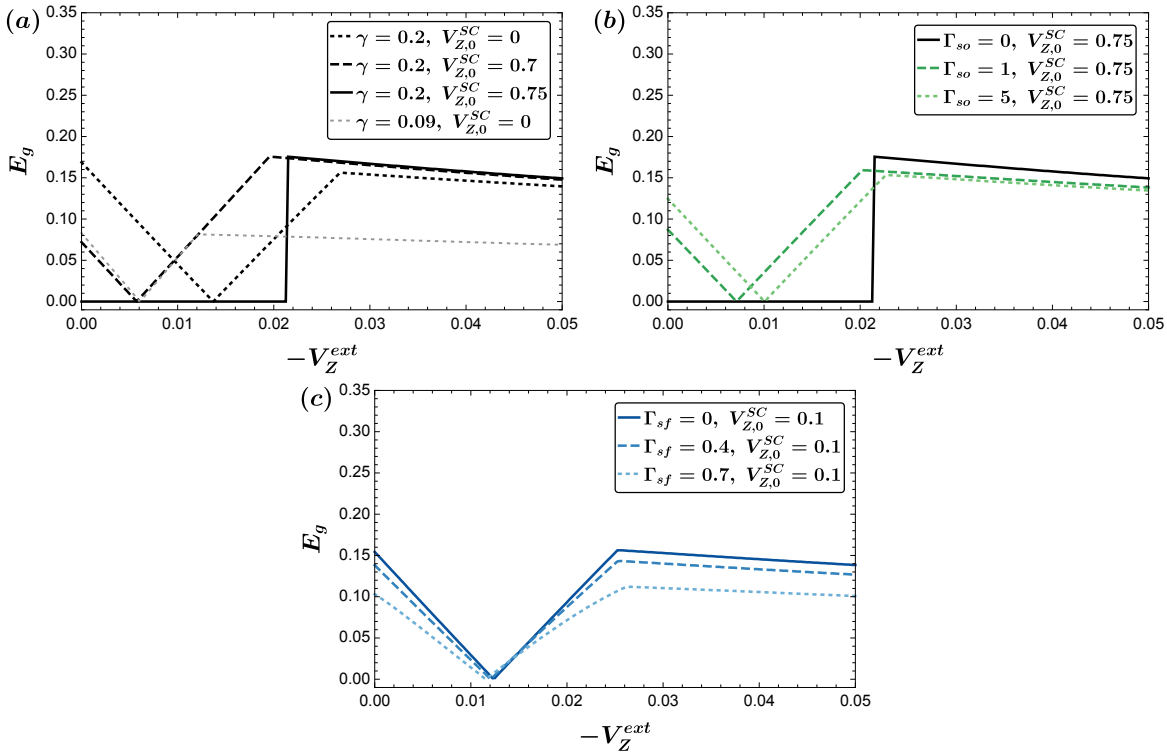

Figure 2.8: Energy gap in the proximitized nanowire as a function of external magnetic field $V_Z^{ext} = -\mu_B B/2$ for various values of SC-SM coupling γ, MI-induced Zeeman energy in the superconductor $V_{Z,0}^{SC}$, spin-orbit scattering Γ_{so} and magnetic scattering Γ_{sf}. $\Gamma_{so} = 0$ in (a),(c), $\Gamma_{sf} = 0$ in (a),(b) and $\gamma = 0.2$ in (b,c),(c). All curves are plotted for zero chemical potential in the nanowire. All energies are measured in units of the parent superconductor's bare gap Δ_{00}.

advantageous for the topological phase. First, we consider impact of $V_{Z,0}^{SC}$ in Fig. 2.8(a) in the absence of the spin-orbit and magnetic scattering. The black dotted curve in Fig. 2.8(a) shows the typical behavior of the energy gap as the system undergoes the topological transition between the s-wave (small $|V_Z^{ext}|$) and the p-wave (large $|V_Z^{ext}|$) superconductivity in the weak coupling regime ($\gamma = 0.2$) in the absence of any zero-field Zeeman splitting in the SC. The kink exhibited by the curve at $-V_Z^{ext} \approx 0.027$ appears where the minimum gap as a function of momentum jumps from $k = 0$ to $k \sim k_F$. Inducing finite Zeeman splitting in the SC results in the decrease of the critical Zeeman field as illustrated by the dashed line. Analogous reduction of the critical field can be

achieved by lowering the coupling between the SM and the SC (grey dotted line), but that also results in the reduction of the topological gap, whereas addition of the Zeeman energy to the SC keeps the gap approximately the same as long as $V_{Z,0}^{SC}$ is below the Clogston limit. Adding Zeeman energy larger than the Clogston limit leads to an interesting behavior; see solid line in Fig. 2.8(a). In this case at zero field the superconductivity in the parent SC is broken due to the proximitizing MI, but application of the external field restores it back. As a result, the system undergoes the first order transition from the normal phase directly into the p-wave superconducting phase with the topological gap close to the one of the MI-free system.

As we have previously pointed out while discussing Fig. 2.6, spin-orbit scattering can quench the Zeeman effect in the superconductor, enhancing its Clogston limit, but also reducing the Zeeman energy effectively transferred to the nanowire. This is illustrated in Fig. 2.8(b) where we plot the gap as a function of the external field for different values of Γ_{so}. We consider the case when Zeeman energy above the Clogston limit is induced in the superconductor [solid line, same as in Fig. 2.8(a)]. Increasing the spin-orbit scattering in the parent SC restores its superconductivity, and a regular transition between the s- and p-wave phase is observed at finite Γ_{so}. Further increase of Γ_{so} leads to the enhancement of the critical field due to the suppression of the Zeeman splitting in the superconductor.

Effects of the magnetic impurity scattering on the topological gap are illustrated in Fig. 2.8(c). As has been discussed in Section 2.5.2, magnetic scattering reduces the pairing potential in the parent SC. This leads to a minute reduction of the critical field in Fig. 2.8(c) and a visible suppression of the topological gap. Overall, we conclude that the presence of the magnetic scattering in the parent SC is not desirable for creating the topological phase in the nanowire.

2.6 Conclusion

In this chapter we have presented a theoretical approach to calculate properties of disordered superconductors affected by various physical mechanisms, such as Zeeman splitting, orbital magnetic field, magnetic and spin-orbit scattering, and furthermore topological properties of nanowires proximitized by such superconductors. We have used the Usadel equation to calculate how these mechanisms affect the intrinsic properties of the superconductors, and further calculated how the superconductor changes the topological properties of a proximate semiconducting wire. Using this approach, we have studied how heavy atoms such as Pt and the spin-orbit scattering they introduce can reduce the spin-splitting effect in the parent superconductor and thus push the critical Zeeman field further from the conventional (spin-orbit-scattering-free) value. Using these results, we have estimated the degree of the spin-orbit scattering in the Pt-Al-InSb heterostructure experiments depending on the thickness of the Pt layer, and obtained the correct scaling of the spin-orbit scattering energy with the Pt layer thickness.

Furthermore, we have applied the developed Usadel formalism to study nanowires proximitized by superconductor-magnetic insulator bilayers and calculated how the presence of the magnetic insulator in the bilayer affects the need for the external magnetic field to induce the topological phase in the nanowire. In particular, similar to other recent theoretical results [35, 36, 37, 39, 40] we report that a finite Zeeman energy in the semiconductor, either induced by coupling to a magnetic insulator or by an applied magnetic field, is required to enter the topological phase – a bound we estimate analytically. When introducing this Zeeman energy as a result of the applied magnetic field, we observe that the critical field and the topological gap depend on the relative orientation of the applied field and the MI-induced Zeeman splitting in the superconductor: only in the configuration when they are antiparallel one finds reduced critical field and

larger stability with respect to the absolute magnitude of the applied field. Introducing magnetic and spin-orbit scattering to the superconductor, we find that the former in general is detrimental to the topological phase – it reduces the Clogston limit in the superconductor and leads to a smaller topological gap. At the same time, spin-orbit scattering quenches the magnetic response of the superconductor, allowing it to sustain larger Zeeman fields, but also increases the critical field required to reach the topological phase.

Chapter 3

Visibility of noisy quantum dot-based measurements of Majorana qubits

3.1 Permissions and Attributions

1. The content of Chapter 3 and Appendix B is the result of a collaboration with Torsten Karzig and Dmitry I. Pikulin, and has previously appeared in the SciPost Physics 10, 127 (2021)[14]. It is reproduced here with the permission of SciPost Foundation: `https://scipost.org`.

3.2 Introduction

Majorana Zero Modes (MZMs) are explored as a promising platform for topological quantum computation [76, 10, 11, 77, 28]. As a direct consequence of their nonlocal nature, Majorana-based qubits are, in principle, less susceptible to decoherence and can pro-

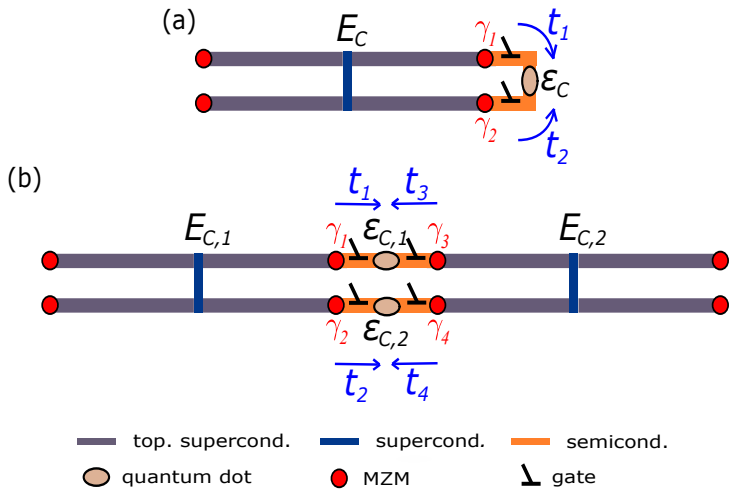

Figure 3.1: Schematic of the measurement setup of multi-MZM qubit islands. Only the measured MZMs of the qubit are labeled. (a) 2-MZM (single qubit) measurement setup. (b) 4-MZM (two qubit) measurement setup.

vide better protected gates when compared to conventional qubits. Throughout the past decade a lot of experimental progress has been made on detecting signatures of the MZMs via observing robust zero-bias conductance peaks [78, 79, 80, 81, 82, 83, 84], a 4π-periodic Josephson effect [85, 86, 87], signatures of exponential length-dependence of energy splittings [88, 89], and coherent single electron charge transfer between superconductors [90]. Though promising, these signatures have been proved inconclusive to make a definitive judgment on the presence of the MZMs in the system [91, 92, 93, 94, 95, 96, 97, 98]. For this reason a measurement of a topological Majorana qubit draws significant attention from both experimental and theoretical standpoints. A successful implementation of such a readout of a topological qubit would mark the transition from studying properties of the topological phase to topologically protected quantum information processing. Moreover, as physically moving MZMs [99] currently appears to be practically challenging, measurement-based schemes [100, 101] come to the forefront as the most likely means of operating a Majorana-based topological quantum computer.

Various theoretical proposals for Majorana qubits and their readout procedure have

been put forward [102, 103, 104, 105, 106, 107, 108, 109] Here we concentrate on the design for the qubit that features a superconducting island in the Coulomb blockaded regime [105, 106] consisting of two or more one-dimensional topological superconductors – realized for example in proximitized semiconductor nanowires [19, 20] – connected by a trivial superconductor. Each topological superconductor carries two MZMs at the ends. The qubit state is encoded by the parity of pairs of MZMs, e.g., $\sigma^z = i\gamma_i\gamma_j$, where σ^z is Pauli operator in the computational space of the qubit and $\gamma_{i/j}$ are the corresponding Majorana operators. The total parity of a qubit island is conserved, which fixes the parity of the other two MZMs in 4-MZM islands. Measurements of the qubits are performed by coupling two (for single qubit measurements, see Fig. 3.1(a)) or four (for two-qubit measurements, see Fig. 3.1(b)) MZMs to quantum dots (QDs) while using parity-dependent shifts of the QD charge or capacitance as the readout signal. Such QD-based measurements are particularly promising since they can be embedded in scalable designs for the operation of topological qubits [106]. Motivated by this prospect, experimental studies of QD measurements in materials suitable for topological qubits are emerging [110, 111].

Despite the topological protection of Majorana qubits, quantum information storage and measurements are never perfect in practice due to sources of noise intrinsic and extrinsic to the qubit system. Quantifying the effect of noise is thus essential to understand the prospective performance of topological qubits. The effect of noise within the topological superconductors has been considered as the cause of the slow decoherence of idle qubits [112, 113] or as a possible reduction of the visibility of 2-MZM measurements [114]. Crucially, coupling the Majorana qubit to the QDs of the readout apparatus introduces new sources of noise. The desired effect of this noise is to collapse the qubit state into the outcome of the measurement [115, 116]. However, noise coupling to the QDs can also have negative effects on the visibility of the measurement and with the known susceptibility of QD to charge noise one might wonder whether QDs are a suitable platform

for high-fidelity measurements. In this chapter we study the effect of such noise on the measurement visibility and show that typical strengths of QD noise allow for high-fidelity qubit measurements.

To study the optimal operation point of measurements we will pay particular attention to the regime where the QD and the qubit island are tuned close to resonance (i.e. energy detuning between the two is much smaller than the MZM-QD coupling) in contrast to the widely applied far-detuned regime where the MZM-QD coupling is much smaller than the energy detuning and can be considered perturbatively [106, 105]. Such careful tuning to resonance can be particularly beneficial for 4-MZM measurements which were previously not discussed in this regime.

The rest of the chapter is organized as follows. First, we review the single qubit measurements paying particular attention to the regime of the resonantly coupled island-QD system. We then extend this analysis to two-qubit measurements. Next, focusing on the single qubit measurement case, we analyze how noise in island-QD detuning affects the measurement visibility by calculating the signal-to-noise ratio (SNR) of the measurements. The Appendix presents details of calculations and treatment of the subleading noise sources – flux and coupling noise.

3.3 QD-based measurements

We start by reviewing how coupling a single QD to a pair of MZMs leads to a measurable change in the properties of the coupled MZM-QD system that depend on the parity of the MZMs before generalizing to measurements of four MZMs. As we show below, the regime of maximal measurement visibility is typically achieved when the QD and the qubit island are tuned so that the energy configurations of an electron occupying the QD or the qubit island are close-to degeneracy. We therefore pay particular attention to this

regime, which we refer to as resonant regime, and discuss how careful tuning enhances the visibility of 4-MZM measurements to be of similar order as the 2-MZM measurements.

3.3.1 2-MZM measurement

A typical setup for a 2-MZM single qubit measurement is depicted in Fig. 3.1(a). The effective low-energy Hamiltonian of the qubit-QD system is given by

$$\hat{H} = \hat{H}_{\mathrm{C}} + \hat{H}_{\mathrm{QD}} + \hat{H}_{\text{QD-MZM}}. \tag{3.1}$$

Here $\hat{H}_{\mathrm{C}}$ is the charging energy Hamiltonian of the superconducting island, $\hat{H}_{\mathrm{QD}}$ is a Hamiltonian of the QD and $\hat{H}_{\text{QD-MZM}}$ is a term describing tunneling between the island and the QD through MZMs.

Both $\hat{H}_{\mathrm{C}}$ and $\hat{H}_{\mathrm{QD}}$ contain charging energy contributions due to capacitance to the ground and between the subsystems. Additionally, $\hat{H}_{\mathrm{QD}}$ contains the energy of the single-particle level on the QD. Due to charge conservation these contributions can be combined into:

$$\hat{H}_{\mathrm{C+QD}} = \varepsilon_{\mathrm{C}}(\hat{n} - n_{\mathrm{g}})^2. \tag{3.2}$$

with $\hat{n}$ being the charge occupation of the QD while ε_{C} and n_{g} denote the effective charging energy and effective dimensionless gate voltage of the island-QD system. Expressions for the effective parameters in terms of original parameters of $\hat{H}_{\mathrm{C}}$ and $\hat{H}_{\mathrm{QD}}$ are given in Appendix B.1. Here we assumed a single-level QD without spin degeneracy, which is a valid assumption in high external magnetic field for small enough QD when the energy difference between the two lowest levels of the dot is larger than the MZM-QD coupling.

The tunneling Hamiltonian reads:

$$\hat{H}_{\text{QD-MZM}} = e^{-i\hat{\phi}}(t_1 f^\dagger \gamma_1 + t_2 f^\dagger \gamma_2) + \text{h.c.} \tag{3.3}$$

where t_α, $\alpha = 1, 2$ are coupling matrix elements of the MZMs to the fermionic mode on the QD described by creation operator $f^\dagger$. Note that since the Majorana operators are chargeless charge conservation is ensured by the operator $e^{i\hat{\phi}}$ that raises charge of the island by one electron charge. The couplings can be written as

$$t_\alpha = |t_\alpha| e^{i\phi_\alpha};\ \alpha = 1, 2; \tag{3.4}$$

where the gauge invariant phase difference $\phi_1 - \phi_2$ depends on microscopic details of the matrix elements but can be tuned by varying the magnetic flux penetrating the enclosed area of the interference loop (see Fig. 3.1).

We now focus on the regime close to the QD-Majorana-island resonance, where $n_\text{g} = 1/2 + \Delta/2\varepsilon_\text{C}$ and the detuning Δ between the island and the QD level is $\Delta \ll \varepsilon_\text{C}$. The low energy Hamiltonian is then spanned by four states $|n, p\rangle$ where $n = 0, 1$ and $p = \pm 1$ are eigenvalues of the QD occupation and combined parity $p = p_{12}(-1)^n$ with $p_{12} = i\gamma_1\gamma_2$ being MZM parity. In contrast to the case of large detuning where the charge of the qubit island is fixed except for virtual tunneling events [105, 106] it is important to note that in the presence of the QD p_{12} is no longer conserved. A non-demolition measurement therefore cannot directly determine p_{12}. Instead, the measurement outcome depends on the parity of the combined MZM-QD system p which is a constant of motion in the absence of exponentially weak qubit dynamics [102, 116, 115]. Within the model discussed here, this manifests in a block-diagonal form of the Hamiltonian. Using the basis $|n, p\rangle$ with $|1, p\rangle = e^{-i\hat{\phi}} f^\dagger \gamma_1 |0, p\rangle$ the elements of the Hamiltonian blocks of given

p can be directly read off from Eqs.(4.2) and (3.3) with the parity dependence entering via $\langle 1,p|t_2 e^{-i\hat{\phi}} f^\dagger \gamma_2|0,p\rangle = -ipt_2$ such that

$$\hat{H}_p = \begin{pmatrix} \Delta/2 & \bar{t}_p^* \\ \bar{t}_p & -\Delta/2 \end{pmatrix} . \tag{3.5}$$

Here we introduced the effective MZM-QD coupling $\bar{t}_p = t_1 - ipt_2$. Equation (3.5) allows for a straight forward interpretation of the effect of p on the MZM-QD system. Due to the interference of the two different paths that couple the QD and the qubit island, p will control the strength of the effective coupling $|\bar{t}_p| = \sqrt{|t_1|^2 + |t_2|^2 + 2p|t_1 t_2|\sin\phi}$ where $\phi = \phi_2 - \phi_1$.

The parity-dependence of the coupling has measurable consequences for several observables and is used to diagnose the parity of the MZMs. The energy spectrum of the system takes the form

$$\varepsilon_{p,\pm} = \pm\frac{1}{2}\sqrt{\Delta^2 + 4|\bar{t}_p|^2}. \tag{3.6}$$

Figure 3.2(a) illustrates the energy spectrum in the case of $\phi = \pi/2$ and $|t_1| = 1.5|t_2|$. Even though optimal visibility is achieved when $|t_1| = |t_2|$ where $\bar{t}_p$ is either maximal or zero depending on the parity p, here we present plots away from this fine tuned point since a certain degree of the coupling asymmetry is expected in the QD-based readout experiments. Using the ground state of (3.6) the corresponding charge expectation value of the QD in the $\Delta \ll \varepsilon_{\rm C}$ limit can be obtained as

$$\langle n_{{\rm QD},p}\rangle = n_{\rm g} - \frac{1}{2\varepsilon_{\rm C}}\frac{\partial \varepsilon_{p,-}}{\partial n_{\rm g}} = \frac{1}{2} + \frac{\Delta}{2\sqrt{\Delta^2 + 4|\bar{t}_p|^2}} . \tag{3.7}$$

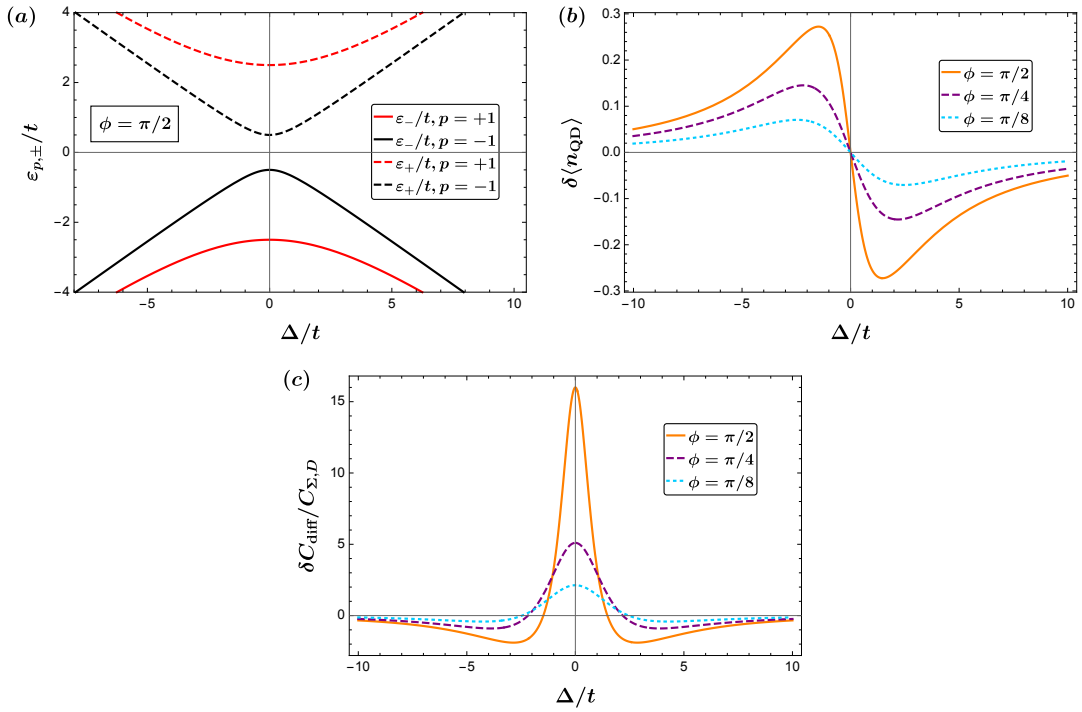

Figure 3.2: (a) MZM parity dependent part of the energies of the two lowest QD-MZM levels (3.6) as a function of island-QD detuning Δ in units of the MZM-QD hopping t. (b) Average QD charge difference between the two parity states $\delta\langle n_{\rm QD}\rangle = \langle n_{{\rm QD},p=+1}\rangle - \langle n_{{\rm QD},p=-1}\rangle$ as a function of detuning. (c) Differential capacitance difference between the two parity states $\delta C_{\rm diff} = C_{\rm diff,+} - C_{\rm diff,-}$ as a function detuning. We set $|t_1| = t,\ |t_2| = 1.5t$ for (a)-(c) and $C_{\rm g}/C_{\Sigma,{\rm D}} = 2$, $\varepsilon_{\rm C} = 5t$ for (c).

The differential capacitance in the same limit takes the form

$$\frac{C_{{\rm diff},p}}{C_{\rm g}^2/C_{\Sigma,{\rm D}}} = \frac{1}{2\varepsilon_{\rm C}}\frac{\partial^2\varepsilon_{p,-}}{\partial n_{\rm g}^2} = -\frac{4\varepsilon_{\rm C}|\bar{t}_p|^2}{(\Delta^2+4|\bar{t}_p|^2)^{3/2}} \tag{3.8}$$

where $C_{\rm g}$ is the capacitance between the gate and the QD and $C_{\Sigma,{\rm D}} \equiv e^2/2\varepsilon_{\rm C}$ is the total capacitance of the QD.

These two observables (3.7)-(3.8) can be measured in charge sensing, or quantum capacitance measurements respectively. Here we do not consider the details of the corresponding measurements but instead use the observables as a proxy for the measurement outcomes.

Fig. 3.2(b)-(c) depict the Δ-dependence for various values of the phase ϕ of the charge expectation and differential capacitance for the ground state of the system at different parities p. In the absence of noise the parity dependence of the observables is strongest at $\phi = \pi/2$ and at or close to zero detuning.

In the most favorable regime close to zero detuning it becomes particularly important that p is measured while we are ultimately interested in p_{12} of the island decoupled from the QD. Failure to correctly infer p_{12} from the measured value of p would result in a measurement error and ultimately decrease readout and (in case of measurement-based topological quantum computing) gate fidelity. Connecting the measurement of p to p_{12} requires a well-defined initialization and finalization procedure of the measurement where the QD charge before and after the measurement is known. Charge conservation then allows to infer p_{12} of the decoupled system from the measured p. A possible procedure is given by adiabatic tuning where the QD starts out and ends up far-detuned from resonance before and after the measurement to ensure a fixed charge state. The measurement is then initiated by first turning the MZM-QD coupling on and then tuning the system to resonance while the decoupling proceeds in opposite order. An alternative to this adiabatic tuning procedure would be to explicitly check the QD charge before and after the measurement by a separate charge measurement. Indeed, even if a close to adiabatic tuning is attempted such additional measurement might be required when one is aiming at very high measurement fidelities.

3.3.2 4-MZM measurement

The setup for a 4-MZM measurement is shown in Fig. 3.1(b). 4-MZM measurements can be done utilizing only one QD. Here we consider two QDs since they provide greater tunability and are likely the generic case in scalable designs [106]. Similarly to 2-MZM

situation, the effective low-energy Hamiltonian of this system has the form of (3.1). $\hat{H}_{\mathrm{C}}$ and $\hat{H}_{\mathrm{QD}}$ contributions are given in Appendix B.1 while the tunneling Hamiltonian reads:

$$\hat{H}_{\text{QD-MZM}} = e^{-i\hat{\phi}_1}(t_1 f_1^\dagger \gamma_1 + t_2 f_2^\dagger \gamma_2) + e^{-i\hat{\phi}_2}(t_3 f_1^\dagger \gamma_3 + t_4 f_2^\dagger \gamma_4) + h.c. \tag{3.9}$$

where t_α are couplings of the QDs described by fermionic operators $f_\beta^\dagger$ to the respective MZMs and $e^{i\hat{\phi}_\beta}$ is the raising operator of the charge of the island β.

For concreteness we consider the case where the system is tuned such that the lowest energy states are given by the 4 configurations of a single excess electron located on one of the QDs or islands. We denote the corresponding energies in the absence of tunnel coupling as ε_α with $\alpha \in \{\mathrm{i1}, \mathrm{i2}, \mathrm{d1}, \mathrm{d2}\}$ denoting the position of the electron. These energies are determined by the individual and mutual charging energies of the islands and QDs, and by the single-electron levels on the QDs. As in the 2-MZM case we will be particularly interested in the resonant regime where the energies ε_α become small. This requires tuning three parameters in general and can be done by tuning gate voltages on the two QDs and one of the islands.

Given that couplings of the low-energy subspace to MZMs other than $\gamma_1 \dots \gamma_4$ are exponentially small, the total parity $p = p_{12}p_{34}(-1)^{n_1+n_2}$, where $n_\beta = f_\beta^\dagger f_\beta$, is conserved. We thus denote the low energy states as $|\alpha, p\rangle$:

$$|\mathrm{i1}, p\rangle = e^{-i\phi_1} e^{i\hat{\phi}_1} \gamma_1 f_1 \, |\mathrm{d1}, p\rangle \tag{3.10}$$

$$|\mathrm{i2}, p\rangle = e^{-i\phi_3} e^{i\hat{\phi}_2} \gamma_3 f_1 \, |\mathrm{d1}, p\rangle \tag{3.11}$$

$$|\mathrm{d2}, p\rangle = e^{i\phi_2} e^{-i\hat{\phi}_1} f_2^\dagger \gamma_2 \, |\mathrm{i1}, p\rangle \tag{3.12}$$

where we included the phases of the tunnel matrix elements $t_\alpha = |t_\alpha| e^{i\phi_\alpha}$ for convenience.

In the above basis the Hamiltonian takes the form

$$H = \begin{pmatrix} \varepsilon_{\mathrm{d}1} & |t_1| & |t_3| & 0 \\ |t_1| & \varepsilon_{\mathrm{i}1} & 0 & |t_2| \\ |t_3| & 0 & \varepsilon_{\mathrm{i}2} & -p|t_4|e^{i\phi} \\ 0 & |t_2| & -p|t_4|e^{-i\phi} & \varepsilon_{\mathrm{d}2} \end{pmatrix}, \tag{3.13}$$

where $\phi = \phi_1 - \phi_2 - \phi_3 + \phi_4$.

From the form of the Hamiltonian (3.13) it becomes clear that the energies of the system are independent on the individual 2-MZM parities and instead will depend via ϕ on the flux passing through the loop of the 4 tunneling junctions and on the overall parity p which acts as a π phase shift of ϕ. Since the goal of the measurement is to ultimately determine 4-MZM parity $p_{12}p_{34}$ a similar tuning procedure as for 2-MZM measurements is required to fix the QD occupation. In fact, while the relation between p and $p_{12}p_{34}$ suggests that the tuning procedure only needs to ensure that the joint QD parity $(-1)^{n_1+n_2}$ is the same before and after the measurement the charge occupation of all islands and QD need to remain unchanged by the measurement. The reason is that the measurement should determine $p_{12}p_{34}$ while not otherwise disturbing the quantum state of the qubits. Any net transfer of electrons between the islands or between the QDs relative to their state before the measurement would result in applying the corresponding operators involved in the electron transfer $\gamma_i\gamma_j$ to the qubit states. Without a tuning procedure that ensures the occupation of the final configuration or an additional measurement to determine the configuration, the application of unknown pairs of Majorana operators would lead to dephasing. A possible tuning procedure from the resonant measurement configuration would work in a circular way: first detune the QD 1 to favor an occupation $n_1 = 1$, then tune island 1 to favor the empty state, followed by tuning QD 2 and island 2 to the empty state as well. Tuning all the couplings to zero then ensures a well defined

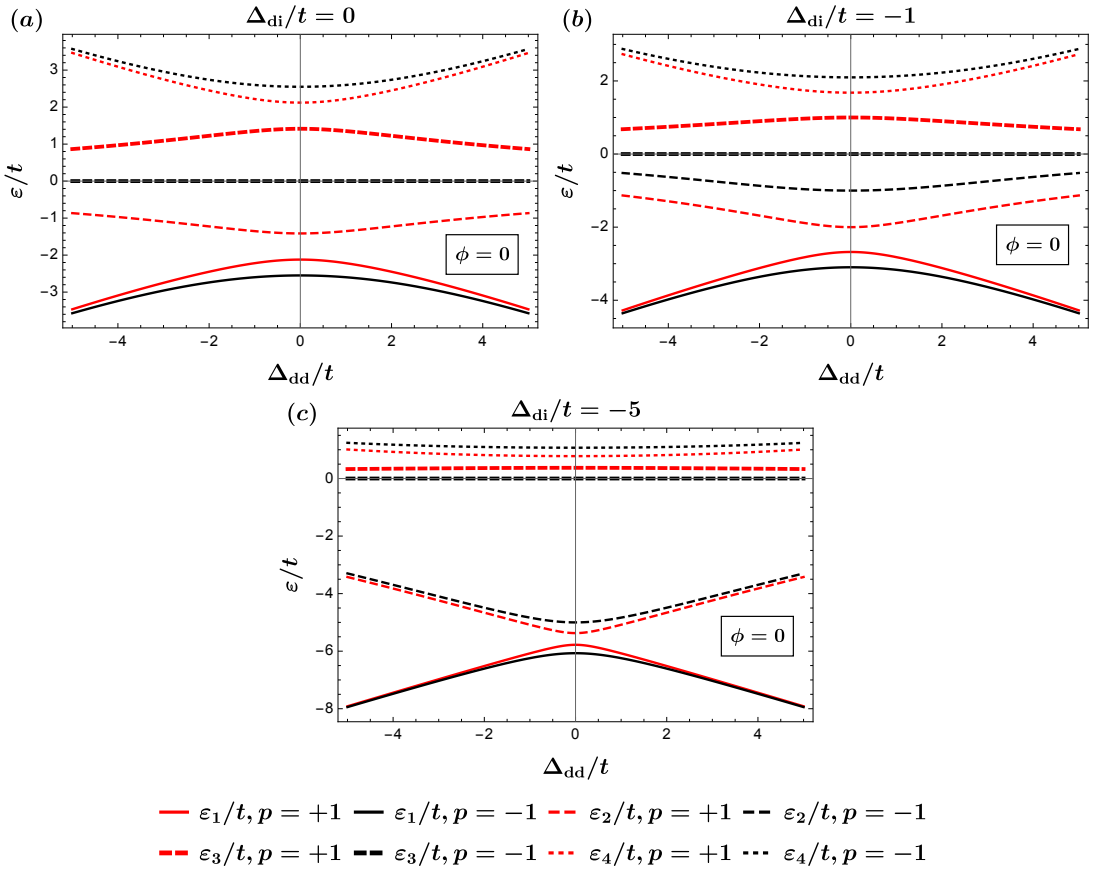

Figure 3.3: Eigenenergies of the Hamiltonian (3.13) for different parities p and as a function of QD-QD detuning $\Delta_{\rm dd}$ for various values of QD-island detuning $\Delta_{\rm di}$. Here we set $|t_1| = |t_2| = 1.5t$, $|t_3| = |t_4| = t$. Panel (a) is given by the analytical expressions of Eq. (3.16). Legends are the same as in Fig. B.1.

charge configuration. The initialization procedure would be done in opposite order.

Exact diagonalization of (3.13) for arbitrary parameters involves cumbersome expressions. To gain intuition about the behavior of the energy levels we keep $\varepsilon_{\rm i1} = \varepsilon_{\rm i2}$ while introducing the QD detuning $\Delta_{\rm dd} = \varepsilon_{\rm d1} - \varepsilon_{\rm d2}$ and the average detuning $\Delta_{\rm di} = (\varepsilon_{\rm d1} + \varepsilon_{\rm d2})/2 - \varepsilon_{\rm i1}$ between the QDs and islands. For now, we will also set $\Delta_{\rm di} = 0$. The energy eigenvalues ε are then given by the equation

$$\varepsilon^4 - \varepsilon^2 \left(\frac{1}{4}\Delta_{\rm dd}^2 + t_\Sigma^2 \right) - \frac{1}{2}\varepsilon \Delta_{\rm dd} t_\delta^2 + \bar{t}_p^{(4)}(\phi)^4 = 0 \tag{3.14}$$

in terms of $t_\Sigma^2 = \sum_{\alpha=1}^4 |t_\alpha|^2$, $t_\delta^2 = |t_1|^2 + |t_3|^2 - |t_2|^2 - |t_4|^2$ and the interference term

$$\bar{t}_p^{(4)}(\phi)^4 = |t_1 t_4|^2 + |t_2 t_3|^2 + 2p|t_1 t_2 t_3 t_4| \cos\phi \,. \tag{3.15}$$

The qualitative behavior is already captured by the case $t_\delta = 0$ which can be solved analytically yielding

$$\varepsilon_p^{(4)}(\phi) = \pm \frac{1}{\sqrt{2}} \sqrt{\frac{\Delta_{\rm dd}^2}{4} + t_\Sigma^2 \pm \sqrt{\left(\frac{\Delta_{\rm dd}^2}{4} + t_\Sigma^2\right)^2 - 4\bar{t}_p^{(4)}(\phi)^4}}. \tag{3.16}$$

The case of $t_\delta \neq 0$ is considered in Appendix B.3.

Going beyond $\Delta_{\rm di} = 0$, Fig. 3.3 shows plots of the energy eigenvalues of (3.13) as functions of $\Delta_{\rm dd}$ for $\phi = 0$, $t_\delta = 0$ and various values of island-QD detuning $\Delta_{\rm di}$. For large negative $\Delta_{\rm di}/t$ we recover the perturbative regime obtained in [106] where the parity dependent energy shift is of order $t^2/\Delta_{\rm di}$. Figure 3.3 demonstrates that the energy differences between the ground states of different parity is maximal when the MZM-QD couplings are symmetric $|t_\alpha| = t$ and the system is on resonance $\Delta_{\rm dd} = \Delta_{\rm di} = 0$. By appropriately tuning the 4-MZM measurement system close to these parameters it becomes possible to reach a similarly strong parity dependence as in the case of 2-MZM measurements. Specifically, in the case of $\phi = 0$, $|t_\alpha| = t$, and $\Delta_{\rm dd} = \Delta_{\rm di} = 0$ one finds $\varepsilon_{+,\rm gs}^{(4)} - \varepsilon_{-,\rm gs}^{(4)} = (\sqrt{2} - 2)t$ which is of similar order as for the 2-MZM case. For a more explicit comparison of the capacitive response see App. B.2.

For the purpose of the following sections we note that the low energy part of the 4-MZM system spectrum in Fig. 3.3 (energies ε_1 and ε_2) qualitatively resembles the one of the 2-MZM system, see Fig. 3.2(a). Since all measurement visibility properties we consider in the next section are derived from the low energy part of the spectrum, we conclude that 4-MZM and 2-MZM cases are qualitatively similar in this regard and thus

concentrate on the simpler 2-MZM case [1].

3.4 Noise and its effects on measurement visibility

We now describe the noise that will broaden the distribution of the observables. Here, we pay particular attention to intrinsic noise sources and their dependence on the system parameters. External noise sources, like amplifier noise, do not depend on the system parameters and are uncorrelated with the system noise – therefore they can be added straight-forwardly. The leading internal noise source in the measurement setup of Fig. 3.1 would likely be the charge noise which affects the on-site energy and thus detuning of the QDs. In our study we assume the $1/f$ power spectrum of the charge noise which has been reported in other QD-based devices, most notably semiconductor charge qubits [117, 118, 119]. We discuss noise in the strength of the tunnel couplings and flux noise which affects the phase ϕ in Appendices B.7 and B.8. Using noise estimates from related experimental setups we conclude that these noise sources likely play a subleading role on the visibility of the measurement compared to the charge noise considered in the main text.

We first formulate the general framework of how we treat noise. Consider an observable $\hat{y}(x(t))$ that depends on the parameter $x(t) = x + \delta x(t)$, where x is the fixed setting of the parameter x and $\delta x(t)$ is the time-dependent noise. We describe the noise perturbatively by considering the second order expansion in the parameter of noise:

$$\hat{y}(x(t)) = \hat{y}_0(x) + \hat{y}_1(x)\delta x(t) + \frac{1}{2}\hat{y}_2(x)\delta x(t)^2\,, \tag{3.17}$$

[1] Technically, the 4-MZM measurement is performed by measuring charge/capacitance of one of the dots and in order to compare it to the 2-MZM case, one needs to plot the spectra of Fig. 3.3 as functions of variables $\varepsilon_{\mathrm{d}1}, \varepsilon_{\mathrm{d}2}$ rather than $\Delta_{\mathrm{dd}}, \Delta_{\mathrm{di}}$. However, the two variable sets are related to each other by simple linear transformation and thus the spectra as a function of, for example, $\varepsilon_{\mathrm{d}1}$ looks rotated with respect to the ones in Fig. 3.3 such that the ground state part still qualitatively resembles the one in Fig. 3.2(a)

where $\hat{y}_0$ is the unperturbed observable and $\hat{y}_1$, $\hat{y}_2$ are first and second derivatives of $\hat{y}_0$ with respect to x. Since measurements are recorded over a finite measurement time $\tau_{\rm m}$ we are ultimately interested in the time averaged quantities $\hat{Y} = \frac{1}{\tau_{\rm m}} \int_0^{\tau_{\rm m}} dt \hat{y}(x(t))$. We use the expectation value $Y = \langle \hat{Y} \rangle$ and variance $\sigma_Y^2 = \langle \hat{Y}^2 \rangle - \langle \hat{Y} \rangle^2$ to determine the measurable signal and internal noise.

The above expectation value $\langle \dots \rangle$ is taken with respect to the environment for the noisy parameter. There are two opposing limits how to incorporate a finite temperature in the expectation values of the system operators. (1) The operator $\hat{Y}$ is temperature independent and the expectation value is taken with respect to the full density matrix of the system which includes both finite-temperature and noise effects; (2) the operator $\hat{Y}$ is already the temperature-averaged observable (i.e. the expectation value with respect to the unperturbed finite-temperature density matrix has been already taken) in which case taking the expectation value $\langle \dots \rangle$ amounts to only performing noise-averaging. Method (1) would give a finite variance even in the absence of noise due to temperature fluctuations while (2) only includes fluctuations due to noise. These differences only become important for temperatures that allow excitations above the ground state. In the case when there is a significant occupation of the excited state, the timescales involved in the temperature fluctuations determine which of the two methods are more appropriate in capturing the variance of the measurement outcomes. If during the measurement time the system transitions frequently between the ground and excited state, the measurement will probe temperature averaged quantities (2), while for transitions slower than the measurement time the distribution of measurement outcomes would be broadened by temperature (1). To focus on the effect of the noise we take the limit (2) of long measurement times.

We assume that the expectation values of the fluctuations are fully described by the spectral function $S_x(\omega)$ of the noise via $\langle \delta x(0) \delta x(t) \rangle = \int d\omega e^{i\omega t} S_x(\omega)$. For the $1/f$ noise

which we assume below $S_x(\omega) = \alpha_x/|\omega|$ we find up to second order in the noise

$$Y = y_0 + y_2\alpha_x\big(1-\gamma-\log(\omega_{\min}\tau_{\rm c}/2)\big) \tag{3.18}$$

$$\sigma_Y^2 = y_1^2\alpha_x c + \frac{y_2^2}{2}\alpha_x^2\left(5+c^2\right) \tag{3.19}$$

where $\gamma \approx 0.577$ is Euler's constant and $c = 3-2\gamma-2\log(\omega_{\min}\tau_{\rm m})$, see Appendix B.4 for details. Note that the nature of $1/f$ noise requires to introduce low and high frequency cutoffs of the noise in addition to the finite measurement time. The cutoffs can be physically motivated. The high frequency cutoff arises due to finite correlation time of the noise. For short times $t \ll \tau_{\rm c}$ one expects $\langle \delta x(0)\delta x(t)\rangle$ to approach a constant. The specific value of this time scale is not important due to the weak logarithmic dependence. We associate $\tau_{\rm c}^{-1}$ with the highest frequency that the measurement apparatus can possibly resolve. Noise at higher frequencies simply averages out and cannot be detected during measurement. The measurements are performed by coupling resonators to the quantum dot and observing shifts in the resonance frequency. This frequency thus provides a natural cutoff for the time scale the detector can resolve. Typical resonator frequencies are ~ 1 GHz and thus we set $\tau_{\rm c}^{-1} = 1$ GHz. The low frequency cutoff $\omega_{\min}$ is given by the inverse timescale at which the system is recalibrated since very slow components of the noise act as drift which can be removed by calibration.

While the dependence on $\omega_{\min}$ is weak it should be noted that Eqs. (3.18),(3.19) emphasize that similar to conventional qubits, the measurement apparatus of topological qubits needs to be regularly recalibrated. For numerical estimates we use $\omega_{\min}^{-1} = 10\tau_{\rm m}$ with $\tau_{\rm m} = 1\ \mu$s. For longer recalibration times the noise will grow slowly as $\sqrt{\log(\omega_{\min}\tau_m)}$. This effect becomes relevant when considering very long time-intervals between calibration that might be desirable for quantum computation. For example, for $\omega_{\min}^{-1} \sim 1$day with $\tau_m = 1\ \mu$s the noise would be increased by a factor ~ 3 relative to our estimates.

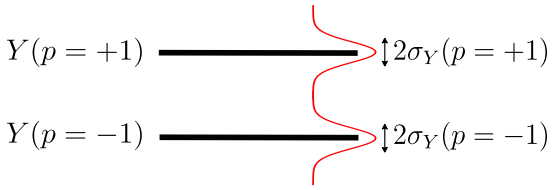

Figure 3.4: Diagram explaining definition of the signal and noise given by Eqs. (3.20),(3.21). Y is a measured quantity which depends on p, black lines indicate respective values of Y. The red line is a level broadening due to the noise with a standard deviation σ_Y.

During the qubit readout the goal is to be able to differentiate between parity $p = +1$ and $p = -1$ states by measuring the observables discussed in the previous section. This is schematically illustrated in Fig. 3.4. Thus, for the particular case of measurement visibility analysis, we define the signal $\mathcal{S}$ and the noise $\mathcal{N}$ in variable Y as

$$\mathcal{S}_Y = |Y(p=+1) - Y(p=-1)| \tag{3.20}$$

$$\mathcal{N}_Y = \sigma_Y(p=+1) + \sigma_Y(p=-1). \tag{3.21}$$

3.5 Detuning noise

The dominant source of noise in the island-QD detuning Δ is the gate voltage noise on the QD n_g which is typically dominated by $1/f$ charge noise

$$S_\Delta(\omega) = \varepsilon_\mathrm{C}^2 \frac{\alpha_\mathrm{C}}{|\omega|}. \tag{3.22}$$

Here we explicitly wrote the coupling strength of the noise to the system which is controlled by the charging energy ε_C and the strength of the noise described by the dimensionless parameter α_C that depends on the environment that is causing the charge noise. The latter depends on the experimental setup and materials.

We estimate α_C by considering the strength of dephasing of charge qubits in InAs/Al

hybrid systems that are investigated for their potential use as building blocks for Majorana qubits. Reference [90] reports coherence time of the InAs/Al based superconducting charge qubit with $\varepsilon_C/h \sim 10$ GHz to be $T_2^* \sim 1$ ns. A simple estimate for the dephasing caused by charge noise is given by $T_2^* \sim \hbar/(\varepsilon_C\sqrt{\alpha_C})$ [112]. We use this relation to estimate the experimentally relevant $\sqrt{\alpha_C} \sim 0.01$. Typical values for the charging energy of InAs QDs are $\varepsilon_C \sim 100\mu$eV [111, 110] which leads to $\varepsilon_C\sqrt{\alpha_C} \sim 1\mu$eV. Note that this gives a conservative estimate for the strength of charge noise for the topological qubit as it assumes no optimization of noise as compared to current experimental capabilities. Similar estimates for charge qubits in much more mature GaAs-based systems yield $\sqrt{\alpha} \sim 10^{-4}$ [118, 112]. The perturbative treatment of the noise in Eq. (3.17) close to $\Delta = 0$ is justified for the charge noise as long as $\sqrt{\alpha_C}\varepsilon_C \ll |\bar{t}_p|$. The above estimate of $\sqrt{\alpha_C} \ll 1$ therefore justifies the perturbative treatment as long as the effective tunnel couplings $\bar{t}_p$ are not too small compared to ε_C. For our numerical estimates we take $|t_1| = t,\ |t_2| = 1.5t,\ t = \varepsilon_C/5$ which guarantees validity of the perturbative treatment for the entire parameter range of Δ and ϕ. The coupling asymmetry $|t_2|/|t_1| = 1.5$ does not correspond to the case of maximum visibility (which is reached for $|t_2|/|t_1| = 1$). However, a certain degree of the coupling asymmetry is expected in the QD-based readout experiments as the coupling fine-tuning might pose a challenge.

Using expressions of Eq. (3.7) (Eq. (3.8)) for the average QD charge (differential capacitance of the QD) in the 2-MZM measurement case we plot the zero-temperature dependence of the signal $\mathcal{S}_n(\mathcal{S}_C)$ and noise $\mathcal{N}_n(\mathcal{N}_C)$ given by Eqs. (3.20) and (3.21) in terms of the phase and detuning in Figs. 3.5 and 3.6. Temperature dependence of detuning noise is analyzed in Appendix B.5.

The dependence on the detuning Δ shows that the charge signal $\mathcal{S}_n$ takes its maximal value for $\Delta = \Delta_n^{\max}$ with $\Delta_n^{\max} \sim t$. This follows from the suppression of the signal at $\Delta = 0$ ($\Delta \to \infty$) due to the QD charge reaching $\langle n_{QD}\rangle = 1/2$ ($\langle n_{QD}\rangle = 1$) independent

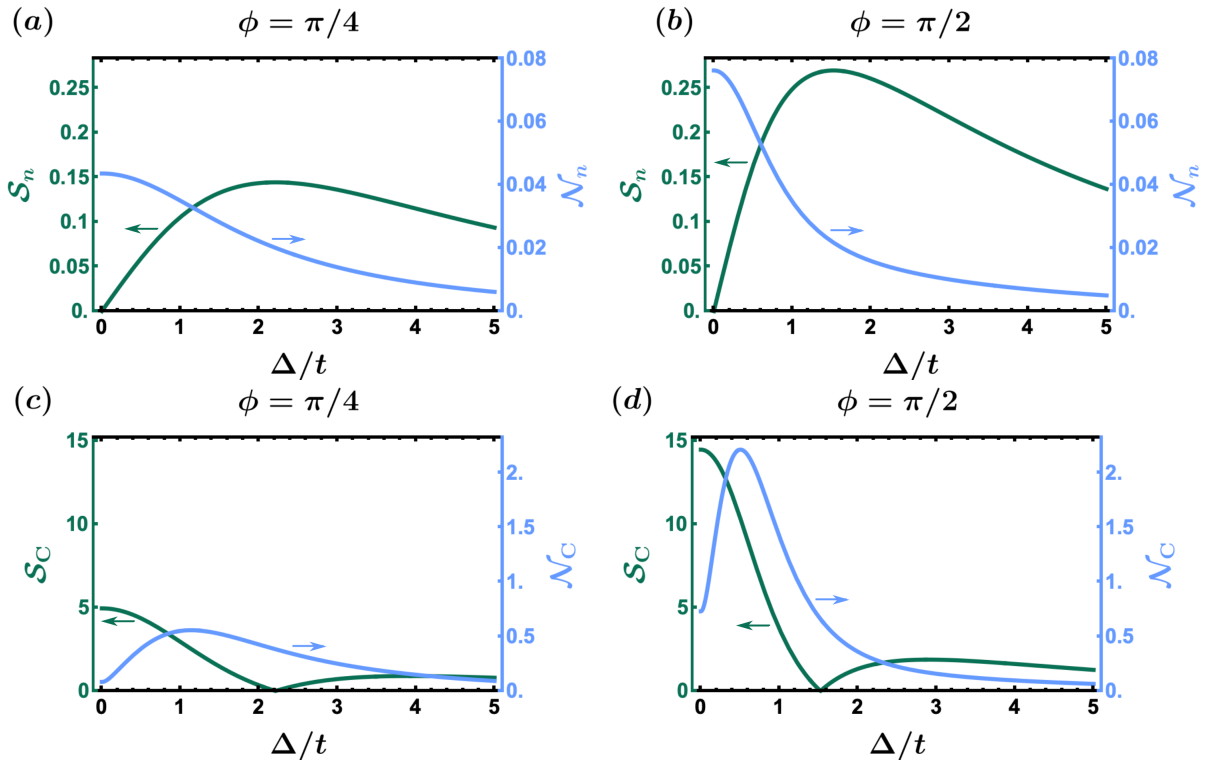

Figure 3.5: Signal (3.20) and noise (3.21) for the 2-MZM measurements of the average QD charge $\langle n_{\rm QD}\rangle$ (a)-(b) and differential QD capacitance $C_{\rm diff}/C_{\Sigma,\rm D}$ (c)-(d) as a function of detuning Δ for different values of ϕ. Here we assume that the system is in its ground state ($T = 0$) and set $|t_1| = t,\ |t_2| = 1.5t,\ t = \varepsilon_{\rm C}/5 = 0.02$ meV, $C_{\rm g}/C_{\Sigma,\rm D} = 2$, and the noise is detuning noise of strength $\sqrt{\alpha_C} = 0.01$.

of parity. Neglecting noise one can find analytically $\Delta_n^{\max} = 2|\bar{t}_-^2\bar{t}_+|^{1/3}/\sqrt{1+|\bar{t}_-/\bar{t}_+|^{2/3}}$. We checked numerically that for our choice of parameters the noise-induced term in $\mathcal{S}_n$ is perturbative, i.e. much smaller then the noise-free term, and thus produces small corrections to this analytical result.

In the regime of perturbative noise and $T = 0$ the differential capacitance signal $\mathcal{S}_{\rm C}$ is always maximal at $\Delta = 0$ while vanishing at $\Delta = \Delta_{\rm C}^{\min} = \Delta_n^{\max}$. The latter marks the point where the differential capacitance corresponding to the smaller of $|\bar{t}_-|$ and $|\bar{t}_+|$, which is generally dominating around small detuning due to a larger curvature, is equal to the differential capacitance of the larger coupling which dominates in the regime of large detuning.

Note that at finite temperature and in the presence of noise $\Delta = 0$ might not always be the point of maximal signal and $\Delta_C^{\min}$ might differ from $\Delta_n^{\max}$. Consider for example the regime of extreme fine tuning where $|\bar{t}_-| \ll T, \sigma_\Delta$ while $|\bar{t}_+| \gg T, \sigma_\Delta$. In that limit the contribution to the differential capacitance of the $p = -1$ parity would vanish as $C_{\text{diff},-} \propto |\bar{t}_-|/(T\sigma_\Delta)$. A derivation of this expression is given in Appendix B.6. Approaching this regime would mean that $\Delta_{\text{C}}^{\min}$ would shift to values smaller than $\Delta_n^{\max}$ and eventually reach $\Delta_{\text{C}}^{\min} = 0$. Further reducing $|\bar{t}_-|$ would make $\mathcal{S}_{\text{C}}$ be dominated by the $p = +1$ branch independent of Δ thus restoring $\Delta = 0$ as the point of maximal signal. Naturally, the limit of very small $|\bar{t}_-|$ breaks the perturbative treatment of noise used in this chapter. Nevertheless, as long as the noise σ_Δ is weak compared to $|\bar{t}_+|$ results for the limit $|\bar{t}_-| \to 0$ can be obtained using our formalism by replacing $\mathcal{S}_{\text{C}} \to C_{\text{diff},+}$ and $\mathcal{S}_n \to \langle n_{\text{QD},+}\rangle - \langle n_\sigma\rangle$, where $\langle n_\sigma\rangle$ is charge expectation value for vanishing coupling broadened by noise [2].

The noise $\mathcal{N}_n$ is maximal at $\Delta = 0$ and falls off quickly for large detuning. From the perspective of pure charge noise the SNR would thus be largest for large detuning where the signal is also becoming suppressed. The presence of other noise sources will limit this behavior. For example the effect of external amplifier noise is typically minimized for the strongest signal. At the maximal signal, i.e. $\Delta = \Delta_n^{\max}$, we find a charge-noise-limited SNR of ≈ 12 for $\phi = \pi/2$. Thus, as long as the integration times are not sufficiently long to extend the amplifier-limited SNR beyond 12 the point of maximal experimental SNR will be close to $\Delta = \Delta_n^{\max}$.

The noise $\mathcal{N}_{\text{C}}$ shows a local minima at $\Delta = 0$ due to the absence of the first-order contribution of charge noise. This emphasizes that for capacitive measurements $\Delta = 0$ is likely the optimal operation point. The only exception is the above-mentioned regime where the smaller of the effective couplings, say $|\bar{t}_-|$, is accidentally of the order of

[2]For Gaussian noise of width σ_Δ the charge of the ground $(-)$ and excited $(+)$ state is broadened via $n_{\sigma,\pm} = (1 \mp \text{erf}(\Delta/\sqrt{2}\sigma_\Delta))/2$. The expectation value $\langle n_\sigma\rangle$ is then given by appropriately temperature averaging the ground and excited state contribution.

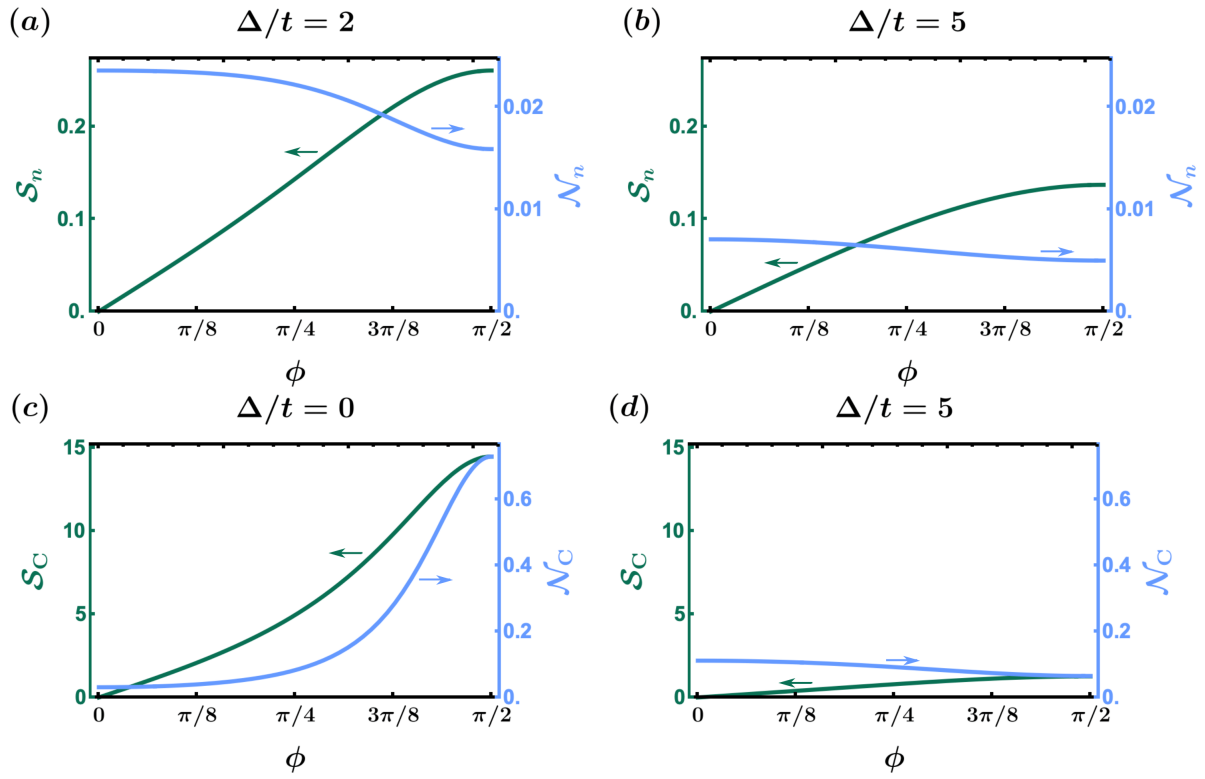

Figure 3.6: Signal (3.20) and noise (3.21) for the 2-MZM measurement of the average QD charge $\langle n_{\rm QD}\rangle$ (a)-(b) and differential QD capacitance $C_{\rm diff}/C_{\Sigma,\rm D}$ (c)-(d) as a function of phase ϕ for different values of Δ/t. We used the same parameters as in Fig. 3.5.

$T\sigma_\Delta/|\bar{t}_+|$. For the parameters we used, we find a charge-noise-limited SNR of ≈ 20 for $\phi = \pi/2$.

Figure 3.6 shows the ϕ-dependence of the signal and noise. The main effect of changing ϕ is to increase the difference between $|\bar{t}_+|$ and $|\bar{t}_-|$ as ϕ approaches $\pi/2$. This generally increases the signal for all observables as long as the noise remains perturbative. Away from $\Delta = 0$ changing ϕ has only a relatively weak effect on the noise which means that for charge measurements $\phi \to \pi/2$ is always preferable. In the case of capacitance measurements that are operated at $\Delta = 0$ approaching $\phi = \pi/2$ not only increases the signal but also the noise. The optimal SNR can thus be obtained away from $\phi = \pi/2$. Similar to the discussion of the effect of noise for the charge measurements at large

detuning, external constraints will determine whether the increase in the signal or the reduction of the noise are more important for obtaining the best experimental SNR.

3.6 Conclusion

In the present work we identified detuning charge noise as the dominant source of intrinsic noise that affects the measurement visibility of Majorana qubits probed by QDs. We studied the Hamiltonian for 2-MZM and 4-MZM measurements non-perturbatively in the tunnel coupling and emphasized the similarity of their description in the regime of small detunings which in general optimizes SNR in the presence of external noise. 4-MZM measurements require more tuning and more manipulations to bring the system into the optimal measurement regime, but can produce signal of the *same* order as 2-MZM measurements. We thus analyzed the 2-MZM measurement for SNR in detail and claim the 4-MZM one will behave similarly.

Generally we obtain large SNRs $\gtrsim 10$ for conservative assumptions on the charge noise of the system that is tuned to the optimal measurement regime. Since we did not explicitly treat external noise sources like amplifiers our SNRs should be understood as the limiting SNRs that can be obtained after long measurement times. The large obtained SNRs indicate that charge noise will likely not be limiting the fidelity of measurements of topological qubits.

We make concrete predictions for the visibility of the topological qubit measurement, but our results are relevant for and can be tested in simpler setups. For example, test devices replacing the qubit island with another QD show similar interference effects. Our SNRs can then be understood as describing the difference between measurements where the enclosed phases of the tunnel couplings are ϕ and $\phi + \pi$.

Chapter 4

Effects of coupling between quantum dot and quasiparticle continuum modes in topological superconductor-quantum dot-topological superconductor junctions

4.1 Permissions and Attributions

1. The content of Chapter 4 and Appendix C is the result of a collaboration with Torsten Karzig, Roman M. Lutchyn and Dmitry I. Pikulin.

4.2 Introduction

An unambiguous detection of Majorana zero-energy modes (MZMs) [76] and demonstration of their non-Abelian statistics are among central problems in the field of topological quantum computing [10, 11, 28]. The potential for long coherence times makes Majorana-based qubits a promising alternative to other conventional qubit implementations. While various MZM implementation and detection schemes have been proposed theoretically, experimental realizations proved to be challenging. A variety of experimental signatures reported throughout the past decade [78, 79, 80, 81, 82, 83, 120, 86, 87, 88, 89, 90, 121], while plentiful and promising, turned out to be inconclusive regarding the presence of MZMs in the system [91, 92, 93, 94, 95, 96, 97, 98, 99, 25]. Recent experiments [122] present a stronger set of data suggesting topological superconductivity in InAs/Al heterostructures. The ultimate test for MZMs, however, remains the measurement of their non-Abelian statistics, which can be done by fusing MZMs and reading out their parity. Such a measurement would not only reveal the presence of MZMs in the system but also pave the way to coherent quantum information processing in topological Majorana qubits [100, 101].

Among the various ideas for MZM parity readout [102, 103, 104, 106, 105, 107, 108, 123, 124, 125, 126], a key set of proposal relies on coupling one-dimensional topological superconductors to a quantum dot (QD) thus forming a topological superconductor-QD-topological superconductor (T-QD-T) junction. Such junctions provide controlled coupling of the QD to the MZMs formed at the ends of the topological superconductors. The parity of a pair of MZMs coupled to a QD can then be read out by measuring properties of the QD such as its charge [102, 106, 105, 107, 115, 116, 108, 127, 128, 124, 129, 125, 126].

Additional interest in T-QD-T junctions comes from the unconventional physics of

the $0-\pi$ transition of the supercurrent: while the $0-\pi$ transition is generally present in regular superconductor-QD-superconductor (S-QD-S) junctions in the Coulomb blockade regime [130, 131, 132, 133, 134, 135, 136, 137], it does not appear in T-QD-T junctions [138, 139, 140, 141]. The absence of the $0-\pi$ transition has been recently observed experimentally in full-shell InAs/Al nanowires [142][1].

Previous studies on T-QD-T junctions [106, 105, 102, 107, 115, 116, 108, 127, 128, 124, 129, 125] typically have been focusing on MZM-QD-MZM degrees of freedom in the system, while neglecting the effect of quasiparticle continuum modes present in the superconductors. These continuum modes generate additional Andreev reflection processes between the superconductors and the dot, and thus produce conventional contributions to the supercurrent flowing through the junction, which can be important in the study of T-QD-T junctions as they can mask the signatures of MZMs. The impact of the continuum modes can be especially important in the case of multi-mode topological superconductors. In this chapter, we investigate T-QD-T junctions, paying particular attention to the continuum modes in the superconductors, and their effect on the well studied MZM-QD-MZM part of the system. Working in the regime of weak continuum-QD coupling, we employ perturbation theory to calculate the energy shift associated with the tunneling between the QD and the quasiparticle continuum modes. Using these results, we analyze effects of the continuum-QD coupling on the QD-based measurements of the Majorana qubits and the phenomenology of the $0-\pi$ transition in the T-QD-T junctions.

The rest of the chapter is organized as follows. Section 4.3 describes the model of the T-QD-T junction that we utilize throughout the chapter. In Section 4.4 we review results for the MZM-QD-MZM system in the absence of the continuum-QD coupling. The effects of the continuum-QD coupling on the system are considered in Sections 4.5 and 4.6. First,

[1]It has been pointed out, however, that the absence of the $0-\pi$ transition is not limited solely to the topological junctions as the trivial Andreev zero-energy states coupled to the QD can produce similar effect [143].

using second order perturbation theory in the continuum-QD couplings we estimate their impact on the QD-based measurement of the Majorana qubit in Section 4.5. Second, we further employ fourth order perturbation theory in Section 4.6 and analyze the effects of the continuum-QD coupling on the equilibrium supercurrent through the junction. In particular, we investigate how the presence of a coupling between the QD and the continuum modes alters the absence of the $0-\pi$ transition in the T-QD-T junctions. Section 4.7 presents concluding remarks. Details of the calculations are given in the Appendix.

4.3 Setup and Model

A typical layout for a T-QD-T junction is illustrated in Fig. 4.1. The MZMs γ_L, γ_R are formed at the ends of the topological superconductors (grey) and are coupled to the QD (black) via couplings $t_{L/R}$. It is assumed implicitly that there are MZMs formed at the other ends of the topological superconductors but for simplicity we neglect them. In addition to the MZM-QD couplings, the dot also couples to the modes in the quasiparticle continuum of the topological superconductors (orange) via couplings $s_{L/R}$. The two topological superconductors are joined together by a superconducting backbone (blue) to form a single island. It is not important for the backbone to be topological and in practice it is sometimes convenient for it to be trivial [106]. Magnetic flux Φ penetrating the ring formed by the superconductors can be used to control the phases of the MZM-QD and continuum-QD couplings.

We describe the system with the following effective low-energy Hamiltonian:

$$\hat{H} = \hat{H}_{\mathrm{C}} + \hat{H}_{\mathrm{QD}} + \hat{H}_{\text{T-MZM}} + \hat{H}_{\mathrm{NW}} + \hat{H}_{\text{T-NW}}. \tag{4.1}$$

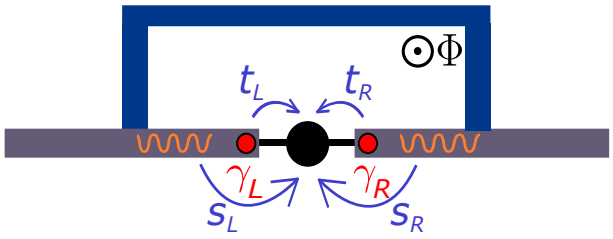

Figure 4.1: A schematic depiction of the T-QD-T junction. The MZMs γ_L, γ_R (red) are formed at the ends of topological superconductors (grey) and are coupled to a QD (black) via couplings $t_{L/R}$. Quasiparticle continuum modes (orange waves) are coupled to the QD via couplings $s_{L/R}$. The two topological superconductors are joined together by a superconductor (blue) and form one island. Magnetic flux Φ is used to control the phases of the MZM-QD and continuum-QD couplings. The MZMs forming at the further ends of the topological superconductors are not depicted here.

Here $\hat{H}_{\mathrm{C}}$ is the Hamiltonian of the superconducting island including charging energy, $\hat{H}_{\mathrm{QD}}$ is the Hamiltonian of the QD, and $\hat{H}_{\text{T-MZM}}$ is the term describing the MZM-QD coupling present in the topological regime. As a model for the topological superconductor we take a semiconducting nanowire (NW) with strong Rashba spin-orbit coupling, proximitized by an s-wave superconductor and subject to a parallel magnetic field [19, 20]. $\hat{H}_{\mathrm{NW}}$ in Eq. (4.1) denotes the proximitized NW Hamiltonian and $\hat{H}_{\text{T-NW}}$ is the term describing coupling between the QD and the continuum modes in the nanowire.

To simplify the calculations we assume a small-size QD such that the Zeeman energy h on the dot is much smaller than the dot's orbital level spacing. Given this assumption we take into account only the dot's lowest in energy orbital level split by the Zeeman energy into two spin-resolved levels; we denote occupation of the spin-down (spin-up) level as $\hat{n}_{\downarrow}(\hat{n}_{\uparrow})$ [2]. Given that, the first two terms in Eq. (4.1), $\hat{H}_{\mathrm{C}} + \hat{H}_{\mathrm{QD}}$, can be separated into the Zeeman and the charging terms:

$$\hat{H}_{\mathrm{C+QD}} = h\hat{n}_{\downarrow} + \varepsilon_{\mathrm{C}}(\hat{n}_{\downarrow} + \hat{n}_{\uparrow} - n_{\mathrm{g}})^2, \tag{4.2}$$

[2] As long as there are only two spin-resolved QD levels under consideration, the formalism developed in this chapter can be applied in the opposite scenario when Zeeman energy is much larger than the orbital level spacing.

where ε_{C} and n_{g} are the effective charging energy and the effective dimensionless gate voltage of the QD-island system. The charging term can be written as a single term for both parts of the system due to the charge conservation. Throughout this work we assume that the charging energy ε_{C} is sufficiently large such that only one excess electron can be present on the dot at a time, i.e. $\varepsilon_{\mathrm{C}} + h \gg \Delta_{\mathrm{ind}}$.

For simplicity, here we consider the case of a single-band nanowire and take the two nanowires on the left and on the right side of the QD to be identical. Then, the effective Hamiltonian of the NWs in the momentum space is given by

$$\hat{H}_{\mathrm{NW}} = \frac{1}{2} \sum_{l=L,R} \sum_{k} C_{kl}^{\dagger} \mathcal{H}_k C_{kl}, \tag{4.3}$$

where $C_{kl} = (c_{k\uparrow l}\ c_{k\downarrow l}\ c_{-k\uparrow l}^{\dagger}\ c_{-k\downarrow l}^{\dagger})^T$ is a column of electronic operators and the wire Hamiltonian takes a familiar form:

$$\mathcal{H}_k = \left(\frac{k^2}{2m^*} - \mu \right) \hat{\tau}_z + V_{\mathrm{Z}} \hat{\tau}_z \hat{\sigma}_x + \alpha_{\mathrm{R}} k \hat{\sigma}_z + \Delta_{\mathrm{ind}} \hat{\tau}_y \hat{\sigma}_y. \tag{4.4}$$

Here $l = L, R$ corresponds to the left or right NW, k is the momentum, $c_{k\sigma l}$ is the annihilation operator of an electron on the lth NW with momentum k and spin σ, while m^*, μ, α_{R}, V_{Z}, Δ_{ind} are the effective electron mass, chemical potential, Rashba spin-orbit coupling, Zeeman energy, and induced pairing potential in the nanowires, respectively. $\hat{\tau}_i(\hat{\sigma}_i)$ are Pauli matrices in the Nambu(spin) space. The Bloch Hamiltonian (4.4) is real and has the particle-hole symmetry $\mathcal{P} = \hat{\tau}_x \mathcal{K}$, where $\mathcal{K}$ is complex conjugation operation, and the time-reversal symmetry $\mathcal{T}_+ = \hat{\tau}_z \hat{\sigma}_x \mathcal{K}$, $\mathcal{T}_+^2 = +1$, placing it in the BDI symmetry class [144]. Presence of the BDI symmetry simplifies certain calculations that we describe below but is not required for the validity of our results. In the limit $V_{\mathrm{Z}} \to 0$, $\alpha_{\mathrm{R}} \to 0$, the Hamiltonian (4.4) reduces to the conventional s-wave superconductor one.

The nanowire Hamiltonian of Eqs. (4.3)-(4.4) can be straightforwardly diagonalized via the Bogoliubov transformations

$$C_{kl} = \begin{pmatrix} u_{k1\uparrow} & u_{k2\uparrow} & v_{k1\uparrow} & v_{k2\uparrow} \\ u_{k1\downarrow} & u_{k2\downarrow} & v_{k1\downarrow} & v_{k2\downarrow} \\ v_{-k1\uparrow} & v_{-k2\uparrow} & u_{-k1\uparrow} & u_{-k2\uparrow} \\ v_{-k1\downarrow} & v_{-k2\downarrow} & u_{-k1\downarrow} & u_{-k2\downarrow} \end{pmatrix} A_{kl} \tag{4.5}$$

yielding

$$\hat{H}_{\mathrm{NW}} = \frac{1}{2} \sum_{l=L,R} \sum_{k} A^{\dagger}_{kl} E_k A_{kl}. \tag{4.6}$$

Here $A_{kl} = (a_{k1l}\ a_{k2l}\ a^{\dagger}_{-k1l}\ a^{\dagger}_{-k2l})^T$ is a column of Bogoliubov quasiparticle operators, $E_k = \mathrm{diag}\{\varepsilon_1(k), \varepsilon_2(k), -\varepsilon_1(-k), -\varepsilon_2(-k)\}$ are eigenenergies of the Hamiltonian (4.4) and the coefficients $u_{kj\sigma}, v_{kj\sigma},\ j = 1, 2,\ \sigma = \uparrow, \downarrow$, are components of the eigenvectors of the Hamiltonian (4.4). Note that since the Hamiltonian (4.4) is real and symmetric in Nambu $\otimes$ spin space, the coefficients $u_{kj\sigma}, v_{kj\sigma}$ can be chosen real. The particle-hole symmetry fixes the form of the Bogoliubov transformation matrix as presented in Eq. (4.5) and two out of four eigenenergies in E_k, while the time-reversal symmetry leads to the following relations between the $u_{kj\sigma}$ and $v_{kj\sigma}$ amplitudes:

$$u_{kj\uparrow} = \pm u_{-kj\downarrow},\ v_{-kj\uparrow} = \mp v_{kj\downarrow}. \tag{4.7}$$

The sign here can be chosen arbitrarily as it does not affect measurable quantities. Analytic expressions for the energies $\varepsilon_1, \varepsilon_2$ are presented in Appendix C.1, while analytic expressions for the coefficients $u_{kj\sigma}, v_{kj\sigma}$ are cumbersome and not illuminating and we choose not to present them in the manuscript.

We write the MZM-QD tunneling Hamiltonian as

$$\hat{H}_{\text{T-MZM}} = e^{-i\hat{\phi}/2} \sum_{\rho=\downarrow,\uparrow} \sum_{l=L,R} t_{\rho l} f_\rho^\dagger \gamma_l + \text{h.c.}, \tag{4.8}$$

where $f_\rho^\dagger$ is the fermionic creation operator on the ρth dot level, γ_l is the MZM operator at the end of the lth topological superconductor, operator $e^{-i\hat{\phi}/2}$ describes charge transfer from the island onto the dot, and $t_{\rho l}$ is the MZM-QD coupling. Similarly, the tunneling Hamiltonian between the nanowire continuum and the QD can be written as

$$\hat{H}_{\text{T-NW}} = e^{-i\hat{\phi}/2} \sum_{\rho,\sigma=\downarrow,\uparrow} \sum_{l=L,R} \sum_{k} s_{\rho\sigma l} f_\rho^\dagger c_{k\sigma l} + \text{h.c.}, \tag{4.9}$$

where $s_{\rho\sigma l}$ is the spin-dependent continuum-QD coupling. Using Eq. (4.5), one can rewrite Hamiltonian (4.9) in terms of the Bogoliubov quasiparticle operators as

$$\hat{H}_{\text{T-NW}} = e^{-i\hat{\phi}/2} \sum_{\rho,\sigma=\downarrow,\uparrow} \sum_{l=L,R} \sum_{j=1,2} \sum_{k} s_{\rho\sigma l} f_\rho^\dagger \times (u_{kj\sigma} a_{kjl} + v_{-kj\sigma} a_{kjl}^\dagger) + \text{h.c.} \tag{4.10}$$

In the simplest form the MZM-QD and the continuum-QD couplings can be written as

$$t_{\rho l} = |t_{\rho l}| e^{-i\phi_l/2};\ \rho = \downarrow,\uparrow;\ l = L, R, \tag{4.11}$$

$$s_{\rho\sigma l} = |s_{\rho\sigma l}| e^{-i\phi_l/2};\ \rho = \downarrow,\uparrow;\ \sigma = \uparrow,\downarrow;\ l = L, R. \tag{4.12}$$

Here we assumed for simplicity that the phases ϕ_l are the same for the two dot levels $\rho = \uparrow, \downarrow$ and the same for both the MZM-QD and the continuum-QD couplings. Furthermore, we take the couplings $s_{\rho\sigma l}$ to be independent of energy, which is a good approximation for narrow but high tunnel barriers. Note that the phase difference $\phi = \phi_L - \phi_R$ can be tuned using magnetic flux Φ, see Fig. 4.1.

The relative strength of the couplings (4.11),(4.12) can be estimated by rewriting

them through the tunneling matrix elements, see Appendix C.2 for details. The result of such estimate is

$$\frac{|t_{\rho l}|}{|s_{\rho\sigma l}|} \approx \sqrt{\frac{L}{\xi}}, \tag{4.13}$$

where L is the length of the nanowire and ξ is the coherence length in the nanowire. In the subsequent sections, we will use Eq. (4.13) when comparing the continuum and the MZM contributions.

4.4 MZM-only diagonalization

As a first step, we consider the system without the continuum-QD couplings, $s_{\rho\sigma l} = 0$, where the Hamiltonian simplifies to

$$\hat{H} = \hat{H}_{\text{C+QD}} + \hat{H}_{\text{T-MZM}}. \tag{4.14}$$

To write the low-energy part of the Hamiltonian (4.14) in a convenient basis of occupations of the QD levels, $n_\uparrow$ and $n_\downarrow$, we need to introduce a combined MZM-QD parity, $p = p_{LR}(-1)^{n_\uparrow + n_\downarrow} = \pm 1$, where $p_{LR} = i\gamma_L\gamma_R$ is the Majorana parity. Focussing on a single charge transition of the QD, the relevant basis states then take the form $|n_\uparrow, n_\downarrow, p\rangle$, with $|1_\uparrow, 0_\downarrow, p\rangle = e^{-i\hat{\phi}/2} f_\uparrow^\dagger \gamma_1 |0_\uparrow, 0_\downarrow, p\rangle$ and $|0_\uparrow, 1_\downarrow, p\rangle = e^{-i\hat{\phi}/2} f_\downarrow^\dagger \gamma_1 |0_\uparrow, 0_\downarrow, p\rangle$. We notice that the Hamiltonian (4.14) has a block-diagonal form with each block being a 3×3 matrix corresponding to a fixed parity p. Up to an additive constant, each block is

$$\hat{H}_p = \begin{pmatrix} \Delta/2 & \bar{t}_{p,\downarrow}^* & \bar{t}_{p,\uparrow}^* \\ \bar{t}_{p,\downarrow} & h - \Delta/2 & 0 \\ \bar{t}_{p,\uparrow} & 0 & -\Delta/2 \end{pmatrix}, \tag{4.15}$$

where $\Delta = \varepsilon_{\rm C} n_{\rm g}^2 - \varepsilon_{\rm C}(1-n_{\rm g})^2$ is the energy detuning between the island and the lowest dot level, and $\bar{t}_{p,\rho} = t_{\rho L} - ipt_{\rho R}$ is the effective coupling between the MZMs and the dot level ρ. Due to the phase factors in the MZM-QD couplings, the absolute value of the effective coupling is equal to $|\bar{t}_{p,\rho}(\phi)| = \sqrt{|t_{\rho L}|^2 + |t_{\rho R}|^2 + 2p|t_{\rho L}t_{\rho R}|\sin(\phi/2)}$. General diagonalization of the Hamiltonian (4.15) leads to cumbersome expressions so here we only present analytical results for its eigenenergies in the limit of large Zeeman splitting h relative to the MZM-QD couplings $t_{p,\sigma}$ and the island-QD detuning Δ, i.e. $h \gg t_{p,\sigma}, \Delta$. The expressions for the eigenenergies in this limit are:

$$\varepsilon_{p,-}^{(0)} = -\frac{1}{2}\sqrt{\Delta^2 + 4|\bar{t}_{p,\uparrow}|^2} - \frac{|\bar{t}_{p,\downarrow}|^2}{2h}\frac{\sqrt{\Delta^2 + 4|\bar{t}_{p,\uparrow}|^2} - \Delta}{\sqrt{\Delta^2 + 4|\bar{t}_{p,\uparrow}|^2}} + \ldots, \tag{4.16}$$

$$\varepsilon_{p,+}^{(0)} = \frac{1}{2}\sqrt{\Delta^2 + 4|\bar{t}_{p,\uparrow}|^2} - \frac{|\bar{t}_{p,\downarrow}|^2}{2h}\frac{\sqrt{\Delta^2 + 4|\bar{t}_{p,\uparrow}|^2} + \Delta}{\sqrt{\Delta^2 + 4|\bar{t}_{p,\uparrow}|^2}} + \ldots, \tag{4.17}$$

$$\varepsilon_{p,h}^{(0)} = h - \frac{\Delta}{2} + \frac{|\bar{t}_{p,\downarrow}|^2}{h}, \tag{4.18}$$

where we denoted the three eigenstates of the Hamiltonian (4.15) as $|-\rangle$, $|+\rangle$ and $|h\rangle$. In general, these eigenstates are certain linear combinations of the three basis states $|0_\uparrow, 0_\downarrow, p\rangle, |1_\uparrow, 0_\downarrow, p\rangle$ and $|0_\uparrow, 1_\downarrow, p\rangle$. However, in the limit of large the Zeeman splitting on the dot, $h \gg t_{p,\downarrow}, \Delta$, we can neglect hybridization of the higher-in-energy QD level with the MZMs and consider only hybridization between the MZMs and the lower-in-energy dot level. In this limit, the eigenstates of the Hamiltonian (4.15) are given by

$$|-\rangle_p = \beta_{p,0}|0_\uparrow, 0_\downarrow, p\rangle + \beta_{p,1}|1_\uparrow, 0_\downarrow, p\rangle, \tag{4.19}$$

$$|+\rangle_p = \alpha_{p,0}|0_\uparrow, 0_\downarrow, p\rangle + \alpha_{p,1}|1_\uparrow, 0_\downarrow, p\rangle, \tag{4.20}$$

$$|h\rangle_p = |0_\uparrow, 1_\downarrow, p\rangle, \tag{4.21}$$

and the corresponding energies read

$$\varepsilon^{(0)}_{p,\mp} = \mp\frac{1}{2}\sqrt{\Delta^2 + 4|\bar{t}_p(\phi)|^2}, \tag{4.22}$$

$$\varepsilon^{(0)}_{p,h} = h - \frac{\Delta}{2}, \tag{4.23}$$

where for notational convenience we denoted $\bar{t}_{p,\uparrow}$ as $\bar{t}_p$. Analytic expressions for the coefficients $\alpha_{p,n}, \beta_{p,n}$, $n = 0, 1$, are presented in Appendix C.3.

4.5 Second order perturbative correction in the continuum-QD couplings

4.5.1 Derivation of the second order correction

Having taken into account the effect of the MZM-QD coupling non-perturbatively in Section 4.4, in the following sections we investigate how the continuum-QD coupling of Eq. (4.9) shifts the ground state energy (4.22) of the MZM-QD system. To this end, we consider weak continuum-QD coupling and employ perturbation theory to calculate the energy shift. The perturbative expansion is controlled by the parameters $\Gamma_{\rho l}/\Delta_{\mathrm{g}}$, where $\Gamma_{\rho l} = (\nu_{\mathrm{NW}} L) \sum_{\sigma=\downarrow,\uparrow} |s_{\rho\sigma l}|^2$ is the broadening of the QD level ρ due to the tunneling into the continuum of the nanowire l, ν_{NW} is the normal density of states in the nanowire, and Δ_{g} is the gap to the quasiparticle excitations in the nanowires. Throughout the study we consider the regime of small $\Gamma_{\rho l}/\Delta_{\mathrm{g}}$. Furthermore, we assume that the charging energy of the QD is sufficiently large such that only one excess electron can be present on the dot at a time, i.e. $\varepsilon_{\mathrm{C}} + h \gg \Delta_{\mathrm{ind}}$.

When considering the second order correction, we neglect the tunneling into the higher-in-energy dot level $\rho = \downarrow$ which is justified if the Zeeman splitting on the dot is

much larger than the respective level broadening, $h \gg \Gamma_{\downarrow l}$. Furthermore, for simplicity we assume that the continuum-QD couplings on the left and on the right are the same, $|s_{\uparrow\sigma L}| = |s_{\uparrow\sigma R}| \equiv |s_{\uparrow\sigma}|$, and introduce direct (spin-conserving) $|s_{\rm dir}| \equiv |s_{\uparrow\uparrow}|$ and spin-flip $|s_{\rm sf}| \equiv |s_{\uparrow\downarrow}|$ couplings to the spin-up dot level $\rho =\uparrow$. In general, the spin-flip tunneling can be appreciable due to the presence of the spin-orbit coupling in the system. However, here for simplicity we consider the case when $s_{\rm sf} = 0$. Given that, the second order perturbative correction to the ground state energy in the limit $\Delta_{\rm g} \gg \Delta, |t_L|, |t_R|$ is given by

$$\varepsilon^{(2)}_{p,-} = -\frac{|s_{\rm dir}|^2}{\Delta_{\rm ind}} K_1^{(2)} \frac{\Delta}{\sqrt{\Delta^2 + 4|\bar{t}_p(\phi)|^2}}. \tag{4.24}$$

The details of the derivation as well as the expression for $\varepsilon^{(2)}_{p,-}$ in the case of the nonzero spin-flip tunneling are presented in Appendix C.4. When deriving expression (4.24), we have dropped the terms independent of the detuning Δ and the phase difference ϕ, since ultimately we are interested in calculating measurable quantities proportional to either $\partial\varepsilon^{(2)}_{p,-}/\partial\Delta$ (the average charge on the dot), $\partial^2\varepsilon^{(2)}_{p,-}/\partial\Delta^2$ (the differential capacitance of the dot) or $\partial\varepsilon^{(2)}_{p,-}/\partial\phi$ (the supercurrent through the dot). The limit $\Delta_{\rm g} \gg \Delta, |t_L|, |t_R|$ is imposed in Eq. (4.24) to separate the detuning and the phase dependence from other parameters of the model included in the coefficient $K_1^{(2)}$. $K_1^{(2)}$ is given by

$$K_1^{(2)} = \frac{L}{2\pi} \int_{-\infty}^{\infty} dk \sum_{j=1,2} \frac{u^2_{kj\uparrow} - v^2_{-kj\uparrow}}{\varepsilon_{k,j}/\Delta_{\rm ind}}, \tag{4.25}$$

where L is the length of the nanowires. Physically, $|s_{\rm dir}|^2 K_1^{(2)}/\Delta_{\rm ind}$ in Eq. (4.24) represents the second-order amplitude of the single-electron tunneling between the dot and the superconductor, while factor $\Delta/(2\sqrt{\Delta^2 + 4|\bar{t}_p(\phi)|^2})$ represents how the electron wavefunction in the ground state is distributed between the dot and the island, see Eq. (4.19)

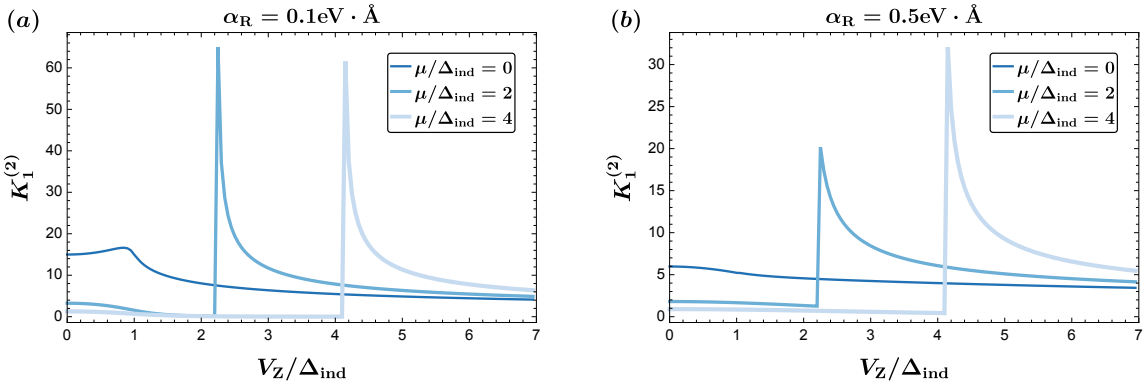

Figure 4.2: $K_1^{(2)}$ plotted as a function of the Zeeman energy V_Z in the nanowire for various values of the chemical potential μ and the Rashba spin-orbit coupling α_R. The effective electron mass, the length of the nanowire, and the induced gap are taken to be $m^* = 0.015m_e$, $L = 5\mu m$, and $\Delta_{ind} = 0.2$meV, respectively.

and Eq. (C.10). Combining Eqs. (4.22) and (4.24) yields the following expression for the ground state energy calculated up to the second order in the continuum-QD coupling:

$$\varepsilon_{p,-} = -\frac{1}{2}\sqrt{\Delta^2 + 4|\bar{t}_p(\phi)|^2} - \frac{|s_{dir}|^2}{\Delta_{ind}} K_1^{(2)} \frac{\Delta}{\sqrt{\Delta^2 + 4|\bar{t}_p(\phi)|^2}}. \tag{4.26}$$

The momentum integration in Eq. (4.25) cannot be in general performed analytically due to the complexity of the coefficients $u_{kj\sigma}, v_{kj\sigma}$. However, in the s-wave limit, i.e. when $V_Z \to 0$, $\alpha_R \to 0$, the expression for $K_1^{(2)}$ can be dramatically simplified yielding

$$K_{1,s\text{-wave}}^{(2)} = \frac{L}{2\pi}\sqrt{\frac{2m^*}{\mu\hbar^2}} \int_{-\mu/\Delta_{ind}}^{\infty} d\kappa \frac{\Delta_{ind}}{\sqrt{\kappa\Delta_{ind}/\mu + 1}} \frac{\kappa}{1+\kappa^2}. \tag{4.27}$$

For general values of V_Z and α_R we calculate the integral in Eq. (4.25) numerically and plot $K_1^{(2)}$ in Fig. 4.2 as a function of V_Z for various values of α_R and μ. Figure 4.2 demonstrates that the value of $K_1^{(2)}$ has a sharp discontinuity and a peak at the topological phase transition for larger values of μ, while for $\mu = 0$ the discontinuity in $K_1^{(2)}$ smoothens out. Note that the values of $K_1^{(2)}$ close to the critical point correspond to a closing of the gap Δ_g at the phase transition where the perturbation theory becomes invalid. As for the

effect of the spin-orbit coupling, larger $\alpha_{\rm R}$ leads to a larger induced gap in the nanowire and hence to a smaller value of $K_1^{(2)}$ as can be seen when comparing Figs. 4.2(a) and 4.2(b).

Realistic nanowires have multiple bands located at the different chemical potentials μ. With raising Zeeman energy (due to, for example, an external magnetic field) the band closest to the Fermi level ($\mu = 0$ in Fig. 4.2) undergoes the topological phase transition first. The rest of the bands are likely to stay trivial in the optimal range of the magnetic fields. In principal, all bands would contribute to the continuum-QD electron tunneling and thus to the energy shift of Eq. (4.24). However, Fig. 4.2 illustrates that the trivial band contribution to $\varepsilon_{p,-}$ in the second order is significantly suppressed when compared to the one of the topological band. For this reason, we neglect effect of multiple bands in Eq. (4.26) and consider only one (topological) band when analyzing QD-based measurements of the Majorana qubits below.

4.5.2 Effect of the continuum-QD coupling on QD-based Majorana qubit measurements

To quantify the effect of the continuum-QD couplings on the QD-based measurements of the Majorana qubits, we consider two potentially measurable quantities: the expectation value of the QD charge

$$\langle n_{{\rm QD},p}\rangle = n_{\rm g} - \frac{1}{2\varepsilon_{\rm C}}\frac{\partial\varepsilon_{p,-}}{\partial n_{\rm g}} \tag{4.28}$$

and the differential capacitance

$$\frac{C_{{\rm diff},p}}{C_{\rm g}^2/C_{\Sigma,{\rm D}}} = \frac{1}{2\varepsilon_{\rm C}}\frac{\partial^2\varepsilon_{p,-}}{\partial n_{\rm g}^2}, \tag{4.29}$$

where $C_{\rm g}$ is the capacitance between the gate and the dot and $C_{\Sigma,{\rm D}} \equiv e^2/2\varepsilon_{\rm C}$ is the total QD capacitance. In the absence of noise [128, 127] visibility of the QD-based measurement can be quantified by the difference in the corresponding measurable quantity between the two parity states $p = +1$ and $p = -1$. These differences for $\varepsilon_{p,-}$, $\langle n_{{\rm QD},p}\rangle$ and $C_{{\rm diff},p}$ are plotted in Fig. 4.3 as functions of the island-QD detuning Δ for various values of ξ/L, where we have utilized Eq. (4.13) to convert $|s_{\rm dir}|/|t_R|$ into ξ/L. As discussed in the previous paragraph, trivial bands do not contribute significantly to the second order energy correction and, hence, to the measurable quantities. For this reason, when plotting Fig. 4.3, we ignored the trivial bands contribution and focused solely on the topological band. Figure 4.2 indicates that the function $K_1^{(2)}$ in the topological phase ranges between 5 and 15 for typical values of the nanowire parameters, so, for concreteness, we take a typical value of $K_1^{(2)} = 10$ when plotting Fig. 4.3. Based on Fig. 4.3, we note that the continuum-QD couplings have a noticeable effect on the visibility of the QD-based measurements if $\xi/L \gtrsim 0.5$. In realistic devices the criterion $\xi/L \ll 1$ is necessary to ensure the stability of the topological phase and long qubit coherence times. This likely means that for a good Majorana qubit, the continuum-QD coupling would not considerably affect the visibility of the QD-based measurements.

4.6 Fourth order perturbative correction in the continuum-QD couplings

4.6.1 General discussion

Since the perturbative expansion in the continuum-QD couplings gives the correct results only in the limit of small $\Gamma_{\rho l}/\Delta_{\rm g}$, generally the fourth order contribution to the ground state energy is smaller than the second order contribution. However, as we shall

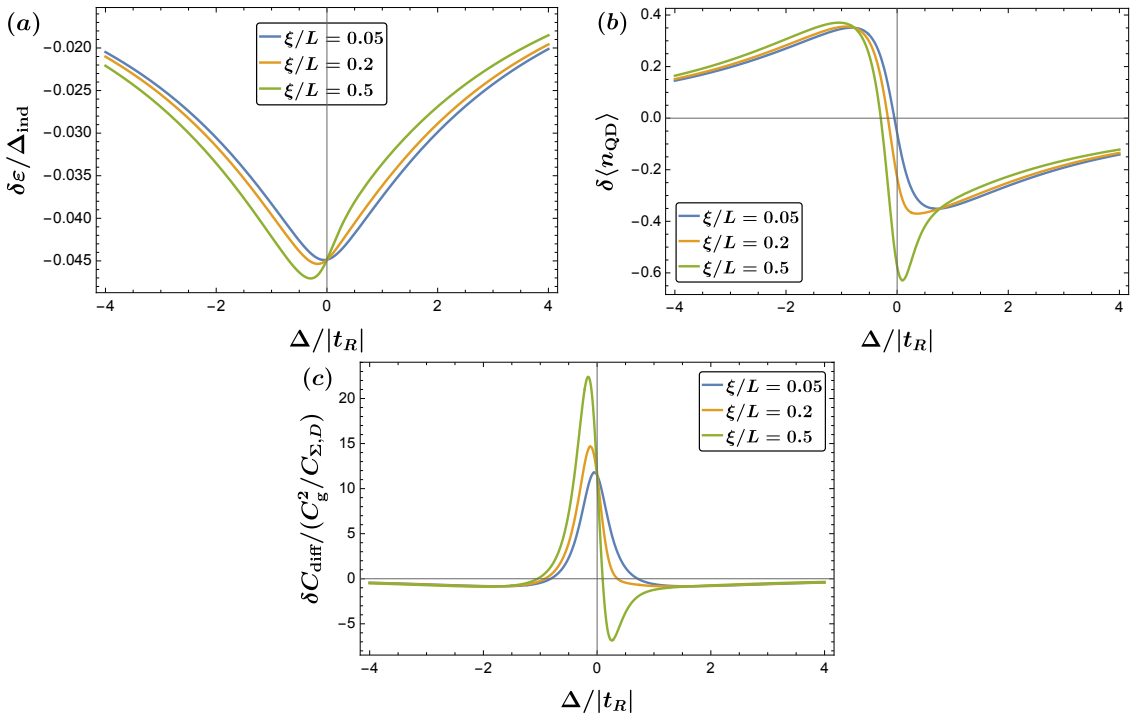

Figure 4.3: (a) The ground state energy difference between the two parity states $\delta\varepsilon = \varepsilon_{p=+1,-} - \varepsilon_{p=-1,-}$, (b) the average QD charge difference between the two parity states $\delta\langle n_{\rm QD}\rangle = \langle n_{{\rm QD},p=+1}\rangle - \langle n_{{\rm QD},p=-1}\rangle$, and (c) the differential capacitance difference between the two parity states $\delta C_{\rm diff} = C_{{\rm diff},p=+1} - C_{{\rm diff},p=-1}$ plotted as functions of the island-QD detuning for various values of ξ/L. The MZM-QD couplings are set to $|t_L| = |t_R| = 0.025\Delta_{\rm ind}$, while the phase difference is $\phi = 7\pi/8$. Value of the coefficient $K_1^{(2)}$ is taken to be $K_1^{(2)} = 10$.

show in this section, in the limit of the large charging energy on the dot (which we assume here) there are terms arising in the fourth order whose phase dependence does not vanish in the limit of the large detuning, $\Delta \gg |t_L|, |t_R|$, when the phase dependence of both the zeroth order term (calculated in Section 4.4) and the second order term (calculated in Section 4.5) disappears. Describing perturbation theory in terms of virtual processes, these fourth order terms represent processes where one electron of a Cooper pair is transferred from one topological superconductor onto the other through the QD, at the same time creating virtual quasiparticles in both superconductors. Then, these quasiparticles are annihilated by a similar superconductor-QD-superconductor transfer of another electron. Such fourth order processes include the ones when both electrons are transferred through the same QD level (single-level contribution) and the ones when the two electrons are transferred through different QD levels (two-level contribution). In the s-wave limit the single-level contribution vanishes due to the presence of time-reversal symmetry, but in general it is present and we analyze it in Section 4.6.2. On the contrary, the two-level contribution is present in the s-wave limit and it gives rise to the conventional $0 - \pi$ transition in the S-QD-S junctions, which has been extensively studied before [130, 131, 132, 133, 134, 135]. We calculate this term for generic nanowire parameters and present it in Section 4.6.3. The details of the fourth order calculations are given in Appendix C.5.

Since the visibility of QD-based measurements is maximal on- or close to the resonance, i.e. near $\Delta = 0$, the effect of the fourth order terms on the measurement would be significantly smaller than the effect of the second order terms analyzed in Section 4.5. However, as mentioned in the previous paragraph, the fourth order contribution can be important at the large detuning values, $\Delta \gg |t_L|, |t_R|$, and thus is crucial for the understanding of the $0 - \pi$ transition in the T-QD-T junctions. We present analysis of the $0 - \pi$ transition in Section 4.6.4.

4.6.2 Single-level tunneling contribution

In this subsection we present the fourth order term that includes virtual tunnelings through a single QD level. In principle, it can be either an $\rho =\uparrow$ or $\rho =\downarrow$ QD level. However, for simplicity, here we ignore the tunneling through the higher in energy $\rho =\downarrow$ level and focus on the tunneling through the $\rho =\uparrow$ level. In the limit $\Delta_{\rm g} \gg \Delta, |t_L|, |t_R|$ the single-level contribution is given by

$$\varepsilon_{p,-}^{(4,1)} = -\cos(\phi)\frac{|s_{\rm dir}|^4}{\Delta_{\rm ind}^3}K_1^{(4)}, \tag{4.30}$$

where, similarly to Section 4.5, we have set the spin-flip couplings to zero, $s_{\rm sf} = 0$. Coefficient $K_1^{(4)}$ in Eq. (4.30) is a function of the nanowire parameters:

$$K_1^{(4)} = \frac{L^2}{2\pi^2}\int_{-\infty}^{\infty} dkdk' \sum_{j,j'=1,2} \frac{u_{kj\uparrow}v_{-kj\uparrow}u_{k'j'\uparrow}v_{-k'j'\uparrow}}{\varepsilon_{kj}(\varepsilon_{kj}+\varepsilon_{k'j'})\varepsilon_{k'j'}/\Delta_{\rm ind}^3}. \tag{4.31}$$

The derivation of Eqs. (4.30)-(4.31) is presented in Appendix C.5.1, along with general expressions for the case of $s_{\rm sf} \neq 0$. Note that the energy correction of Eq. (4.30) is 2π-periodic in phase and independent of the island-QD detuning. In the s-wave limit, i.e. when $V_{\rm Z} \to 0$, $\alpha_{\rm R} \to 0$, the coefficient (4.31) vanishes due to the presence of the reflection symmetry, $\mathcal{R}$, and the time-reversal symmetry $\mathcal{T}_- = i\hat{\sigma}_y\mathcal{K}$, $\mathcal{T}_-^2 = -1$, in 1D s-wave superconductors. Specifically, the combination of these symmetries leads to the spin degeneracy of the quasiparticle energies, $\varepsilon_{k1} = \varepsilon_{k2}$, and the following constraints on the Bogoliubov amplitudes: $u_{k2\uparrow} = \pm u_{k1\downarrow}$, $u_{k2\downarrow} = \mp u_{k1\uparrow}$, $v_{-k2\uparrow} = \pm v_{-k1\downarrow}$, $v_{-k2\downarrow} = \mp v_{-k1\uparrow}$. Together with expressions (4.7), these conditions lead to

$$u_{k2\uparrow} = \pm u_{-k1\uparrow},\ v_{-k2\uparrow} = \mp v_{k1\uparrow}. \tag{4.32}$$

Plugging identities (4.32) into expression (4.31) for $K_1^{(4)}$ gives

$$K_{1,s\text{-wave}}^{(4)} = 0. \tag{4.33}$$

Hence, the fourth order single-level contribution is absent in the s-wave limit.

4.6.3 Two-level tunneling contribution

When analyzing the fourth order tunneling processes involving both QD levels, $\rho = \uparrow, \downarrow$, similarly to the treatment in the preceding sections we assume that the continuum-QD couplings on the left and on the right are the same, $|s_{\rho\sigma L}| = |s_{\rho\sigma R}| \equiv |s_{\rho\sigma}|$. For further convenience, we take the couplings to the spin-up and spin-down QD levels to be identical, i.e. $|s_{\rm dir}| \equiv |s_{\uparrow\uparrow}| = |s_{\downarrow\downarrow}|$, $|s_{\rm sf}| \equiv |s_{\uparrow\downarrow}| = |s_{\downarrow\uparrow}|$, and set the spin-flip tunneling to zero, $s_{\rm sf} = 0$. Given these assumptions and the limit $\Delta_{\rm g} \gg \Delta, |t_L|, |t_R|$, the two-level contribution to the energy correction in the fourth order reads

$$\varepsilon_{p,-}^{(4,2)} = \cos(\phi)\frac{|s_{\rm dir}|^4}{\Delta_{\rm ind}^3} \times \left[K_3^{(4)} - \frac{K_2^{(4)}}{2} - \left(K_3^{(4)} + \frac{K_2^{(4)}}{2}\right)\frac{\Delta}{\sqrt{\Delta^2 + 4|\bar{t}_p(\phi)|^2}}\right], \tag{4.34}$$

where similarly to Eqs. (4.25) and (4.31) we have introduced coefficients

$$K_2^{(4)} = \frac{L^2}{2\pi^2}\int_{-\infty}^{\infty} dk dk' \sum_{j,j'=1,2} \frac{u_{kj\uparrow}v_{-kj\downarrow}u_{k'j'\uparrow}v_{-k'j'\downarrow}}{\varepsilon_{kj}(\varepsilon_{kj} + \varepsilon_{k'j'} + h)\varepsilon_{k'j'}/\Delta_{\rm ind}^3}, \tag{4.35}$$

$$K_3^{(4)} = \frac{L^2}{2\pi^2}\int_{-\infty}^{\infty} dk dk' \sum_{j,j'=1,2} \frac{u_{kj\uparrow}v_{-kj\downarrow}u_{k'j'\uparrow}v_{-k'j'\downarrow}}{(\varepsilon_{kj} + h)(\varepsilon_{kj} + \varepsilon_{k'j'})\varepsilon_{k'j'}/\Delta_{\rm ind}^3}. \tag{4.36}$$

The details of the derivation as well as general expressions for the case of $s_{\rm sf} \neq 0$ are presented in Appendix C.5.2. In the s-wave limit, i.e. when $V_{\rm Z} \to 0$, $\alpha_{\rm R} \to 0$, the

coefficients $K_2^{(4)}$ and $K_3^{(4)}$ become

$$K_{2,s\text{-wave}}^{(4)} = \frac{m^* L^2 \Delta_{\text{ind}}^2}{4\pi^2\hbar^2} \int_{-\mu/\Delta_{\text{ind}}}^{\infty} d\kappa_L d\kappa_R \frac{1}{\sqrt{\kappa_L \Delta_{\text{ind}}/\mu + 1}} \frac{1}{\sqrt{\kappa_R \Delta_{\text{ind}}/\mu + 1}} \times \\ \times \frac{1}{(\kappa_L^2+1)(\sqrt{\kappa_L^2+1}+\sqrt{\kappa_R^2+1}+h/\Delta_{\text{ind}})(\kappa_R^2+1)}, \tag{4.37}$$

$$K_{3,s\text{-wave}}^{(4)} = \frac{m^* L^2 \Delta_{\text{ind}}^2}{4\pi^2\hbar^2} \int_{-\mu/\Delta_{\text{ind}}}^{\infty} d\kappa_L d\kappa_R \frac{1}{\sqrt{\kappa_L \Delta_{\text{ind}}/\mu + 1}} \frac{1}{\sqrt{\kappa_R \Delta_{\text{ind}}/\mu + 1}} \times \\ \times \frac{1}{(\kappa_L^2+1+h\sqrt{\kappa_L^2+1}/\Delta_{\text{ind}})(\sqrt{\kappa_L^2+1}+\sqrt{\kappa_R^2+1})(\kappa_R^2+1)}. \tag{4.38}$$

Note that in general the phase dependence of $\varepsilon_{p,-}^{(4,1)}$ in Eq. (4.34) comes not only from the 2π-periodic $\cos(\phi)$ factor, but also through the dependence of $|\bar{t}_p|^2$ on ϕ which is 4π-periodic.

In the trivial s-wave case when no MZM-QD couplings are present in the system, $|\bar{t}_p| = 0$, Eq. (4.34) simplifies to $\varepsilon_{p,-}^{(4,2)} \propto \text{sign}(\Delta)\cos\phi$ with a Δ-independent and ϕ-independent prefactor, while Eq. (4.30) yields $\varepsilon_{p,-}^{(4,1)} = 0$. The supercurrent through the junction in this case is given by $I_{\text{s}} \propto \partial\varepsilon_{p,-}^{(4,2)}/\partial\phi \propto \text{sign}(\Delta)\sin\phi$ and it abruptly changes its sign at $\Delta = 0$. This illustrates the simplest case of the well-known $0-\pi$ transition in the S-QD-S junctions [130, 131, 132, 133, 134, 135] since the condition $\Delta < 0$ corresponds to the empty dot (even parity), while the condition $\Delta > 0$ corresponds to the dot occupied by a single electron (odd parity). Further simplification is possible in the case of degenerate QD level, i.e. when $h = 0$. In this case $K_2^{(4)}$ and $K_3^{(4)}$ are equal, $K_{2,h=0}^{(4)} = K_{3,h=0}^{(4)} \equiv K_{h=0}^{(4)}$, and Eq. (4.34) becomes

$$\varepsilon_{p,-}^{(4,2)} = \lambda K_{h=0}^{(4)} \frac{|s_{\text{dir}}|^4}{\Delta_{\text{ind}}^3} \cos\phi, \tag{4.39}$$

where $\lambda = 2$ if $\Delta < 0$ and $\lambda = -1$ if $\Delta > 0$. This expression for the fourth order phase-dependent energy shift is identical to the one derived in Ref. [131].

In the topological phase the presence of the MZM-QD couplings and the associated 4π-periodic phase dependence would alter the simple picture of the $0-\pi$ transition discussed in the previous paragraph. In the next subsection we analyze the $0-\pi$ transition in the presence of the MZM-QD couplings.

4.6.4 Critical current and the $0-\pi$ transition

Combining Eqs. (4.26),(4.30),(4.34), we obtain the expression for the ground state energy of the junction up to the fourth order in the continuum-QD coupling:

$$\varepsilon_{p,-} = -\frac{1}{2}\sqrt{\Delta^2+4|\bar{t}_p(\phi)|^2} - \frac{|s_{\rm dir}|^2}{\Delta_{\rm ind}}K_1^{(2)}\frac{\Delta}{\sqrt{\Delta^2+4|\bar{t}_p(\phi)|^2}} - \\ - \cos(\phi)\frac{|s_{\rm dir}|^4}{\Delta_{\rm ind}^3}\left(-\tilde{K}_1^{(4)} + \tilde{K}_2^{(4)}\frac{\Delta}{\sqrt{\Delta^2+4|\bar{t}_p(\phi)|^2}}\right), \tag{4.40}$$

where we have introduced $\tilde{K}_1^{(4)} = -K_1^{(4)} + K_3^{(4)} - K_2^{(4)}/2$ and $\tilde{K}_2^{(4)} = K_3^{(4)} + K_2^{(4)}/2$. Note that the term with $\tilde{K}_1^{(4)}$ factor is a detuning-independent energy shift, while the term with $\tilde{K}_2^{(4)}$ factor has an explicit detuning dependence. For general values of the system parameters we calculate the integrals in Eqs. (4.25),(4.31) and (4.35)-(4.36) numerically and plot the values of the phase- and detuning-independent constants $\tilde{K}_1^{(4)}$ and $\tilde{K}_2^{(4)}$ entering Eq. (4.40) in Fig. 4.4. Similarly to the dependence of the second order coefficient $K_1^{(2)}$ on $V_{\rm Z}$, see Fig. 4.2, the fourth order coefficients plotted against $V_{\rm Z}$ undergo a discontinuity at the critical point for higher values of the chemical potential. This discontinuity is present even for the $\mu = 0$ value of the chemical potential which is not the case for the $K_1^{(2)}$ coefficient. Since at the topological transition the quasiparticle gap closes and the perturbation theory breaks down, values of $\tilde{K}_1^{(4)}$ and $\tilde{K}_2^{(4)}$ near the critical point are beyond the regime of validity, particularly the apparent singularity of $\tilde{K}_1^{(4)}$ at the critical point, see Fig. 4.4(a). Contrary to the second order case depicted in

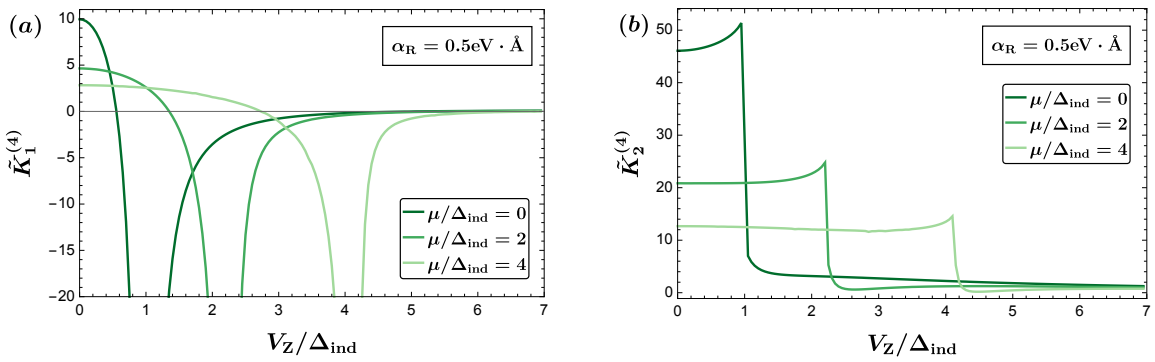

Figure 4.4: (a) $\tilde{K}_1^{(4)}$ and (b) $\tilde{K}_2^{(4)}$ plotted as functions of the Zeeman energy V_Z in the nanowire for various values of the chemical potential μ and Rashba spin-orbit coupling α_R. The Zeeman splitting on the dot, the effective electron mass, the length of the nanowire, and the induced gap are taken to be $h = \Delta_{ind}$, $m^* = 0.015m_e$, $L = 5\mu m$, and $\Delta_{ind} = 0.2$meV, respectively.

Fig. 4.2, in the fourth order, trivial bands (the ones at the higher chemical potential) have a considerable contribution to the energy. Particularly, Fig. 4.4(b) illustrates that the coefficient $\tilde{K}_2^{(4)}$ of a trivial band can be larger than the one of the $\mu = 0$ band in the topological phase.

Equation (4.40) captures the ground state energy of the T-QD-T junction with single-band nanowires calculated up to the fourth order. Calculating this energy for the junction with realistic multi-band nanowires is not a simple task, even if the junction is assumed to be made of the identical nanowires. To begin with, in the case of the multi-band nanowires one needs to include different contributions to the ground state energy coming from each band. Additionally, the fourth order processes in the multi-band T-QD-T junction can include QD-mediated virtual tunneling between the different energy bands of the opposite nanowires. These multi-band effects cannot be fully captured by Eq. (4.40), so we propose the following simplified treatment of the multi-band T-QD-T junction: we implicitly perform an averaging over multiple bands and consider the nanowires with multiple identical "average" bands. In this case, one can analyze the multi-band T-QD-T junctions by simply modifying Eq. (4.40). If the total number of the average bands is

N_{bands}, the ground state energy of the multi-band T-QD-T junction up to the forth order is given by

$$\varepsilon_{p,-} = -\frac{1}{2}\sqrt{\Delta^2 + 4|\bar{t}_p(\phi)|^2} - \frac{|s_{\text{dir}}|^2}{\Delta_{\text{ind}}} K_1^{(2)} \frac{\Delta}{\sqrt{\Delta^2 + 4|\bar{t}_p(\phi)|^2}} - \\ - \cos(\phi) N_{\text{bands}}^2 \frac{|s_{\text{dir}}|^4}{\Delta_{\text{ind}}^3} \left(-\tilde{K}_1^{(4)} + \tilde{K}_2^{(4)} \frac{\Delta}{\sqrt{\Delta^2 + 4|\bar{t}_p(\phi)|^2}} \right). \tag{4.41}$$

Here we did not multiply the second order term by N_{bands} since only the topological band mainly contributes to the energy shift in the second order as we have shown in Section 4.5. The fourth order correction is proportional to N_{bands}^2 because the fourth order processes include virtual tunneling between the QD and both nanowires.

Using expression (4.41) for the ground state energy of the junction one can straightforwardly calculate the equilibrium supercurrent through the junction:

$$-\frac{I_{\text{s}}}{I_0}\Delta_{\text{ind}} = \\ = \frac{\partial \varepsilon_{p,-}}{\partial \phi} = -\frac{p|t_L t_R|\cos(\phi/2)}{\sqrt{\Delta^2 + 4|\bar{t}_p(\phi)|^2}} + \frac{|s_{\text{dir}}|^2}{\Delta_{\text{ind}}} K_1^{(2)} \frac{2p\Delta|t_L t_R|\cos(\phi/2)}{(\Delta^2 + 4|\bar{t}_p(\phi)|^2)^{3/2}} + N_{\text{bands}}^2 \frac{|s_{\text{dir}}|^4}{\Delta_{\text{ind}}^3} \times \\ \times \left\{ -\tilde{K}_1^{(4)} \sin\phi + \tilde{K}_2^{(4)} \left[\frac{2p\Delta|t_L t_R|\cos(\phi/2)}{(\Delta^2 + 4|\bar{t}_p(\phi)|^2)^{3/2}} \cos\phi + \frac{\Delta}{\sqrt{\Delta^2 + 4|\bar{t}_p(\phi)|^2}} \sin\phi \right] \right\}, \tag{4.42}$$

where we have introduced parameter $I_0 = 2e\Delta_{\text{ind}}/\hbar$. The supercurrent is plotted as a function of the island-QD detuning in Figs. 4.5-4.6. When plotting the supercurrent, we use the values of the coefficients $K_1^{(2)}$,$\tilde{K}_1^{(4)}$ and $\tilde{K}_2^{(4)}$ calculated for the average band at $\mu = 2\Delta_{\text{ind}}$ and take the number of bands to be $N_{\text{bands}} = 8$. Figure 4.5 depicts the equilibrium supercurrent in the trivial phase when the MZM-QD couplings are absent. The abrupt sign switch of the supercurrent at $\Delta = 0$ corresponds to the $0-\pi$ transition in the trivial S-QD-S junction mentioned in the previous subsection, see Eq. (4.39) and the

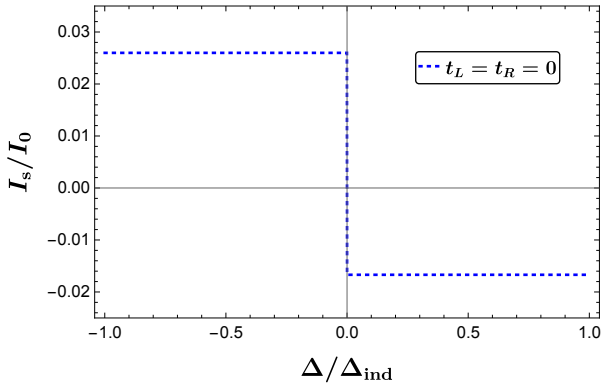

Figure 4.5: The supercurrent I_s of Eq. (4.42) plotted as a function of the island-QD detuning in the trivial regime with $V_Z = \Delta_{ind}/4$. The continuum-QD coupling is $|s_{dir}| = \sqrt{0.4} \times 0.1\Delta_{ind}$, while the chemical potential, the number of bands and the phase are $\mu = 2\Delta_{ind}$, $N_{bands} = 8$ and $\phi = \pi/2$, respectively. The coefficients $K_1^{(2)}$, $\tilde{K}_1^{(4)}$ and $\tilde{K}_2^{(4)}$ in Eq. (4.42) are computed for $h = \Delta_{ind}$, $\alpha_R = 0.5\text{eV} \cdot \text{Å}$, $m^* = 0.015m_e$, $L = 5\mu m$, and $\Delta_{ind} = 0.2\text{meV}$, and the aforementioned values of V_Z and μ. Here $I_0 = 2e\Delta_{ind}/\hbar$.

corresponding discussion. Solid lines (black and red) in Fig. 4.6 illustrate the supercurrent in the topological regime when both the MZM-QD and the continuum-QD couplings are present, while the blue dotted lines and the dashed lines (both black and red) in Fig. 4.6 represent the supercurrent in the absence of the MZM-QD and the continuum-QD couplings, respectively. Red-colored lines in the left column of Fig. 4.6 are plotted for the state with $p = +1$ parity, whereas black-colored lines in the right column of Fig. 4.6 correspond to the supercurrent when the junction is in the state with $p = -1$. Solid lines in Figs. 4.6(a)-(b) represent the supercurrent in the case when $\xi/L = 0.05$, which via Eq. (4.13) corresponds to a weak continuum-QD coupling when compared to the MZM-QD coupling, $|s_{dir}|/|t| \approx 0.3$. The continuum-QD contribution to the supercurrent (dotted blue line) in this case is small when compared to the MZM-QD contribution (dashed lines). For this reason, the values of the total supercurrent (solid lines) are close to the values of the MZM-QD contribution and the total supercurrent does not cross zero meaning that the $0 - \pi$ transition is absent in this case. When the ratio of

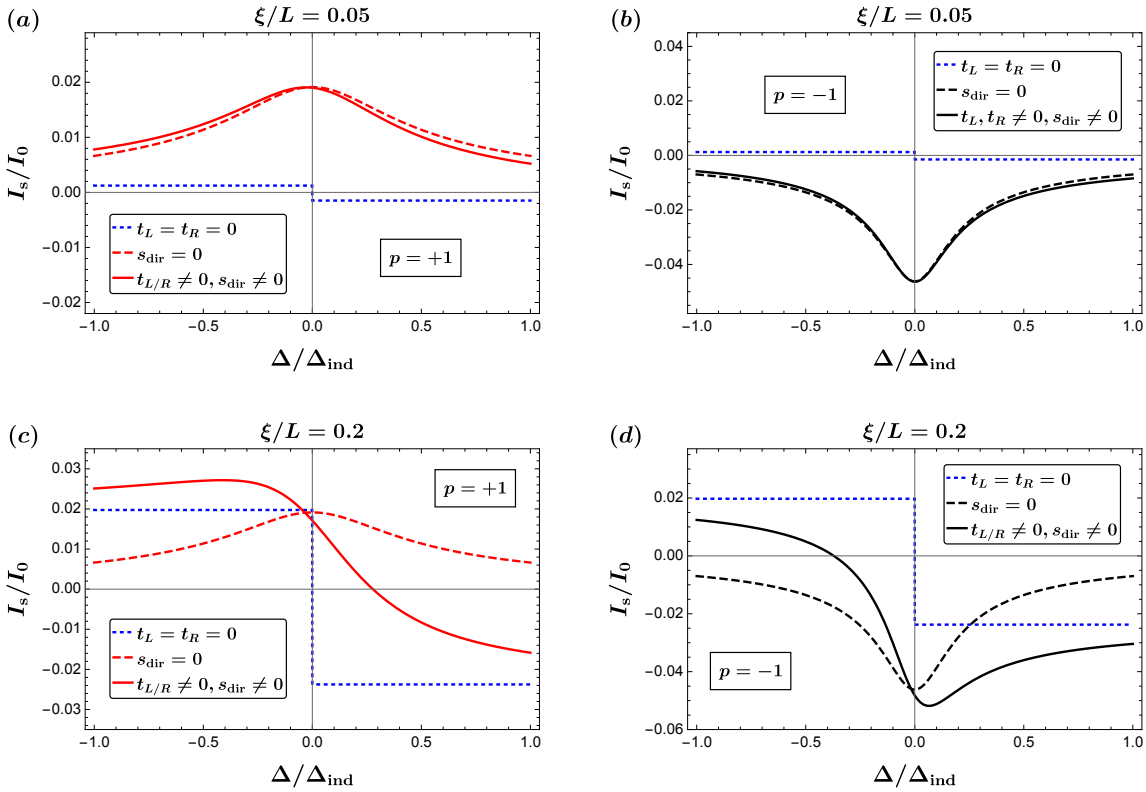

Figure 4.6: The supercurrent $I_{\rm s}$ of Eq. (4.42) plotted as a function of the island-QD detuning in the topological regime with $V_{\rm Z} = 1.5\Delta_{\rm ind}$ in the case of $\xi/L = 0.05$ (upper row, solid lines) and $\xi/L = 0.2$ (lower row, solid lines). The red(black) color in the left(right) column marks the case of the $p = +1(p = -1)$ parity. The MZM-QD couplings are $|t_L| = |t_R| = \Delta_{\rm ind}/10$, while the chemical potential, the number of bands, and the phase are $\mu = 2\Delta_{\rm ind}$, $N_{\rm bands} = 8$, and $\phi = \pi/2$, respectively. The coefficients $K_1^{(2)}$, $\tilde{K}_1^{(4)}$ and $\tilde{K}_2^{(4)}$ in Eq. (4.42) are computed for $h = \Delta_{\rm ind}$, $\alpha_{\rm R} = 0.5{\rm eV}\cdot$ Å, $m^* = 0.015m_e$, $L = 5\mu m$, and $\Delta_{\rm ind} = 0.2$meV, and the aforementioned values of $V_{\rm Z}$ and μ. As a reference, we also plot the supercurrent in the absence of the MZM-QD (blue dotted lines) and the continuum-QD (dashed lines) couplings, while keeping the rest of the parameters entering Eq. (4.42) the same. Here $I_0 = 2e\Delta_{\rm ind}/\hbar$.

the continuum-QD coupling to the MZM-QD coupling is increased such that $\xi/L = 0.2$, which corresponds to $|s_{\rm dir}|/|t| \approx 0.6$, the continuum-QD contribution to the supercurrent becomes comparable to the MZM-QD contribution. This case is depicted in Figs. 4.6(c)-(d) The total supercurrent in this case does change its sign as a function of the detuning. There are, however, two crucial differences between this sign change and the conventional $0-\pi$ transition present in the absence of the MZM-QD coupling and depicted in Fig. 4.5. First, in the topological regime the sign switch, if present, is continuous, signifying that the $0-\pi$ transition becomes the "$0-\pi$ crossover" in this case. Second, the crossover takes place at non-zero detuning. The value of the detuning at which the crossover takes place depends on the relative ratio of the MZM-QD and the continuum-QD contributions to the supercurrent: the larger is Majorana contribution, the further from $\Delta = 0$ the crossover takes place. Hence, contrary to the conventional $0-\pi$ transition in the S-QD-S junctions, the $0-\pi$ crossover in this case does not correspond to the change in the QD occupation parity. This shows that the mere presence of a supercurrent sign change in the junction when changing the island-QD detuning does not necessarily rule out the presence of a topological phase and MZMs. In order to rule out the topological phase, one needs to detect a sharp $0-\pi$ transition exactly at the zero detuning when the parity of the QD occupation changes.

Figure 4.7 illustrates the supercurrent plotted as a function of both the island-QD detuning and the phase. The relevant parameter controlling the Majorana contribution to the current is $\Delta/|t|$. Hence, for smaller values of Δ the Majorana contribution is dominant and the current is 4π-periodic in phase, while an increase in Δ leads to the suppression of the Majorana contribution and crossover to an approximate 2π periodicity at learge detuning.

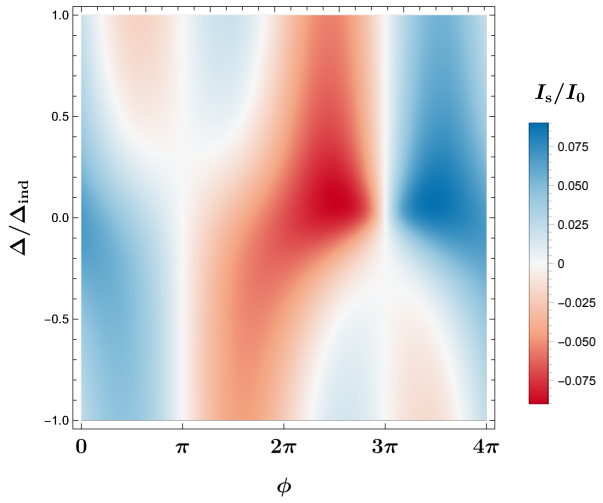

Figure 4.7: The supercurrent I_s of Eq. (4.42) as a function of the phase ϕ and the island-QD detuning Δ in the topological regime with $V_\mathrm{Z} = 1.5\Delta_\mathrm{ind}$. Here the MZM-QD couplings are set to $|t_L| = \Delta_\mathrm{ind}/10$, $|t_R|/|t_L| = 1.5$, while the continuum-QD couplings are chosen such that, via Eq. (4.13), $|s_\mathrm{dir}|/|t_L| = \sqrt{2\xi/L}$ with $\xi/L = 0.2$. The chemical potential, the number of bands, and the parity are $\mu = 2\Delta_\mathrm{ind}$, $N_\mathrm{bands} = 8$, and $p = +1$, respectively. The coefficients $K_1^{(2)}$, $\tilde{K}_1^{(4)}$ and $\tilde{K}_2^{(4)}$ in Eq. (4.42) are computed for $h = \Delta_\mathrm{ind}$, $\alpha_\mathrm{R} = 0.5\mathrm{eV}\cdot\text{Å}$, $m^* = 0.015m_e$, $L = 5\mu m$, $\Delta_\mathrm{ind} = 0.2\mathrm{meV}$, and the aforementioned values of V_Z and μ. Here $I_0 = 2e\Delta_\mathrm{ind}/\hbar$.

4.7 Conclusion

In this work we investigated how the coupling between the quantum dot and the superconductor continuum modes alters properties of T-QD-T junctions. As a model for the topological superconductor we took a semiconducting nanowire with strong Rashba spin-orbit coupling, proximitized by an s-wave superconductor and subject to a parallel magnetic field. Treating the MZM-QD coupling non-perturbatively and applying perturbation theory in the continuum-QD coupling up to the fourth order we analyzed the extent to which the continuum-QD coupling affects the QD-based charge-readout measurement of the Majorana qubits and the $0-\pi$ transition in the T-QD-T junctions.

We found that for reasonable system parameters the continuum-QD coupling does not considerably impact the visibility of the Majorana qubit measurement, even in the

presence of multiple trivial bands in the superconductors. At the same time, we discovered that the magnitude of the effect of the continuum-QD coupling on the $0-\pi$ transition depends on the relative ratio between the MZM and the continuum contributions to the supercurrent. For small or absent MZM-QD coupling a conventional sharp $0-\pi$ transition occurs as the parity of the QD switches from even to odd, whereas in the case of a strong MZM contribution the supercurrent does not switch sign as one sweeps through the island-QD energy detuning. In the intermediate regime when the Majorana and the continuum contributions to the supercurrent are comparable, we found that the supercurrent changes direction continuously as a function of the detuning and that the sign crossing occurs at a non-zero value Δ_0 of the detuning. The value of Δ_0 depends on the ratio between the MZM and the continuum contributions to the supercurrent. This implies that in the intermediate regime the $0-\pi$ transition becomes a "$0-\pi$ crossover" which does not occur simultaneously with the switch of the QD parity.

Our results have direct experimental consequences. For the experiments conducting measurements of the supercurrent in T-QD-T junctions, this work we have shown that such junctions can potentially exhibit the phenomenology of a $0-\pi$ crossover. For experiments aiming to perform a measurements of topological qubits, we showed that the coupling between the QD and the continuum modes in the superconductors should not be a factor limiting the visibility and the fidelity of such measurements.

Chapter 5

Random-matrix theory of a dynamical measurement-induced phase transition in nonlocal Floquet quantum circuits

5.1 Permissions and Attributions

1. The content of Chapter 5 and Appendix D is the result of a collaboration with Igor L. Aleiner.

5.2 Introduction

Monitored quantum systems have been investigated extensively in recent years by both theorists and experimentalists to study novel quantum effects arising due to the interplay of the unitary dynamics and measurements. One such effect is the existence of

distinct phases in the long-time dynamics of monitored systems, arising as a function of the monitoring rate and the degree of scrambling, as well as the associated measurement-induced phase transitions (MIPTs) between these phases [145, 146, 147, 148, 149, 150, 151, 152, 153, 154, 155, 156, 157, 158, 159, 160, 161, 162, 163, 164, 165, 166, 167, 168, 169, 170, 171, 172, 173, 174, 175, 176, 177, 178, 179, 180, 181, 182, 183, 184, 185, 186, 187, 188, 189, 190, 191, 192, 193, 194, 195, 196, 197, 154, 198, 199, 200, 201, 202, 203, 204, 205, 206, 207, 208, 209, 210, 211, 212, 213, 214, 215, 216, 217, 218, 219, 220, 221, 222, 223, 224, 225, 226, 227, 228, 229, 230, 231, 232, 233, 234, 235, 236, 237, 238, 239, 240, 241] (see also reviews [242, 243]). Contrary to conventional phase transitions, these MIPTs cannot be described in terms of the trajectory-averaged density operator; instead, one needs to track individual quantum trajectories to reveal the presence of MIPTs. Consequently, only quantities nonlinear in the density operator can be utilized to characterize MIPTs.

One such quantity is entanglement entropy, in terms of which the weak monitoring phase can be described as the volume law phase, while the strong monitoring phase corresponds to the area law of entanglement entropy. In monitored quantum circuits (see, e.g., [145, 146]) the transition occurs between the volume law and the area law phases, while at the critical point the entanglement entropy scales logarithmically with the system size. Another quantity that can be utilized to analyze MIPTs is purity [147, 148], in terms of which the weak monitoring phase corresponds to the mixed phase, where the purification time of an initially mixed state scales exponentially with the system size, whereas the strong monitoring phase corresponds to the pure phase, where an initially mixed state purifies on a timescale independent of the system size.

Observing the MIPT in an experiment requires postselecting on a given quantum trajectory multiple times. However, in a generic monitored quantum circuit the probability to measure a generic quantum trajectory diminishes exponentially with the number of measurements. This fact, makes the experimental detection of MIPTs in a direct way

a formidable problem. Nevertheless, various ways have been proposed to overcome this postselection barrier, either by incorporating active feedback conditioned onto the measurement outcomes [179, 180, 181, 182, 183, 184, 185], utilizing classical simulations [186, 187, 188, 189], or with the help of space-time duality mappings [190, 191, 192, 193]. Recently, signatures of MIPTs have been reported in multiple experiments [244, 245, 246].

In this work, we study MIPTs in monitored all-to-all interacting Floquet quantum circuits. We focus on postselected quantum trajectories, which puts the transitions we analyze in a class of "forced" MIPTs [154]. The non-unitary Floquet evolution cycle that we consider in the simplest case is described by an operator $W_0 = P_0 U^\dagger P_0 U P_0$, where U is a (random) unitary and P_0 is a projective measurement. To qualitatively understand the transition that occurs in this setting, we note that in the limit of no measurement, $P_0 = 1$, the evolution is trivial, $W_0 = 1$, and the system completely retains the knowledge of its initial conditions. On the other hand, in the limit when the majority of qubits are measured, $\mathrm{Tr}[P_0] \ll N$, where N is the Hilbert space dimension of the system, the operators $P_0 U^\dagger P_0$ and $P_0 U P_0$ acting within the projected part of the Hilbert space are unrelated to each other, and the evolution becomes highly non-trivial, such that the system rapidly loses the memory of its initial conditions. Based on these considerations, at some intermediate strength of the measurement one might expect a phase transition between the two regimes described above; the corresponding phases can be understood in the sense of retaining some part or losing the memory of the system's initial conditions as it evolves.

Using the random-matrix theory (RMT), we analytically show the existence of such transition in the thermodynamic limit, which is revealed in the *spectrum* of non-unitary Floquet operators governing the evolution of the system. We identify two types of such spectral transitions. One type is a transition between two distinct gapped phases, and it is marked by a closure of the spectral gap at the critical point. The other type is a

transition between a gapped and a gapless phase, where the gapless phase can be described as an "extended criticality"[1]. Since these transitions can be understood in terms of retaining some part or losing the memory of the system's initial conditions, they also exhibit signatures in the long-time dynamics of the system. We show that by numerically calculating for small-sized systems the dynamics of certain physical quantities. One of the quantities we consider is the purity of an initially mixed state, while the other quantity is the probability to measure a specific Floquet quantum trajectory given the intrinsic randomness in measurement outcomes.

We note here that spectral signatures of MIPTs have been studied priorly in various monitored free-fermionic and spin chain models with non-Hermitian Hamiltonians and postselected measurement outcomes [205, 206, 202, 204, 201, 200, 203], revealing both volume-to-area law [200, 201, 203, 202] and log-to-area law [204, 205, 206] transitions. The critical point in these models typically corresponds to the closure of the gap in the imaginary part of the spectra of the corresponding non-Hermitian Hamiltonians. Additionally, Refs. [203, 204] analyzed MIPTs in the spectrum of monitored periodically driven Floquet systems within the framework of non-Hermitian Hamiltonians. The one-dimensional transverse field Ising model (with next-nearest-neighbor couplings and imaginary fields) of Ref. [203] exhibited a volume-to-area law MIPT associated with the Yang-Lee singularity, while the free-fermionic model of Ref. [204] revealed a log-to-area law MIPT and the emergence of a non-Hermitian i0 mode. Our work complements the aforementioned studies, providing a different gate-based model of a monitored Floquet system, and presenting analytically calculated spectral signatures of MIPTs occurring in the model. To the best of our knowledge, the RMT-based approach that we use to perform calculations in our work has not been utilized priorly to study MIPTs.

[1]Note that signatures of the MIPT between a gapped and a gapless phase have been previously reported in monitored free-fermionic systems [178, 173, 174].

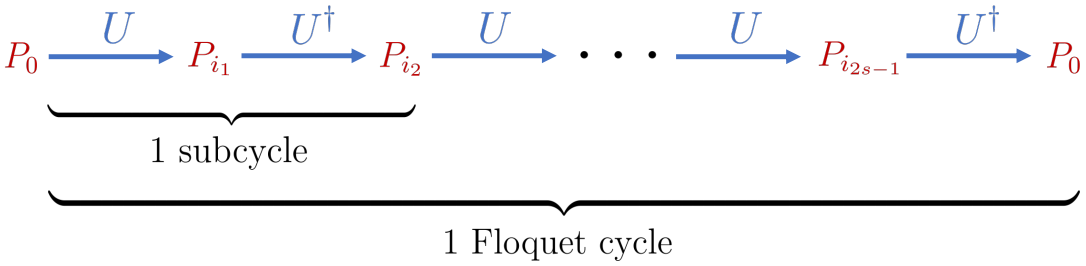

Figure 5.1: Schematic depiction of one Floquet cycle considered in our setup. Each cycle is made out of s subcycles, with each subcycle consisting of unitary evolution U, projective measurement, inverse unitary evolution $U^\dagger$, and another measurement. The system is initialized by measuring P_0 at $t = 0$, and the measurement at the end of each cycle is fixed to be P_0. Quantum trajectory within a cycle is determined by a sequence of measurement outcomes, $\boldsymbol{m} = (i_1, i_2, \ldots, i_{2s-1})$.

5.3 Model

In our setup we consider a Floquet system of n qubits subject to a unitary evolution and projective measurements. The measurement outcomes are recorded and postselected. Characterizing each measurement by a projection operator $P_i = P_i^2$, where $i = 0$ or 1 depending on the measurement outcome, we initialize the system by performing the projective measurement P_0. After that, we consider a Floquet evolution with each Floquet cycle built out of s subcycles, and each subcycle consisting of a unitary evolution U, a projective measurement, an inverse unitary evolution $U^\dagger$, and another measurement. Measurement outcomes can differ between different subcycles; they are taken to be postselected but arbitrary, except for the last measurement in a cycle, which we require to be P_0. Schematic depiction of one Floquet cycle is shown in Fig. 5.1: each quantum trajectory within the Floquet cycle can be characterized by a sequence of $2s - 1$ measurement outcomes, $\boldsymbol{m} = (i_1, i_2, \ldots, i_{2s-1})$. For such quantum trajectory the evolution of the density operator within each cycle is described by a non-unitary operator

$$W_{\boldsymbol{m}} = P_0 U^\dagger P_{i_{2s-1}} U \ldots P_{i_2} U^\dagger P_{i_1} U P_0, \tag{5.1}$$

and thus following one cycle of evolution the system density operator is given by

$$\rho_1 = \frac{W_{\boldsymbol{m}}\rho_0 W_{\boldsymbol{m}}}{\mathrm{Tr}[W_{\boldsymbol{m}}^2\rho_0]}, \tag{5.2}$$

where ρ_0 is the density operator at time $t = 0$. After k Floquet cycles the system density operator reads

$$\rho_k = \frac{W_{\boldsymbol{m}}^k\rho_0 W_{\boldsymbol{m}}^k}{\mathrm{Tr}[W_{\boldsymbol{m}}^{2k}\rho_0]}. \tag{5.3}$$

We start by considering the simplest quantum trajectory allowed in our setup: it corresponds to one subcycle within each Floquet cycle, $\boldsymbol{m} = i_1$, and, for concreteness, we take $i_1 = 0$. In Section 5.6 we show that the case of $\boldsymbol{m} = 1$ and other, more complicated trajectories can be analyzed using the results obtained for the case of $\boldsymbol{m} = 0$. Evolution along the $\boldsymbol{m} = 0$ trajectory is described by a non-unitary Hermitian operator

$$W_0 = P_0 U^\dagger P_0 U P_0. \tag{5.4}$$

As we show in Appendix D.1, eigenvalues of W_0 are confined between 0 and 1.

We consider projective operators in the form $P_0 = \mathrm{diag}\{1, 1, \ldots, 1, 0, 0, \ldots, 0\}$ and characterize P_0 by its rank, $\mathrm{Tr}P_0 = bN$, where $N = 2^n$ is the Hilbert space dimensionality. The parameter b controls the strength of the measurement in our model. If simply n_P qubits are measured in the computational basis, then $b = 1/2^{n_P}$; however, arbitrary values of $b = M/N$ with $M = 1, \ldots, N$ can be realized by coupling the system to ancilla qubits using unitary gates and then measuring the ancillas [3]. The unitary evolution operator U in our model is taken to be random. We model U as a Cayley transform of

a random matrix H sampled from the Gaussian unitary ensemble (GUE):

$$U = (i + H)(i - H)^{-1}, \tag{5.5}$$

$$\langle H_{ij} \rangle = 0, \tag{5.6}$$

$$\langle H_{ij} H_{kl} \rangle = \frac{\gamma}{N} \delta_{il} \delta_{jk}, \tag{5.7}$$

where δ_{il} is the Kronecker delta and $\langle ... \rangle$ denotes the random matrix ensemble averaging. Parameter γ characterizes the ensemble of random matrices U. For example, for small values of $\gamma \to 0$ the distribution of H is narrow and U is sampled close to the identity matrix 1. However, for larger values of γ the distribution of U is nontrivial. Numerically, we find that the CUE and the ensemble (5.5)-(5.7) give the same results for the moments of W_0 up to arbitrary order when $\gamma = 2$, and later in the manuscript (see Eq. (5.50) and the subsequent discussion) we show analytically that those moments are equivalent up to the third order. However, while suspecting that the ensemble (5.5)-(5.7) with $\gamma = 2$ and the CUE are equivalent to each other when it comes to computing the moments of W_0, we lack a formal analytical proof of this fact.

In this work, we show that W_0 as a function of b and γ exhibits spectral phase transitions in the thermodynamic limit. As a preview of our results, here we present numerical signatures of the transition in the spectrum of a randomly generated matrix W_0 for $N = 2048$. Histograms depicting the eigenvalue distribution of W_0 for various values of γ and b are illustrated in Fig. 5.2; for visual clarity, the zero eigenvalue is excluded from the histograms. There are two types of transitions that can be found in the spectrum of W_0. The first type occurs when the parameter b is tuned: for $b < 1/2$, the eigenvalue 1 is absent from the spectrum of W_0, see Fig. 5.2(a) plotted for $b = 1/8$. Upon increasing b, the gap between the largest eigenvalue and 1 decreases, eventually closing at the critical value of $b_c = 1/2$, as depicted in Fig. 5.2(b). Further increase in b

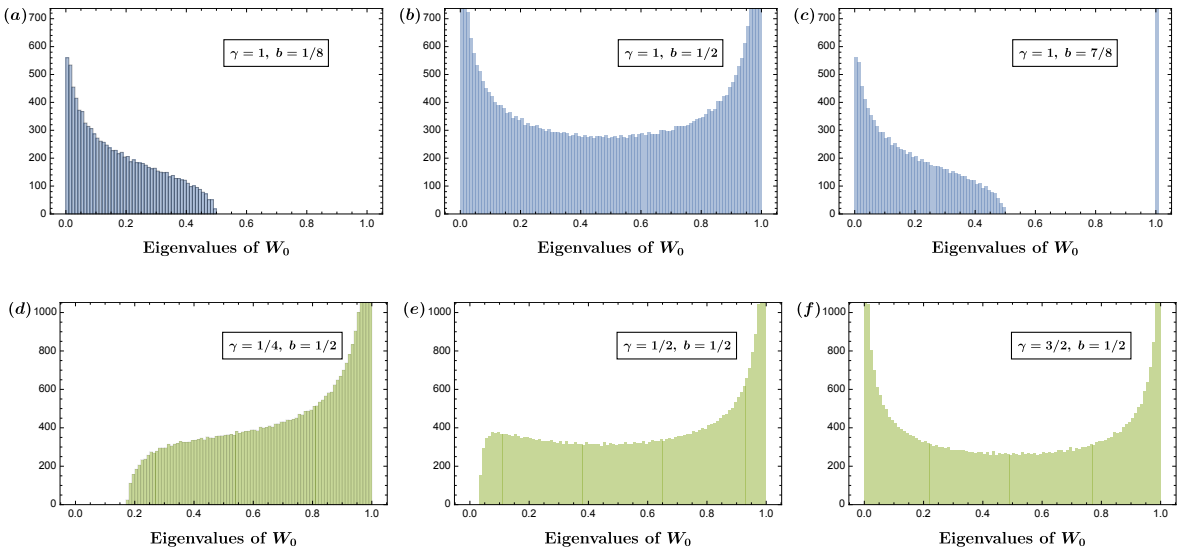

Figure 5.2: Histograms representing the eigenvalue distributions of a numerically generated random matrix W_0 for various values of γ and b. Dimensionality of the Hilbert space is $N = 2048$. Averaging is performed over 40 random matrix realizations. For visual clarity, the zero eigenvalue is excluded from the histograms. The gap near the eigenvalue 0, while present, is too small to be noticed in subfigures (a),(c). We display this gap in Fig. D.1 of Appendix D.2.

beyond the critical value, see Fig. 5.2(c), reopens the gap, but already in the presence of the eigenvalue 1 in the spectrum.

Since here the Floquet evolution is determined by a non-unitary operator W_0^k, where k is the number of the Floquet cycle, the presence (or the absence) of the eigenvalue 1 in the spectrum of W_0 has a profound effect on the long-time evolution of the system when $k \to \infty$. Specifically, the presence of the eigenvalues 1 leads to the evolution where the system retains some part of memory of its initial conditions, while in the absence of the eigenvalues 1 that is no longer the case. Thus, the two aforementioned phases exhibit distinct dynamical behavior.

The second type of transitions occurs in the vicinity of the eigenvalue 0: for $\gamma < \gamma_c$ the spectrum has a gap near 0. This gap closes at the critical point $\gamma = \gamma_c$ and remains

closed for larger values of γ. In this work, we show that in the thermodynamic limit

$$\gamma_c = \frac{1/2 - \sqrt{b(1-b)}}{(b-1/2)^2}. \tag{5.8}$$

The described phenomenology of the transition near 0 is illustrated in numerically plotted Figs. 5.2(d)-(f): for $b = 1/2$, Eq. (5.8) gives $\gamma_c = 1$, and thus Figs. 5.2(d),(e) reveal a gap present in between the lowest eigenvalue and 0, while in Fig. 5.2(f) this gap is closed. For $b = 1/8$ and $b = 7/8$, Eq. (5.8) gives $\gamma_c \approx 1.2$, and thus Figs. 5.2(a),(c) should reveal a gap near the eigenvalue 0. However, this gap is too small to be noticed on the scales of Figs. 5.2(a),(c), and we present it in Fig. D.1 of Appendix D.2.

While the presence/absence of the eigenvalues 0 would not be revealed in the long-time dynamics of the system, one can consider an operator

$$W_1 = P_0 U^\dagger P_1 U P_0 = P_0 - W_0, \tag{5.9}$$

where $P_1 = 1 - P_0$. Evidently, the eigenvalues 0 of the operator W_0 correspond to the eigenvalues 1 of the operator W_1, and thus the second type of spectral transitions would exhibit signatures in the long-time Floquet evolution governed by a non-unitary operator W_1^k, where k is the number of the Floquet cycle.

Figure 5.3 depicts the critical curves γ_c vs b_c for the eigenvalue 1 and the eigenvalue 0 transitions described above.

We study the aforementioned transitions analytically by considering moments of the random matrix distribution. Ensemble averaged moments of W_0 are proportional to the projection operator, $\langle W_0^k \rangle \propto P_0$, and thus one can write

$$\langle W_0^k \rangle = P_0 \frac{\mathrm{Tr}_N \left[\langle W_0^k \rangle \right]}{bN} \equiv \mu_k P_0, \tag{5.10}$$

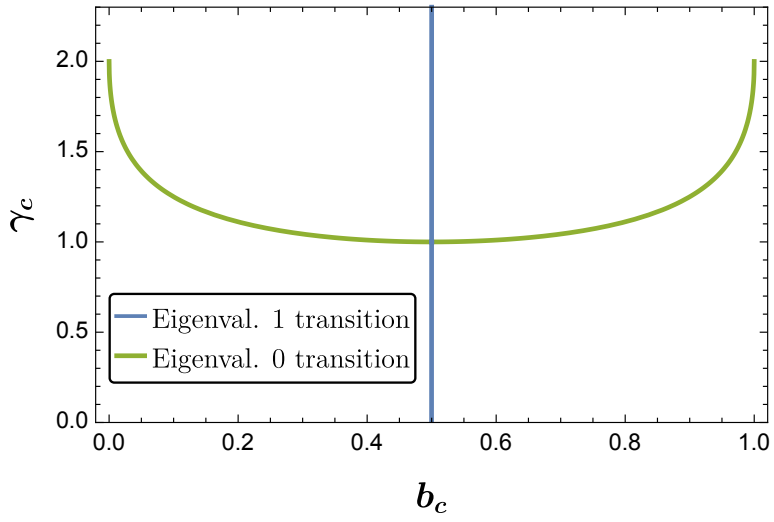

Figure 5.3: Critical curves γ_c vs b_c for the eigenvalue 1 transition (blue line, $b_c = 1/2$) and the eigenvalue 0 transition (green line, Eq. (5.8)).

where we have introduced parameters μ_k and $\mathrm{Tr}_N[...]$ denotes trace over the $N \times N$ Hilbert space. Writing the moment generating function as an infinite series,

$$\Gamma_1(\lambda) = \sum_{k=1}^{\infty} \lambda^{2k} \mu_k, \tag{5.11}$$

we note that the presence of the eigenvalues 1 in the spectrum of W_0 reveals itself as a singularity in $\Gamma_1(\lambda)$ as $\lambda \to 1^-$. Hence, the aforementioned spectral transition in the vicinity of the eigenvalue 1 can be diagnosed by calculating $\Gamma_1(\lambda)$ in the limit $\lambda \to 1^-$. Similarly, the transition in the vicinity of the eigenvalue 0 can be revealed by analyzing moments of $P_0 - W_0$. Introducing parameters ν_k as $\langle (P_0 - W_0)^k \rangle \equiv \nu_k P$ and the corresponding moment generating function as

$$\Gamma_2(\lambda) = \sum_{k=1}^{\infty} \lambda^{2k} \nu_k, \tag{5.12}$$

we analytically reveal the 0 eigenvalue transition by calculating $\Gamma_2(\lambda)$ in the limit $\lambda \to 1^-$.

The rest of the manuscript is organized as follows. In Sections 5.4 and 5.5, we analytically study the transitions in the spectrum of W_0. In Section 5.4, we employ the RMT to analytically obtain $\Gamma_1(\lambda)|_{\lambda\to 1^-}$ and find the critical point of the spectral measurement-induced transition in the vicinity of the eigenvalue 1. We do the same for the transition in the vicinity of the eigenvalue 0 by evaluating $\Gamma_2(\lambda)|_{\lambda\to 1^-}$ in Section 5.5. Section 5.6 describes how the results from Sections 5.4 and 5.5 obtained for W_0 can be used to analyze spectral measurement-induced transitions in other, more complicated quantum trajectories. In Section 5.7, we numerically study how the aforementioned transitions in the spectrum are revealed in the long-time dynamics of various physical quantities in the system, such as the purity and the probability to measure a specific Floquet quantum trajectory given the randomness in measurement outcomes. Summary and concluding remarks are presented in Section 5.8.

5.4 Transition in the vicinity of the eigenvalue one

5.4.1 The RMT description of the transition

To characterize analytically the transition in the vicinity of the eigenvalue 1, we calculate $\Gamma_1(\lambda)|_{\lambda\to 1^-}$. To this end, we start our calculation by writing the following $4N \times 4N$ matrix:

$$\hat{\mathcal{M}}(\lambda) = \begin{pmatrix} \check{0} & \check{L} \\ \check{L}^\dagger & \check{0} \end{pmatrix} + \lambda \begin{pmatrix} \check{t}_1 & \check{0} \\ \check{0} & \check{t}_2 \end{pmatrix} \equiv \hat{\mathcal{L}} + \lambda \hat{\mathcal{T}}, \tag{5.13}$$

where $2N \times 2N$ matrices $\check{L}, \check{t}_1$ and $\check{t}_2$ are defined as

$$\check{L} = \begin{pmatrix} 1 & 1 \\ H & i \end{pmatrix}, \tag{5.14}$$

$$\check{t}_1 = 2P_0 \begin{pmatrix} 1 & 0 \\ 0 & 0 \end{pmatrix}, \tag{5.15}$$

$$\check{t}_2 = \frac{P_0}{2} \begin{pmatrix} 1 & -1 \\ -1 & 1 \end{pmatrix}, \tag{5.16}$$

respectively. We use hats and checks to distinguish operators in $4N$, $2N$ and N dimensions. In Appendix D.3, we show that the function $\Gamma_1(\lambda)$ of Eq. (5.11) can be expressed as

$$\Gamma_1(\lambda) = -\frac{\lambda}{2bN} \mathrm{Tr}_{4N} \left[\hat{\mathcal{T}} \hat{\mathcal{G}} \right], \tag{5.17}$$

where we have introduced $\hat{\mathcal{G}} \equiv \langle \hat{\mathcal{M}}^{-1} \rangle$. To calculate $\hat{\mathcal{G}}$, we write matrix $\hat{\mathcal{M}}(\lambda)$ as

$$\hat{\mathcal{M}} = \hat{\mathcal{M}}_0 + H \Pi_x^{4\times 4}, \tag{5.18}$$

where we have introduced $\hat{\mathcal{M}}_0 \equiv \hat{\mathcal{M}}|_{H=0}$ and

$$\Pi_x^{4\times 4} = \begin{pmatrix} 0 & 0 & 0 & 0 \\ 0 & 0 & 1 & 0 \\ 0 & 1 & 0 & 0 \\ 0 & 0 & 0 & 0 \end{pmatrix}. \tag{5.19}$$

Hence, the Green's function

$$\hat{\mathcal{G}} = \left\langle \frac{1}{\hat{\mathcal{M}}_0 + H\Pi_x^{4\times4}} \right\rangle \tag{5.20}$$

can be computed with the help of the self-consistent Born approximation (SCBA), which is valid in the infinite Hilbert space limit, $N \to \infty$. The self-energy $\hat{\Sigma}$, defined in a usual way as

$$\hat{\Sigma} = \hat{\mathcal{G}}_0^{-1} - \hat{\mathcal{G}}^{-1}, \tag{5.21}$$

where $\hat{\mathcal{G}}_0 \equiv \hat{\mathcal{M}}_0^{-1}$, in the SCBA can be written as (here we do not imply summation over repeated indices)

$$\hat{\Sigma}_{il} = \sum_{j,k} \langle (H_{ij}\Pi_x^{4\times4})\hat{\mathcal{G}}_{jk}(H_{kl}\Pi_x^{4\times4})\rangle. \tag{5.22}$$

Hence, $\hat{\Sigma} = \Sigma^{4\times4} \otimes 1$, where 1 is the $N \times N$ identity matrix, $\otimes$ denotes the tensor product and

$$\Sigma^{4\times4} = \frac{\gamma}{N}\Pi_x^{4\times4}\mathrm{Tr}_N[\hat{\mathcal{G}}]\Pi_x^{4\times4}. \tag{5.23}$$

Since only the inner 2×2 block of the matrix $\Pi_x^{4\times4}$ is nonzero, Eq. (5.23) can be projected onto the 2-dimensional inner block subspace without any loss of information. Denoting the inner 2×2 block of the matrix $\Sigma^{4\times4}$ as $\bar{\Sigma}$, and the inner $2N \times 2N$ block of the matrix $\hat{\mathcal{G}}$ as $\check{G}$, we write the projected version of Eq. (5.23) as

$$\bar{\Sigma} = \frac{\gamma}{N}\bar{\sigma}_x\mathrm{Tr}_N[\check{G}]\bar{\sigma}_x, \tag{5.24}$$

where $\bar{\sigma}_x$ is the 2×2 Pauli matrix. Here, we utilize bars to distinguish 2×2 matrices. Expressing $\check{G}$ in terms of its projected components as

$$\check{G} = P_0\bar{g}_1 + (1 - P_0)\bar{g}_2, \tag{5.25}$$

where $\bar{g}_{1,2}$ are 2×2 matrices, we simplify Eq. (5.24) into

$$\bar{\Sigma} = \gamma \bar{\sigma}_x [b\bar{g}_1 + (1-b)\bar{g}_2]\bar{\sigma}_x = \bar{\sigma}_x(\beta \bar{g}_1 + \alpha \bar{g}_2)\bar{\sigma}_x, \tag{5.26}$$

with $\alpha \equiv \gamma(1-b)$ and $\beta \equiv \gamma b$. To obtain the self-consistent system of equations, we need to express $\bar{g}_1, \bar{g}_2$ in terms of $\bar{\Sigma}$. Projecting Eq. (5.21) onto the $2N$-dimensional subspace yields

$$\check{G} = (\check{G}_0^{-1} - \check{\Sigma})^{-1}, \tag{5.27}$$

where $\check{G}_0 = \check{G}|_{H=0}$ and $\check{\Sigma} = \bar{\Sigma} \otimes 1$. We calculate $\check{G}_0^{-1}$ in Appendix D.4 using the explicit form of matrices $\hat{\mathcal{L}}_0 = \hat{\mathcal{L}}|_{H=0}$ and $\hat{\mathcal{T}}$. The result of the calculation is given by

$$\check{G}_0^{-1} = P_0(f_y \bar{\sigma}_y - f_1 \bar{1}) + (1 - P_0)\bar{\sigma}_y, \tag{5.28}$$

where

$$f_y = \frac{1+\lambda^2}{1-\lambda^2}, \tag{5.29}$$

$$f_1 = -\frac{2\lambda}{1-\lambda^2}. \tag{5.30}$$

Note that

$$f_y^2 - f_1^2 = 1. \tag{5.31}$$

Plugging Eq. (5.28) into Eq. (5.27) yields an expression for $\check{G}$,

$$\check{G} = P_0 \left(f_y \bar{\sigma}_y - f_1 \bar{1} - \bar{\Sigma}\right)^{-1} + (1 - P_0)\left(\bar{\sigma}_y - \bar{\Sigma}\right)^{-1}, \tag{5.32}$$

comparing which with Eq. (5.25) allows one to express $\bar{g}_1$ and $\bar{g}_2$ in terms of $\bar{\Sigma}$ as

$$\bar{g}_1 = \left(f_y\bar{\sigma}_y - f_1\bar{1} - \bar{\Sigma}\right)^{-1}, \tag{5.33}$$

$$\bar{g}_2 = \left(\bar{\sigma}_y - \bar{\Sigma}\right)^{-1}, \tag{5.34}$$

thus completing the self-consistent system of equations (5.26),(5.33) and (5.34). This system of equations can be further simplified by parametrizing $\bar{\Sigma}$ in the following way:

$$\bar{\Sigma} = u\bar{1} - v\bar{\sigma}_y. \tag{5.35}$$

In that case, $\bar{g}_1$ and $\bar{g}_2$ can be expressed in terms of parameters u, v as

$$\bar{g}_1 = \frac{(f_1+u)\bar{1} + (f_y+v)\bar{\sigma}_y}{(f_y+v)^2 - (u+f_1)^2}, \tag{5.36}$$

$$\bar{g}_2 = \frac{u\bar{1} + (1+v)\bar{\sigma}_y}{(1+v)^2 - u^2}, \tag{5.37}$$

while the system of equations (5.26),(5.33),(5.34) becomes a system of equations on u and v:

$$\begin{cases} u = \dfrac{\beta(f_1+u)}{(f_y+v)^2-(u+f_1)^2} + \dfrac{\alpha u}{(1+v)^2-u^2}, \\ v = \dfrac{\beta(f_y+v)}{(f_y+v)^2-(u+f_1)^2} + \dfrac{\alpha(1+v)}{(1+v)^2-u^2}. \end{cases} \tag{5.38}$$

The moment generating function $\Gamma_1(\lambda)$ of Eq. (5.17) can also be expressed in terms of the parameters u and v:

$$\Gamma_1(\lambda) = \frac{\lambda^2}{1-\lambda^2}\left[1 - \frac{2}{\lambda}\frac{uf_y - vf_1}{(f_y+v)^2-(u+f_1)^2}\right]. \tag{5.39}$$

The corresponding derivation is presented in Appendix D.5. For convenience, we introduce a new set of variables,

$$v_\pm = v \pm u, \tag{5.40}$$

in terms of which system of equations (5.38) simplifies into

$$\begin{cases} v_+ = \dfrac{\alpha}{v_- + 1} + \dfrac{\beta}{v_- + f_-}, \\ v_- = \dfrac{\alpha}{v_+ + 1} + \dfrac{\beta}{v_+ + f_+}, \end{cases} \tag{5.41}$$

where

$$f_\pm = f_y \pm f_1 = \frac{1 \mp \lambda}{1 \pm \lambda}. \tag{5.42}$$

Note that $f_+ f_- = 1$. $\Gamma_1(\lambda)$ in terms of the new variables can be written as

$$\Gamma_1(\lambda) = \frac{\lambda^2}{1-\lambda^2}\left[1 - \frac{4\alpha}{(1-\lambda^2)\mathcal{F}}\right] \tag{5.43}$$

with

$$\mathcal{F} = (v_- + 1)(v_+ + 1)(v_+ + f_+)(v_- + f_-) - \alpha(v_+ + f_+)(v_- + f_-) - \beta(v_- + 1)(v_+ + 1). \tag{5.44}$$

5.4.2 Analysis of the self-consistent system of equations

System of equations (5.41) is of the fifth order and thus cannot be solved analytically for general values of the system parameters. However, as described in the Introduction, we only need to find the asymptotics of $\Gamma_1(\lambda)$ as $\lambda \to 1^-$ in order to characterize the transition in the spectrum. Before doing that, though, we analyze system (5.41) in the simpler case of $\lambda \to 0$.

$\lambda \to 0$ limit

The limit of $\lambda \to 0$ yields $f_\pm = 1$, and system of equations (5.41) becomes

$$\begin{cases} v_+ = \dfrac{\gamma}{v_- + 1}, \\ v_- = \dfrac{\gamma}{v_+ + 1}, \end{cases} \tag{5.45}$$

where we have utilized the fact that $\alpha + \beta = \gamma$. Solution of this system of equations is given by

$$v_+ = v_- \equiv v = \frac{1}{2}\left(-1 + \sqrt{1+4\gamma}\right). \tag{5.46}$$

Here we pick a positive sign due to a constraint on $\Gamma_1(\lambda)|_{\lambda\to 0}$ that we describe below. Expression (5.44) for $\mathcal{F}$ in the case of $\lambda \to 0$ can be rewritten as

$$\mathcal{F} = (v+1)^4 - \gamma(v+1)^2 = (v+1)^3, \tag{5.47}$$

and thus

$$\Gamma_1(\lambda)|_{\lambda\to 0} = \lambda^2\left[1 - \frac{4\alpha}{(v+1)^3}\right] = \lambda^2\left[1 - \frac{4\alpha}{\gamma}A(\gamma)\right], \tag{5.48}$$

where

$$A(\gamma) = \frac{8\gamma}{\left(1+\sqrt{1+4\gamma}\right)^3}. \tag{5.49}$$

By definition, $\Gamma_1(\lambda)|_{\lambda\to 0}$ represents the first moment of the distribution of W_0. Specifically,

$$\Gamma_1(\lambda)|_{\lambda\to 0} = \lambda^2\mu_1, \tag{5.50}$$

and thus the requirement $0 \le \mu_1 \le 1$ justifies picking the positive sign in Eq. (5.46). Note that $A(\gamma)$ reaches the maximum of $A^{max}(\gamma) = 1/4$ at $\gamma = 2$, in which case $\Gamma_1(\lambda) = \lambda^2(1-\alpha/\gamma) = b\lambda^2$, which corresponds to the RMT value of $\langle W_0\rangle = \langle P_0 U^\dagger P_0 U P_0\rangle$ if the

random matrix U is sampled from the CUE. By expanding $\Gamma_1(\lambda)$ to higher orders in λ, one can also show analytically that for $\gamma = 2$ second and third moments of W_0 are $\mu_2 = -b^3 + 2b^2$, $\mu_3 = 2b^5 - 6b^4 + 5b^4$, which are as well identical to the moments of W_0 if U is sampled from the CUE. Numerically, we find that the CUE and the ensemble (5.5)-(5.7) with $\gamma = 2$ are equivalent to each other when comparing moments of W_0 up to arbitrary order, but we lack a formal analytical proof that it is actually the case.

$\lambda \to 1^-$ limit

The limit of $\lambda \to 1^-$ corresponds to $f_- \to +\infty$, $f_+ \to 0^+$. In this case, system of equations (5.41) can be solved by the following ansatz:

$$v_-|_{\lambda\to 1^-} = f_-\xi + \sqrt{f_-^2\xi^2 + f_-\eta}, \tag{5.51}$$

where ξ, η are unknown functions of α, β and

$$\xi \begin{cases} > 0, \ \alpha < \beta, \\ = 0, \ \alpha = \beta, \\ < 0, \ \alpha > \beta. \end{cases} \tag{5.52}$$

Hence, up to the leading order

$$v_-|_{\lambda\to 1^-} = \begin{cases} 2f_-\xi, \ \alpha < \beta, \\ \sqrt{f_-\eta}, \ \alpha = \beta, \\ -\dfrac{\eta}{2\xi}, \ \alpha > \beta, \end{cases} \tag{5.53}$$

plugging which into system of equations (5.41) allows us to obtain the expressions for ξ and η:

$$\xi = \frac{1}{4}\left[-(\alpha+1) + \sqrt{(\alpha-1)^2 + 4\beta}\right], \tag{5.54}$$

$$\eta = -2\xi \frac{2\beta + \alpha\left[\beta - 1 + \sqrt{4\alpha + (\beta-1)^2}\right]}{2(\alpha-\beta)}. \tag{5.55}$$

At the same time, Eq. (5.44) in the limit $\lambda \to 1^-$ yields

$$\mathcal{F}|_{\lambda\to 1^-} = \left(\alpha + \frac{v_-}{f_-}\right)(v_- + f_-). \tag{5.56}$$

Plugging expression (5.51) for $v_-|_{\lambda\to 1^-}$ with ξ and η given by Eqs. (5.54),(5.55) into Eq. (5.56), we obtain the following asymptotics of $\Gamma_1(\lambda)$ in the limit $\lambda \to 1^-$:

$$(1-\lambda^2)\Gamma_1(\lambda)|_{\lambda\to 1^-} = \begin{cases} 0, \ \alpha > \beta, \\ 1 - \alpha/\beta, \ \alpha < \beta, \end{cases} \tag{5.57}$$

or, rewriting α and β in terms of b and γ,

$$(1-\lambda^2)\Gamma_1(\lambda)|_{\lambda\to 1^-} = \begin{cases} 0, \ b < 1/2, \\ (2b-1)/b, \ b > 1/2. \end{cases} \tag{5.58}$$

As described in Section 5.3, the singularity in $\Gamma_1(\lambda)|_{\lambda\to 1^-}$ corresponds to the presence of the eigenvalue 1 in the spectrum of W_0. Hence, Eq. (5.58) reveals the second order phase transition in the spectrum of W_0 at the critical point $b = b_c = 1/2$. This transition for a numerically generated random matrix W_0 is depicted in Figs. 5.2(a)-(c), while the corresponding critical curve is depicted in Fig. (5.3). The independence of the critical point on the value of γ signifies the *universality* of the transition. At the critical point,

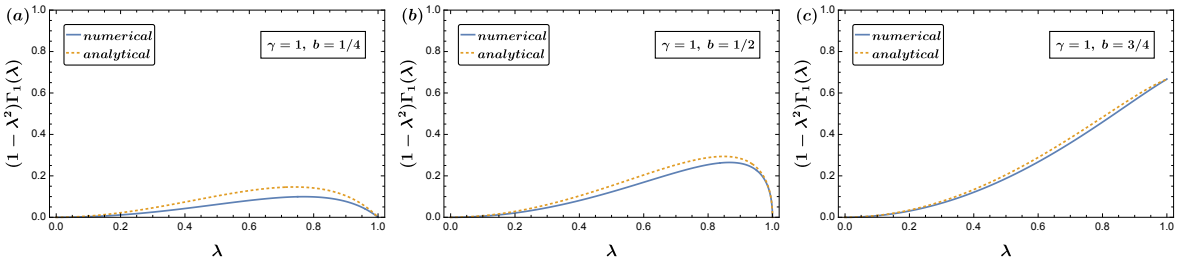

Figure 5.4: Function $(1-\lambda^2)\Gamma_1(\lambda)$ calculated numerically using Eqs. (5.41)-(5.44) (blue solid lines) and analytically using Eqs. (5.43),(5.51),(5.54)-(5.56) (orange dashed lines) plotted for (a) $b < 1/2$, (b) $b = 1/2$, and (c) $b > 1/2$.

we obtain

$$\Gamma_1^{(c)}(\lambda)|_{\lambda\to 1^-} = \frac{1+\gamma/2}{2\sqrt{\gamma(1-\lambda)}}. \tag{5.59}$$

Figure 5.4 depicts function $(1-\lambda^2)\Gamma_1(\lambda)$ calculated numerically using Eqs. (5.41)-(5.44) and analytically using Eqs. (5.43),(5.51),(5.54)-(5.56) for various values of b. Numerical and analytical values are equal at $\lambda \to 1^-$, while for other values of λ the analytical curves are only qualitatively similar to the numerical ones.

5.5 Transition in the vicinity of the eigenvalue zero

As described in Section 5.3, the transition in the vicinity of the eigenvalue 0 can be obtained by computing $\Gamma_2(\lambda)|_{\lambda\to 1^-}$. This can be done by performing calculations given in Section 5.4.1 and Appendices D.3-D.5 with slight modifications. In particular, redefining matrix $\check{t}_2$ as

$$\check{t}_2 = \frac{1-P_0}{2}\begin{pmatrix} 1 & -1 \\ -1 & 1 \end{pmatrix} \tag{5.60}$$

and keeping the definitions of $\hat{\mathcal{L}}$, $\hat{\mathcal{T}}$, $\hat{\mathcal{M}}$ and $\hat{\mathcal{G}}$ the same as in Section 5.4.1 in terms of $\check{t}_1$ and the redefined $\check{t}_2$, we can rewrite $\Gamma_2(\lambda)$ in the form identical to Eq. (5.17):

$$\Gamma_2(\lambda) = -\frac{\lambda}{2bN}\mathrm{Tr}_{4N}\left[\hat{\mathcal{T}}\hat{\mathcal{G}}\right]. \tag{5.61}$$

The form of matrix $\hat{\mathcal{G}}$ remains the same as in Eq. (5.20) and thus the self-energy in terms of $\check{G}$ is given by Eq. (5.26):

$$\bar{\Sigma} = \bar{\sigma}_x(\beta\bar{g}_1 + \alpha\bar{g}_2)\bar{\sigma}_x, \tag{5.62}$$

where $\alpha \equiv \gamma(1-b)$, $\beta \equiv \gamma b$ and

$$\check{G} = P_0\bar{g}_1 + (1-P_0)\bar{g}_2. \tag{5.63}$$

Similarly to Appendix D.4, in Appendix D.6 we calculate $\check{G}_0^{-1}$ for the modified matrix $\check{t}_2$, which yields

$$\check{G}_0^{-1} = P_0[\bar{\sigma}_y + \lambda(1+\bar{\sigma}_z)] + (1-P_0)[\bar{\sigma}_y + \lambda(1-\bar{\sigma}_z)]. \tag{5.64}$$

Using this result and the fact that

$$\check{G} = (\check{G}_0^{-1} - \check{\Sigma})^{-1}, \tag{5.65}$$

we obtain the expressions for $\bar{g}_1$,$\bar{g}_2$ in terms of $\bar{\Sigma}$:

$$\bar{g}_1 = \left[\bar{\sigma}_y + \lambda(1+\bar{\sigma}_z) - \bar{\Sigma}\right]^{-1}, \tag{5.66}$$

$$\bar{g}_2 = \left[\bar{\sigma}_y + \lambda(1-\bar{\sigma}_z) - \bar{\Sigma}\right]^{-1}. \tag{5.67}$$

Parametrizing $\bar{\Sigma}$ as

$$\bar{\Sigma} = u\bar{1} - v\bar{\sigma}_y - w\bar{\sigma}_z \tag{5.68}$$

and plugging it into Eqs. (5.62), (5.66) and (5.67), we obtain the self-consistent system of equations on u, v and w:

$$\begin{cases} u &= \dfrac{\alpha(u-\lambda)}{(v+1)^2 - u^2 + w^2 + 2\lambda(u-w)} \\ &+\dfrac{\beta(u-\lambda)}{(v+1)^2 - u^2 + w^2 + 2\lambda(u-w)}, \\ w &= \dfrac{\alpha(w-\lambda)}{(v+1)^2 - u^2 + w^2 + 2\lambda(u-w)} \\ &+\dfrac{\beta(w+\lambda)}{(v+1)^2 - u^2 + w^2 + 2\lambda(u-w)}, \\ v &= \dfrac{\alpha(v+1)}{(v+1)^2 - u^2 + w^2 + 2\lambda(u-w)} \\ &+\dfrac{\beta(v+1)}{(v+1)^2 - u^2 + w^2 + 2\lambda(u-w)}. \end{cases} \tag{5.69}$$

Note that here we have to use three parameters (u, v and w) to parametrize $\bar{\Sigma}$ instead of only two parameters used for the same purpose in Section 5.4.1. Introducing new variables, $u_\pm = u \pm w$, we rewrite system (5.69) as

$$\begin{cases} u_+ = \dfrac{\alpha(u_+ - 2\lambda)}{(v+1)^2 - u_-(u_+ - 2\lambda)} + \dfrac{\beta u_+}{(v+1)^2 - u_+(u_- - 2\lambda)}, \\ u_- = \dfrac{\alpha u_-}{(v+1)^2 - u_-(u_+ - 2\lambda)} + \dfrac{\beta(u_- - 2\lambda)}{(v+1)^2 - u_+(u_- - 2\lambda)}, \\ v = \dfrac{\alpha(v+1)}{(v+1)^2 - u_-(u_+ - 2\lambda)} + \dfrac{\beta(v+1)}{(v+1)^2 - u_+(u_- - 2\lambda)}. \end{cases} \tag{5.70}$$

Expressing $\Gamma_2(\lambda)$ of Eq. (5.61) in terms of the parameters $u_\pm$ and v yields

$$\Gamma_2(\lambda) = -\frac{\lambda}{\beta}\left[\alpha\frac{u_-}{(v+1)^2 - u_-(u_+ - 2\lambda)} + \beta\frac{u_+}{(v+1)^2 - u_+(u_- - 2\lambda)}\right]. \tag{5.71}$$

The corresponding derivation is presented in Appendix D.7.

$\lambda \to 0$ limit

Similarly to the previous section, we first solve system of equations (5.70) in the limit $\lambda \to 0$. The result reads

$$u_+ = -\frac{4\alpha\lambda}{1+\sqrt{1+4\gamma}}, \tag{5.72}$$

$$u_- = -\frac{4\beta\lambda}{1+\sqrt{1+4\gamma}}, \tag{5.73}$$

$$v = \frac{1}{2}\left(-1+\sqrt{1+4\gamma}\right), \tag{5.74}$$

plugging which into Eq. (5.71), we obtain

$$\Gamma_2(\lambda)|_{\lambda\to 0} = \frac{32\alpha\lambda^2}{\left(1+\sqrt{1+4\gamma}\right)^3}. \tag{5.75}$$

Here the positive sign in the expression (5.74) for v is taken to ensure the positivity of $\Gamma_2(\lambda)|_{\lambda\to 0}$. Recalling the definitions of $\Gamma_1(\lambda)$ and $\Gamma_2(\lambda)$, see Eqs. (5.11) and (5.12), we note that in the limit $\lambda \to 0$,

$$\Gamma_1(\lambda)|_{\lambda\to 0} = \mu_1\lambda^2, \tag{5.76}$$

$$\Gamma_2(\lambda)|_{\lambda\to 0} = \nu_1\lambda^2, \tag{5.77}$$

where by definition $\mu_1 P_0 \equiv \langle W_0\rangle$ and $\nu_1 P_0 \equiv \langle P_0 - W_0\rangle$. Thus,

$$\left[\Gamma_1(\lambda)+\Gamma_2(\lambda)\right]|_{\lambda\to 0} = \lambda^2, \tag{5.78}$$

which is consistent with the RMT results (5.48),(5.49) and (5.75).

$\lambda \to 1^-$ limit

In general, system (5.70) can be rewritten as a fifth order equation on v. Solution of this equation in the limit $\lambda \to 1^-$ is given by

$$v_-|_{\lambda\to 1^-} = \begin{cases} O(1),\ \gamma < \gamma_c, \\ \sqrt[3]{\dfrac{\gamma^2 - 4(\gamma-1)}{2(1-\lambda)}},\ \gamma = \gamma_c, \\ \sqrt{\dfrac{4(\gamma-1) - \gamma^2(2b-1)^2}{8(1-\lambda)}},\ \gamma > \gamma_c, \end{cases} \tag{5.79}$$

where

$$\gamma_c = \frac{1/2 - \sqrt{b(1-b)}}{(b-1/2)^2}. \tag{5.80}$$

At the same time, $\Gamma_2(\lambda)$ can be rewritten solely in terms of v:

$$\Gamma_2(\lambda) = \frac{v(v+1) - \gamma}{\beta(v+2)}. \tag{5.81}$$

Plugging solution (5.79) for v into Eq. (5.81), we obtain the asymptotics of $\Gamma_2(\lambda)$ in the limit $\lambda \to 1^-$:

$$\sqrt{1-\lambda}\Gamma_2(\lambda)|_{\lambda\to 1^-} = \begin{cases} 0,\ \gamma < \gamma_c, \\ \sqrt{\dfrac{4(\gamma-1) - \gamma^2(2b-1)^2}{8\gamma^2 b^2}},\ \gamma > \gamma_c. \end{cases} \tag{5.82}$$

The derivation of Eqs. (5.79)-(5.82) is given in Appendix D.8. Figure 5.5 depicts function $\sqrt{1-\lambda}\Gamma_2(\lambda)$ calculated numerically using the fifth order equation (D.55) and Eq. (5.81) for various values of γ and b. The dotted orange line in Fig. 5.5(c) indicates the analytically calculated value of $\sqrt{1-\lambda}\Gamma_2(\lambda)|_{\lambda\to 1^-}$ for $\gamma > \gamma_c$ given in Eq. (5.82). Figure 5.5 demonstrates consistency between the analytically calculated results at $\lambda \to 1^-$ and the

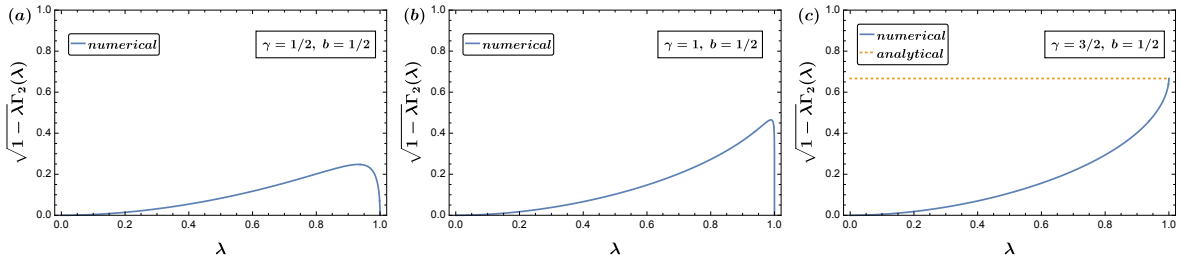

Figure 5.5: Function $\sqrt{1-\lambda}\Gamma_2(\lambda)$ calculated numerically using Eqs. (5.41)-(5.44) (blue solid lines) and analytically using Eqs. (5.43),(5.51),(5.54)-(5.56) (orange dashed lines) plotted for (a) $b < 1/2$, (b) $b = 1/2$, and (c) $b > 1/2$.

numerically calculated ones.

The singularity in $\Gamma_2(\lambda)|_{\lambda\to 1^-}$ indicates the closed gap near the eigenvalue 0 in the spectrum of W_0, and thus the result (5.82) shows the presence of the spectral phase transition at $\gamma = \gamma_c$. This eigenvalue 0 transition is illustrated in Figs. 5.2(d)-(f) for numerically generated random matrix W_0, while the corresponding critical curve is depicted in Fig. (5.3). The dependence of γ_c on b in this case indicates that the transition near the eigenvalue 0 is *non-universal*, as opposed to the transition near the eigenvalue 1, which occurs at the universal critical point $b_c = 1/2$, see Section 5.4.

5.6 Spectral transitions for other quantum trajectories

In Sections 5.4 and 5.5, we analyzed transitions in the spectrum of W_0, the non-unitary Floquet evolution operator that represents the simplest possible quantum trajectory in our setup, $\boldsymbol{m} = 0$. For other, more generic quantum trajectories, see Eq. (5.1), the corresponding non-unitary Floquet evolution operator can be rewritten as a polynomial of W_0 and P_0. For example,

$$W_1 = P_0 U^\dagger P_1 U P_0 = P_0 - W_0, \tag{5.83}$$

where P_1 is a projective measurement operator corresponding to the measurement outcome 1: $P_1 = 1 - P_0$. Another example is

$$W_{(0,1,1)} = P_0 U^\dagger P_1 U P_1 U^\dagger P_0 U P_0 = W_0^2 - W_0. \tag{5.84}$$

Given the fact that generic $W_{\boldsymbol{m}}$ can be rewritten as a polynomial of W_0 and P_0, and since all terms in the polynomial commute with each other, the spectrum of $W_{\boldsymbol{m}}$ and its spectral transitions can be obtained from the spectrum of W_0 and the corresponding W_0 spectral transitions described in Sections 5.4 and 5.5. For example, given Eq. (5.83), the eigenvalues w_1 of W_1 can be written as

$$w_1 = 1 - w_0, \tag{5.85}$$

except for the trivial zero eigenvalues coming from the projector P_0. Here w_0 denotes the eigenvalues of W_0. Equation (5.85) shows that the eigenvalue 0(1) transition in the spectrum of W_0 translates into the eigenvalue 1(0) transition in the spectrum of W_1, while properties of the corresponding transitions remain the same. Likewise, given Eq. (5.84), the eigenvalues of $W_{(0,1,1)}$ can be written as

$$w_{(0,1,1)} = w_0^2 - w_0, \tag{5.86}$$

and hence both the eigenvalue 0 and the eigenvalue 1 transitions in the spectrum of W_0 correspond to the eigenvalue 0 transition in the spectrum of $W_{(0,1,1)}$. Similar arguments can be applied for generic $W_{\boldsymbol{m}}$.

5.7 Signatures of the transitions in the long-time dynamics of the system

In Section 5.4, we have shown that the operator W_0 exhibits a spectral phase transition in the vicinity of the eigenvalue 1 between two distinct gapped phases, with one phase (when $b > 0.5$) characterized by the presence of the eigenvalue 1 in the operator's spectrum, while in the other phase (when $b < 0.5$) the eigenvalue 1 is absent from the spectrum. Considering a system of qubits whose Floquet evolution is determined by a non-unitary operator W_0^k, where k is the number of the Floquet cycle, one could expect that at large k the two aforementioned spectral phases give rise to two distinct dynamical phases. In particular, the presence of the eigenvalues 1 would lead to the system retaining some part of the memory of its initial conditions, while in the absence of the eigenvalues 1 such memory is rapidly lost as the system evolves. In this Section, we numerically calculate certain physical quantities in the system evolving under W_0^k and demonstrate how the two phases in the spectrum of W_0, as well as the corresponding eigenvalue 1 phase transition analyzed in Section 5.4, reveal themselves in the long-time behavior of these quantities.

The first quantity we consider is the purity of the evolving state. If at $k = 0$ the initial state is completely mixed, the density operator for a given k can be written as

$$\rho_{k,0} = \frac{W_0^{2k}}{\mathrm{Tr}[W_0^{2k}]}, \tag{5.87}$$

and thus the purity reads

$$\mathrm{Tr}[\langle \rho_{k,0}^2 \rangle] = \left\langle \frac{\mathrm{Tr}[W_0^{4k}]}{\mathrm{Tr}[W_0^{2k}]^2} \right\rangle, \tag{5.88}$$

where as before $\langle ... \rangle$ denotes the random matrix ensemble averaging. Figure 5.6 illustrates

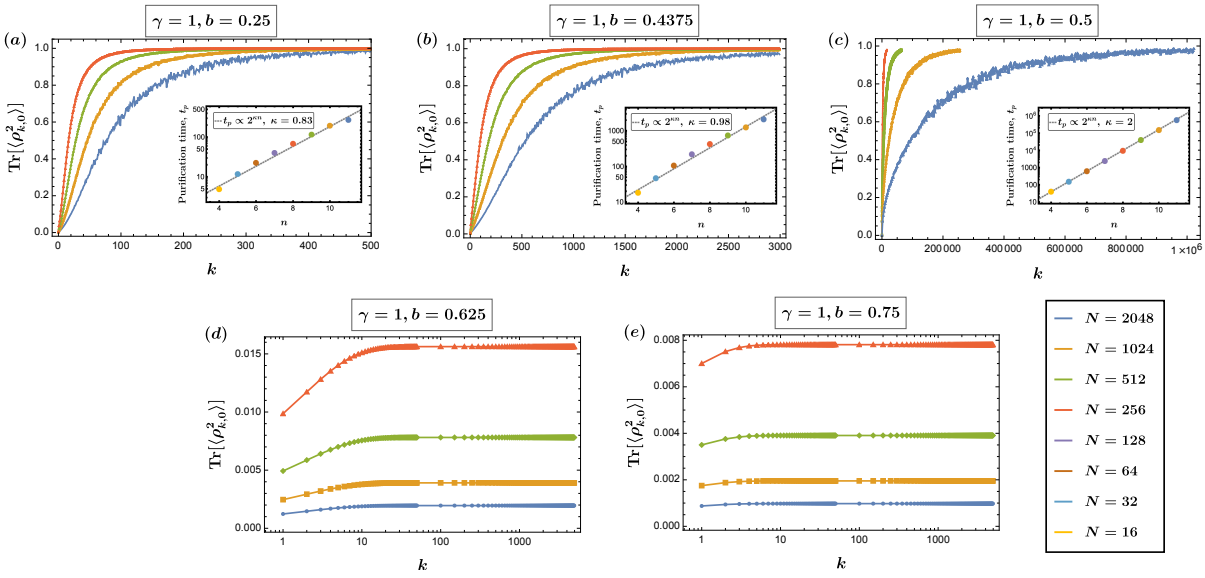

Figure 5.6: Numerically calculated purity (5.88) of an initially completely mixed state plotted as a function of a Floquet cycle k for $\gamma = 1$ and various values of b, N, when the cycle evolution is described by a non-unitary operator W_0. The insets in (a)-(c) depict the purification time $t_p = \min\left[k\middle|\mathrm{Tr}\langle\rho^2_{k,0}\rangle > 0.95\right]$ as a function of the number of qubits $n = \log_2 N$ in the system. In (a) the averaging is performed over 10000 random matrix realizations for $N = 16, 32, 64, 128, 256$; 5000 realizations for $N = 512$; 1000 realizations for $N = 1024$; and 100 realizations for $N = 2048$. In (b) the averaging is performed over 10000 random matrix realizations for $N = 16, 32, 64, 128, 256$; 5000 realizations for $N = 512$; 1000 realizations for $N = 1024$; and 150 realizations for $N = 2048$. In (c) the averaging is performed over 1000 random matrix realizations for $N = 16, 32, 64, 128, 256, 512$; 500 realizations for $N = 1024$; and 100 realizations for $N = 2048$. In (d),(e) the averaging is performed over 320 random matrix realizations.

the evolution of the numerically calculated purity of Eq. (5.88) for various parameter values and system sizes. Within the strong monitoring phase (see Fig. 5.6a and 5.6b plotted for $\gamma = 1$, $b = 0.25$ and $\gamma = 1$, $b = 0.4375$, respectively) an initially mixed state purifies with time; however, the purification time increases with the system size. To quantify this increase, we formally define the purification time as $t_p = \min\left[k\middle|\mathrm{Tr}\langle\rho^2_{k,0}\rangle > 0.95\right]$ and plot it as a function of the number of qubits in the system $n = \log_2 N$; these plots are shown as insets in Fig. 5.6(a),(b). Note that the vertical axis in these plots is logarithmic. These results suggest that for the small system sizes that we use to numerically

calculate the purity, the purification time scales sub-exponentially with the system size (exponential scaling is shown as a gray dashed line on the t_p vs n plots), and the pace of the purification decreases with the increase in b. However, we stress that the exponential scaling might be reached for larger system sizes which are beyond the ones that we have considered – it is hard to draw definitive conclusions on the t_p vs n scaling for the small system sizes studied in our work. More studies are necessary to determine the details of the purification dynamics in the strong monitoring phase, and it could be an interesting topic for future works.

At the critical point, $\gamma = 1$, $b = 0.5$ (see Fig. 5.6c), an initially mixed state purifies, and the purification time t_p scales exponentially with the system size as $t_p \propto 2^{2n}$, or $t_p \propto N^2$. The inset in Fig. 5.6(c) depicting t_p as a function of n illustrates this scaling behavior. Note that the exponential scaling of t_p with the system size is a signature of the "mixed", or the "volume law", phase, and contrary to the situation in other MIPT models [147], here it corresponds to the critical point. The reason for such peculiar behavior is the role that the measurement operator plays in our model: while in conventional MIPT models the measurement is used to disentangle qubits from the rest of the system, here it determines whether the system retains some part of the memory of its initial conditions or not.

The weak monitoring case, i.e. when $b > 0.5$, is qualitatively different. The numerically calculated dynamics of the purification in this case is depicted in Fig. 5.6(d),(e) plotted for $\gamma = 1$, $b = 0.625$ and $\gamma = 1$, $b = 0.75$, respectively. The presence of the eigenvalues 1 in the spectrum of the evolution operator in the weak monitoring phase, which has been shown in Sections 5.3 and 5.4 (see also Fig. 5.2c), leads to the system retaining some part of the memory of its initial conditions as it evolves. Due to this effect an initially mixed state fails to purify entirely, as depicted in Fig. 5.6(d),(e).

Another quantity, the dynamics of which we consider, is the probability that the

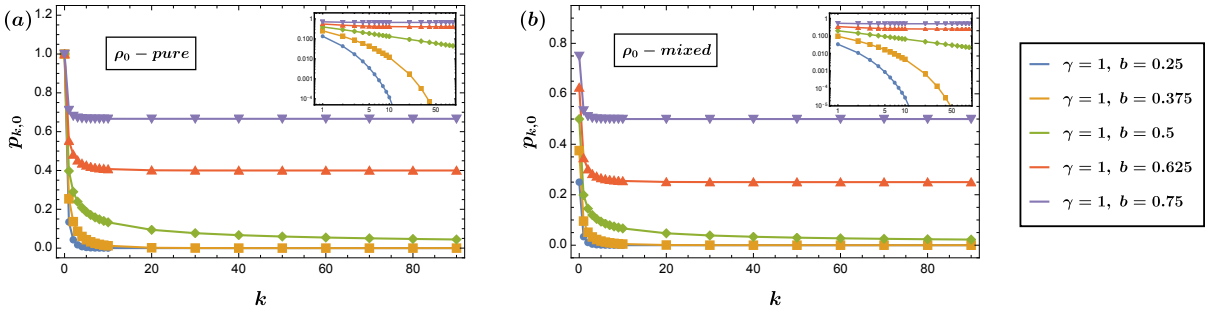

Figure 5.7: (a),(b) Numerically calculated probability (5.89) of the Floquet quantum trajectory, representing the evolution under W_0^k, plotted as a function of a time step k for $\gamma = 1$ and various values of b, when the initial state at $k = 0$ is (a) pure and (b) completely mixed. The insets in the figures are log-log versions of the corresponding curves. Dimensionality of the Hilbert space is $N = 2048$. The averaging is performed over 320 random matrix realizations.

system evolution is given by an operator W_0^k, given that in general the outcome of each measurement is random. The probability of observing such Floquet quantum trajectory of length k is given by

$$p_{k,0} = \mathrm{Tr}[\langle P_0 W_0^{2k} \rho_0 \rangle], \tag{5.89}$$

where ρ_0 is the density operator at $k = 0$. Figure 5.7 depicts the numerically calculated probability (5.89) for small system sizes as a function of k in the case of a pure (Fig. 5.7a) and a completely mixed (Fig. 5.7b) initial state. The insets in Fig. 5.7 depict the log-log versions of the plots. In the strong monitoring phase (i.e. when $b < 1/2$) the probability exponentially decays to zero with time for both the pure and the mixed initial states: $p_{k\to\infty,0} \to 0$. This behavior is consistent with the system losing the memory of its initial conditions (which is the property of the strong monitoring phase in our model): under such evolution, the number of possible quantum trajectories grows exponentially with time, and correspondingly the probability to measure one specific quantum trajectory decays exponentially to zero.

The situation changes qualitatively if one considers the weak monitoring phase, i.e. the case with $b > 1/2$. Within this phase the probability (5.89) decreases to a finite

value $p_{k\to\infty,0}$ as k increases from zero, and stays constant at this value as the system evolves further, both for the pure and the mixed initial states. Such behavior can be understood by computing the probability to measure the outcome "0" throughout the evolution. After k cycles of the Floquet evolution and a unitary operation U, the density operator reads

$$\rho_{k,k+1} = U\frac{W_0^k\rho_0 W_0^k}{\mathrm{Tr}[W_0^{2k}\rho_0]}U^\dagger. \tag{5.90}$$

Thus, the probability to measure the outcome "0" in the middle of the $k+1$-st Floquet cycle is equal to

$$\mathrm{Tr}[P_0\rho_{k,k+1}] = \frac{\mathrm{Tr}[P_0 U W_0^k\rho_0 W_0^k U^\dagger]}{\mathrm{Tr}[W_0^{2k}\rho_0]} = \frac{\mathrm{Tr}[W_0^{2k+1}\rho_0]}{\mathrm{Tr}[W_0^{2k}\rho_0]}. \tag{5.91}$$

This probability reaches 1 in the limit of $k\to\infty$ if W_0 has eigenvalues 1 in its spectrum, which is the case in the weak monitoring phase. The probability = 1 means that throughout the evolution at late times the system remains in the appropriate part of its Hilbert space, and thus it retains part of the memory of its initial condition. Finite probability to measure this Floquet quantum trajectory at $k\to\infty$ also signifies that this trajectory is unique in the sense that for every other trajectory the probability to measure it goes to zero as $k\to\infty$.

We note here that since the probability (5.89) is essentially defined in terms of the moments of the operator W_0, one can calculate the steady-state value $p_{k\to\infty,0}$ using the moment generating function $\Gamma_1(\lambda)$ of Eq. (5.11). In particular, since $\langle W_0^{2k}\rangle = \mu_{2k}P_0$, we note that $p_{k,0} = \mu_{2k}$ for a pure initial state and $p_{k,0} = b\mu_{2k}$ for the completely mixed initial state, and moments μ_{2k} can be calculated via $\Gamma_1(\lambda)$. Taking the limit $\lambda\to 1^-$ in $\Gamma_1(\lambda)$, we note that in this case all moments contribute (almost) equally to Γ_1, and since in the steady state all moments are (almost) equal to each other, $\mu_{k\to\infty}\equiv\tilde{\mu}$, we

can write

$$(1-\lambda^2)\Gamma_1(\lambda)|_{\lambda\to 1^-} = \tilde{\mu} \tag{5.92}$$

where the left-hand side has already been calculated and is given by Eq. (5.58). Thus, for $b \leq 1/2$ we find that $p_{k\to\infty,0} = 0$, whereas in the weak monitoring phase

$$p_{k\to\infty,0} = \begin{cases} (2b-1)/b, \text{ if } \rho_0 \text{ is pure,} \\ 2b-1, \text{ if } \rho_0 \text{ is completely mixed,} \end{cases} \tag{5.93}$$

which is in a perfect agreement with numerical results of Fig. 5.7. In particular, using Eq. (5.93) for a pure initial state we find that $p_{k\to\infty,0} = 2/3$ for $b = 0.75$ and $p_{k\to\infty,0} = 0.4$ for $b = 0.625$, whereas for the completely mixed initial state we obtain $p_{k\to\infty,0} = 0.5$ for $b = 0.75$ and $p_{k\to\infty,0} = 0.25$ for $b = 0.625$.

The critical point $b = 1/2$ corresponds to the power law decay of the probability (5.89), which can be clearly seen in the log-log versions of the plots shown as insets in Fig. 5.7. Here we would also like to note that while Fig. 5.7 is plotted for $N = 2048$, numerically we find no meaningful dependence of the probability (5.89) on N for numerically accessible small system sizes.

As for the eigenvalue 0 transition studied in Section 5.5, its signatures in terms of physical quantities can be analyzed by considering a Floquet evolution described by an operator W_1^k, where W_1 is given by Eq. (5.83), since the eigenvalue 0 transition for W_0 corresponds to the eigenvalue 1 transition for W_1. However, since the spectrum of W_0 does not exhibit two gapped phases at the eigenvalue 0, instead showing signatures of a gapped and a gapless phase (see Fig. 5.2(d-f)), the corresponding weak monitoring phase is not present when analyzing the evolution of physical quantities under W_1^k. The details of such analysis are presented in Appendix D.9.

5.8 Summary & Conclusion

In the present work we have analyzed, both analytically and numerically, forced measurement-induced transitions in all-to-all coupled monitored Floquet quantum circuits. The model that we have studied features a Floquet cycle that consists of a forward and a backward unitary evolution intermixed with projective measurements. The simplest quantum trajectory described within our model is defined by a non-unitary Floquet cycle operator $W_0 = P_0 U^\dagger P_0 U P_0$, where U is a unitary operator and P_0 is a projective measurement operator. Here we write the measurement operator as $P_0 = \mathrm{diag}\{1, 1, \ldots, 1, 0, 0, \ldots, 0\}$, such that the strength of the measurement is characterized by the rank of the projection operator, $\mathrm{Tr} P_0 = bN$.

To study the spectrum of the non-unitary operator W_0 in the thermodynamic limit, we have developed a novel RMT-based approach that treats unitary operators U as random matrices drawn from an ensemble characterized by a parameter γ, see Eqs. (5.5)-(5.7). Using this RMT-based mean-field approach, we have analytically demonstrated the existence of the measurement-induced transitions in the spectrum of W_0. Specifically, we have uncovered two types of transitions: one type occurs between two distinct gapped phases in the vicinity of the eigenvalue 1, with the spectral gap closing at the critical point. The two gapped phases in this case differ by the presence of the eigenvalue 1 in the spectrum of the evolution operator. The other type of transition occurs between a gapped and a gapless phase, taking place in the vicinity of the eigenvalue 0 of the operator W_0. Considering b and γ as system parameters, we have analytically calculated phase diagrams describing both types of transitions, and performed numerical simulations for small system sizes supporting our findings.

In addition, we have demonstrated how spectral transitions can be identified for other, more complicated quantum trajectories, based on the results obtained for the simplest

case of W_0.

Furthermore, we have suggested that spectral MIPTs uncovered in our work can be interpreted as transitions in terms of either losing completely or retaining part of the memory of the system's initial conditions as it evolves. In particular, considering the eigenvalue 1 transition between the two gapped phases of the operator W_0, the weak monitoring phase corresponds to the phase where the system retains part of the memory of its initial condition throughout its evolution, while in the strong monitoring phase the memory of the initial conditions is rapidly lost. We note that these signatures of the strong and the weak monitoring phases differ from the ones in conventional MIPT models, where the measurement-induced phases are typically interpreted as volume vs area law phases or pure vs mixed purification phases. Such peculiar nature of the phases in our case is due to the unique details of our model, where the evolution consists of both forward evolution and backward evolution operators, intermixed with the measurement operations.

To support our interpretation of the measurement-induced phases and the corresponding transition occurring within our model, we have numerically studied the long-time dynamics of certain physical quantities for small-sized systems. One quantity that we have considered is the purity of an initially completely mixed state. For the evolution governed by a non-unitary operator W_0^k, where k is the number of Floquet cycles, we have shown that in the strong monitoring phase (which features the absence of the eigenvalues 1 in the spectrum of W_0) an initially mixed state purifies, and the purification timescale increases with the system size and decreases with the measurement strength. However, more studies are necessary in order to definitively determine the system size scaling of the purification time in the strong monitoring phase. At the critical point, when the gap in the spectrum of W_0 closes, we have demonstrated that $t_p \propto 2^{\kappa n}$ with $\kappa = 2$. Such exponential scaling of the purification time with the system size is a typical

signature of the mixed or the volume law phase in conventional MIPT models. On the other hand, in the weak monitoring phase (which features the presence of the eigenvalues 1 in the spectrum of W_0) an initially mixed state fails to purify entirely, a property that is consistent with our interpretation of the system retaining part of the memory of its initial conditions as it evolves within this phase.

Another physical quantity, the dynamics of which we have numerically studied, is the probability to measure the Floquet quantum trajectory described by an operator W_0^k, given that the measurement outcomes at each step are random. We have shown that in the strong monitoring phase this probability exponentially decays to zero as the system evolves, while in the weak monitoring phase after an initial decrease it remains constant and finite for $k \to \infty$. This behavior is also consistent with the system losing(retaining) memory of its initial condition as it evolves within the strong(weak) monitoring phase. At the critical measurement strength the probability exhibits a power-law decay to zero.

Dynamical signatures of the eigenvalue 0 transition between a gapped and a gapless phase in the spectrum of W_0 can be studied by considering a Floquet evolution governed by an operator W_1^k, where $W_1 = P_0 - W_0$, since the eigenvalues 0 of the operator W_0 correspond to the eigenvalues 1 of W_1. Similarly to the case of the eigenvalue 1 transition in the spectrum of W_0 discussed above, we have calculated the dynamics of the purity and the measurement probability in the system evolving under the operator W_1^k. We have found that the late-time dynamics of these quantities exhibits signatures of a gapped and a gapless phase, consistent with our results obtained for the eigenvalue 0 transition in the spectrum of W_0. Overall, these numerical results for the purity and the measurement probability illustrate that the spectral phases and the corresponding transitions, uncovered analytically in our work, manisfest themselves in the long-time dynamics of various physical quantities.

Generally, a full understanding of the physics in monitored quantum circuits lacks

due to the scarcity of analytically solvable models. The present study provides such theoretical model and its analytical treatment via an RMT-based approach applied to identify spectral signatures of MIPTs. Moreover, this model features measurement-induced phases and transitions that do not fall within the conventional MIPT paradigm of volume law-area law phases (or pure-mixed purification phases). Our work can serve as an inspiration for the development of other analytically treatable MIPT models and for the application of the RMT to study monitored quantum circuits.

While we have provided some numerical results showing signatures of the transitions in the long-time dynamics of certain physical quantities, such as purity and the measurement probability, more systematic studies are necessary to make definitive conclusions about the properties of the measurement-induced phases in our model and the corresponding transitions.

The possibility of an experimental implementation of our theoretical model on modern NISQ devices is an open question. While theoretically the probability (5.89) to measure the W_0^k Floquet quantum trajectory can provide an experimentally detectable signature of the transition without the need for performing the postselection (see Fig. 5.7), realistic experiment would inevitably encounter multiple obstacles that would have to be resolved. In addition to standard issues crippling modern devices such as decoherence and imperfect gate fidelities, a practical implementation of the gate U utilized in our model that scrambles the entire system would require the application of many single-qubit and two-qubit gate layers which would effectively decrease the circuit depth that can be efficiently simulated. Besides, gate imperfections would lead to the discrepancy between practically implemented gates U and $U^\dagger$, which would in turn produce results differing from the theoretical predictions made in our work.

Appendix A

Appendix for Chapter 2

A.1 Analytical expressions for the proximity-induced terms of the nanowire Green's function in the absence of spin-orbit and magnetic scattering in the SC

In the absence of magnetic and spin-orbit scattering $\Gamma_{so} = \Gamma_{sf} = 0$ pair potential in the superconductor is constant as a function of Zeeman energy $\Delta = \Delta_{00}$ up to the Clogston limit, and analytical solution to the Usadel equations (2.9a)-(2.9b) can be obtained[56]:

$$\tan\theta = \frac{\sqrt{4\omega_n^2\Delta^2 + \left[(V_Z^{SC})^2 + \omega_n^2 - \Delta^2\right]^2} - (V_Z^{SC})^2 - \omega_n^2 + \Delta^2}{2\omega_n\Delta} \tag{A.1}$$

$$\cosh\phi = \frac{\omega_n + \Delta\tan\theta}{\sqrt{\omega_n^2 + [\Delta^2 - (V_Z^{SC})^2]\tan^2\theta + 2\omega_n\Delta\tan\theta}} \tag{A.2}$$

$$\sinh\phi = \frac{V_Z^{SC}\tan\theta}{\sqrt{\omega_n^2 + [\Delta^2 - (V_Z^{SC})^2]\tan^2\theta + 2\omega_n\Delta\tan\theta}} \tag{A.3}$$

Performing analytical continuation of the Matsubara frequencies $\omega_n \to -i\omega$, we obtain the proximity induced terms of the Green's function (2.18)

$$i\cos\theta\cosh\phi = -\frac{-\omega^2+S}{2\omega\sqrt{1-\frac{(\omega^2+S)^2}{4\Delta^2\omega^2}}\sqrt{S-\frac{(-h^2+\Delta^2)(\omega^2+S)^2}{4\Delta^2\omega^2}}} \tag{A.4}$$

$$\sin\theta\sinh\phi = -\frac{h(\omega^2+S)^2}{4\Delta^2\omega^2\sqrt{1-\frac{(\omega^2+S)^2}{4\Delta^2\omega^2}}\sqrt{S-\frac{(-h^2+\Delta^2)(\omega^2+S)^2}{4\Delta^2\omega^2}}} \tag{A.5}$$

$$\sin\theta\cosh\phi = -\frac{(-\omega^2+S)(\omega^2+S)}{4\Delta\omega^2\sqrt{1-\frac{(\omega^2+S)^2}{4\Delta^2\omega^2}}\sqrt{S-\frac{(-h^2+\Delta^2)(\omega^2+S)^2}{4\Delta^2\omega^2}}} \tag{A.6}$$

$$i\cos\theta\sinh\phi = -\frac{h(\omega^2+S)^2}{2\Delta\omega\sqrt{1-\frac{(\omega^2+S)^2}{4\Delta^2\omega^2}}\sqrt{S-\frac{(-h^2+\Delta^2)(\omega^2+S)^2}{4\Delta^2\omega^2}}} \tag{A.7}$$

where for notational purposes we denoted

$$S = -(V_Z^{SC})^2+\Delta^2+\sqrt{-4\Delta^2\omega^2+\left(\omega^2-(V_Z^{SC})^2+\Delta^2\right)^2}. \tag{A.8}$$

Appendix B

Appendix for Chapter 3

B.1 Island(s) and QD(s) contributions to the total low-energy Hamiltonian of the qubit(s)-QD(s) system

B.1.1 2-MZM case

In this Appendix we derive effective Hamiltonian $\hat{H}_{\mathrm{C+QD}}$ of Eq. (4.2). The island and QD contributions to the total low-energy Hamiltonian (3.1) of the coupled island-QD system take the form $\hat{H}_{\mathrm{C}} = E_{\mathrm{C}}(\hat{N}-N_{\mathrm{g}})^2+E_{\mathrm{M}}(\hat{N}-N_{\mathrm{g}})(\hat{n}-n_{\mathrm{g}})$ and $\hat{H}_{\mathrm{QD}} = h\hat{n}+\varepsilon_{\mathrm{C}}(\hat{n}-n_{\mathrm{g}})^2$ respectively, where $\hat{N}(\hat{n})$ is a charge occupation of the island(QD), $E_{\mathrm{C}}(\varepsilon_{\mathrm{C}})$ is a charging energy of the island(QD), $N_{\mathrm{g}}(n_{\mathrm{g}})$ is a dimensionless gate voltage of the island(QD), E_{M} is a mutual charging energy between the island and the QD and h is energy of a single electron level of the QD. Here we assumed a single-level QD without spin degeneracy, which is a valid assumption in high external magnetic field for small enough QD.

Total charge conservation in the system dictates that $\hat{N} + \hat{n} = N_{\mathrm{tot}}$, where N_{tot} is a

total number of electrons in the system. Using this, $\hat{H}_{\rm C} + \hat{H}_{\rm QD}$ can be rewritten in terms of only one operator, e.g. $\hat{n}$, yielding up to a constant term:

$$\hat{H}_{\rm C} + \hat{H}_{\rm QD} = (E_{\rm C} + \varepsilon_{\rm C} - E_{\rm M})(\hat{n} - \tilde{n}_{\rm g})^2 \tag{B.1}$$

with effective dimensionless gate voltage given by

$$\tilde{n}_{\rm g} = \frac{E_{\rm C}(N_{\rm tot} - N_{\rm g}) + \varepsilon_{\rm C} n_{\rm g} - h/2 - E_{\rm M}(N_{\rm tot} - N_{\rm g} + n_{\rm g})/2}{E_{\rm C} + \varepsilon_{\rm C} - E_{\rm M}}. \tag{B.2}$$

Relabeling parameters in terms of effective ones as $E_{\rm C} + \varepsilon_{\rm C} - E_{\rm M} \to \varepsilon_{\rm C}$, $\tilde{n}_{\rm g} \to n_{\rm g}$, we get $\hat{H}_{\rm C} + \hat{H}_{\rm QD} \to \hat{H}_{\rm C+QD}$ with $\hat{H}_{\rm C+QD}$ given by Eq. (4.2).

B.1.2 4-MZM case

Denoting $\hat{N}_i(\hat{n}_i),\ i = 1, 2$ as a charge occupation of the ith island(QD), $N_{{\rm g},i}(n_{{\rm g},i}),\ i = 1, 2$ as a dimensionless gate voltage of the ith island(QD), $h_i,\ i = 1, 2$ as energy of a single electron level of the ith QD, we describe the islands and QDs contribution to the low-energy Hamiltonian of the 4-MZM system as

$$\hat{H}_{\rm C} + \hat{H}_{\rm QD} = \frac{e^2}{2} \sum_{i,j=1}^{4} \hat{\nu}_i P_{ij} \hat{\nu}_j + \sum_{i=1,2} h_i \hat{n}_i \tag{B.3}$$

up to a constant. Here $\hat{\nu}_i$ represent dimensionless excess charge of the islands/QDs, i.e.

$$\hat{\nu}_i = \begin{cases} (\hat{N}_i - N_{{\rm g},i}),\ i = 1, 2 \\ (\hat{n}_{i-2} - n_{{\rm g},i-2}),\ i = 3, 4 \end{cases} \tag{B.4}$$

and P_{ij} are matrix elements of the inverse of the 4×4 capacitance matrix of the system with the first(last) two indices representing the islands(QDs) degrees of freedom. The

first term in Eq. (B.3) corresponds to the total electrostatic energy of the system while the second term is a total orbital energy of the QD levels. Notice that the Hamiltonian is always diagonal in the basis of the occupation numbers of islands and quantum dots. Thus, energies ε_α, $\alpha \in \{\mathrm{i1}, \mathrm{i2}, \mathrm{d1}, \mathrm{d2}\}$ introduced in Section 3.3.2 can be found by plugging appropriate values $\hat{n}_i, \hat{N}_i \in \{0, 1\}$ of the island and QD charges into Eq. (B.3).

B.2 Quantitative comparison of capacitance of 2- and 4-MZM measurements

To gain intuition about the different signal strengths of the 2- and 4-MZM measurements we compare the corresponding curvatures $\partial^2\varepsilon/\partial\Delta^2$ of the two cases which are proportional to the capacitive response $C_{\mathrm{diff},p}$. In particular we consider the case $\Delta_{\mathrm{dd}} = \Delta = 0$ using Eqs. (3.6) and (3.16) since finite Δ_{dd} expressions are too complicated in the 4-MZM case to be illuminating. We find:

$$\frac{\partial^2}{\partial\Delta^2}\Big|_{\Delta=0} \varepsilon_{p,\mathrm{gs}}(\phi) = -\frac{1}{4|\bar{t}_p(\phi)|} \tag{B.5}$$

$$\frac{\partial^2}{\partial\Delta_{\mathrm{dd}}^2}\Big|_{\Delta_{\mathrm{dd}}=0} \varepsilon^{(4)}_{p,\mathrm{gs}}(\phi) = -\frac{\sqrt{t_\Sigma^2 + \sqrt{t_\Sigma^4 - 4\bar{t}_p^{(4)}(\phi)^4}}}{4\sqrt{2}\sqrt{t_\Sigma^4 - 4\bar{t}_p^{(4)}}} \tag{B.6}$$

Note that $t_\Sigma^4 \geq 4\bar{t}_p^{(4)}$, we therfore see that $\sqrt{t_\Sigma^4 - 4\bar{t}_p^{(4)}(\phi)^4}/t_\Sigma$ plays a similar role for the 4-MZM case as $|\bar{t}_p(\phi)|$ does for the 2-MZM case.

As mentioned in the main text, for perfectly symmetric tuning $|t_\alpha| = t$, the 2- and 4-MZM cases show parity-dependent energy shifts of similar order. We now look at the capacitive responses in the same limit. Let's consider $p = 1$ ($p = -1$ can be obtained by

shifting $\phi \to \phi + \pi$). We then find,

$$\frac{\partial^2}{\partial \Delta^2}\Big|_{\Delta=0} \varepsilon_{+,\mathrm{gs}}(\phi - \pi/2) = -\frac{1}{8t}\frac{1}{\sin(\phi/2)} \tag{B.7}$$

$$\frac{\partial^2}{\partial \Delta_{\mathrm{dd}}^2}\Big|_{\Delta_{\mathrm{dd}}=0} \varepsilon^{(4)}_{+,\mathrm{gs}}(\phi) = -\frac{1}{8t}\frac{\cos(\phi/4 - \pi/4)}{\sin(\phi/2)} \tag{B.8}$$

where we used simplifications that apply without loss of generality for $0 \leq \phi \leq 2\pi$ which bounds $1/\sqrt{2} \leq \cos(\phi/4 - \pi/4) \leq 1$. We therfore see that in this limit the 2- and 4-MZM capacitive response behaves very similarly differing by at most a factor of $\sqrt{2}$.

B.3 4-MZM measurement in case $t_\delta \neq 0$

In case of $t_\delta \neq 0$ solutions of the quartic equation (3.14) have cumbersome analytical form and we do not present them here. Instead, we parametrize the coupling asymmetry giving rise to finite t_δ using the parameter β such that $|t_1| = |t_3| = t$, $|t_2| = |t_4| = t(1-\beta)/(1+\beta)$, $t_\delta^2 = 8\beta t^2/(1+\beta)^2$ and plot solutions of Eq. (3.14) as functions of Δ_{dd} in Fig. B.1 for $\phi = 0$ and various values of β. Fig. B.1 illustrates that finite values of t_δ introduce a shift of the crossings (or avoided crossings if $|t_1| \neq |t_3|$ and/or $|t_2| \neq |t_4|$) away from $\Delta_{\mathrm{dd}} = 0$ which can be calculated analytically giving

$$\Delta_{\mathrm{dd}}^{\mathrm{shift}} = \pm\sqrt{2}t_\delta^2 \sqrt{\frac{t_\Sigma^2 - \sqrt{t_\Sigma^4 - 4\bar{t}_p^{(4)}(\phi)^4 - t_\delta^4}}{4\bar{t}_p^{(4)}(\phi)^4 + t_\delta^4}}. \tag{B.9}$$

Taking into account this shift in Δ_{dd}, the ground state part of the 4-MZM system spectrum in case the of $t_\delta \neq 0$ still looks qualitatively similar to the one of the 2-MZM system spectrum depicted in Fig. 3.2(a) for all cases shown in Fig. B.1.

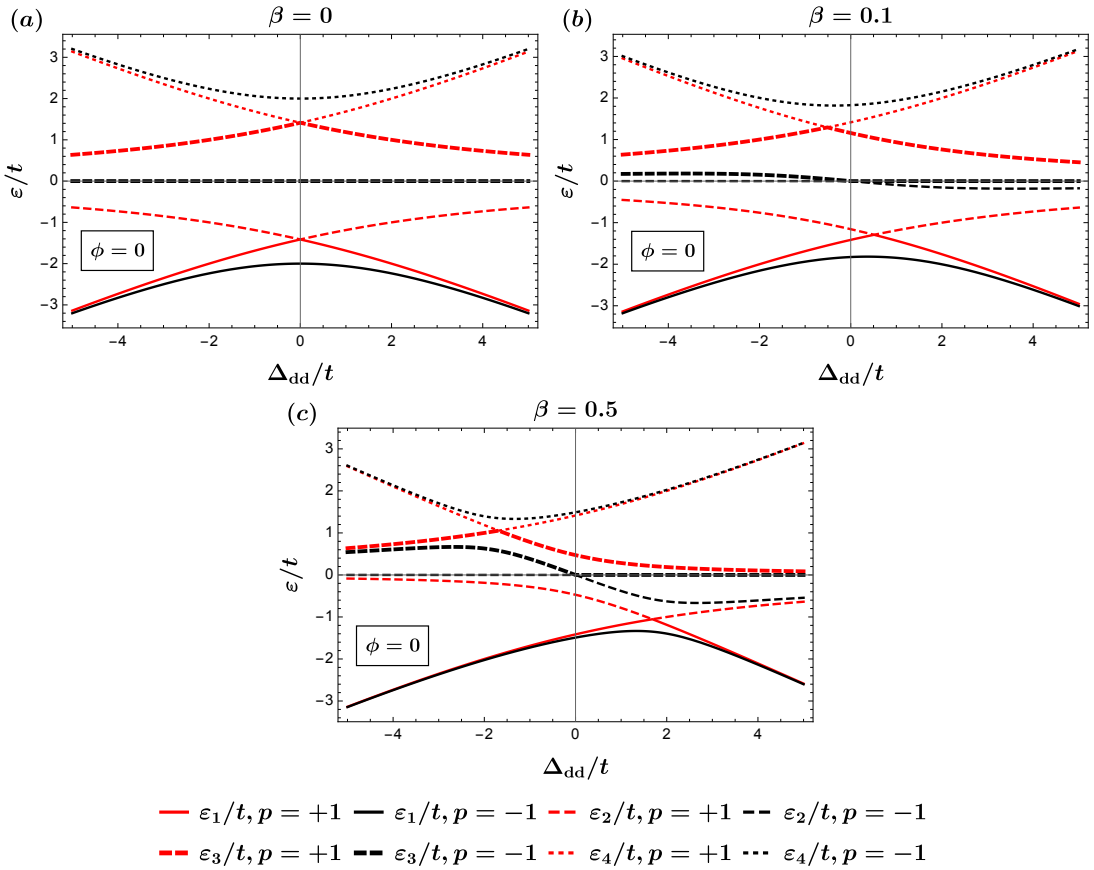

Figure B.1: Eigenenergies of the Hamiltonian (3.13) for different parities p and as a function of QD-QD detuning $\Delta_{\rm dd}$ for various values of coupling asymmetry β. Here we set $|t_1| = |t_3| = t$, $|t_2| = |t_4| = t(1-\beta)/(1+\beta)$, $\Delta_{\rm di} = 0$. Panel (a) is given by the analytical expressions of Eq. (3.16).

B.4 SNR for $1/f$ noise

In this appendix we derive expressions for Y and σ_Y for Gaussian noise that is fully described by a two-point correlation function with $1/f$ spectral power density $S_x(\omega) = \alpha_x/|\omega|$. Using the expansion of Eq. (3.17) together with $\langle \delta x \rangle = 0$ we find

$$Y = y_0 + \frac{y_2}{2\tau_{\rm m}} \int_0^{\tau_{\rm m}} dt \langle \delta x(t)^2 \rangle = y_0 + \frac{y_2}{2} \int d\omega S_x(\omega)\,. \tag{B.10}$$

Strictly speaking this expression is divergent but physical constraints provide frequency cutoffs for $S(\omega)$. The low frequency cutoff $\omega_{\min}$ is given by the time that passed since the measurement apparatus was calibrated. Calibration redefines very slow noise components into the signal. In general $\omega_{\min}^{-1} > \tau_{\mathrm{m}}$ but depending on the way the qubit is operated $\omega_{\min}^{-1}$ could exceed τ_{m} by several orders of magnitude. The high frequency cutoff is given by the inverse of the correlation time of the noise τ_{c} since for $t' < \tau_{\mathrm{c}}$ one would expect $\langle \delta x(0)\delta x(0)\rangle \approx \langle \delta x(0)\delta x(t')\rangle$. We thus regularize Eq. (B.10) via

$$Y = y_0 + y_2\alpha_x \int_{\omega_{\min}}^{\infty} d\omega \frac{1}{\omega}\frac{1}{\tau_{\mathrm{c}}}\int_{-\tau_{\mathrm{c}}/2}^{\tau_{\mathrm{c}}/2} dt e^{i\omega t} \approx y_0 + y_2\alpha_x\big(1-\gamma-\log(\omega_{\min}\tau_{\mathrm{c}}/2)\big) \tag{B.11}$$

where $\gamma \approx 0.577$ is the Euler's constant and we used that $\omega_{\min}\tau_{\mathrm{c}} \ll 1$.

The variance is given by

$$\sigma_Y^2 = \frac{1}{\tau_{\mathrm{m}}^2}\int_0^{\tau_{\mathrm{m}}}\int_0^{\tau_{\mathrm{m}}} dtdt' \Big\{ y_1^2\langle \delta x(t)\delta x(t')\rangle + \\ + \frac{y_2^2}{4}\big(\langle \delta x(t)\delta x(t)\delta x(t')\delta x(t')\rangle - \langle \delta x(t)\delta x(t)\rangle\langle \delta x(t')\delta x(t')\rangle\big)\Big\} \tag{B.12}$$

The integral of the first order term can be evaluated as

$$\int_0^{\tau_{\mathrm{m}}}\int_0^{\tau_{\mathrm{m}}} dtdt' \langle \delta x(t)\delta x(t')\rangle = \int_0^{\tau_{\mathrm{m}}}\int_0^{\tau_{\mathrm{m}}} dtdt' \int_{-\infty}^{\infty} d\omega e^{i\omega(t-t')}S_x(\omega) = \\ = 4\tau_{\mathrm{m}}^2\int_{-\infty}^{\infty} d\omega \frac{\sin^2(\omega\tau_{\mathrm{m}}/2)}{(\omega\tau_{\mathrm{m}})^2}S_x(\omega) \tag{B.13}$$

We again regularize the integral by introducing the low frequency cutoff $\omega_{\min}$, this yields a first order contribution to σ_Y^2 of

$$8y_1^2\alpha_x\int_{\omega_{\min}\tau_{\mathrm{m}}}^{\infty} d\zeta \frac{\sin^2(\zeta/2)}{\zeta^3} \approx y_1^2\alpha_x\big(3-2\gamma-2\log(\omega_{\min}\tau_{\mathrm{m}})\big) \tag{B.14}$$

where for simplicity we used the limit $\omega_{\min}\tau_{\rm m} \ll 1$.

The second term in (B.12) can be evaluated with the help of Wick's theorem which is valid given the assumption of the Gaussian noise. Specifically, we write

$$\begin{aligned}&\int_0^{\tau_{\rm m}}\int_0^{\tau_{\rm m}} dtdt' \langle \delta x(t)\delta x(t)\delta x(t')\delta x(t')\rangle = \\ &= \int_0^{\tau_{\rm m}}\int_0^{\tau_{\rm m}} dtdt' \left\{\langle \delta x(t)\delta x(t)\rangle\langle \delta x(t')\delta x(t')\rangle + 2\langle \delta x(t)\delta x(t')\rangle\langle \delta x(t)\delta x(t')\rangle\right\} \end{aligned} \tag{B.15}$$

Note that the first term in (B.15) cancels with the last term in (B.12), while the second term in (B.15) can be written as

$$\begin{aligned}&\int_0^{\tau_{\rm m}}\int_0^{\tau_{\rm m}} dtdt' \langle \delta x(t)\delta x(t')\rangle\langle \delta x(t)\delta x(t')\rangle = \\ &= \int_0^{\tau_{\rm m}}\int_0^{\tau_{\rm m}} dtdt' \int_{-\infty}^{\infty}\int_{-\infty}^{\infty} d\omega d\omega' e^{i(\omega+\omega')(t-t')} S_x(\omega)S_x(\omega') = \\ &= \tau_{\rm m}^2 \int_{-\infty}^{\infty}\int_{-\infty}^{\infty} d\omega d\omega' S_x(\omega)S_x(\omega') \frac{\sin^2((\omega+\omega')\tau_{\rm m}/2)}{((\omega+\omega')\tau_{\rm m}/2)^2}. \end{aligned} \tag{B.16}$$

Once again, we regularize the integral by introducing the low frequency cutoff $\omega_{\min}$ and get

$$2\tau_{\rm m}^2\alpha_x^2 \int_{\omega_{\min}\tau_{\rm m}}^{\infty}\int_{\omega_{\min}\tau_{\rm m}}^{\infty} d\zeta d\zeta' \frac{1}{\zeta\zeta'}\left(\frac{\sin^2((\zeta+\zeta')/2)}{((\zeta+\zeta')/2)^2} + \frac{\sin^2((\zeta-\zeta')/2)}{((\zeta-\zeta')/2)^2}\right) \tag{B.17}$$

The integral given above cannot be computed analytically for arbitrary values of $\omega_{\min}\tau_{\rm m}$. However, in the limit $\omega_{\min}\tau_{\rm m} \ll 1$ certain simplifications are possible. First, we perform

one of the integrals in (B.17) and expand the result in powers of $\omega_{\min}\tau_{\rm m}$:

$$\int_{\omega_{\min}\tau_{\rm m}}^{\infty} d\zeta \frac{1}{\zeta\zeta'}\left(\frac{\sin^2((\zeta+\zeta')/2)}{((\zeta+\zeta')/2)^2}+\frac{\sin^2((\zeta-\zeta')/2)}{((\zeta-\zeta')/2)^2}\right)= \\ =\frac{4}{\zeta'^3}\left\{-1+(1+\gamma)\cos\zeta'-\mathrm{Ci}(\zeta')+\log(\zeta')+\zeta'\mathrm{Si}(\zeta')-\log(\omega_{\min}\tau_{\rm m})(1-\cos(\zeta'))\right\}+ \\ +O(\omega_{\min}\tau_{\rm m}) \tag{B.18}$$

where $\mathrm{Ci}(\zeta')=-\int_{\zeta'}^{\infty} dt\cos(t)/t$ and $\mathrm{Si}(\zeta')=\int_0^{\zeta'} dt\sin(t)/t$. Next, we integrate (B.18) over ζ' and expand the result in powers of $\omega_{\min}\tau_{\rm m}$ once again. This yields the expression for the second order contribution to σ_Y^2 in the limit $\omega_{\min}\tau_{\rm m}\ll 1$:

$$y_2^2\alpha_x^2\int_{\omega_{\min}\tau_{\rm m}}^{\infty}\int_{\omega_{\min}\tau_{\rm m}}^{\infty} d\zeta d\zeta' \frac{1}{\zeta\zeta'}\left(\frac{\sin^2((\zeta+\zeta')/2)}{((\zeta+\zeta')/2)^2}+\frac{\sin^2((\zeta-\zeta')/2)}{((\zeta-\zeta')/2)^2}\right)\approx \\ \approx y_2^2\alpha_x^2\left(7-6\gamma+2\gamma^2+(4\gamma-6)\log(\omega_{\min}\tau_{\rm m})+2\log^2(\omega_{\min}\tau_{\rm m})\right) \tag{B.19}$$

Hence, the expression for variance in the limit $\omega_{\min}\tau_{\rm m}\ll 1$ takes the form

$$\sigma_Y^2 \approx y_1^2\alpha_x\big(3-2\gamma-2\log(\omega_{\min}\tau_{\rm m})\big)+ \\ +y_2^2\alpha_x^2\left(7-6\gamma+2\gamma^2+(4\gamma-6)\log(\omega_{\min}\tau_{\rm m})+2\log^2(\omega_{\min}\tau_{\rm m})\right). \tag{B.20}$$

B.5 Temperature dependence of detuning noise

In this Appendix we briefly analyze temperature dependence of the detuning noise described in Section 3.5 of the main text. Fig. B.2 illustrates signal (3.20) and noise (3.21) calculated as a function of system temperature for the average QD charge ($\mathcal{S}_n$, $\mathcal{N}_n$) and the differential capacitance of the QD ($\mathcal{S}_{\rm C}$, $\mathcal{N}_{\rm C}$). Both dependencies in Fig. B.2 are plotted for values of detuning and phase corresponding to (or close to) the maximum

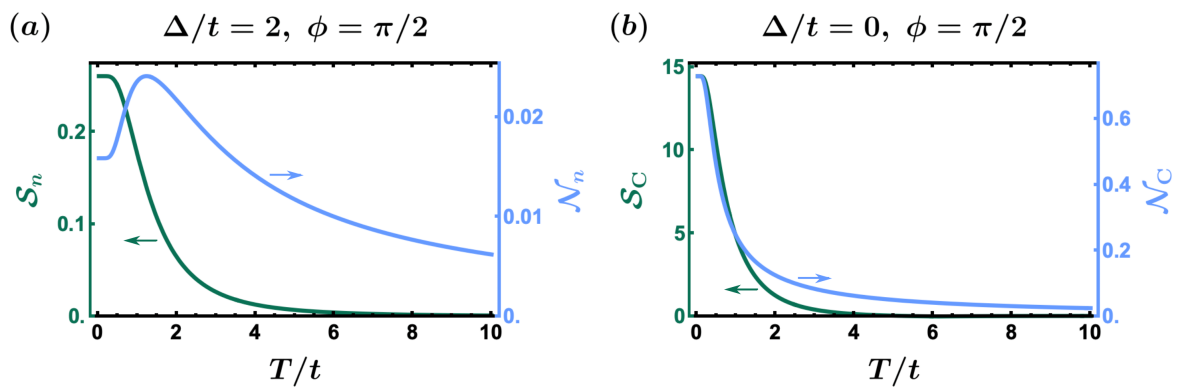

Figure B.2: Signal (3.20) and noise (3.21) for the 2-MZM measurement of the average QD charge $\langle n_{\rm QD}\rangle$(a) and differential QD capacitance $C_{\rm diff}/C_{\Sigma,\rm D}$(b) as a function of temperature T for $\phi = \pi/2$ and different values of Δ/t. Here we set $|t_1| = t,\ |t_2| = 1.5t,\ t = \varepsilon_{\rm C}/5 = 0.02$ meV, $C_{\rm g}/C_{\Sigma,\rm D} = 2$ and the noise is detuning noise of strength $\sqrt{\alpha_C} = 0.01$.

visibility points, see discussion in Section 3.5 of the main text.

The signal strength in Fig. B.2 decreases with temperature due to the fact that the energies (3.6) are symmetric with respect to $\varepsilon = 0$ line, see Fig. 3.2(a), and hence the difference between the observables for $p = +1$ and $p = -1$ vanishes at large T. The noise strength also usually decreases with temperature because the slope of the observables plotted as a function of Δ decreases with temperature too. However, there are certain parameter regimes when the slope is already in the saturation and hence it rises with T thus increasing the noise strength as well, see for example Fig. B.2(a) for $T/t \lesssim 1.5$. Overall, based on Fig. B.2 we conclude that lowering T benefits the measurement visibility.

B.6 Derivation of the expression for $C_{diff,-}$ in the limit $|\bar{t}_-| \ll T, \sigma_\Delta$

Expressions for energy and differential capacitance for the ground and exited states are given in Eqs. (3.6) and (3.8):

$$\varepsilon_p^{gr} = -\frac{1}{2}\sqrt{\Delta^2 + 4|\bar{t}_p|^2} = -\varepsilon_p^{exc}, \tag{B.21}$$

$$\frac{C_{\mathrm{diff},p}^{gr}}{C_{\mathrm{g}}^2/C_{\Sigma,\mathrm{D}}} = -\frac{4\varepsilon_{\mathrm{C}}|\bar{t}_p|^2}{(\Delta^2 + 4|\bar{t}_p|^2)^{3/2}} = -\frac{C_{\mathrm{diff},p}^{exc}}{C_{\mathrm{g}}^2/C_{\Sigma,\mathrm{D}}}. \tag{B.22}$$

In the high temperature limit temperature-averaged $C_{\mathrm{diff},-}$ becomes

$$C_{\mathrm{diff},-} = \frac{C_{\mathrm{diff},-}^{gr} e^{-\varepsilon_-^{gr}/T} + C_{\mathrm{diff},-}^{exc} e^{-\varepsilon_-^{exc}/T}}{e^{-\varepsilon_-^{gr}/T} + e^{-\varepsilon_-^{exc}/T}} \xrightarrow[T \gg |\bar{t}_-|, \Delta]{} -\frac{C_{\mathrm{diff},-}^{exc}\varepsilon_-^{exc}}{T} \propto \frac{|\bar{t}_-|^2}{T(\Delta^2 + 4|\bar{t}_-|^2)}. \tag{B.23}$$

Given Gaussianly distributed random varaible Δ with variance σ_Δ^2, averaging $C_{\mathrm{diff},-}$ over the distribution gives in the limit $\sigma_\Delta \gg |\bar{t}_-|$

$$C_{\mathrm{diff},-} \propto \frac{|\bar{t}_-|^2}{T\sigma_\Delta} \times \frac{1}{|\bar{t}_-|} = \frac{|\bar{t}_-|}{T\sigma_\Delta}. \tag{B.24}$$

B.7 Noise in MZM-QD couplings

Noise in the MZM-QD coupling amplitudes $|t_1|, |t_2|$ results from the noise in electrostatic gates controlling those couplings. Similarly to the case of the detuning noise (3.22) in the main text we assume that the coupling noise has $1/f$ power spectrum:

$$S_t(\omega) = t^2 \frac{\alpha_t}{|\omega|} \tag{B.25}$$

where we explicitly separated MZM-QD coupling energy $|t_1|, |t_2| \sim t$ and dimensionless noise strength α_t.

We estimate α_t using experimental measurements of the dephasing time in gatemon qubits that use quantum wire suitable for topological superconductivity. Reference [247] reports $T_2^* \sim 4$ μs in InAs/Al based gatemon with qubit frequencies $f_Q \sim 5$GHz. We assume that $f_Q \propto \sqrt{E_J} \propto \sqrt{g_J}$, where E_J, g_J are the Josephson energy and dimensionless conductance of the junction. We can then obtain an upper bound on the fluctuations of g_J by assuming that the dephasing is dominated by noise in the dimensionless conductance of order Δg_J which yields the estimate $\Delta g_J/g_J = 1/(\pi T_2^* f_Q) \sim 2 \times 10^{-5}$. This can be used to estimate the fluctuations in t which is proportional to $\sqrt{g_J}$ of the junction connecting the qubit island and the QD. Assuming similar relative fluctuations of g_J yields $\sqrt{\alpha_t} \sim 10^{-5}$. Note that the amount of variations in the conductance of a junction due to charge noise in the environment does depend on the regime in which the junction is operated. Junctions that are operated close to pinch off will likely show a stronger susceptibility to fluctuations. Nevertheless, the significantly smaller value of $\sqrt{\alpha_t} \ll \sqrt{\alpha_C}$ obtained in the above estimate makes it unlikely that the noise in the tunnel coupling overcomes the detuning noise.

Similar to the case of the detuning noise in the main text we analyze effects of the coupling noise perturbatively. Using expressions for expectation value and variance of the observables (3.18),(3.19) we calculate signal and noise via Eqs. (3.20),(3.21). The perturbative treatment of the noise is well satisfied since $\sqrt{\alpha_t} \ll 1$. Fig. B.3 illustrates the signal $\mathcal{S}_n$ ($\mathcal{S}_C$) and the noise $\mathcal{N}_n$ ($\mathcal{N}_C$) calculated for the average QD charge (a)-(b) (differential capacitance of the QD (c)-(d)) as a function of detuning. The signal lines in Fig. B.3 resemble the ones in Fig. 3.6 and we refer reader to the main text for the discussion of the signal. Coupling noise, on the other hand, has a behavior qualitatively different from its detuning counterpart. First, in contrast to the detuning noise, the

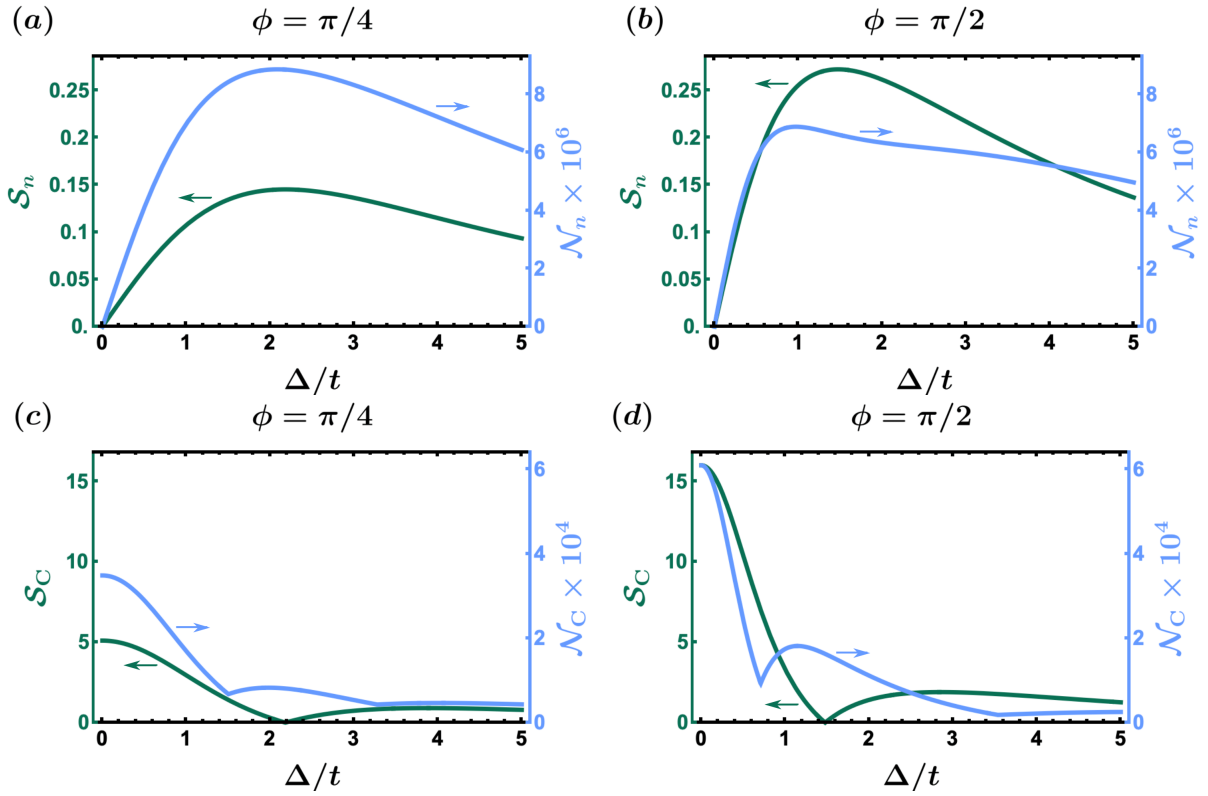

Figure B.3: Effect of noise in the MZM-QD coupling. Signal (3.20) and noise (3.21) for the 2-MZM measurement of the average QD charge $\langle n_{\rm QD}\rangle$ (a)-(b) and differential QD capacitance $C_{\rm diff}/C_{\Sigma,\rm D}$ (c)-(d) as a function of detuning Δ for different values of ϕ. Here we assume that the system is in its ground state ($T = 0$) and set $|t_1| = t,\ |t_2| = 1.5t,\ t = \varepsilon_{\rm C}/5 = 0.02$ meV, $C_{\rm g}/C_{\Sigma,\rm D} = 2$, and the strength of the coupling noise $\sqrt{\alpha_t} \sim 10^{-5}$.

coupling noise $\mathcal{N}_n$ vanishes at zero detuning as illustrated in Fig. B.3(a)-(b). This is associated with $\langle n_{{\rm QD},p}\rangle$ being identically zero at $\Delta = 0$ for any value of $|\bar{t}_p|$. At the same time, the local minimum at $\Delta = 0$ of the detuning noise $\mathcal{N}_{\rm C}$, see Fig. 3.6(c)-(d), is not present in the case of the coupling noise as can be observed in Fig. B.3(c)-(d). The reason for this is that at $\Delta = 0$ the capacitance is affected by noise in the coupling already to first order as opposed of detuning noise which only acts at second order. Akin to the detuning noise, the effect of coupling noise vanishes together with the signal for large detuning values emphasizing that external noise sources, e.g. amplifier noise, would likely be dominant in that regime.

Overall, the SNR for the coupling noise exceeds 10^4 in case of $\langle n_{\rm QD}\rangle$ and $C_{\rm diff}$ for most of the parameter values except vicinity of a few isolated points where the signal is fine tuned to zero. This signifies that due to $\sqrt{\alpha_t} \ll \sqrt{\alpha_{\rm C}}$ the MZM-QD coupling noise is not significant enough to affect the measurement visibility.

Intuitively, the weaker effect of noise on the tunnel coupling can be explained by differences in the sensitivity of the voltages controlling the tunnel coupling and the charge occupation. Assuming for simplicity a lever arm close to unity, the detuning changes significantly when the corresponding voltage of the QD changes the charge occupation by one electron. This corresponds to voltages $\sim \varepsilon_C/e$ which is typically or the order of $0.1 - 1$mV. Changing the strength of the tunnel coupling on the other hand requires to sufficiently change the electrostatic potential in the tunneling barrier. The corresponding voltages are typically much larger $\sim 10 - 100$mV. Nevertheless, we caution that for sufficiently ill-behaved junctions which show sharp resonances in the dependency of the dimensionless conductance with respect to the junction gate voltage the general trend of weak coupling noise might be broken.

B.8 Phase noise

The phase noise arises due to the noise in magnetic flux penetrating the enclosed area of the interference loop in the coupled island-QD setup, see Fig. 3.1. The flux noise, in turn, can originate from fluctuations in external magnetic field needed to tune the nanowires into the topological regime and/or from magnetic moments of electrons trapped in defect states of superconductors [248]. We estimate it by referring to the noise measurements in flux qubits which have interference loop based architecture similar to our topological setup. Refs. [249, 250] observe $1/f$ behavior of the flux noise in flux qubits and report the noise value of $S_\Phi^{1/2}(1\text{ Hz}) \sim 1\mu\Phi_0\text{Hz}^{-1/2}$, where $\Phi_0 = h/(2e)$ is the

superconducting flux quantum. Based on this we write the phase noise spectral power in our setup as

$$S_\phi(\omega) = \frac{\alpha_\phi}{|\omega|} \tag{B.26}$$

with $\sqrt{\alpha_\phi} \sim 10^{-6}$.

Following analysis of the detuning noise in the main text and the MZM-QD coupling noise in Appendix B.7, here we treat $1/f$ phase noise perturbatively and calculate corresponding signal $\mathcal{S}$ and noise $\mathcal{N}$ via Eqs. (3.20),(3.21). Note that $\sqrt{\alpha_\phi} \ll 1$ is needed for the perturbative treatment of the noise to work. The results of the phase noise calculations are illustrated in Fig. B.4(a)-(b) for the average QD charge ($\mathcal{S}_n$, $\mathcal{N}_n$) and Fig. B.4(c)-(d) for the differential capacitance of the QD ($\mathcal{S}_\mathrm{C}$, $\mathcal{N}_\mathrm{C}$) as a function of detuning. The signal lines in Fig. B.4 closely resemble the ones in Fig. 3.6 so the discussion of the signal can be found in the main text. On the other hand, the phase noise lines in Fig. B.4 are qualitatively similar to the coupling noise lines in Fig. B.3, see Appendix B.7 for the corresponding discussion. The main difference between the phase noise and the coupling noise is that the phase noise is smaller: the SNR for the phase noise exceeds 10^5 in case of both $\langle n_\mathrm{QD}\rangle$ and C_diff for most of the parameter values except vicinity of a few isolated points in parameter space where the signal is fine tuned to zero. Near $\phi = \pi/2$ the SNR is greater than 10^{10} for most of detuning values. Note also that the dependence on ϕ of the phase noise is much more significant than the dependence on ϕ of the coupling noise, cf. Fig. B.4(a)-(b) and Fig. B.3(a)-(b). Overall, we predict the phase noise to be not strong enough to affect the measurement visibility.

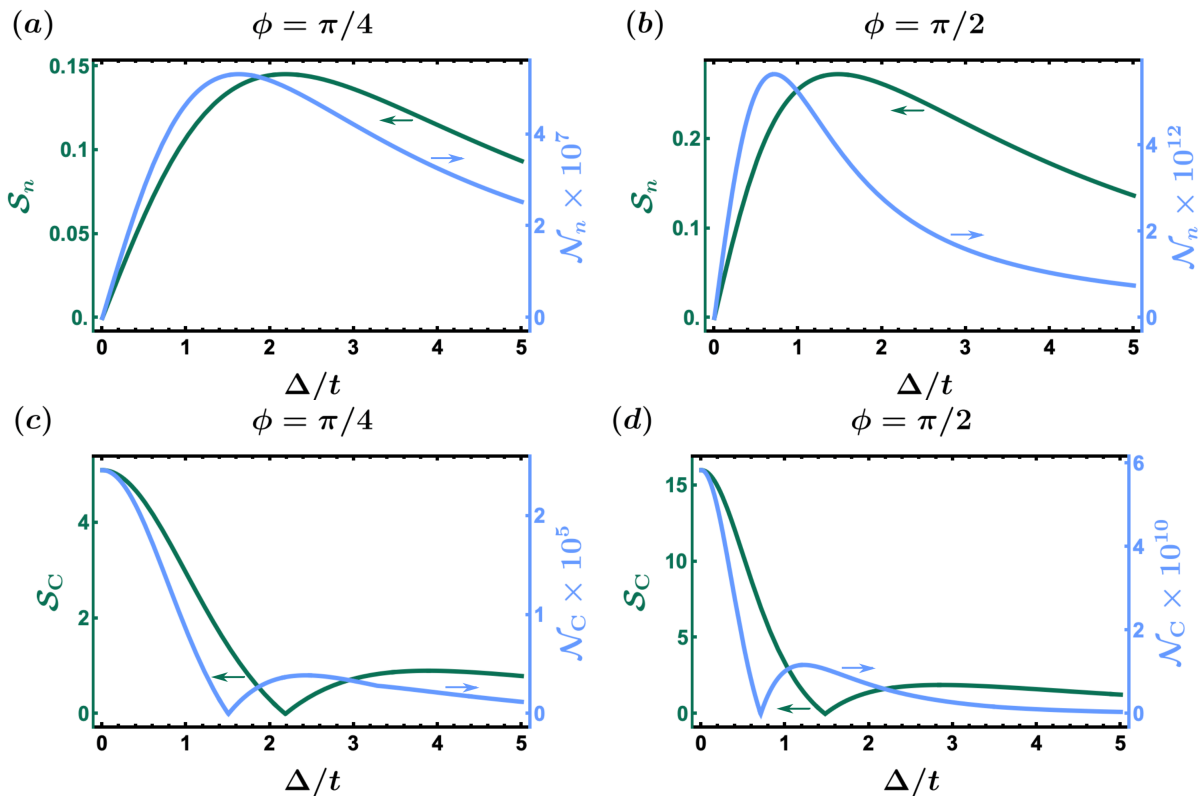

Figure B.4: Effect of phase noise. Signal (3.20) and noise (3.21) for the 2-MZM measurement of the average QD charge $\langle n_{\rm QD}\rangle$ (a)-(b) and differential QD capacitance $C_{\rm diff}/C_{\Sigma,\rm D}$ (c)-(d) as a function of detuning Δ for different values of ϕ. Here we assume that the system is in its ground state ($T = 0$) and set $|t_1| = t,\ |t_2| = 1.5t,\ t = \varepsilon_{\rm C}/5 = 0.02$ meV, $C_{\rm g}/C_{\Sigma,\rm D} = 2$, and the strength of the flux noise $\sqrt{\alpha_\phi} \sim 10^{-6}$.

Appendix C

Appendix for Chapter 4

C.1 Analytic expressions for the eigenenergies of the Hamiltonian (4.4)

The eigenergies of the Hamiltonian (4.4) are given by

$$\varepsilon_1 = \sqrt{\Delta_{\text{ind}}^2 + V_{\text{Z}}^2 + \xi_k^2 + (\alpha_{\text{R}}k)^2 - 2\sqrt{V_{\text{Z}}^2\Delta_{\text{ind}}^2 + (V_{\text{Z}}^2 + \alpha_{\text{R}}^2k^2)\xi_k^2}}, \tag{C.1}$$

$$\varepsilon_2 = \sqrt{\Delta_{\text{ind}}^2 + V_{\text{Z}}^2 + \xi_k^2 + (\alpha_{\text{R}}k)^2 + 2\sqrt{V_{\text{Z}}^2\Delta_{\text{ind}}^2 + (V_{\text{Z}}^2 + \alpha_{\text{R}}^2k^2)\xi_k^2}}, \tag{C.2}$$

where $\xi_k = k^2/2m^* - \mu$.

C.2 Relative strength of the MZM-QD and the continuum-QD couplings of Eqs. (4.11),(4.12)

The MZM-QD and the continuum-QD couplings can be rewritten in terms of the tunneling matrix elements with the help of Ref. [251]. In particular, Eq. (52) from

Ref. [251] gives the following expression for the MZM-QD tunneling Hamiltonian:

$$\hat{H}_{\text{T-MZM}} = e^{-i\hat{\phi}/2} \sum_{\rho=\downarrow,\uparrow} \sum_{l=L,R} W_l \phi_\rho(\boldsymbol{r}_l) u_{\text{MZM},l}(\boldsymbol{r}_l) f_\rho^\dagger \gamma_l + \text{h.c.}, \tag{C.3}$$

where W_ρ are the tunneling matrix elements, $u_{\text{MZM}}(\boldsymbol{r})$ is the Majorana wavefunction and $\phi_\rho(\boldsymbol{r})$ are wavefunctions of the QD orbitals. Comparing this expression for the MZM-QD tunneling Hamiltonian with expression (4.8) of the main text, and taking into account that the Majorana wavefunction normalization requires $|u_{\text{MZM}}(\boldsymbol{r})|^2 \sim 1/\xi$, where ξ is the coherence length in the nanowire, we can express the MZM-QD coupling as

$$|t_{\rho l}|^2 \approx W_l^2 |u_{\text{MZM,l}}(\boldsymbol{r}_l)|^2 |\phi_\rho(\boldsymbol{r}_l)|^2 = W_l^2 |\phi_\rho(\boldsymbol{r}_l)|^2 \frac{1}{\xi}. \tag{C.4}$$

As for the continuum-QD coupling, Eq. (12) from Ref. [251] provides an expression for the corresponding tunneling Hamiltonian:

$$\hat{H}_{\text{T-NW}} = e^{-i\hat{\phi}/2} \sum_{\rho,\sigma=\downarrow,\uparrow} \sum_{l=L,R} \sum_{k} W_l \phi_\rho(\boldsymbol{r}_l) \psi_{k\sigma l}(\boldsymbol{r}_l) f_\rho^\dagger c_{k\sigma l} + \text{h.c.}, \tag{C.5}$$

where compared to Eq. (12) from Ref. [251] we have neglected tunneling from the superconducting shell as it is not part of our model, and refrained from expressing the nanowire electronic operators in terms of their Bogoliubov counterparts. Here $\psi_{k\sigma l}(\boldsymbol{r})$ are wavefunctions of the electronic modes in the nanowires, normalized as $|\psi_{k\sigma l}(\boldsymbol{r})|^2 \sim 1/L$. Comparing this expression for the continuum-QD tunneling Hamiltonian with expression (4.9) of the main text, we find that the continuum-QD coupling can be expressed as:

$$|s_{\rho\sigma l}|^2 \approx W_l^2 |\psi_{k\sigma l}(\boldsymbol{r}_l)|^2 |\phi_\rho(\boldsymbol{r}_l)|^2 = W_l^2 |\phi_\rho(\boldsymbol{r}_l)|^2 \frac{1}{L}. \tag{C.6}$$

From Eqs. (C.4),(C.6) it follows that

$$\frac{|t_{\rho l}|}{|s_{\rho\sigma l}|} \approx \sqrt{\frac{L}{\xi}}. \tag{C.7}$$

C.3 Analytic expressions for the coefficients α, β of Eqs. (4.19)-(4.20)

The expressions for the coefficients $\alpha_{p,n}, \beta_{p,n}$, $n = 0, 1$, read

$$\alpha_{p,0} = \frac{\Delta + \sqrt{\Delta^2 + 4|\bar{t}_p|^2}}{\bar{t}_p \sqrt{8 + \frac{2\Delta}{|\bar{t}_p|^2}\left(\Delta + \sqrt{\Delta^2 + 4|\bar{t}_p|^2}\right)^2}}, \; \alpha_{p,1} = \frac{2}{\sqrt{8 + \frac{2\Delta}{|\bar{t}_p|^2}\left(\Delta + \sqrt{\Delta^2 + 4|\bar{t}_p|^2}\right)^2}}, \tag{C.8}$$

$$\beta_{p,0} = \frac{\Delta - \sqrt{\Delta^2 + 4|\bar{t}_p|^2}}{\bar{t}_p \sqrt{8 + \frac{2\Delta}{|\bar{t}_p|^2}\left(\Delta - \sqrt{\Delta^2 + 4|\bar{t}_p|^2}\right)^2}}, \; \beta_{p,1} = \frac{2}{\sqrt{8 + \frac{2\Delta}{|\bar{t}_p|^2}\left(\Delta - \sqrt{\Delta^2 + 4|\bar{t}_p|^2}\right)^2}}, \tag{C.9}$$

where for notational convenience we denoted $\bar{t}_{p,\uparrow}$ as $\bar{t}_p$. We further note that

$$|\beta_{p,0}|^2 = \frac{1}{2}\left(1 - \frac{\Delta}{\sqrt{\Delta^2 + 4|\bar{t}_p|^2}}\right), \; |\beta_{p,1}|^2 = \frac{1}{2}\left(1 + \frac{\Delta}{\sqrt{\Delta^2 + 4|\bar{t}_p|^2}}\right). \tag{C.10}$$

These identities are used throughout the chapter.

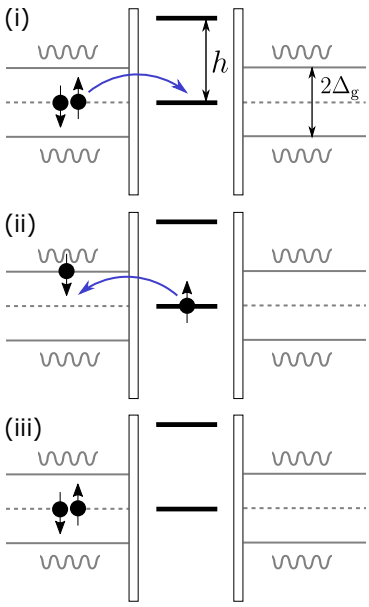

Figure C.1: Schematic illustration of an example of the second order tunneling process. Solid black dots represent the electrons hopping between the superconductor with the gap Δ_{g} and the two-level QD with the Zeeman splitting h. Grey wavy lines represent the quasiparticle continuum in the superconductors.

C.4 Details of the second order perturbative calculations

The second order processes include virtual tunnelings from a T(QD) onto the QD(T) and back onto the same T(QD), with a creation and annihilation of a virtual quasiparticle during the process. Importantly, since the same topological superconductor is involved in the tunneling events, no overall phase is accumulated during the second order processes, and the only phase dependence would come from the MZM-QD coupling which is treated unperturbatively. Formally, the second order correction in the continuum-QD couplings is given by

$$\varepsilon_{p,-}^{(2)} = \sum_{m} \frac{\left|\langle m|\hat{H}_{\text{T-NW}}|-\rangle_p\right|^2}{\varepsilon_{p,-}^{(0)} - \varepsilon_m}. \tag{C.11}$$

The excited states $|m\rangle$ correspond to a quasiparticle created in either L or R topological superconductor. Figure C.1 schematically illustrates an example of a second order process. States $|m\rangle$ have parity $-p$ and can be either the $|-\rangle_{-p}$ or the $|+\rangle_{-p}$ eigenstates of the MZM-QD Hamiltonian, see Eqs. (4.19)-(4.20). Hence, we write

$$\varepsilon_{p,-}^{(2)} = \varepsilon_{I}^{(2)} + \varepsilon_{II}^{(2)} \tag{C.12}$$

with

$$\varepsilon_{I}^{(2)} = \sum_{l=L,R} \sum_{j=1,2} \sum_{k} \frac{\left| {}_{-p}\langle -, 1_{kjl} | \hat{H}_{\text{T-NW}} | - \rangle_{p} \right|^2}{\varepsilon_{p,-}^{(0)} - (\varepsilon_{-p,-}^{(0)} + \varepsilon_{kjl})}, \tag{C.13}$$

$$\varepsilon_{II}^{(2)} = \sum_{l=L,R} \sum_{j=1,2} \sum_{k} \frac{\left| {}_{-p}\langle +, 1_{kjl} | \hat{H}_{\text{T-NW}} | - \rangle_{p} \right|^2}{\varepsilon_{p,-}^{(0)} - (\varepsilon_{-p,+}^{(0)} + \varepsilon_{kjl})}, \tag{C.14}$$

where $\varepsilon_{p,\pm}^{(0)}$ are the "unperturbed" energies (4.22) of the MZM-QD Hamiltonian and 1_{kjl} indicates the creation of the type j quasiparticle in the lth topological superconductor with the momentum k and the energy ε_{kjl} given by Eqs. (C.1)-(C.2). Recalling expressions (4.19)- (4.20) for the states $|\pm\rangle$ and expression (4.10) for the continuum-QD tunneling Hamiltonian, we calculate the matrix elements in Eq. (C.14) and obtain

$$\varepsilon_{I}^{(2)} = -\sum_{l=L,R} \sum_{j=1,2} \sum_{k} \frac{|\beta_{p,1}\beta_{-p,0}^{*}(s_{\uparrow\uparrow l}^{*}u_{kj\uparrow} + s_{\uparrow\downarrow l}^{*}u_{kj\downarrow}) + \beta_{p,0}\beta_{-p,1}^{*}(s_{\uparrow\uparrow l}v_{-kj\uparrow} + s_{\uparrow\downarrow l}v_{-kj\downarrow})|^2}{\varepsilon_{kjl} + \varepsilon_{-p,-}^{(0)} - \varepsilon_{p,-}^{(0)}}, \tag{C.15}$$

$$\varepsilon_{II}^{(2)} = -\sum_{l=L,R} \sum_{j=1,2} \sum_{k} \frac{|\beta_{p,1}\alpha_{-p,0}^{*}(s_{\uparrow\uparrow l}^{*}u_{kj\uparrow} + s_{\uparrow\downarrow l}^{*}u_{kj\downarrow}) + \beta_{p,0}\alpha_{-p,1}^{*}(s_{\uparrow\uparrow l}v_{-kj\uparrow} + s_{\uparrow\downarrow l}v_{-kj\downarrow})|^2}{\varepsilon_{kjl} + \varepsilon_{-p,+}^{(0)} - \varepsilon_{p,-}^{(0)}}, \tag{C.16}$$

where we have only considered tunneling into the lower in energy dot level $\rho =\uparrow$ which is justified if the Zeeman splitting on the dot is much larger than the respective level broadening $h \gg \Gamma_{\downarrow l}$. In the denominator, the expressions
$\varepsilon^{(0)}_{-p,-} - \varepsilon^{(0)}_{p,-} = \left(-\sqrt{\Delta^2 + |\bar{t}_{-p}|^2} + \sqrt{\Delta^2 + |\bar{t}_p|^2}\right)/2$ and
$\varepsilon^{(0)}_{-p,+} - \varepsilon^{(0)}_{p,-} = \left(\sqrt{\Delta^2 + |\bar{t}_{-p}|^2} + \sqrt{\Delta^2 + |\bar{t}_p|^2}\right)/2$ are much smaller than ε_{kjl} in the limit $\Delta_{\rm g} \gg \Delta, |t_L|, |t_R|$ and hence can be neglected. This makes the denominators in Eqs. (C.15) and (C.16) identical. The enumerator in Eq. (C.15) can be rewritten as

$$
\begin{aligned}
&|\beta_{p,1}\beta^*_{-p,0}|^2 \left(|s_{\uparrow\uparrow l}|^2 u^2_{kj\uparrow} + |s_{\uparrow\downarrow l}|^2 u^2_{kj\downarrow} + 2|s_{\uparrow\uparrow l}s_{\uparrow\downarrow l}|u_{kj\uparrow}u_{kj\downarrow}\right) + \\
&+ |\beta_{p,0}\beta^*_{-p,1}|^2 \left(|s_{\uparrow\uparrow l}|^2 v^2_{-kj\uparrow} + |s_{\uparrow\downarrow l}|^2 v^2_{-kj\downarrow} + 2|s_{\uparrow\uparrow l}s_{\uparrow\downarrow l}|v_{-kj\uparrow}v_{-kj\downarrow}\right) + \\
&+ \left[\beta_{p,1}\beta^*_{-p,0}\beta^*_{p,0}\beta_{-p,1}\left(s^*_{\uparrow\uparrow l}u_{kj\uparrow} + s^*_{\uparrow\downarrow l}u_{kj\downarrow}\right)\left(s^*_{\uparrow\uparrow l}v_{-kj\uparrow} + s^*_{\uparrow\downarrow l}v_{-kj\downarrow}\right) + \text{c.c.}\right]. \qquad \text{(C.17)}
\end{aligned}
$$

Similarly, the enumerator in Eq. (C.16) can be rewritten as

$$
\begin{aligned}
&|\beta_{p,1}\alpha^*_{-p,0}|^2 \left(|s_{\uparrow\uparrow l}|^2 u^2_{kj\uparrow} + |s_{\uparrow\downarrow l}|^2 u^2_{kj\downarrow} + 2|s_{\uparrow\uparrow l}s_{\uparrow\downarrow l}|u_{kj\uparrow}u_{kj\downarrow}\right) + \\
&+ |\beta_{p,0}\alpha^*_{-p,1}|^2 \left(|s_{\uparrow\uparrow l}|^2 v^2_{-kj\uparrow} + |s_{\uparrow\downarrow l}|^2 v^2_{-kj\downarrow} + 2|s_{\uparrow\uparrow l}s_{\uparrow\downarrow l}|v_{-kj\uparrow}v_{-kj\downarrow}\right) + \\
&+ \left[\beta_{p,1}\alpha^*_{-p,0}\beta^*_{p,0}\alpha_{-p,1}\left(s^*_{\uparrow\uparrow l}u_{kj\uparrow} + s^*_{\uparrow\downarrow l}u_{kj\downarrow}\right)\left(s^*_{\uparrow\uparrow l}v_{-kj\uparrow} + s^*_{\uparrow\downarrow l}v_{-kj\downarrow}\right) + \text{c.c.}\right]. \qquad \text{(C.18)}
\end{aligned}
$$

Since the denominators are the same, the sum of the two enumerators (C.17) and (C.18) enters the expression for $\varepsilon^{(2)}_{p,-}$. In this sum, the last terms in the expressions (C.17) and (C.18) (i.e. the cross terms) cancel one another due to the fact that $\beta^*_{-p,0}\beta_{-p,1} + \alpha^*_{-p,0}\alpha_{-p,1} = 0$. Besides, given that $|\beta^*_{-p,0}|^2 + |\alpha^*_{-p,0}|^2 = |\beta^*_{-p,1}|^2 + |\alpha^*_{-p,1}|^2 = 1$, the other terms in the sum of (C.17) and (C.18) can be combined yielding for the total energy

correction

$$\varepsilon^{(2)}_{p,-} = -2|\beta_{p,1}|^2 \sum_{j=1,2}\sum_{k} \frac{|s_{\rm dir}|^2 u^2_{kj\uparrow} + |s_{\rm sf}|^2 u^2_{kj\downarrow} + 2|s_{\rm dir}s_{\rm sf}|u_{kj\uparrow}u_{kj\downarrow}}{\varepsilon_{kj}} - \\ - 2|\beta_{p,0}|^2 \sum_{j=1,2}\sum_{k} \frac{|s_{\rm dir}|^2 v^2_{-kj\uparrow} + |s_{\rm sf}|^2 v^2_{-kj\downarrow} + 2|s_{\rm dir}s_{\rm sf}|v_{-kj\uparrow}v_{-kj\downarrow}}{\varepsilon_{kj}}, \tag{C.19}$$

where the sum over $l = L, R$ results in the factor of 2. When writing Eq. (C.19) we assumed for simplicity that the continuum-QD couplings on the left and on the right are the same $|s_{\uparrow\sigma L}| = |s_{\uparrow\sigma R}| \equiv |s_{\uparrow\sigma}|$, and introduced the direct $|s_{\rm dir}| \equiv |s_{\uparrow\uparrow}|$ and the spin-flip $|s_{\rm sf}| \equiv |s_{\uparrow\downarrow}|$ couplings to the spin-up dot level $\rho = \uparrow$. Equation (C.19) has a clear physical meaning: due to the MZM-QD couplings, the electron wavefunction is spreaded across the QD and the island. Recalling Eqs. (4.19)-(4.20), one can note that $|\beta_{p,1}|^2$ is a probability for the electron to be found on the dot, while $|\beta_{p,0}|^2$ is a probability for the electron to be found on the island. Thus Eq. (C.19) represents the contributions to the energy coming from the dot-to-island virtual electron tunneling (the first term in Eq. (C.19)) and the island-to-dot virtual electron tunneling (the second term in Eq. (C.19)) multiplied by the respective probabilities. Taking into account the fact that $u^2_{kj\uparrow} = u^2_{-kj\downarrow}$, $j = 1, 2$, and $v^2_{-kj\uparrow} = v^2_{kj\downarrow}$, $j = 1, 2$, see Eq. (4.7), Eq. (C.19) becomes

$$\varepsilon^{(2)}_{p,-} = -2|\beta_{p,1}|^2 \sum_{j=1,2}\sum_{k} \frac{(|s_{\rm dir}|^2 + |s_{\rm sf}|^2) u^2_{kj\uparrow} + 2|s_{\rm dir}s_{\rm sf}|u_{kj\uparrow}u_{kj\downarrow}}{\varepsilon_{kj}} - \\ - 2|\beta_{p,0}|^2 \sum_{j=1,2}\sum_{k} \frac{(|s_{\rm dir}|^2 + |s_{\rm sf}|^2) v^2_{-kj\uparrow} + 2|s_{\rm dir}s_{\rm sf}|v_{-kj\uparrow}v_{-kj\downarrow}}{\varepsilon_{kj}}. \tag{C.20}$$

Rewriting the summation over the momentum in Eq. (C.20) as an integral via

$$\sum_k = \frac{L}{2\pi}\int_{-\infty}^{\infty} dk, \tag{C.21}$$

where L is the length of the nanowires, and recalling the expressions for $|\beta_{p,0}|^2$, $|\beta_{p,1}|^2$ given in Eq. (C.10), we obtain

$$\varepsilon^{(2)}_{p,-} = -\frac{(|s_{\rm dir}|^2+|s_{\rm sf}|^2)K_1^{(2)} + |s_{\rm dir}s_{\rm sf}|K_2^{(2)}}{\Delta_{\rm ind}} \frac{\Delta}{\sqrt{\Delta^2+4|\bar{t}_p(\phi)|^2}}, \tag{C.22}$$

where we neglected the part independent of the detuning Δ and the phase difference ϕ (note that in the second order the dependence on ϕ only enters through $|\bar{t}_p|$). Here

$$K_1^{(2)} = \frac{L}{2\pi}\int_{-\infty}^{\infty} dk \sum_{j=1,2} \frac{u^2_{kj\uparrow} - v^2_{-kj\uparrow}}{\varepsilon_{k,j}/\Delta_{\rm ind}}, \tag{C.23}$$

$$K_2^{(2)} = \frac{L}{\pi}\int_{-\infty}^{\infty} dk \sum_{j=1,2} \frac{u_{kj\uparrow}u_{kj\downarrow} - v_{-kj\uparrow}v_{-kj\downarrow}}{\varepsilon_{k,j}/\Delta_{\rm ind}}. \tag{C.24}$$

Finally, setting here $s_{\rm sf}=0$ we derive Eq. (4.24) of the main text:

$$\varepsilon^{(2)}_{p,-} = -\frac{|s_{\rm dir}|^2}{\Delta_{\rm ind}} K_1^{(2)} \frac{\Delta}{\sqrt{\Delta^2+4|\bar{t}_p(\phi)|^2}}. \tag{C.25}$$

C.5 Details of the fourth order perturbative calculations

As described in the main text, out of all terms in the expression for the perturbative correction to the ground state energy in the fourth order we only consider the ones that give rise to the 2π-periodic phase dependence and hence are important for the analysis of the $0-\pi$ transition. All the other terms in the fourth order involve processes appearing in the second order, and thus are parametrically smaller that their second

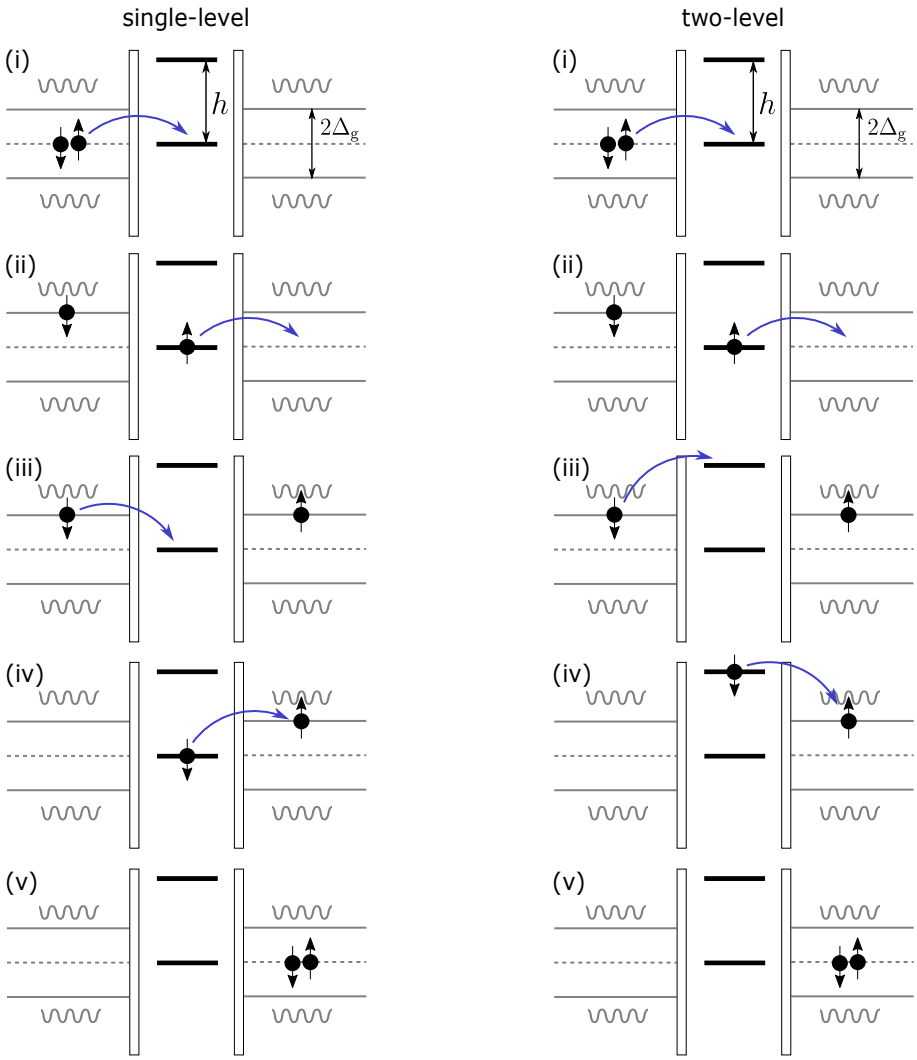

Figure C.2: Schematic illustration of an example of the fourth order tunneling process for the single-level (left panel) and the two-level (right panel) tunneling. Solid black dots represent the electrons hopping between the superconductor with gap Δ_g and the two-level QD with the Zeeman splitting h. Grey wavy lines represent the quasiparticle continuum in the superconductors.

order counterparts. Thus, the relevant fourth order term is given by

$$\varepsilon^{(4)}_{p,-} = \sum_{m_2,m_3,m_4} \frac{{}_p\langle -|\hat{H}_{\text{T-NW}}|m_4\rangle\langle m_4|\hat{H}_{\text{T-NW}}|m_3\rangle\langle m_3|\hat{H}_{\text{T-NW}}|m_2\rangle\langle m_2|\hat{H}_{\text{T-NW}}|-\rangle_p}{(\varepsilon_{p,-}-\varepsilon_{m_2})(\varepsilon_{p,-}-\varepsilon_{m_3})(\varepsilon_{p,-}-\varepsilon_{m_4})}. \quad \text{(C.26)}$$

The excited states $|m_2\rangle$ have parity $-p$ and correspond to a quasiparticle created in the $L(R)$ topological superconductor, the states $|m_3\rangle$ have parity $+p$ and correspond to a quasiparticle created in each of the two topological superconductors, while the states $|m_4\rangle$ have parity $-p$ and correspond to a quasiparticle created in the $R(L)$ topological superconductor. In addition, the states $|m_2\rangle$, $|m_3\rangle$ and $|m_4\rangle$ can be either $|-\rangle$, $|+\rangle$ or $|h\rangle$ eigenstates of the MZM-QD Hamiltonian, see Eqs. (4.19)-(4.21).

C.5.1 Single-level tunneling contribution

In this subsection we consider the tunneling only through the lower in energy spin-up QD level. Left panel in Fig. C.2 schematically illustrates an example of this type of virtual processes. In this case the states $|m_2\rangle$, $|m_3\rangle$ and $|m_4\rangle$ are either $|-\rangle$ or $|+\rangle$. First, we study the case with $|m_2\rangle = |-, 1_{kjl}\rangle_{-p}$, $|m_3\rangle = |-, 1_{kjl}, 1_{k'j'l'}\rangle_p$ and $|m_4\rangle = |-, 1_{k'j'l'}\rangle_{-p}$, where 1_{kjl} indicates the creation of the type j quasiparticle in the lth topological superconductor with the momentum k. Note that here $j, j' = 1, 2$ and $l, l' = L, R$ but $l \neq l'$, i.e. when two quasiparticles are present, they are present in the different topological superconductors. Otherwise, the phase dependence would not appear. Then, the matrix

elements in Eq. (C.26) read

$$\langle m_2|\hat{H}_{\text{T-NW}}|-\rangle_p = \beta_{p,0}\beta^*_{-p,1}(s_{\uparrow\uparrow l}v_{-kj\uparrow} + s_{\uparrow\downarrow l}v_{-kj\downarrow}) + \beta_{p,1}\beta^*_{-p,0}(s^*_{\uparrow\uparrow l}u_{kj\uparrow} + s^*_{\uparrow\downarrow l}u_{kj\downarrow}), \quad \text{(C.27)}$$

$$\langle m_3|\hat{H}_{\text{T-NW}}|m_2\rangle = \beta_{-p,0}\beta^*_{p,1}(s_{\uparrow\uparrow l'}v_{-k'j'\uparrow} + s_{\uparrow\downarrow l'}v_{-k'j'\downarrow}) + \beta_{-p,1}\beta^*_{p,0}(s^*_{\uparrow\uparrow l'}u_{k'j'\uparrow} + s^*_{\uparrow\downarrow l'}u_{k'j'\downarrow}), \quad \text{(C.28)}$$

$$\langle m_4|\hat{H}_{\text{T-NW}}|m_3\rangle = \beta_{p,0}\beta^*_{-p,1}(s_{\uparrow\uparrow l}u_{kj\uparrow} + s_{\uparrow\downarrow l}u_{kj\downarrow}) + \beta_{p,1}\beta^*_{-p,0}(s^*_{\uparrow\uparrow l}v_{-kj\uparrow} + s^*_{\uparrow\downarrow l}v_{-kj\downarrow}), \quad \text{(C.29)}$$

$${}_p\langle -|\hat{H}_{\text{T-NW}}|m_4\rangle = \beta_{-p,0}\beta^*_{p,1}(s_{\uparrow\uparrow l'}u_{k'j'\uparrow} + s_{\uparrow\downarrow l'}u_{k'j'\downarrow}) + \beta_{-p,1}\beta^*_{p,0}(s^*_{\uparrow\uparrow l'}v_{-k'j'\uparrow} + s^*_{\uparrow\downarrow l'}v_{-k'j'\downarrow}). \quad \text{(C.30)}$$

Recalling the phase dependence of the couplings given in Eq. (4.12), we note that only two terms in the product of the matrix elements (C.27)-(C.30) have a non-trivial phase dependence and the rest of the terms can be neglected. The first non-trivial term is

$$\begin{aligned}
&e^{i(\phi_{l'}-\phi_l)}|\beta_{p,0}|^4|\beta_{-p,1}|^4(|s_{\uparrow\uparrow l}|v_{-kj\uparrow} + |s_{\uparrow\downarrow l}|v_{-kj\downarrow})(|s_{\uparrow\uparrow l'}|u_{k'j'\uparrow} + |s_{\uparrow\downarrow l'}|u_{k'j'\downarrow})\times \\
&\times (|s_{\uparrow\uparrow l}|u_{kj\uparrow} + |s_{\uparrow\downarrow l}|u_{kj\downarrow})(|s_{\uparrow\uparrow l'}|v_{-k'j'\uparrow} + |s_{\uparrow\downarrow l'}|v_{-k'j'\downarrow}) = \\
&= e^{i(\phi_{l'}-\phi_l)}|\beta_{p,0}|^4|\beta_{-p,1}|^4(|s_{\uparrow\uparrow l}|^2v_{-kj\uparrow}u_{kj\uparrow} + |s_{\uparrow\downarrow l}|^2v_{-kj\downarrow}u_{kj\downarrow})\times \\
&\times (|s_{\uparrow\uparrow l'}|^2u_{k'j'\uparrow}v_{-k'j'\uparrow} + |s_{\uparrow\downarrow l'}|^2u_{k'j'\downarrow}v_{-k'j'\downarrow}) = \\
&= e^{i(\phi_{l'}-\phi_l)}|\beta_{p,0}|^4|\beta_{-p,1}|^4(|s_{\text{dir}}|^2v_{-kj\uparrow}u_{kj\uparrow} + |s_{\text{sf}}|^2v_{-kj\downarrow}u_{kj\downarrow})\times \\
&\times (|s_{\text{dir}}|^2u_{k'j'\uparrow}v_{-k'j'\uparrow} + |s_{\text{sf}}|^2u_{k'j'\downarrow}v_{-k'j'\downarrow}),
\end{aligned} \quad \text{(C.31)}$$

where in the first equality we have utilized the fact that $v_{-kj\uparrow}u_{kj\downarrow} + v_{-kj\downarrow}u_{kj\uparrow}$, $j = 1, 2$, are odd functions of the momentum, see Eq. (4.7), and thus eventually summing them over k would yield zero, hence allowing us to drop these terms at this stage. In the second equality of the expression (C.31) we have introduced the direct and the spin-flip couplings. Given the fact that $v_{-kj\uparrow}u_{kj\uparrow} = -v_{kj\downarrow}u_{-kj\downarrow}$, see Eq. (4.7), and keeping in mind that the expressions are eventually summed over the momenta k, k', we simplify (C.31)

into

$$e^{i(\phi_{l'}-\phi_l)}|\beta_{p,0}|^4|\beta_{-p,1}|^4(|s_{\rm dir}|^2-|s_{\rm sf}|^2)^2 u_{kj\uparrow}v_{-kj\uparrow}u_{k'j'\uparrow}v_{-k'j'\uparrow}. \tag{C.32}$$

The second non-trivial term in the product of the matrix elements (C.27)-(C.30) can be simplified in the same way into

$$\begin{aligned} &e^{i(\phi_l-\phi_{l'})}|\beta_{p,1}|^4|\beta_{-p,0}|^4(s^*_{\uparrow\uparrow l}u_{kj\uparrow}+s^*_{\uparrow\downarrow l}u_{kj\downarrow})(s_{\uparrow\uparrow l'}v_{-k'j'\uparrow}+s_{\uparrow\downarrow l'}v_{-k'j'\downarrow})\times \\ &\times(s^*_{\uparrow\uparrow l}v_{-kj\uparrow}+s^*_{\uparrow\downarrow l}v_{-kj\downarrow})(s_{\uparrow\uparrow l'}u_{k'j'\uparrow}+s_{\uparrow\downarrow l'}u_{k'j'\downarrow}) = \\ &= e^{i(\phi_l-\phi_{l'})}|\beta_{p,1}|^4|\beta_{-p,0}|^4(|s_{\rm dir}|^2-|s_{\rm sf}|^2)^2 u_{kj\uparrow}v_{-kj\uparrow}u_{k'j'\uparrow}v_{-k'j'\uparrow}. \end{aligned} \tag{C.33}$$

Using expressions (C.32)-(C.33) and summing over $l,l'=L,R;\ l\neq l'$, we write the single-level contribution to the fourth order energy correction as

$$\begin{aligned} \varepsilon^{(4,1)}_{p,-} =& -2\cos(\phi)(|\beta_{p,0}|^4|\beta_{-p,1}|^4+|\beta_{p,1}|^4|\beta_{-p,0}|^4)(|s_{\rm dir}|^2-|s_{\rm sf}|^2)^2\times \\ &\times\sum_{j,j'=1,2}\sum_{k,k'}\frac{u_{kj\uparrow}v_{-kj\uparrow}u_{k'j'\uparrow}v_{-k'j'\uparrow}}{(\varepsilon_{kj}+\varepsilon^{(0)}_{-p,-}-\varepsilon^{(0)}_{p,-})(\varepsilon_{kj}+\varepsilon_{k'j'})(\varepsilon_{k'j'}+\varepsilon^{(0)}_{-p,-}-\varepsilon^{(0)}_{p,-})}, \end{aligned} \tag{C.34}$$

where $\phi=\phi_R-\phi_L$. As in the second order case, applying the limit $\Delta_{\rm g}\gg\Delta,|t_L|,|t_R|$ allows us to neglect the expressions $\varepsilon^{(0)}_{-p,-}-\varepsilon^{(0)}_{p,-}$ and $\varepsilon^{(0)}_{-p,+}-\varepsilon^{(0)}_{p,-}$ in the denominator:

$$\begin{aligned} \varepsilon^{(4,1)}_{p,-} =& -2\cos(\phi)(|\beta_{p,0}|^4|\beta_{-p,1}|^4+|\beta_{p,1}|^4|\beta_{-p,0}|^4)(|s_{\rm dir}|^2-|s_{\rm sf}|^2)^2\times \\ &\times\sum_{j,j'=1,2}\sum_{k,k'}\frac{u_{kj\uparrow}v_{-kj\uparrow}u_{k'j'\uparrow}v_{-k'j'\uparrow}}{\varepsilon_{kj}(\varepsilon_{kj}+\varepsilon_{k'j'})\varepsilon_{k'j'}}. \end{aligned} \tag{C.35}$$

Next, we include the processes when the excited states $|m_2\rangle$, $|m_3\rangle$ and $|m_4\rangle$ can be $|+\rangle$. This simply amounts to replacing some of the β's with α's in Eqs. (C.27)-(C.30). Summing over all the possible states then gives the following full fourth order single-level

energy correction

$$\begin{aligned}\varepsilon^{(4,1)}_{p,-} =& -2\cos(\phi)(|s_{\rm dir}|^2-|s_{\rm sf}|^2)^2\left[|\beta_{p,0}|^2(|\beta_{-p,1}|^2+|\alpha_{-p,1}|^2)(|\beta_{p,0}|^2+|\alpha_{p,0}|^2)\times\right.\\ &\times(|\beta_{-p,1}|^2+|\alpha_{-p,1}|^2)+|\beta_{p,1}|^2(|\beta_{-p,0}|^2+|\alpha_{-p,0}|^2)(|\beta_{p,1}|^2+|\alpha_{p,1}|^2)\times\\ &\left.\times(|\beta_{-p,0}|^2+|\alpha_{-p,0}|^2)\right]\sum_{j,j'=1,2}\sum_{k,k'}\frac{u_{kj\uparrow}v_{-kj\uparrow}u_{k'j'\uparrow}v_{-k'j'\uparrow}}{\varepsilon_{kj}(\varepsilon_{kj}+\varepsilon_{k'j'})\varepsilon_{k'j'}},\end{aligned} \tag{C.36}$$

which can be simplified into

$$\varepsilon^{(4,1)}_{p,-} = -\cos(\phi)\frac{(|s_{\rm dir}|^2-|s_{\rm sf}|^2)^2}{\Delta^3_{\rm ind}}K_1^{(4)} \tag{C.37}$$

with

$$K_1^{(4)} = \frac{L^2}{2\pi^2}\int_{-\infty}^{\infty}dkdk'\sum_{j,j'=1,2}\frac{u_{kj\uparrow}v_{-kj\uparrow}u_{k'j'\uparrow}v_{-k'j'\uparrow}}{\varepsilon_{kj}(\varepsilon_{kj}+\varepsilon_{k'j'})\varepsilon_{k'j'}/\Delta^3_{\rm ind}}. \tag{C.38}$$

Note that we have replaced the summation over the momentum with the integration via Eq. (C.21). Setting $s_{\rm sf}=0$ in Eq. (C.37), we derive Eq. (4.30) of the main text.

C.5.2 Two-level tunneling contribution

In this subsection we consider the contribution to the fourth order energy correction (C.26) originating due to the tunneling through both of the QD levels. The right panel in Fig. C.2 schematically illustrates an example of this type of virtual process. In particular, we study the case when one of the virtual states $|m_2\rangle$, $|m_3\rangle$, $|m_4\rangle$ is the state with an occupied spin-down dot level, $|h\rangle$. Other terms with more than one virtual excited state being $|h\rangle$ are much smaller due to the assumed large Zeeman splitting on the dot, $h\gg\Delta$.

First, we focus on the case $|m_3\rangle = |h, 1_{kjl}, 1_{k'j'l'}\rangle_p$. Taking for concreteness $|m_2\rangle =$

$|-,1_{kjl}\rangle_{-p}$, $|m_4\rangle = |-,1_{k'j'l'}\rangle_{-p}$, the matrix elements in Eq. (C.26) read:

$$\langle m_2|\hat{H}_{\text{T-NW}}|-\rangle_p = \beta_{p,0}\beta^*_{-p,1}(s_{\uparrow\uparrow l}v_{-kj\uparrow} + s_{\uparrow\downarrow l}v_{-kj\downarrow}) + \beta_{p,1}\beta^*_{-p,0}(s^*_{\uparrow\uparrow l}u_{kj\uparrow} + s^*_{\uparrow\downarrow l}u_{kj\downarrow}), \quad \text{(C.39)}$$

$$\langle m_3|\hat{H}_{\text{T-NW}}|m_2\rangle = \beta_{-p,0}(s_{\downarrow\uparrow l'}v_{-k'j'\uparrow} + s_{\downarrow\downarrow l'}v_{-k'j'\downarrow}), \quad \text{(C.40)}$$

$$\langle m_4|\hat{H}_{\text{T-NW}}|m_3\rangle = \beta^*_{-p,0}(s^*_{\downarrow\uparrow l}v_{-kj\uparrow} + s^*_{\downarrow\downarrow l}v_{-kj\downarrow}), \quad \text{(C.41)}$$

$${}_p\langle -|\hat{H}_{\text{T-NW}}|m_4\rangle = \beta_{-p,0}\beta^*_{p,1}(s_{\uparrow\uparrow l'}u_{k'j'\uparrow} + s_{\uparrow\downarrow l'}u_{k'j'\downarrow}) + \beta_{-p,1}\beta^*_{p,0}(s^*_{\uparrow\uparrow l'}v_{-k'j'\uparrow} + s^*_{\uparrow\downarrow l'}v_{-k'j'\downarrow}). \quad \text{(C.42)}$$

Product of the matrix elements (C.39)-(C.42) has only one term with a nontrivial phase dependence that reads

$$\begin{aligned} &e^{i(\phi_{l'}-\phi_l)}|\beta_{p,1}|^2|\beta_{-p,0}|^4(|s_{\uparrow\uparrow l}|u_{kj\uparrow} + |s_{\uparrow\downarrow l}|u_{kj\downarrow})(|s_{\downarrow\uparrow l'}|v_{-k'j'\uparrow} + |s_{\downarrow\downarrow l'}|v_{-k'j'\downarrow})\times \\ &\times (|s_{\downarrow\uparrow l}|v_{-kj\uparrow} + |s_{\downarrow\downarrow l}|v_{-kj\downarrow})(|s_{\uparrow\uparrow l'}|u_{k'j'\uparrow} + |s_{\uparrow\downarrow l'}|u_{k'j'\downarrow}) = \\ &= e^{i(\phi_{l'}-\phi_l)}|\beta_{p,1}|^2|\beta_{-p,0}|^4(|s_{\text{dir}}|u_{kj\uparrow} + |s_{\text{sf}}|u_{kj\downarrow})(|s_{\text{sf}}|v_{-kj\uparrow} + |s_{\text{dir}}|v_{-kj\downarrow})\times \\ &\times (|s_{\text{sf}}|v_{-k'j'\uparrow} + |s_{\text{dir}}|v_{-k'j'\downarrow})(|s_{\text{dir}}|u_{k'j'\uparrow} + |s_{\text{sf}}|u_{k'j'\downarrow}), \end{aligned} \quad \text{(C.43)}$$

where we have assumed that the couplings to the left and to the right topological superconductor are identical and have introduced the direct and the spin-flip couplings as $|s_{\text{dir}}| \equiv |s_{\uparrow\uparrow}| = |s_{\downarrow\downarrow}|$ and $|s_{\text{sf}}| \equiv |s_{\uparrow\downarrow}| = |s_{\downarrow\uparrow}|$. Using the fact that $u_{kj\uparrow}v_{-kj\uparrow} = -u_{-kj\downarrow}v_{kj\downarrow}$ and $u_{kj\uparrow}v_{-kj\downarrow} = -u_{-kj\downarrow}v_{kj\uparrow}$, see Eq. (4.7), the expression (C.43) can be simplified into

$$e^{i(\phi_{l'}-\phi_l)}|\beta_{p,1}|^2|\beta_{-p,0}|^4(|s_{\text{dir}}|^2 - |s_{\text{sf}}|^2)^2u_{kj\uparrow}v_{-kj\downarrow}u_{k'j'\uparrow}v_{-k'j'\downarrow}, \quad \text{(C.44)}$$

where we have utilized the fact that the above expression is eventually summed over the momenta k, k'. Using the expression (C.44) and summing over $l, l' = L, R$; $l \neq l'$, the corresponding contribution to the energy correction in the limit $\Delta_{\text{g}} \gg \Delta, |t_L|, |t_R|$ is

given by

$$\varepsilon^{(4,2)}_{p,-}|_{m_3=h} = -\,2\cos(\phi)|\beta_{p,1}|^2|\beta_{-p,0}|^4(|s_{\rm dir}|^2-|s_{\rm sf}|^2)^2\sum_{j,j'=1,2}\sum_{k,k'}\frac{u_{kj\uparrow}v_{-kj\downarrow}u_{k'j'\uparrow}v_{-k'j'\downarrow}}{\varepsilon_{kj}(\varepsilon_{kj}+\varepsilon_{k'j'}+h)\varepsilon_{k'j'}}. \tag{C.45}$$

Furthermore, adding the possibility that the states $|m_2\rangle$, $|m_4\rangle$ can be $|+\rangle$, we obtain

$$\begin{aligned}\varepsilon^{(4,2)}_{p,-}|_{m_3=h} = -2\cos(\phi)|\beta_{p,1}|^2\left(|\beta_{-p,0}|^2+|\alpha_{-p,0}|^2\right)^2(|s_{\rm dir}|^2-|s_{\rm sf}|^2)^2\times\\ \times\sum_{j,j'=1,2}\sum_{k,k'}\frac{u_{kj\uparrow}v_{-kj\downarrow}u_{k'j'\uparrow}v_{-k'j'\downarrow}}{\varepsilon_{kj}(\varepsilon_{kj}+\varepsilon_{k'j'}+h)\varepsilon_{k'j'}},\end{aligned} \tag{C.46}$$

which using the fact that $|\beta_{-p,0}|^2+|\alpha_{-p,0}|^2=1$ can be simplified into

$$\varepsilon^{(4,2)}_{p,-}|_{m_3=h} = -\cos(\phi)\frac{(|s_{\rm dir}|^2-|s_{\rm sf}|^2)^2}{\Delta^3_{\rm ind}}\frac{K^{(4)}_2}{2}\left(1+\frac{\Delta}{\sqrt{\Delta^2+4|\bar{t}_p(\phi)|^2}}\right) \tag{C.47}$$

with

$$K^{(4)}_2 = \frac{L^2}{2\pi^2}\int_{-\infty}^{\infty}dkdk'\sum_{j,j'=1,2}\frac{u_{kj\uparrow}v_{-kj\downarrow}u_{k'j'\uparrow}v_{-k'j'\downarrow}}{\varepsilon_{kj}(\varepsilon_{kj}+\varepsilon_{k'j'}+h)\varepsilon_{k'j'}/\Delta^3_{\rm ind}}. \tag{C.48}$$

Second, we study the case with $|m_2\rangle = |h,1_{kjl}\rangle_{-p}$ and $|m_3\rangle = |-,1_{kjl},1_{k'j'l'}\rangle_p$, $|m_4\rangle = |-,1_{k'j'l'}\rangle_{-p}$. The relevant matrix elements are

$$\langle m_2|\hat{H}_{\text{T-NW}}|-\rangle_p = \beta_{p,0}(s_{\downarrow\uparrow l}v_{-kj\uparrow}+s_{\downarrow\downarrow l}v_{-kj\downarrow}), \tag{C.49}$$

$$\langle m_3|\hat{H}_{\text{T-NW}}|m_2\rangle = \beta^*_{p,0}(s^*_{\downarrow\uparrow l'}u_{k'j'\uparrow}+s^*_{\downarrow\downarrow l'}u_{k'j'\downarrow}), \tag{C.50}$$

$$\langle m_4|\hat{H}_{\text{T-NW}}|m_3\rangle = \beta_{p,0}\beta^*_{-p,1}(s_{\uparrow\uparrow l}u_{kj\uparrow}+s_{\uparrow\downarrow l}u_{kj\downarrow})+\beta_{p,1}\beta^*_{-p,0}(s^*_{\uparrow\uparrow l}v_{-kj\uparrow}+s^*_{\uparrow\downarrow l}v_{-kj\downarrow}), \tag{C.51}$$

$${}_p\langle -|\hat{H}_{\text{T-NW}}|m_4\rangle = \beta_{-p,0}\beta^*_{p,1}(s_{\uparrow\uparrow l'}u_{k'j'\uparrow}+s_{\uparrow\downarrow l'}u_{k'j'\downarrow})+\beta_{-p,1}\beta^*_{p,0}(s^*_{\uparrow\uparrow l'}v_{-k'j'\uparrow}+s^*_{\uparrow\downarrow l'}v_{-k'j'\downarrow}). \tag{C.52}$$

Product of the matrix elements (C.49)-(C.52) has only one term with a nontrivial phase dependence:

$$\begin{aligned}
&e^{i(\phi_{l'}-\phi_l)}|\beta_{-p,1}|^2|\beta_{p,0}|^4(s_{\downarrow\uparrow l}v_{-kj\uparrow}+s_{\downarrow\downarrow l}v_{-kj\downarrow})(s_{\downarrow\uparrow l'}u_{k'j'\uparrow}+s_{\downarrow\downarrow l'}u_{k'j'\downarrow})\times\\
&\times(s_{\uparrow\uparrow l}u_{kj\uparrow}+s_{\uparrow\downarrow l}u_{kj\downarrow})(s_{\uparrow\uparrow l'}v_{-k'j'\uparrow}+s_{\uparrow\downarrow l'}v_{-k'j'\downarrow})=\\
&=e^{i(\phi_{l'}-\phi_l)}|\beta_{-p,1}|^2|\beta_{p,0}|^4(s_{\rm sf}v_{-kj\uparrow}+s_{\rm dir}v_{-kj\downarrow})(s_{\rm dir}u_{kj\uparrow}+s_{\rm sf}u_{kj\downarrow})\times\\
&\times(s_{\rm sf}u_{k'j'\uparrow}+s_{\rm dir}u_{k'j'\downarrow})(s_{\rm dir}v_{-k'j'\uparrow}+s_{\rm sf}v_{-k'j'\downarrow}),
\end{aligned}\tag{C.53}$$

which similarly to Eq. (C.44) can be simplified into

$$-e^{i(\phi_{l'}-\phi_l)}|\beta_{-p,1}|^2|\beta_{p,0}|^4(|s_{\rm dir}|^2-|s_{\rm sf}|^2)^2u_{kj\uparrow}v_{-kj\downarrow}u_{k'j'\uparrow}v_{-k'j'\downarrow}.\tag{C.54}$$

Note the overall minus sign present in the expression (C.54); this minus sign was absent in the expression (C.44). The different signs in the expressions (C.44) and (C.54) ultimately lead to the $0-\pi$ transition. The contribution to the energy correction coming from the expression (C.54) in the limit $\Delta_{\rm g}\gg\Delta,|t_L|,|t_R|$ is given by

$$\varepsilon^{(4,2)}_{p,-}|_{m_2=h}=2\cos(\phi)|\beta_{-p,1}|^2|\beta_{p,0}|^4(|s_{\rm dir}|^2-|s_{\rm sf}|^2)^2\sum_{j,j'=1,2}\sum_{k,k'}\frac{u_{kj\uparrow}v_{-kj\downarrow}u_{k'j'\uparrow}v_{-k'j'\downarrow}}{(\varepsilon_{kj}+h)(\varepsilon_{kj}+\varepsilon_{k'j'})\varepsilon_{k'j'}},\tag{C.55}$$

which when summed with the terms where the states $|m_2\rangle$, $|m_4\rangle$ are $|+\rangle$, becomes

$$\begin{aligned}
\varepsilon^{(4,2)}_{p,-}|_{m_2=h}=2\cos(\phi)|\beta_{p,0}|^2(|\beta_{p,0}|^2+|\alpha_{p,0}|^2)(|\beta_{-p,1}|^2+|\alpha_{-p,1}|^2)(|s_{\rm dir}|^2-|s_{\rm sf}|^2)^2\times\\
\times\sum_{j,j'=1,2}\sum_{k,k'}\frac{u_{kj\uparrow}v_{-kj\downarrow}u_{k'j'\uparrow}v_{-k'j'\downarrow}}{(\varepsilon_{kj}+h)(\varepsilon_{kj}+\varepsilon_{k'j'})\varepsilon_{k'j'}}.
\end{aligned}\tag{C.56}$$

This can be simplified into

$$\varepsilon^{(4,2)}_{p,-}|_{m_2=h} = \cos(\phi)\frac{(|s_{\rm dir}|^2-|s_{\rm sf}|^2)^2}{\Delta^3_{\rm ind}}\frac{K_3^{(4)}}{2}\left(1+\frac{\Delta}{\sqrt{\Delta^2+4|\bar{t}_p(\phi)|^2}}\right) \tag{C.57}$$

with

$$K_3^{(4)} = \frac{L^2}{2\pi^2}\int_{-\infty}^{\infty}dkdk'\sum_{j,j'=1,2}\frac{u_{kj\uparrow}v_{-kj\downarrow}u_{k'j'\uparrow}v_{-k'j'\downarrow}}{(\varepsilon_{kj}+h)(\varepsilon_{kj}+\varepsilon_{k'j'})\varepsilon_{k'j'}/\Delta^3_{\rm ind}}. \tag{C.58}$$

Third, we analyze the case with $|m_4\rangle = |h,1_{k'j'l'}\rangle_{-p}$ and $|m_2\rangle = |-,1_{kjl}\rangle_{-p}$, $|m_3\rangle = |-,1_{kjl},1_{k'j'l'}\rangle_p$. The relevant matrix elements read:

$$\begin{aligned}
&\langle m_2|\hat{H}_{\text{T-NW}}|-\rangle_p = \beta_{p,0}\beta^*_{-p,1}(s_{\uparrow\uparrow l}v_{-kj\uparrow}+s_{\uparrow\downarrow l}v_{-kj\downarrow})+\beta_{p,1}\beta^*_{-p,0}(s^*_{\uparrow\uparrow l}u_{kj\uparrow}+s^*_{\uparrow\downarrow l}u_{kj\downarrow}),\\
&\langle m_3|\hat{H}_{\text{T-NW}}|m_2\rangle = \beta_{-p,0}\beta^*_{p,1}(s_{\uparrow\uparrow l'}v_{-k'j'\uparrow}+s_{\uparrow\downarrow l'}v_{-k'j'\downarrow})+\beta_{-p,1}\beta^*_{p,0}(s^*_{\uparrow\uparrow l'}u_{k'j'\uparrow}+s^*_{\uparrow\downarrow l'}u_{k'j'\downarrow}),\\
&\langle m_4|\hat{H}_{\text{T-NW}}|m_3\rangle = \beta_{p,0}(s_{\downarrow\uparrow l}u_{kj\uparrow}+s_{\downarrow\downarrow l}u_{kj\downarrow}),\\
&{}_p\langle -|\hat{H}_{\text{T-NW}}|m_4\rangle = \beta^*_{p,0}(s^*_{\downarrow\uparrow l'}v_{-k'j'\uparrow}+s^*_{\downarrow\downarrow l'}v_{-k'j'\downarrow}).
\end{aligned}$$

Performing the same manipulations as in the $|m_2\rangle = |h,1_{kjl}\rangle_{-p}$ case, one can show that the energy corrections in the two cases are identical:

$$\varepsilon^{(4,2)}_{p,-}|_{m_4=h} = \varepsilon^{(4,2)}_{p,-}|_{m_2=h}. \tag{C.59}$$

Finally, summing over the three cases $|m_2\rangle = |h,1_{kjl}\rangle_{-p}$, $|m_3\rangle = |h,1_{kjl},1_{k'j'l'}\rangle_p$ and $|m_4\rangle = |h,1_{kjl}\rangle_{-p}$ considered above, we obtain the total fourth order two-level energy

correction:

$$\begin{aligned}\varepsilon_{p,-}^{(4,2)} &= \varepsilon_{p,-}^{(4,2)}|_{m_2=h} + \varepsilon_{p,-}^{(4,2)}|_{m_3=h} + \varepsilon_{p,-}^{(4,2)}|_{m_4=h} = \\ &= \cos\phi \frac{\left(|s_{\rm dir}|^2 - |s_{\rm sf}|^2\right)^2}{\Delta_{\rm ind}^3} \left[K_3^{(4)} - \frac{K_2^{(4)}}{2} - \left(K_3^{(4)} + \frac{K_2^{(4)}}{2} \right) \frac{\Delta}{\sqrt{\Delta^2 + 4|\bar{t}_p(\phi)|^2}} \right].\end{aligned} \tag{C.60}$$

Setting $s_{\rm sf} = 0$ in Eq. (C.60), we derive Eq. (4.34) of the main text.

Appendix D

Appendix for Chapter 5

D.1 Constraints on the eigenvalues of the $W_0 = P_0 U^\dagger P_0 U P_0$ operator

$W_0 = P_0 U^\dagger P_0 U P_0$ is a Hermitian operator, and since it can be written as $W_0 = (P_0 U P_0)^\dagger (P_0 U P_0)$, it is positive semidefinite. Thus, its eigenvalues are $\lambda_{W_0} \geq 0$.

On the other hand, W_0 can be considered an orthogonal projection of a Hermitian operator $A = U^\dagger P_0 U$, and thus, by Cauchy Interlacing Theorem, eigenvalues of W_0 are interlaced with eigenvalues of A. In particular, it follows from the theorem that $\lambda_{W_0} \leq \max[\lambda_A]$, where λ_A denotes eigenvalues of A. At the same time, eigenvalues of the operator A are either 0 or 1, and hence $\lambda_{W_0} \leq 1$.

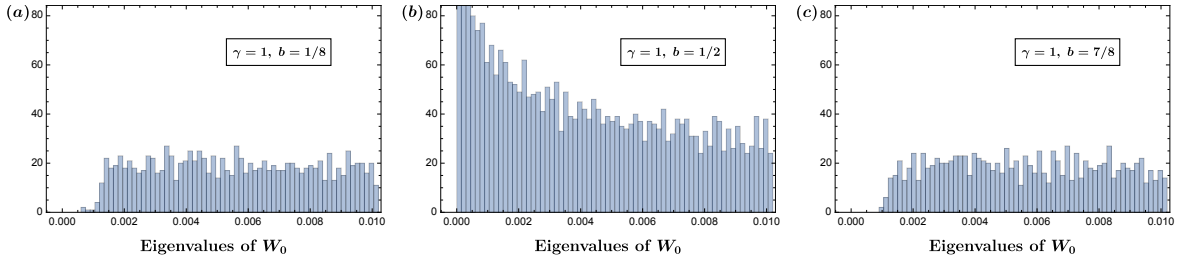

Figure D.1: Histograms representing the zoomed in near zero eigenvalue distributions of a numerically generated random matrix W_0 for $\gamma = 1$ and various values of b. Dimensionality of the Hilbert space is $N = 2048$. Averaging is performed over 80 random matrix realizations. For visual clarity, the zero eigenvalue is excluded from the histograms.

D.2 Histograms revealing the eigenvalue 0 gap for $\gamma = 1,\ b = 1/8$ and $\gamma = 1,\ b = 7/8$

Fig. D.1 illustrates numerically calculated and zoomed in near zero spectra of a randomly generated matrix W_0 for the same values of parameters γ, b, as spectra of Fig. 5.2(a)-(c). For $b = 1/8$, Eq. (5.8) gives $\gamma_c \approx 1.2$ for the critical value of γ, and thus Fig. D.1(a) plotted for $\gamma = 1$, $b = 1/8$ reveals a gap between the smallest eigenvalue and the 0 eigenvalue. The same gap is present for $\gamma = 1$, $b = 7/8$, as shown in Fig. D.1(c). On the other hand, for $\gamma = 1$, $b = 1/2$, one finds that $\gamma = \gamma_c$, and hence the 0 eigenvalue gap is closed, as depicted in Fig. D.1(b).

D.3 The derivation of expression (5.17) for the moment-generating function $\Gamma_1(\lambda)$

Matrix $\hat{\mathcal{M}}(\lambda)$ of Eq. (5.13) can be written as

$$\hat{\mathcal{M}}(\lambda) = (\hat{1} + \lambda\hat{\mathcal{T}}\hat{\mathcal{L}}^{-1})\hat{\mathcal{L}}, \tag{D.1}$$

and thus its inverse reads

$$\hat{\mathcal{M}}^{-1} = \hat{\mathcal{L}}^{-1}(\hat{1} + \lambda\hat{\mathcal{T}}\hat{\mathcal{L}}^{-1})^{-1} = \hat{\mathcal{L}}^{-1} + \hat{\mathcal{L}}^{-1}(-\lambda\hat{\mathcal{T}} + \lambda^2\hat{\mathcal{T}}\hat{\mathcal{L}}^{-1}\hat{\mathcal{T}})\sum_{k=0}^{\infty}\lambda^{2k}(\hat{\mathcal{L}}^{-1}\hat{\mathcal{T}}\hat{\mathcal{L}}^{-1}\hat{\mathcal{T}})^k\hat{\mathcal{L}}^{-1}, \tag{D.2}$$

where

$$\hat{\mathcal{L}}^{-1} = \begin{pmatrix} \check{0} & (\check{L}^{\dagger})^{-1} \\ \check{L}^{-1} & \check{0} \end{pmatrix}. \tag{D.3}$$

The inverse of the matrix $\check{L}$ can be straightforwardly calculated from Eq. (5.14):

$$\check{L}^{-1} = (i - H)^{-1}\begin{pmatrix} i & -1 \\ -H & 1 \end{pmatrix}. \tag{D.4}$$

Note that the unitary evolution operators U and $U^{\dagger}$ can be expressed in terms of $\check{L}^{-1}$ as

$$U = \begin{pmatrix} 1 & -1 \end{pmatrix}\check{L}^{-1}\begin{pmatrix} 1 \\ 0 \end{pmatrix}, \tag{D.5}$$

$$U^{\dagger} = \begin{pmatrix} 1 & 0 \end{pmatrix}(\check{L}^{\dagger})^{-1}\begin{pmatrix} 1 \\ -1 \end{pmatrix}. \tag{D.6}$$

Using Eq. (D.3) and the definition of the matrix $\hat{\mathcal{T}}$ given by the second part of Eq. (5.13), it is straightforward to show that

$$\hat{\mathcal{L}}^{-1}\hat{\mathcal{T}}\hat{\mathcal{L}}^{-1}\hat{\mathcal{T}} = \begin{pmatrix} (\check{L}^{\dagger})^{-1}\check{t}_2\check{L}^{-1}\check{t}_1 & \check{0} \\ \check{0} & \check{L}^{-1}\check{t}_1(\check{L}^{\dagger})^{-1}\check{t}_2 \end{pmatrix} \tag{D.7}$$

and

$$\mathrm{Tr}_{4N}\left[\hat{\mathcal{T}}\hat{\mathcal{L}}^{-1}\right]=0, \tag{D.8}$$

$$\mathrm{Tr}_{4N}\left[\left(\hat{\mathcal{L}}^{-1}\hat{\mathcal{T}}\hat{\mathcal{L}}^{-1}\hat{\mathcal{T}}\right)^{k}]=2\mathrm{Tr}_{2N}[\left((\check{L}^{\dagger})^{-1}\check{t}_2\check{L}^{-1}\check{t}_1\right)^{k}\right], \tag{D.9}$$

$$\mathrm{Tr}_{4N}\left[\hat{\mathcal{L}}^{-1}\hat{\mathcal{T}}\left(\hat{\mathcal{L}}^{-1}\hat{\mathcal{T}}\hat{\mathcal{L}}^{-1}\hat{\mathcal{T}}\right)^{k}\right]=0. \tag{D.10}$$

Next, we consider a function $\lambda\mathrm{Tr}_{4N}\left[\hat{\mathcal{T}}\hat{\mathcal{M}}^{-1}\right]$, which with the help of Eqs. (D.8)-(D.10) can be written as

$$\begin{aligned}
\lambda\mathrm{Tr}_{4N}\left[\hat{\mathcal{T}}\hat{\mathcal{M}}^{-1}\right]=&\\
&\lambda\mathrm{Tr}_{4N}\left[\hat{\mathcal{T}}\hat{\mathcal{L}}^{-1}\hat{\mathcal{T}}(-\lambda\hat{1}+\lambda^2\hat{\mathcal{L}}^{-1}\hat{\mathcal{T}})\sum_{k=0}^{\infty}\lambda^{2k}(\hat{\mathcal{L}}^{-1}\hat{\mathcal{T}}\hat{\mathcal{L}}^{-1}\hat{\mathcal{T}})^{k}\hat{\mathcal{L}}^{-1}\right]=\\
&\mathrm{Tr}_{4N}\left[(-\hat{1}+\lambda\hat{\mathcal{L}}^{-1}\hat{\mathcal{T}})\sum_{k=0}^{\infty}\lambda^{2k+2}(\hat{\mathcal{L}}^{-1}\hat{\mathcal{T}}\hat{\mathcal{L}}^{-1}\hat{\mathcal{T}})^{k}\hat{\mathcal{L}}^{-1}\hat{\mathcal{T}}\hat{\mathcal{L}}^{-1}\hat{\mathcal{T}}\right]=\\
&\mathrm{Tr}_{4N}\left[(-\hat{1}+\lambda\hat{\mathcal{L}}^{-1}\hat{\mathcal{T}})\sum_{k=1}^{\infty}\lambda^{2k}(\hat{\mathcal{L}}^{-1}\hat{\mathcal{T}}\hat{\mathcal{L}}^{-1}\hat{\mathcal{T}})^{k}\right]=\\
&-2\sum_{k=1}^{\infty}\lambda^{2k}\mathrm{Tr}_{2N}\left[\left((\check{L}^{\dagger})^{-1}\check{t}_2\check{L}^{-1}\check{t}_1\right)^{k}\right].
\end{aligned} \tag{D.11}$$

Plugging in the explicit form of the matrices $\check{t}_1,\check{t}_2$ given by Eqs. (5.15),(5.16) and employing identities (D.5),(D.6), we rewrite Eq. (D.11) as

$$-\frac{\lambda}{2}\mathrm{Tr}_{4N}\left[\hat{\mathcal{T}}\hat{\mathcal{M}}^{-1}\right]=\sum_{k=1}^{\infty}\lambda^{2k}\mathrm{Tr}_{N}\left[\left(U^{\dagger}P_0UP_0\right)^{k}\right]=\sum_{k=1}^{\infty}\lambda^{2k}\mathrm{Tr}_{N}\left[W_0^{k}\right]. \tag{D.12}$$

Averaging the above equation over the ensemble of random matrices H, we obtain the following identity:

$$-\frac{\lambda}{2}\mathrm{Tr}_{4N}\left[\hat{\mathcal{T}}\hat{\mathcal{G}}\right]=\sum_{k=1}^{\infty}\lambda^{2k}\mathrm{Tr}_{N}\left[\left\langle\hat{W}_0^{k}\right\rangle\right], \tag{D.13}$$

where we have introduced $\hat{\mathcal{G}} \equiv \langle \hat{\mathcal{M}}^{-1} \rangle$. Recalling Eq. (5.10) and the definition of the moment generating function $\Gamma_1(\lambda)$ introduced in Eq. (5.11), we obtain identity (5.17) of the main text,

$$\Gamma_1(\lambda) = -\frac{\lambda}{2bN} \mathrm{Tr}_{4N} \left[\hat{\mathcal{T}} \hat{\mathcal{G}} \right]. \tag{D.14}$$

D.4 The derivation of expression (5.28) for $\check{G}_0^{-1}$ in the case of $\Gamma_1(\lambda)$

From Eq. (D.2) it follows that

$$\hat{\mathcal{G}}_0 \equiv \hat{\mathcal{M}}_0^{-1} = \hat{\mathcal{L}}_0^{-1} + \hat{\mathcal{L}}_0^{-1}(-\lambda\hat{\mathcal{T}} + \lambda^2 \hat{\mathcal{T}} \hat{\mathcal{L}}_0^{-1} \hat{\mathcal{T}}) \sum_{k=0}^{\infty} \lambda^{2k} (\hat{\mathcal{L}}_0^{-1} \hat{\mathcal{T}} \hat{\mathcal{L}}_0^{-1} \hat{\mathcal{T}})^k \hat{\mathcal{L}}_0^{-1}, \tag{D.15}$$

where $\hat{\mathcal{L}}_0^{-1} = \hat{\mathcal{L}}^{-1}|_{H=0}$. Using explicit forms of matrices $\hat{\mathcal{T}}$ and $\hat{\mathcal{L}}_0^{-1}$, we obtain the following identity:

$$\hat{\mathcal{T}} \hat{\mathcal{L}}_0^{-1} \hat{\mathcal{T}} \hat{\mathcal{L}}_0^{-1} \hat{\mathcal{T}} = \hat{\mathcal{T}}, \tag{D.16}$$

using which we simplify expression (D.15) for $\hat{\mathcal{G}}_0$ into

$$\hat{\mathcal{G}}_0 = \hat{\mathcal{L}}_0^{-1} + \hat{\mathcal{L}}_0^{-1}(-\lambda\hat{\mathcal{T}} + \lambda^2 \hat{\mathcal{T}} \hat{\mathcal{L}}_0^{-1} \hat{\mathcal{T}}) \sum_{k=0}^{\infty} \lambda^{2k} \hat{\mathcal{L}}_0^{-1} = \hat{\mathcal{L}}_0^{-1} + \hat{\mathcal{L}}_0^{-1} \left(-\frac{\lambda\hat{\mathcal{T}}}{1-\lambda^2} + \frac{\lambda^2 \hat{\mathcal{T}} \hat{\mathcal{L}}_0^{-1} \hat{\mathcal{T}}}{1-\lambda^2} \right) \hat{\mathcal{L}}_0^{-1}. \tag{D.17}$$

Defining a projector onto the $2N$-dimensional inner block subspace as

$$\hat{\Pi} = \begin{pmatrix} 0 & 0 & 0 & 0 \\ 0 & 1 & 0 & 0 \\ 0 & 0 & 1 & 0 \\ 0 & 0 & 0 & 0 \end{pmatrix}, \tag{D.18}$$

we obtain the following identities:

$$\hat{\Pi}\hat{\mathcal{L}}_0^{-1}\hat{\Pi} = \begin{pmatrix} 0 & 0 & 0 & 0 \\ 0 & 0 & -i & 0 \\ 0 & i & 0 & 0 \\ 0 & 0 & 0 & 0 \end{pmatrix}, \tag{D.19}$$

$$\hat{\Pi}\hat{\mathcal{L}}_0^{-1}\hat{\mathcal{T}}\hat{\mathcal{L}}_0^{-1}\hat{\Pi} = 2\begin{pmatrix} 0 & 0 & 0 & 0 \\ 0 & 1 & 0 & 0 \\ 0 & 0 & 1 & 0 \\ 0 & 0 & 0 & 0 \end{pmatrix} P_0, \tag{D.20}$$

$$\hat{\Pi}\hat{\mathcal{L}}_0^{-1}\hat{\mathcal{T}}\hat{\mathcal{L}}_0^{-1}\hat{\mathcal{T}}\hat{\mathcal{L}}_0^{-1}\hat{\Pi} = 2\begin{pmatrix} 0 & 0 & 0 & 0 \\ 0 & 0 & -i & 0 \\ 0 & i & 0 & 0 \\ 0 & 0 & 0 & 0 \end{pmatrix} P_0. \tag{D.21}$$

We utilize these identities to project Eq. (D.17) onto the $2N$-dimensional subspace, which yields

$$\check{G}_0 = (1 - P_0)\bar{\sigma}_y + P_0\left(f_y\bar{\sigma}_y + f_1\bar{1}\right), \tag{D.22}$$

where $\bar{\sigma}_y$ and $\bar{1}$ are the two-dimensional Y Pauli and the identity matrices, respectively, and we have introduced the following functions of λ:

$$f_y = \frac{1+\lambda^2}{1-\lambda^2}, \tag{D.23}$$

$$f_1 = -\frac{2\lambda}{1-\lambda^2}. \tag{D.24}$$

Expression (5.28) of the main text is obtained by inverting $\check{G}_0$ of Eq. (D.22):

$$\check{G}_0^{-1} = (1 - P_0)\bar{\sigma}_y + P_0(f_y\bar{\sigma}_y - f_1\bar{1}). \tag{D.25}$$

D.5 The derivation of expression (5.39) for $\Gamma_1(\lambda)$ in terms of the parameters u and v

First, we would like to derive certain identities, which we will make use of when obtaining the expression for $\Gamma_1(\lambda)$. We start by noting that

$$\hat{\mathcal{T}} = \frac{\partial \hat{\mathcal{G}}_0^{-1}}{\partial \lambda} = -\hat{\mathcal{G}}_0^{-1}\frac{\partial \hat{\mathcal{G}}_0}{\partial \lambda}\hat{\mathcal{G}}_0^{-1}, \tag{D.26}$$

and hence

$$\hat{\Pi}\hat{\mathcal{G}}_0\hat{\mathcal{T}}\hat{\mathcal{G}}_0\hat{\Pi} = -\frac{\partial \check{G}_0}{\partial \lambda} = \frac{2P_0}{1-\lambda^2}\left(f_1\bar{\sigma}_y + f_y\bar{1}\right). \tag{D.27}$$

Next, given the fact that $\mathrm{Tr}_{4N}\left[\hat{\mathcal{L}}_0^{-1}\hat{\mathcal{T}}\right] = 0$ and

$$\hat{\mathcal{L}}_0^{-1}\hat{\mathcal{T}}\hat{\mathcal{L}}_0^{-1}\hat{\mathcal{T}} = \begin{pmatrix} 1 & 0 & 0 & 0 \\ -2i & 0 & 0 & 0 \\ 0 & 0 & 1 & -1 \\ 0 & 0 & 0 & 0 \end{pmatrix} P_0, \tag{D.28}$$

we obtain

$$\mathrm{Tr}_{4N}\left[\hat{\mathcal{G}}_0\hat{\mathcal{T}}\right] = -\frac{2\lambda}{1-\lambda^2}bN, \tag{D.29}$$

where we have used expression (D.17) for $\hat{\mathcal{G}}_0$ and identity (D.16).

Moving on to the expression for $\Gamma_1(\lambda)$ itselt, plugging Eq. (5.21) into expression (5.17)

for $\Gamma_1(\lambda)$ yields

$$\Gamma_1(\lambda) = -\frac{\lambda}{2bN}\mathrm{Tr}_{4N}\left[\hat{\mathcal{T}}(\hat{1}-\hat{\mathcal{G}}_0\hat{\Sigma})^{-1}\hat{\mathcal{G}}_0\right], \tag{D.30}$$

which, after expanding $(\hat{1}-\hat{\mathcal{G}}_0\hat{\Sigma})^{-1}$ into a series and separating the first two terms from the rest, can be transformed into

$$\begin{aligned}\Gamma_1(\lambda) = &\\ &-\frac{\lambda}{2bN}\left\{\mathrm{Tr}_{4N}\left[\hat{\mathcal{G}}_0\hat{\mathcal{T}}\right]+\mathrm{Tr}_{4N}\left[\hat{\mathcal{G}}_0\hat{\mathcal{T}}\hat{\mathcal{G}}_0\hat{\Sigma}\right]+\mathrm{Tr}_{4N}\left[\hat{\mathcal{G}}_0\hat{\mathcal{T}}\hat{\mathcal{G}}_0\hat{\Sigma}\left(\hat{1}+\hat{\mathcal{G}}_0\hat{\Sigma}+\dots\right)\hat{\mathcal{G}}_0\hat{\Sigma}\right]\right\} = \\ &-\frac{\lambda}{2bN}\left\{\mathrm{Tr}_{4N}\left[\hat{\mathcal{G}}_0\hat{\mathcal{T}}\right]+\mathrm{Tr}_{4N}\left[\hat{\mathcal{G}}_0\hat{\mathcal{T}}\hat{\mathcal{G}}_0\hat{\Sigma}\right]+\mathrm{Tr}_{4N}\left[\hat{\mathcal{G}}_0\hat{\mathcal{T}}\hat{\mathcal{G}}_0\hat{\Sigma}\hat{\mathcal{G}}\hat{\Sigma}\right]\right\}.\end{aligned} \tag{D.31}$$

Since $\hat{\Sigma} = \hat{\Pi}\hat{\Sigma}\hat{\Pi}$, we can rewrite Eq. (D.31) as

$$\begin{aligned}\Gamma_1(\lambda) &= -\frac{\lambda}{2bN}\left\{\mathrm{Tr}_{4N}\left[\hat{\mathcal{G}}_0\hat{\mathcal{T}}\right]+\mathrm{Tr}_{4N}\left[\hat{\Pi}\hat{\mathcal{G}}_0\hat{\mathcal{T}}\hat{\mathcal{G}}_0\hat{\Pi}\hat{\Sigma}\right]+\mathrm{Tr}_{4N}\left[\hat{\Pi}\hat{\mathcal{G}}_0\hat{\mathcal{T}}\hat{\mathcal{G}}_0\hat{\Pi}\hat{\Sigma}\hat{\Pi}\hat{\mathcal{G}}\hat{\Pi}\hat{\Sigma}\right]\right\} = \\ &= -\frac{\lambda}{2bN}\left\{\mathrm{Tr}_{4N}\left[\hat{\mathcal{G}}_0\hat{\mathcal{T}}\right]+\mathrm{Tr}_{4N}\left[\hat{\Pi}\hat{\mathcal{G}}_0\hat{\mathcal{T}}\hat{\mathcal{G}}_0\hat{\Pi}\left(\hat{1}+\hat{\Sigma}\hat{\Pi}\hat{\mathcal{G}}\hat{\Pi}\right)\hat{\Sigma}\right]\right\} = \\ &= -\frac{\lambda}{2bN}\left\{\mathrm{Tr}_{4N}\left[\hat{\mathcal{G}}_0\hat{\mathcal{T}}\right]+\mathrm{Tr}_{4N}\left[\hat{\Pi}\hat{\mathcal{G}}_0\hat{\mathcal{T}}\hat{\mathcal{G}}_0\hat{\Pi}\hat{\mathcal{G}}_0^{-1}\hat{\Pi}\hat{\mathcal{G}}\hat{\Pi}\hat{\Sigma}\hat{\Pi}\right]\right\},\end{aligned} \tag{D.32}$$

where in the last equality we have made use of the Dyson's equation,

$$\hat{\mathcal{G}} = \hat{\mathcal{G}}_0 + \hat{\mathcal{G}}_0\hat{\Sigma}\hat{\mathcal{G}} = \hat{\mathcal{G}}_0\left(\hat{1}+\hat{\Sigma}\hat{\mathcal{G}}\right). \tag{D.33}$$

Finally, plugging Eqs. (5.25),(5.28),(5.35),(D.27) and (D.29) into Eq. (D.32), we obtain

$$\Gamma_1(\lambda) = \frac{\lambda^2}{1-\lambda^2}\left[1-\frac{2}{\lambda}\frac{uf_y - vf_1}{(f_y+v)^2-(u+f_1)^2}\right], \tag{D.34}$$

where we have utilized expression (5.36) for $\bar{g}_1$ and identity (5.31). The derived expression for $\Gamma_1(\lambda)$ is Eq. (5.39) of the main text.

D.6 The derivation of expression (5.64) for $\check{G}_0^{-1}$ in the case of $\Gamma_2(\lambda)$

Equation (D.15) remains valid with the redefined matrix $\check{t}_2$ of Eq. (5.60), and we use it to calculate expressions for $\check{G}_0$ and $\check{G}_0^{-1}$. Noting that

$$\hat{\mathcal{L}}_0^{-1}\hat{\mathcal{T}}\hat{\mathcal{L}}_0^{-1}\hat{\mathcal{T}} = 0, \tag{D.35}$$

Eq. (D.15) can be simplified into

$$\hat{\mathcal{G}}_0 = \hat{\mathcal{L}}_0^{-1} - \lambda\hat{\mathcal{L}}_0^{-1}\hat{\mathcal{T}}\hat{\mathcal{L}}_0^{-1}. \tag{D.36}$$

Taking into account the explicit form of the matrices $\hat{\mathcal{T}}$ and $\hat{\mathcal{L}}_0^{-1}$, we find that

$$\hat{\Pi}\hat{\mathcal{L}}_0^{-1}\hat{\mathcal{T}}\hat{\mathcal{L}}_0^{-1}\hat{\Pi} = 2\begin{pmatrix} 0 & 0 & 0 & 0 \\ 0 & 1-P_0 & 0 & 0 \\ 0 & 0 & P_0 & 0 \\ 0 & 0 & 0 & 0 \end{pmatrix}, \tag{D.37}$$

which together with Eq. (D.19) allows us to derive the expression for $\check{G}_0$,

$$\check{G}_0 = P_0[\bar{\sigma}_y - \lambda(1-\bar{\sigma}_z)] + (1-P_0)[\bar{\sigma}_y - \lambda(1+\bar{\sigma}_z)]. \tag{D.38}$$

Inverting this expression yields

$$\check{G}_0^{-1} = P_0[\bar{\sigma}_y + \lambda(1+\bar{\sigma}_z)] + (1-P_0)[\bar{\sigma}_y + \lambda(1-\bar{\sigma}_z)], \tag{D.39}$$

which is nothing but Eq. (5.64) of the main text.

D.7 The derivation of expression (5.71) for $\Gamma_2(\lambda)$ in terms of the parameters u and v

$\Gamma_2(\lambda)$ can be expressed in terms of $\hat{\mathcal{G}}_0$, $\hat{\mathcal{G}}$, $\hat{\mathcal{T}}$ and $\hat{\Sigma}$ using Eq. (D.32):

$$\Gamma_2(\lambda) = -\frac{\lambda}{2bN}\left\{\mathrm{Tr}_{4N}\left[\hat{\mathcal{G}}_0\hat{\mathcal{T}}\right] + \mathrm{Tr}_{4N}\left[\hat{\Pi}\hat{\mathcal{G}}_0\hat{\mathcal{T}}\hat{\mathcal{G}}_0\hat{\Pi}\hat{\mathcal{G}}_0^{-1}\hat{\Pi}\hat{\mathcal{G}}\hat{\Pi}\hat{\Sigma}\hat{\Pi}\right]\right\}, \tag{D.40}$$

where all the involved matrices are from Section 5.5. Recalling expression (D.36) for $\hat{\mathcal{G}}_0$, identity (D.35), and the explicit form of matrices $\hat{\mathcal{L}}_0^{-1}$, $\hat{\mathcal{T}}$, we find that

$$\mathrm{Tr}_{4N}\left[\hat{\mathcal{G}}_0\hat{\mathcal{T}}\right] = 0 \tag{D.41}$$

and

$$\hat{\mathcal{G}}_0\hat{\mathcal{T}}\hat{\mathcal{G}}_0 = \hat{\mathcal{L}}_0^{-1}\hat{\mathcal{T}}\hat{\mathcal{L}}_0^{-1}. \tag{D.42}$$

Plugging Eqs. (5.63),(5.64),(5.68),(D.37),(D.41),(D.42) into expression (D.40) yields

$$\Gamma_2(\lambda) = -\frac{\lambda}{b}\left[(1-b)\frac{u-w}{(v+1)^2-u^2+w^2+2\lambda(u-w)} + \right. \\ \left. + b\frac{u+w}{(v+1)^2-u^2+w^2+2\lambda(u+w)}\right], \tag{D.43}$$

where we have used expressions (5.66)-(5.68) for $\bar{g}_1, \bar{g}_2$. Switching variables to $u_\pm = u \pm w$ and expressing b in terms of α, β leads to Eq. (5.71) of the main text:

$$\Gamma_2(\lambda) = -\frac{\lambda}{\beta}\left[\alpha\frac{u_-}{(v+1)^2-u_+u_-+2\lambda u_-} + \beta\frac{u_+}{(v+1)^2-u_+u_-+2\lambda u_+}\right]. \tag{D.44}$$

D.8 The solution of the system (5.70) in the limit $\lambda \to 1^-$

System (5.70),

$$u_+ = \frac{\alpha(u_+ - 2\lambda)}{(v+1)^2 - u_-(u_+ - 2\lambda)} + \frac{\beta u_+}{(v+1)^2 - u_+(u_- - 2\lambda)}, \tag{D.45}$$

$$u_- = \frac{\alpha u_-}{(v+1)^2 - u_-(u_+ - 2\lambda)} + \frac{\beta(u_- - 2\lambda)}{(v+1)^2 - u_+(u_- - 2\lambda)}, \tag{D.46}$$

$$\frac{v}{v+1} = \frac{\alpha}{(v+1)^2 - u_-(u_+ - 2\lambda)} + \frac{\beta}{(v+1)^2 - u_+(u_- - 2\lambda)}, \tag{D.47}$$

can be simplified by plugging Eq. (D.47) into Eqs. (D.45) and (D.46), which yields

$$u_+ \left[(v+1)^2 - u_- u_+ + 2\lambda u_-\right] = -2\alpha\lambda(v+1), \tag{D.48}$$

$$u_- \left[(v+1)^2 - u_- u_+ + 2\lambda u_+\right] = -2\beta\lambda(v+1). \tag{D.49}$$

Plugging Eqs. (D.48) and (D.49) back into Eq. (D.45), we obtain the following identity:

$$2\lambda v + u_+ + u_- = 0, \tag{D.50}$$

while summing Eqs. (D.48) and (D.49) yields

$$u_+ u_- = \frac{(v+1)\left[v(v+1) - \gamma\right]}{v+2}. \tag{D.51}$$

Using Eqs. (D.50) and (D.51), we express u_+ and u_- in terms of v:

$$u_+ = -v\lambda + \text{sign}(\beta - \alpha)\frac{\sqrt{(v+2)\left\{\gamma + v\left[-1 + \gamma + v(v+2)(\lambda^2 - 1)\right]\right\}}}{v+2}, \tag{D.52}$$

$$u_- = -v\lambda + \text{sign}(\alpha - \beta)\frac{\sqrt{(v+2)\left\{\gamma + v\left[-1 + \gamma + v(v+2)(\lambda^2 - 1)\right]\right\}}}{v+2}, \tag{D.53}$$

where the signs are picked to produce the correct solution at $\lambda = 0$. Furthermore, plugging Eqs. (D.51) and (D.52) into Eq. (D.48) allows us to obtain a fifth order equation on v,

$$(v+2)^3(\alpha-\beta)^2\lambda^2 - (\gamma+2v+2)^2\left\{\gamma + v\left[-1+\gamma+v(v+2)(\lambda^2-1)\right]\right\} = 0, \quad \text{(D.54)}$$

which can be rewritten as

$$\begin{aligned} 4v^5(\lambda^2-1) + 4v^4(\gamma+4)(\lambda^2-1) + v^3\left\{\gamma^2(\lambda^2-1) + 4\gamma(3\lambda^2-2) + \right. \\ \left. + \left[20 - (\alpha-\beta)^2\right]\lambda^2 - 24\right\} + 2v^2\left\{\gamma^2(\lambda^2+1) + \left[4(\gamma+1) - 3(\alpha-\beta)^2\right]\lambda^2 - 8\right\} + \\ v\left[\gamma^3 + 7\gamma^2 + 8\gamma - 12(\alpha-\beta)^2\lambda^2 - 4\right] + \gamma^3 + 4\gamma^2 + 4\gamma - 8(\alpha-\beta)^2 = 0. \end{aligned} \quad \text{(D.55)}$$

Note that Eq. (D.55) is valid for an arbitrary value of λ. In the limit $\lambda \to 1^-$, the phase transition corresponds to the change of sign in the term $\propto v^3$. This term is equal to zero when

$$\gamma = 1 + \frac{(\alpha-\beta)^2}{4}, \quad \text{(D.56)}$$

using which we obtain the critical condition on γ,

$$\gamma_c = \frac{1/2 - \sqrt{b(1-b)}}{(b-1/2)^2}, \quad \text{(D.57)}$$

i.e. Eq. (5.80) of the main text. Using Eq. (D.55), we derive the asymptotics (5.79) of v in the limit $\lambda \to 1^-$,

$$v_-|_{\lambda\to 1^-} = \begin{cases} O(1),\ \gamma < \gamma_c, \\ \sqrt[3]{\dfrac{\gamma^2 - 4(\gamma-1)}{2(1-\lambda)}},\ \gamma = \gamma_c, \\ \sqrt{\dfrac{4(\gamma-1) - \gamma^2(2b-1)^2}{8(1-\lambda)}},\ \gamma > \gamma_c. \end{cases} \tag{D.58}$$

Plugging Eqs. (D.48) and (D.49) into expression (5.71) for $\Gamma_2(\lambda)$ and making use of identity (D.51), we obtain expression (5.81) for $\Gamma_2(\lambda)$ in terms of v,

$$\Gamma_2(\lambda) = \frac{v(v+1) - \gamma}{\beta(v+2)}, \tag{D.59}$$

combining which with the results for $v_-|_{\lambda\to 1^-}$ yields the asymptotics of $\Gamma_2(\lambda)$ in the limit $\lambda \to 1^-$:

$$\sqrt{1-\lambda}\Gamma_2(\lambda)|_{\lambda\to 1^-} = \begin{cases} 0,\ \gamma < \gamma_c, \\ \sqrt{\dfrac{4(\gamma-1) - \gamma^2(2b-1)^2}{8\gamma^2 b^2}},\ \gamma > \gamma_c. \end{cases} \tag{D.60}$$

This is Eq. (5.82) of the main text.

D.9 Dynamics of the purity and the Floquet trajectory probability under the evolution of W_1^k operator

Since $W_1 = P_0 - W_0$, the eigenvalue 0 transition for W_0 corresponds to the eigenvalue 1 transition for W_1. Thus, the transition studied in Section 5.5 can be revealed by considering the dynamics of physical quantities evolving under W_1^k operator. Similarly to Section 5.7 of the main text, here we study the purity of an initially completely mixed state,

$$\mathrm{Tr}[\rho_{k,1}^2] = \frac{\mathrm{Tr}[W_1^{4k}]}{\mathrm{Tr}[W_1^{2k}]^2}, \tag{D.61}$$

and the probability to measure the W_1^k Floquet trajectory given the intrinsic randomness in the measurement outcomes,

$$p_{k,1} = \mathrm{Tr}[P_0 W_1^{2k} \rho_0], \tag{D.62}$$

as physical quantities of interest. Figure D.2 depicts the numerically calculated purity (D.61) for $b = 0.5$ and various values of γ, N, while Fig. D.3 shows the numerically calculated probability (D.62) for a pure and a completely mixed initial state at $k = 0$. In the main text we have shown that the spectrum of W_0 does not exhibit two gapped phases at the eigenvalue 0, instead showing signatures of a gapped and a gapless phase. For this reason, contrary to Figs. 5.6,5.7 of the main text, Figs. D.2,D.3 do not reveal one of the gapped phases where an initially mixed state fails to purify, and the probability $p_{k,1}$ saturates at a nonzero value as k increases. Instead, Figs. D.2,D.3 demonstrate signatures only of the gapped phase without the eigenvalue 1 (in the spectrum of W_1) and the critical phase with the closed gap. For the mixed state purification dynamics,

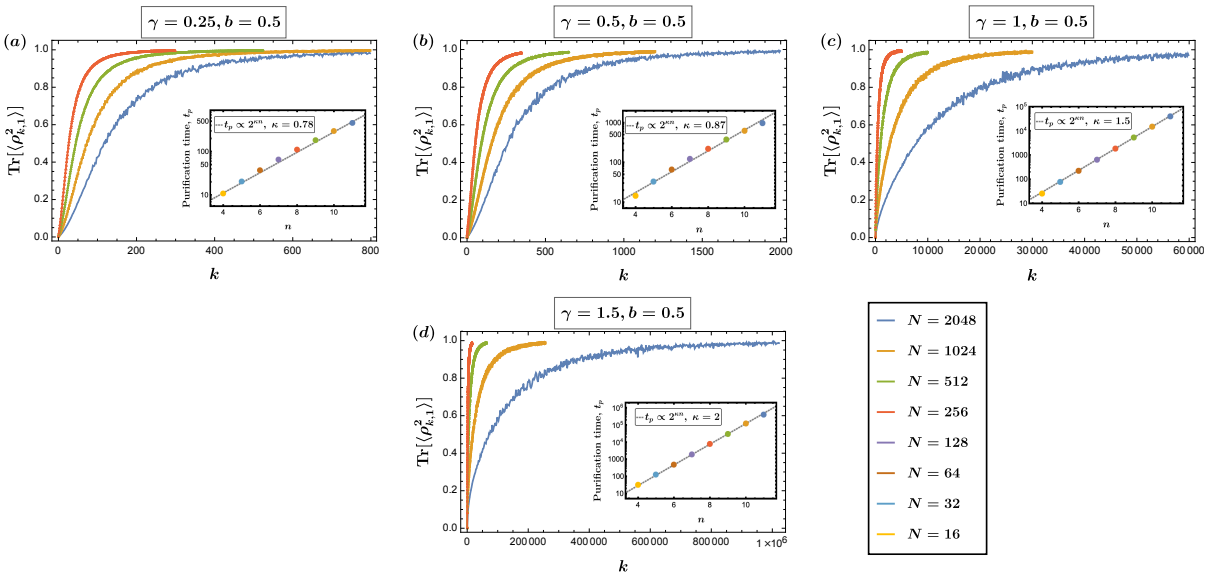

Figure D.2: Numerically calculated purity (D.61) of an initially completely mixed state plotted as a function of a Floquet cycle k for $b = 0.5$ and various values of γ, N, when the cycle evolution is described by a non-unitary operator W_1. The insets depict the purification time $t_p = \min\left[k \middle| \mathrm{Tr}\langle\rho^2_{k,0}\rangle > 0.95\right]$ as a function of the number of qubits $n = \log_2 N$ in the system. In (a) the averaging is performed over 10000 random matrix realizations for $N = 16, 32, 64, 128, 256$; 5000 realizations for $N = 512$; 1000 realizations for $N = 1024$; and 200 realizations for $N = 2048$. In (b) the averaging is performed over 10000 random matrix realizations for $N = 16, 32, 64, 128, 256$; 5000 realizations for $N = 512$; 1000 realizations for $N = 1024$; and 150 realizations for $N = 2048$. In (c) and (d) the averaging is performed over 1000 random matrix realizations for $N = 16, 32, 64, 128, 256, 512$; 500 realizations for $N = 1024$; and 100 realizations for $N = 2048$.

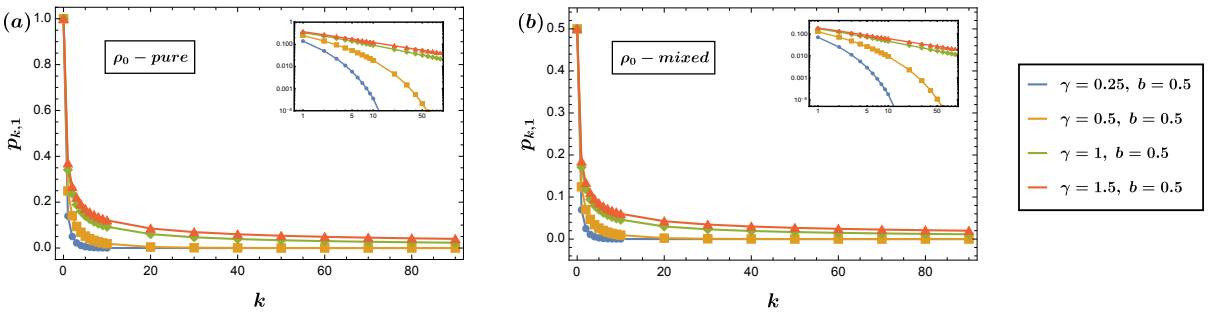

Figure D.3: (a),(b) Numerically calculated probability (D.62) of the Floquet quantum trajectory, representing the evolution under W_1^k, plotted as a function of a time step k for $b = 0.5$ and various values of γ, when the initial state at $k = 0$ is (a) pure and (b) completely mixed. The insets in the figures are log-log versions of the corresponding curves. Dimensionality of the Hilbert space is $N = 2048$. The averaging is performed over 320 random matrix realizations.

within the gapped phase the purification time seems to increases sub-exponentially with the system size, similarly to the case of W_0^k in the main text, although more studies are necessary to make a final conclusion on the t_p vs n scaling behavior within this phase. At the gapped-gapless phase transition critical point, Fig. D.2 suggests the purification time that scales exponentially with the system size as $t_p \propto 2^{1.5n}$, and within the gapless phase the scaling is exponential as well, $t_p \propto 2^{2n}$. At the same time, Fig. D.3 illustrates that the probability (D.62) decays with time in both the gapped and the gapless phases: the decay is exponential within the gapped phase and power-law within the gapless phase.

Bibliography

[1] R. P. Feynman, *Simulating physics with computers*, *International Journal of Theoretical Physics* **21** (1982), no. 6-7 467–488, [9508027].

[2] S. Aaronson, *How much structure is needed for huge quantum speedups?*, 2022.

[3] M. A. Nielsen and I. L. Chuang, *Quantum Computation and Quantum Information: 10th Anniversary Edition*. Cambridge University Press, USA, 10th ed., 2011.

[4] P. Shor, *Algorithms for quantum computation: discrete logarithms and factoring*, in *Proceedings 35th Annual Symposium on Foundations of Computer Science*, pp. 124–134, IEEE Comput. Soc. Press, 1994. 9605043.

[5] M. H. Freedman, A. Kitaev, and Z. Wang, *Simulation of topological field theories by quantum computers*, *Communications in Mathematical Physics* **227** (jan, 2002) 587–603, [0001071].

[6] L. K. Grover, *Quantum mechanics helps in searching for a needle in a haystack*, *Physical Review Letters* **79** (1997), no. 2 325–328, [9706033].

[7] E. Farhi, J. Goldstone, and S. Gutmann, *A quantum approximate optimization algorithm*, 2014.

[8] J. Preskill, *Quantum Computing in the NISQ era and beyond*, *Quantum* **2** (Aug., 2018) 79.

[9] F. Arute, K. Arya, R. Babbush, D. Bacon, J. C. Bardin, R. Barends, R. Biswas, S. Boixo, F. G. S. L. Brandao, D. A. Buell, B. Burkett, Y. Chen, Z. Chen, B. Chiaro, R. Collins, W. Courtney, A. Dunsworth, E. Farhi, B. Foxen, A. Fowler, C. Gidney, M. Giustina, R. Graff, K. Guerin, S. Habegger, M. P. Harrigan, M. J. Hartmann, A. Ho, M. Hoffmann, T. Huang, T. S. Humble, S. V. Isakov, E. Jeffrey, Z. Jiang, D. Kafri, K. Kechedzhi, J. Kelly, P. V. Klimov, S. Knysh, A. Korotkov, F. Kostritsa, D. Landhuis, M. Lindmark, E. Lucero, D. Lyakh, S. Mandrà, J. R. McClean, M. McEwen, A. Megrant, X. Mi, K. Michielsen, M. Mohseni, J. Mutus, O. Naaman, M. Neeley, C. Neill, M. Y. Niu, E. Ostby, A. Petukhov, J. C. Platt, C. Quintana, E. G. Rieffel, P. Roushan, N. C. Rubin,

D. Sank, K. J. Satzinger, V. Smelyanskiy, K. J. Sung, M. D. Trevithick, A. Vainsencher, B. Villalonga, T. White, Z. J. Yao, P. Yeh, A. Zalcman, H. Neven, and J. M. Martinis, *Quantum supremacy using a programmable superconducting processor*, *Nature* **574** (Oct, 2019) 505–510.

[10] C. Nayak, S. H. Simon, A. Stern, M. Freedman, and S. Das Sarma, *Non-Abelian anyons and topological quantum computation*, *Reviews of Modern Physics* **80** (2008), no. 3 1083–1159, [arXiv:0707.1889].

[11] J. Alicea, *New directions in the pursuit of Majorana fermions in solid state systems*, *Reports on Progress in Physics* **75** (2012), no. 7 76501, [arXiv:1202.1293].

[12] A. Khindanov, J. Alicea, P. Lee, W. S. Cole, and A. E. Antipov, *Topological superconductivity in nanowires proximate to a diffusive superconductor–magnetic-insulator bilayer*, *Phys. Rev. B* **103** (Apr, 2021) 134506.

[13] G. P. Mazur, N. van Loo, J.-Y. Wang, T. Dvir, G. Wang, A. Khindanov, S. Korneychuk, F. Borsoi, R. C. Dekker, G. Badawy, P. Vinke, S. Gazibegovic, E. P. A. M. Bakkers, M. Q. Prez, S. Heedt, and L. P. Kouwenhoven, *Spin-mixing enhanced proximity effect in aluminum-based superconductorsemiconductor hybrids*, *Advanced Materials* **34** (2022), no. 33 2202034, [https://onlinelibrary.wiley.com/doi/pdf/10.1002/adma.202202034].

[14] A. Khindanov, D. Pikulin, and T. Karzig, *Visibility of noisy quantum dot-based measurements of Majorana qubits*, *SciPost Phys.* **10** (2021) 127.

[15] A. Khindanov, T. Karzig, R. Lutchyn, and D. Pikulin, *Effects of coupling between quantum dot and quasiparticle continuum modes in topological superconductor-quantum dot-topological superconductor junctions*, *in preparation.*

[16] A. Khindanov and I. Aleiner, *Random-matrix theory of a dynamical measurement-induced phase transition in nonlocal floquet quantum circuits*, *in preparation.*

[17] L. Fu and C. L. Kane, *Josephson current and noise at a superconductor/quantum-spin-hall-insulator/superconductor junction*, *Phys. Rev. B* **79** (Apr, 2009) 161408.

[18] L. Fu and C. L. Kane, *Superconducting Proximity Effect and Majorana Fermions at the Surface of a Topological Insulator*, *Physical Review Letters* **100** (2008), no. 9 096407, [arXiv:0707.1692].

[19] R. M. Lutchyn, J. D. Sau, and S. Das Sarma, *Majorana fermions and a topological phase transition in semiconductor-superconductor heterostructures*, *Physical Review Letters* **105** (feb, 2010) [arXiv:1002.4033].

[20] Y. Oreg, G. Refael, and F. Von Oppen, *Helical liquids and Majorana bound states in quantum wires*, *Physical Review Letters* **105** (mar, 2010) [arXiv:1003.1145].

[21] J. D. Sau, R. M. Lutchyn, S. Tewari, and S. Das Sarma, *Generic new platform for topological quantum computation using semiconductor heterostructures*, *Physical Review Letters* **104** (jul, 2010) [arXiv:0907.2239].

[22] S. Nadj-Perge, I. K. Drozdov, B. A. Bernevig, and A. Yazdani, *Proposal for realizing majorana fermions in chains of magnetic atoms on a superconductor*, *Phys. Rev. B* **88** (Jul, 2013) 020407.

[23] **Microsoft Quantum** Collaboration, M. Aghaee, A. Akkala, Z. Alam, R. Ali, A. Alcaraz Ramirez, M. Andrzejczuk, A. E. Antipov, P. Aseev, M. Astafev, B. Bauer, J. Becker, S. Boddapati, F. Boekhout, J. Bommer, T. Bosma, L. Bourdet, S. Boutin, P. Caroff, L. Casparis, M. Cassidy, S. Chatoor, A. W. Christensen, N. Clay, W. S. Cole, F. Corsetti, A. Cui, P. Dalampiras, A. Dokania, G. de Lange, M. de Moor, J. C. Estrada Saldaña, S. Fallahi, Z. H. Fathabad, J. Gamble, G. Gardner, D. Govender, F. Griggio, R. Grigoryan, S. Gronin, J. Gukelberger, E. B. Hansen, S. Heedt, J. Herranz Zamorano, S. Ho, U. L. Holgaard, H. Ingerslev, L. Johansson, J. Jones, R. Kallaher, F. Karimi, T. Karzig, C. King, M. E. Kloster, C. Knapp, D. Kocon, J. Koski, P. Kostamo, P. Krogstrup, M. Kumar, T. Laeven, T. Larsen, K. Li, T. Lindemann, J. Love, R. Lutchyn, M. H. Madsen, M. Manfra, S. Markussen, E. Martinez, R. McNeil, E. Memisevic, T. Morgan, A. Mullally, C. Nayak, J. Nielsen, W. H. P. Nielsen, B. Nijholt, A. Nurmohamed, E. O'Farrell, K. Otani, S. Pauka, K. Petersson, L. Petit, D. I. Pikulin, F. Preiss, M. Quintero-Perez, M. Rajpalke, K. Rasmussen, D. Razmadze, O. Reentila, D. Reilly, R. Rouse, I. Sadovskyy, L. Sainiemi, S. Schreppler, V. Sidorkin, A. Singh, S. Singh, S. Sinha, P. Sohr, T. c. v. Stankevič, L. Stek, H. Suominen, J. Suter, V. Svidenko, S. Teicher, M. Temuerhan, N. Thiyagarajah, R. Tholapi, M. Thomas, E. Toomey, S. Upadhyay, I. Urban, S. Vaitiekėnas, K. Van Hoogdalem, D. Van Woerkom, D. V. Viazmitinov, D. Vogel, S. Waddy, J. Watson, J. Weston, G. W. Winkler, C. K. Yang, S. Yau, D. Yi, E. Yucelen, A. Webster, R. Zeisel, and R. Zhao, *Inas-al hybrid devices passing the topological gap protocol*, *Phys. Rev. B* **107** (Jun, 2023) 245423.

[24] D. I. Pikulin, B. van Heck, T. Karzig, E. A. Martinez, B. Nijholt, T. Laeven, G. W. Winkler, J. D. Watson, S. Heedt, M. Temurhan, V. Svidenko, R. M. Lutchyn, M. Thomas, G. de Lange, L. Casparis, and C. Nayak, *Protocol to identify a topological superconducting phase in a three-terminal device*, 2021.

[25] H. Pan and S. D. Sarma, *Physical mechanisms for zero-bias conductance peaks in majorana nanowires*, *Physical Review Research* **2** (2020), no. 1 013377.

[26] T. D. Stanescu, R. M. Lutchyn, and S. Das Sarma, *Majorana fermions in semiconductor nanowires*, *Phys. Rev. B - Condens. Matter Mater. Phys.* **84** (oct, 2011) 144522, [arXiv:1106.3078].

[27] A. E. Antipov, A. Bargerbos, G. W. Winkler, B. Bauer, E. Rossi, and R. M. Lutchyn, *Effects of Gate-Induced Electric Fields on Semiconductor Majorana Nanowires*, *Phys. Rev. X* **8** (aug, 2018) 31041, [arXiv:1801.0261].

[28] R. M. Lutchyn, E. P. A. M. Bakkers, L. P. Kouwenhoven, P. Krogstrup, C. M. Marcus, and Y. Oreg, *Majorana zero modes in superconductorsemiconductor heterostructures*, *Nature Reviews Materials* **3** (may, 2018) 52–68.

[29] M. Tinkham, *Introduction to Superconductivity*. Dover, 2nd ed., 2004.

[30] B. S. Chandrasekhar, *A note on the maximum critical field of high-field superconductors*, *Appl. Phys. Lett.* **1** (sep, 1962) 7–8.

[31] A. M. Clogston, *Upper limit for the critical field in hard superconductors*, *Phys. Rev. Lett.* **9** (sep, 1962) 266–267.

[32] Y. Liu, A. Luchini, S. Martí-Sánchez, C. Koch, S. Schuwalow, S. A. Khan, T. Stankevič, S. Francoual, J. R. Mardegan, J. A. Krieger, V. N. Strocov, J. Stahn, C. A. Vaz, M. Ramakrishnan, U. Staub, K. Lefmann, G. Aeppli, J. Arbiol, and P. Krogstrup, *Coherent Epitaxial Semiconductor-Ferromagnetic Insulator InAs/EuS Interfaces: Band Alignment and Magnetic Structure*, *ACS Appl. Mater. Interfaces* **12** (feb, 2020) 8780–8787, [arXiv:1908.0709].

[33] S. Vaitieknas, Y. Liu, P. Krogstrup, and C. M. Marcus, *Zero-bias peaks at zero magnetic field in ferromagnetic hybrid nanowires*, *Nat. Phys.* (sep, 2020).

[34] Y. Liu, S. Vaitieknas, S. Martí-Sánchez, C. Koch, S. Hart, Z. Cui, T. Kanne, S. A. Khan, R. Tanta, S. Upadhyay, M. E. Cachaza, C. M. Marcus, J. Arbiol, K. A. Moler, and P. Krogstrup, *Semiconductor-Ferromagnetic Insulator-Superconductor Nanowires: Stray Field and Exchange Field*, *Nano Lett.* **20** (jan, 2020) 456–462, [arXiv:1910.0336].

[35] B. D. Woods and T. D. Stanescu, *Electrostatic effects and topological superconductivity in semiconductor-superconductor-magnetic insulator hybrid wires*, arXiv:2011.0193.

[36] C.-X. Liu, S. Schuwalow, Y. Liu, K. Vilkelis, A. L. R. Manesco, P. Krogstrup, and M. Wimmer, *Electronic properties of InAs/EuS/Al hybrid nanowires*, arXiv:2011.0656.

[37] S. D. Escribano, E. Prada, Y. Oreg, and A. L. Yeyati, *Microscopic analysis of topological superconductivity in ferromagnetic hybrid nanowires*, arXiv:2011.0656.

[38] A. Maiani, R. Seoane Souto, M. Leijnse, and K. Flensberg, *Topological superconductivity in semiconductor–superconductor–magnetic-insulator heterostructures*, *Phys. Rev. B* **103** (Mar, 2021) 104508.

[39] K. Pöyhönen, D. Varjas, M. Wimmer, and A. R. Akhmerov, *Minimal Zeeman field requirement for a topological transition in superconductors*, arXiv:2011.0826.

[40] J. Langbehn, S. A. Gonzalez, P. W. Brouwer, and F. von Oppen, *Topological superconductivity in tripartite superconductor-ferromagnet-semiconductor nanowires*, arXiv:2012.0005.

[41] P. M. Tedrow, J. E. Tkaczyk, and A. Kumar, *Spin-polarized electron tunneling study of an artificially layered superconductor with internal magnetic field: EuO-Al*, *Phys. Rev. Lett.* **56** (apr, 1986) 1746–1749.

[42] X. Hao, J. S. Moodera, and R. Meservey, *Thin-film superconductor in an exchange field*, *Phys. Rev. Lett.* **67** (sep, 1991) 1342–1345.

[43] M. J. Wolf, C. Sürgers, G. Fischer, and D. Beckmann, *Spin-polarized quasiparticle transport in exchange-split superconducting aluminum on europium sulfide*, *Phys. Rev. B* **90** (oct, 2014) 144509, [arXiv:1408.0176].

[44] E. Strambini, V. N. Golovach, G. De Simoni, J. S. Moodera, F. S. Bergeret, and F. Giazotto, *Revealing the magnetic proximity effect in EuS/Al bilayers through superconducting tunneling spectroscopy*, *Phys. Rev. Mater.* **1** (oct, 2017) 54402, [arXiv:1705.0479].

[45] A. Hijano, S. Ilić, M. Rouco, C. G. Orellana, M. Ilyn, C. Rogero, P. Virtanen, T. T. Heikkilä, S. Khorshidian, M. Spies, F. Giazotto, E. Strambini, and F. S. Bergeret, *Coexistence of superconductivity and spin-splitting fields in superconductor/ferromagnetic insulator bilayers of arbitrary thickness*, arXiv:2012.1554.

[46] J. D. Sau, S. Tewari, and S. Das Sarma, *Experimental and materials considerations for the topological superconducting state in electron- and hole-doped semiconductors: Searching for non-Abelian Majorana modes in 1D nanowires and 2D heterostructures*, *Phys. Rev. B - Condens. Matter Mater. Phys.* **85** (feb, 2012) 064512, [arXiv:1111.2054].

[47] D. A. Ivanov and Y. V. Fominov, *Minigap in superconductor-ferromagnet junctions with inhomogeneous magnetization*, *Phys. Rev. B - Condens. Matter Mater. Phys.* **73** (jun, 2006) 214524, [0511299].

[48] F. S. Bergeret, A. F. Volkov, and K. B. Efetov, *Odd triplet superconductivity and related phenomena in superconductor- ferromagnet structures*, *Rev. Mod. Phys.* **77** (oct, 2005) 1321–1373, [0506047].

[49] D. Gall, *Electron mean free path in elemental metals*, *J. Appl. Phys.* **119** (feb, 2016) 085101.

[50] J. Romijn, T. M. Klapwijk, M. J. Renne, and J. E. Mooij, *Critical pair-breaking current in superconducting aluminum strips far below Tc*, *Phys. Rev. B* **26** (oct, 1982) 3648–3655.

[51] L. Gorkov, *On the energy spectrum of superconductors*, *Sov. Phys. JETP* **34** (1958), no. 7 505.

[52] G. Eilenberger, *Transformation of Gorkov's equation for type II superconductors into transport-like equations*, *Zeitschrift für Phys.* **214** (apr, 1968) 195–213.

[53] A. Larkin and Y. Ovchinnikov, *Quasiclassical Method in the Theory of Superconductivity*, *Sov Phys JETP* **28** (1969), no. 6 1200–1205.

[54] J. A. X. Alexander, T. P. Orlando, D. Rainer, and P. M. Tedrow, *Theory of Fermi-liquid effects in high-field tunneling*, *Phys. Rev. B* **31** (may, 1985) 5811–5825.

[55] E. A. Demler, G. B. Arnold, and M. R. Beasley, *Superconducting proximity effects in magnetic metals*, *Phys. Rev. B* **55** (jun, 1997) 15174–15182.

[56] F. Aikebaier, P. Virtanen, and T. Heikkilä, *Superconductivity near a magnetic domain wall*, *Phys. Rev. B* **99** (mar, 2019) 104504, [arXiv:1812.0841].

[57] T. Kiendl, F. Von Oppen, and P. W. Brouwer, *Proximity-induced gap in nanowires with a thin superconducting shell*, *Phys. Rev. B* **100** (jul, 2019) 035426, [arXiv:1902.0979].

[58] D. E. Liu, E. Rossi, and R. M. Lutchyn, *Impurity-induced states in superconducting heterostructures*, *Phys. Rev. B* **97** (apr, 2018) 161408, [arXiv:1711.0405].

[59] P. G. de Gennes, *Superconductivity of Metals and Alloys*. CRC Press, 1st ed., 1999.

[60] K. Maki, *The Behavior of Superconducting Thin Films in the Presence of Magnetic Fields and Currents*)*, *Progress of Theoretical Physics* **31** (05, 1964) 731–741, [https://academic.oup.com/ptp/article-pdf/31/5/731/5322574/31-5-731.pdf].

[61] R. Meservey and P. Tedrow, *Spin-polarized electron tunneling*, *Phys. Rep.* **238** (1994), no. 4 173–243.

[62] P. Monceau, *Resistive transitions of superconducting thin films in strong electric fields*, *Phys. Lett. A* **47** (1974), no. 3 193–194.

[63] P. M. Tedrow and R. Meservey, *Critical magnetic field of very thin superconducting aluminum films*, *Phys. Rev. B* **25** (Jan, 1982) 171–178.

[64] X. S. Wu, P. W. Adams, Y. Yang, and R. L. McCarley, *Spin proximity effect in ultrathin superconducting Be-Au bilayers*, *Phys. Rev. Lett.* **96** (Mar, 2006) 127002.

[65] J. Alexander, T. Orlando, D. Rainer, and P. Tedrow, *Theory of fermi-liquid effects in high-field tunneling*, *Phys. Rev. B* **31** (1985), no. 9 5811.

[66] W. Wu and P. Adams, *Avalanches and slow relaxation: dynamics of ultrathin granular superconducting films in a parallel magnetic field*, *Phys. Rev. Lett.* **74** (1995), no. 4 610.

[67] L. D. Alegria, C. G. Bøttcher, A. K. Saydjari, A. T. Pierce, S. H. Lee, S. P. Harvey, U. Vool, and A. Yacoby, *High-energy quasiparticle injection into mesoscopic superconductors*, *Nat. Nanotechnol.* **16** (2021), no. 4 404–408.

[68] A. Cottet, D. Huertas-Hernando, W. Belzig, and Y. V. Nazarov, *Spin-dependent boundary conditions for isotropic superconducting Green's functions*, *Phys. Rev. B* **80** (nov, 2009) 184511.

[69] T. Tokuyasu, J. A. Sauls, and D. Rainer, *Proximity effect of a ferromagnetic insulator in contact with a superconductor*, *Phys. Rev. B* **38** (nov, 1988) 8823–8833.

[70] A. C. Potter and P. A. Lee, *Engineering a p+ip superconductor: Comparison of topological insulator and Rashba spin-orbit-coupled materials*, *Phys. Rev. B - Condens. Matter Mater. Phys.* **83** (may, 2011) 184520, [arXiv:1103.2129].

[71] R. M. Lutchyn, T. D. Stanescu, and S. Das Sarma, *Momentum relaxation in a semiconductor proximity-coupled to a disordered s-wave superconductor: Effect of scattering on topological superconductivity*, *Phys. Rev. B - Condens. Matter Mater. Phys.* **85** (apr, 2012) 140513, [arXiv:1110.5643].

[72] G. Sarma, *On the influence of a uniform exchange field acting on the spins of the conduction electrons in a superconductor*, *J. Phys. Chem. Solids* **24** (1963), no. 8 1029–1032.

[73] R. C. Bruno and B. B. Schwartz, *Magnetic field splitting of the density of states of thin superconductors*, *Phys. Rev. B* **8** (oct, 1973) 3161–3178.

[74] F. S. Bergeret, M. Silaev, P. Virtanen, and T. T. Heikkilä, *Colloquium: Nonequilibrium effects in superconductors with a spin-splitting field*, *Rev. Mod. Phys.* **90** (oct, 2018) 041001.

[75] T. T. Heikkilä, M. Silaev, P. Virtanen, and F. S. Bergeret, *Thermal, electric and spin transport in superconductor/ferromagnetic-insulator structures*, *Progress in Surface Science* **94** (Aug, 2019) 100540.

[76] A. Y. Kitaev, *Unpaired Majorana fermions in quantum wires*, *Physics-Uspekhi* **44** (oct, 2001) 131–136.

[77] C. Beenakker, *Search for Majorana Fermions in Superconductors*, *Annual Review of Condensed Matter Physics* **4** (apr, 2013) 113.

[78] V. Mourik, K. Zuo, S. M. Frolov, S. R. Plissard, E. P. A. M. Bakkers, and L. P. Kouwenhoven, *Signatures of Majorana fermions in hybrid superconductor-semiconductor nanowire devices.*, *Science* **336** (may, 2012) 1003.

[79] M. T. Deng, C. L. Yu, G. Y. Huang, M. Larsson, P. Caroff, and H. Q. Xu, *Anomalous Zero-Bias Conductance Peak in a NbInSb NanowireNb Hybrid Device*, *Nano Letters* **12** (dec, 2012) 6414.

[80] A. Das, Y. Ronen, Y. Most, Y. Oreg, M. Heiblum, and H. Shtrikman, *Zero-bias peaks and splitting in an AlInAs nanowire topological superconductor as a signature of Majorana fermions*, *Nature Physics* **8** (dec, 2012) 887.

[81] H. O. H. Churchill, V. Fatemi, K. Grove-Rasmussen, M. T. Deng, P. Caroff, H. Q. Xu, and C. M. Marcus, *Superconductor-nanowire devices from tunneling to the multichannel regime: Zero-bias oscillations and magnetoconductance crossover*, *Physical Review B* **87** (jun, 2013) 241401.

[82] A. D. K. Finck, D. J. Van Harlingen, P. K. Mohseni, K. Jung, and X. Li, *Anomalous Modulation of a Zero-Bias Peak in a Hybrid Nanowire-Superconductor Device*, *Physical Review Letters* **110** (mar, 2013) 126406.

[83] F. Nichele, A. C. Drachmann, A. M. Whiticar, E. C. O'Farrell, H. J. Suominen, A. Fornieri, T. Wang, G. C. Gardner, C. Thomas, A. T. Hatke, P. Krogstrup, M. J. Manfra, K. Flensberg, and C. M. Marcus, *Scaling of Majorana Zero-Bias Conductance Peaks*, *Physical Review Letters* **119** (sep, 2017) 136803.

[84] H. Zhang, C.-X. Liu, S. Gazibegovic, D. Xu, J. A. Logan, G. Wang, N. van Loo, J. D. S. Bommer, M. W. A. de Moor, D. Car, R. L. M. Op het Veld, P. J. van Veldhoven, S. Koelling, M. A. Verheijen, M. Pendharkar, D. J. Pennachio, B. Shojaei, J. S. Lee, C. J. Palmstrøm, E. P. A. M. Bakkers, S. D. Sarma, and L. P. Kouwenhoven, *Quantized Majorana conductance*, *Nature* **556** (apr, 2018) 74.

[85] L. P. Rokhinson, X. Liu, and J. K. Furdyna, *The fractional a.c. Josephson effect in a semiconductorsuperconductor nanowire as a signature of Majorana particles*, *Nature Physics* **8** (nov, 2012) 795.

[86] R. S. Deacon, J. Wiedenmann, E. Bocquillon, F. Domínguez, T. M. Klapwijk, P. Leubner, C. Brüne, E. M. Hankiewicz, S. Tarucha, K. Ishibashi, H. Buhmann, and L. W. Molenkamp, *Josephson radiation from gapless andreev bound states in HgTe-based topological junctions*, *Physical Review X* **7** (apr, 2017) 021011.

[87] D. Laroche, D. Bouman, D. J. van Woerkom, A. Proutski, C. Murthy, D. I. Pikulin, C. Nayak, R. J. J. van Gulik, J. Nygård, P. Krogstrup, L. P. Kouwenhoven, and A. Geresdi, *Observation of the 4π-periodic Josephson effect in indium arsenide nanowires*, *Nature Communications* **10** (dec, 2019) 245.

[88] S. M. Albrecht, A. P. Higginbotham, M. Madsen, F. Kuemmeth, T. S. Jespersen, J. Nygård, P. Krogstrup, and C. M. Marcus, *Exponential protection of zero modes in Majorana islands*, *Nature* **531** (mar, 2016) 206.

[89] S. Vaitiekėnas, G. W. Winkler, B. van Heck, T. Karzig, M.-T. Deng, K. Flensberg, L. I. Glazman, C. Nayak, P. Krogstrup, R. M. Lutchyn, and C. M. Marcus, *Flux-induced topological superconductivity in full-shell nanowires*, *Science* **367** (2020), no. 6485 eaav3392.

[90] D. M. van Zanten, D. Sabonis, J. Suter, J. I. Väyrynen, T. Karzig, D. I. Pikulin, E. C. O'Farrell, D. Razmadze, K. D. Petersson, P. Krogstrup, and C. M. Marcus, *Photon-assisted tunnelling of zero modes in a Majorana wire*, *Nature Physics* **16** (apr, 2020) 663.

[91] J. Liu, A. C. Potter, K. T. Law, and P. A. Lee, *Zero-bias peaks in the tunneling conductance of spin-orbit-coupled superconducting wires with and without Majorana end-states*, *Physical Review Letters* **109** (dec, 2012) 267002.

[92] D. I. Pikulin, J. P. Dahlhaus, M. Wimmer, H. Schomerus, and C. W. J. Beenakker, *A zero-voltage conductance peak from weak antilocalization in a Majorana nanowire*, *New Journal of Physics* **14** (2012) 125011.

[93] G. Kells, D. Meidan, and P. W. Brouwer, *Near-zero-energy end states in topologically trivial spin-orbit coupled superconducting nanowires with a smooth confinement*, *Physical Review B* **86** (sep, 2012) 100503.

[94] C. X. Liu, J. D. Sau, T. D. Stanescu, and S. Das Sarma, *Andreev bound states versus Majorana bound states in quantum dot-nanowire-superconductor hybrid structures: Trivial versus topological zero-bias conductance peaks*, *Physical Review B* **96** (aug, 2017) 075161.

[95] A. Vuik, B. Nijholt, A. R. Akhmerov, and M. Wimmer, *Reproducing topological properties with quasi-Majorana states*, *SciPost Physics* **7** (2019) 061.

[96] D. I. Pikulin and Y. V. Nazarov, *Phenomenology and dynamics of a Majorana Josephson junction*, *Physical Review B* **86** (oct, 2012) 140504.

[97] P. San-Jose, E. Prada, and R. Aguado, *ac Josephson effect in finite-length nanowire junctions with majorana modes*, *Physical Review Letters* **108** (jun, 2012) 257001.

[98] P. San-Jose, J. Cayao, E. Prada, and R. Aguado, *Majorana bound states from exceptional points in non-topological superconductors*, *Scientific Reports* **6** (2016) 21427.

[99] J. Alicea, Y. Oreg, G. Refael, F. von Oppen, and M. Fisher, *Non-abelian anyons and topological quantum information processing in ID wire networks*, *Nature Physics* **7** (2011), no. 5 2011.

[100] P. Bonderson, M. Freedman, and C. Nayak, *Measurement-Only Topological Quantum Computation*, *Physical Review Letters* **101** (2008) 010501.

[101] P. Bonderson, M. Freedman, and C. Nayak, *Measurement-only topological quantum computation via anyonic interferometry*, *Annals of Physics* **324** (apr, 2009) 787.

[102] K. Flensberg, *Non-Abelian Operations on Majorana Fermions via Single-Charge Control*, *Physical Review Letters* **106** (2011) 090503.

[103] T. Hyart, B. Van Heck, I. C. Fulga, M. Burrello, A. R. Akhmerov, and C. W. Beenakker, *Flux-controlled quantum computation with Majorana fermions*, *Physical Review B* **88** (jul, 2013) 035121.

[104] D. Aasen, M. Hell, R. V. Mishmash, A. Higginbotham, J. Danon, M. Leijnse, T. S. Jespersen, J. A. Folk, C. M. Marcus, K. Flensberg, and J. Alicea, *Milestones toward Majorana-based quantum computing*, *Physical Review X* **6** (aug, 2016) 031016.

[105] S. Plugge, A. Rasmussen, R. Egger, and K. Flensberg, *Majorana box qubits*, *New Journal of Physics* **19** (jan, 2017) 012001.

[106] T. Karzig, C. Knapp, R. M. Lutchyn, P. Bonderson, M. B. Hastings, C. Nayak, J. Alicea, K. Flensberg, S. Plugge, Y. Oreg, C. M. Marcus, and M. H. Freedman, *Scalable designs for quasiparticle-poisoning-protected topological quantum computation with Majorana zero modes*, *Physical Review B* **95** (2017) 235305.

[107] A. L. Grimsmo and T. B. Smith, *Majorana qubit readout using longitudinal qubit-resonator interaction*, *Physical Review B* **99** (jun, 2019) 235420.

[108] G. Széchenyi and A. Pályi, *Parity-to-charge conversion for readout of topological Majorana qubits*, *Physical Review B* **101** (2020), no. 23 235441.

[109] J. Manousakis, C. Wille, A. Altland, R. Egger, K. Flensberg, and F. Hassler, *Weak Measurement Protocols for Majorana Bound State Identification*, *Physical Review Letters* **124** (mar, 2020) 096801.

[110] D. De Jong, J. Van Veen, L. Binci, A. Singh, P. Krogstrup, L. P. Kouwenhoven, W. Pfaff, and J. D. Watson, *Rapid detection of coherent tunneling in an in as nanowire quantum dot through dispersive gate sensing*, *Physical Review Applied* **11** (2019), no. 4 044061.

[111] J. van Veen, D. de Jong, L. Han, C. Prosko, P. Krogstrup, J. D. Watson, L. P. Kouwenhoven, and W. Pfaff, *Revealing charge-tunneling processes between a quantum dot and a superconducting island through gate sensing*, *Physical Review B* **100** (2019), no. 17 174508.

[112] C. Knapp, T. Karzig, R. M. Lutchyn, and C. Nayak, *Dephasing of Majorana-based qubits*, *Physical Review B* **97** (2018) 125404.

[113] P. P. Aseev, P. Marra, P. Stano, J. Klinovaja, and D. Loss, *Degeneracy lifting of majorana bound states due to electron-phonon interactions*, *Physical Review B* **99** (2019), no. 20 205435.

[114] M. I. Munk, R. Egger, and K. Flensberg, *Fidelity and visibility loss in majorana qubits by entanglement with environmental modes*, *Physical Review B* **99** (2019), no. 15 155419.

[115] J. F. Steiner and F. von Oppen, *Readout of majorana qubits*, *Phys. Rev. Research* **2** (Aug, 2020) 033255.

[116] M. I. K. Munk, J. Schulenborg, R. Egger, and K. Flensberg, *Parity-to-charge conversion in majorana qubit readout*, *Phys. Rev. Research* **2** (Aug, 2020) 033254.

[117] C. Buizert, F. H. L. Koppens, M. Pioro-Ladrière, H.-P. Tranitz, I. T. Vink, S. Tarucha, W. Wegscheider, and L. M. K. Vandersypen, *insitu reduction of charge noise in* GaAs/al$_x$ga$_{1-x}$As *schottky-gated devices*, *Phys. Rev. Lett.* **101** (Nov, 2008) 226603.

[118] K. D. Petersson, J. R. Petta, H. Lu, and A. C. Gossard, *Quantum Coherence in a One-Electron Semiconductor Charge Qubit*, *Physical Review Letters* **105** (2010) 246804.

[119] E. Paladino, Y. M. Galperin, G. Falci, and B. L. Altshuler, *1/f noise: Implications for solid-state quantum information*, *Reviews of Modern Physics* **86** (apr, 2014) 361.

[120] L. P. Rokhinson, X. Liu, and J. K. Furdyna, *The fractional a.c. Josephson effect in a semiconductor-superconductor nanowire as a signature of Majorana particles*, *Nature Physics* **8** (sep, 2012) 795.

[121] D. Puglia, E. A. Martinez, G. C. Ménard, A. Pöschl, S. Gronin, G. C. Gardner, R. Kallaher, M. J. Manfra, C. M. Marcus, A. P. Higginbotham, and L. Casparis, *Closing of the induced gap in a hybrid superconductor-semiconductor nanowire*, *Phys. Rev. B* **103** (Jun, 2021) 235201.

[122] M. Aghaee, A. Akkala, Z. Alam, R. Ali, A. A. Ramirez, M. Andrzejczuk, A. E. Antipov, M. Astafev, B. Bauer, J. Becker, S. Boddapati, F. Boekhout, J. Bommer, E. B. Hansen, T. Bosma, L. Bourdet, S. Boutin, P. Caroff, L. Casparis, M. Cassidy, A. W. Christensen, N. Clay, W. S. Cole, F. Corsetti, A. Cui, P. Dalampiras, A. Dokania, G. de Lange, M. de Moor, J. C. E. Saldaa, S. Fallahi, Z. H. Fathabad, J. Gamble, G. Gardner, D. Govender, F. Griggio, R. Grigoryan, S. Gronin, J. Gukelberger, S. Heedt, J. H. Zamorano, S. Ho, U. L. Holgaard, W. H. P. Nielsen, H. Ingerslev, P. J. Krogstrup, L. Johansson, J. Jones, R. Kallaher, F. Karimi, T. Karzig, C. King, M. E. Kloster, C. Knapp, D. Kocon, J. Koski, P. Kostamo, M. Kumar, T. Laeven, T. Larsen, K. Li, T. Lindemann, J. Love, R. Lutchyn, M. Manfra, E. Memisevic, C. Nayak, B. Nijholt, M. H. Madsen, S. Markussen, E. Martinez, R. McNeil, A. Mullally, J. Nielsen, A. Nurmohamed, E. O'Farrell, K. Otani, S. Pauka, K. Petersson, L. Petit, D. Pikulin, F. Preiss, M. Q. Perez, K. Rasmussen, M. Rajpalke, D. Razmadze, O. Reentila, D. Reilly, R. Rouse, I. Sadovskyy, L. Sainiemi, S. Schreppler, V. Sidorkin, A. Singh, S. Singh, S. Sinha, P. Sohr, L. Stek, H. Suominen, J. Suter, V. Svidenko, S. Teicher, M. Temuerhan, N. Thiyagarajah, R. Tholapi, M. Thomas, E. Toomey, S. Upadhyay, I. Urban, S. Vaitieknas, K. Van Hoogdalem, D. V. Viazmitinov, S. Waddy, D. Van Woerkom, D. Vogel, J. Watson, J. Weston, G. W. Winkler, C. K. Yang, S. Yau, D. Yi, E. Yucelen, A. Webster, R. Zeisel, and R. Zhao, *Inas-al hybrid devices passing the topological gap protocol*, 2022.

[123] T. B. Smith, M. C. Cassidy, D. J. Reilly, S. D. Bartlett, and A. L. Grimsmo, *Dispersive readout of majorana qubits*, *PRX Quantum* **1** (Nov, 2020) 020313.

[124] Z.-T. Zhang and D. E. Liu, *Readout of majorana bound states via landau-zener transition*, *Phys. Rev. B* **103** (May, 2021) 195401.

[125] S. Krøjer, R. Seoane Souto, and K. Flensberg, *Demonstrating majorana non-abelian properties using fast adiabatic charge transfer*, *Phys. Rev. B* **105** (Jan, 2022) 045425.

[126] J. Schulenborg, S. Krjer, M. Burrello, M. Leijnse, and K. Flensberg, *Detecting majorana modes by readout of poisoning-induced parity flips*, 2022.

[127] V. Derakhshan Maman, M. Gonzalez-Zalba, and A. Pályi, *Charge noise and overdrive errors in dispersive readout of charge, spin, and majorana qubits*, *Phys. Rev. Applied* **14** (Dec, 2020) 064024.

[128] A. Khindanov, D. Pikulin, and T. Karzig, *Visibility of noisy quantum dot-based measurements of Majorana qubits*, *SciPost Phys.* **10** (2021) 127.

[129] J. Schulenborg, M. Burrello, M. Leijnse, and K. Flensberg, *Multilevel effects in quantum dot based parity-to-charge conversion of majorana box qubits*, *Phys. Rev. B* **103** (Jun, 2021) 245407.

[130] L. N. Bulaevskiĭ, V. V. Kuziĭ, and A. A. Sobyanin, *Superconducting system with weak coupling to the current in the ground state*, *JETP Letters* **25** (1977), no. 7 290.

[131] L. e. I. Glazman and K. Matveev, *Resonant Josephson current through Kondo impurities in a tunnel barrier*, *Pis'ma Zh. Eksp. Teor. Fiz.* **49** (1989), no. 10 570–573.

[132] B. I. Spivak and S. A. Kivelson, *Negative local superfluid densities: The difference between dirty superconductors and dirty bose liquids*, *Phys. Rev. B* **43** (Feb, 1991) 3740–3743.

[133] A. V. Rozhkov, D. P. Arovas, and F. Guinea, *Josephson coupling through a quantum dot*, *Phys. Rev. B* **64** (Nov, 2001) 233301.

[134] J. A. van Dam, Y. V. Nazarov, E. P. A. M. Bakkers, S. De Franceschi, and L. P. Kouwenhoven, *Supercurrent reversal in quantum dots*, *Nature* **442** (2006) 667.

[135] H. I. Jrgensen, T. Novotn, K. Grove-Rasmussen, K. Flensberg, and P. E. Lindelof, *Critical current 0 transition in designed josephson quantum dot junctions*, *Nano Letters* **7** (Jul, 2007) 24412445.

[136] J.-Y. Wang, C. Schrade, V. Levajac, D. van Driel, K. Li, S. Gazibegovic, G. Badawy, R. L. M. O. h. Veld, J. S. Lee, M. Pendharkar, C. P. Dempsey, C. J. Palmstrm, E. P. A. M. Bakkers, L. Fu, L. P. Kouwenhoven, and J. Shen, *Supercurrent parity-meter in a nanowire cooper-pair transistor*, 2021.

[137] A. M. Whiticar, A. Fornieri, A. Banerjee, A. C. C. Drachmann, S. Gronin, G. C. Gardner, T. Lindemann, M. J. Manfra, and C. M. Marcus, *Zeeman-driven parity transitions in an andreev quantum dot*, *Phys. Rev. B* **103** (Jun, 2021) 245308.

[138] Z. Gao, W. J. Gong, S. F. Zhang, G. Y. Yi, and Y. S. Zheng, *Tunable fractional josephson effect in the topological superconducting junction with embedded quantum dots*, *Europhys. Lett.* **109** (feb, 2015) 40010.

[139] A. Camjayi, L. Arrachea, A. Aligia, and F. von Oppen, *Fractional spin and josephson effect in time-reversal-invariant topological superconductors*, *Phys. Rev. Lett.* **119** (Jul, 2017) 046801.

[140] C. Schrade and L. Fu, *Andreev or majorana, cooper finds out*, 2018.

[141] O. A. Awoga, J. Cayao, and A. M. Black-Schaffer, *Supercurrent detection of topologically trivial zero-energy states in nanowire junctions*, *Phys. Rev. Lett.* **123** (Sep, 2019) 117001.

[142] D. Razmadze, E. C. T. O'Farrell, P. Krogstrup, and C. M. Marcus, *Quantum dot parity effects in trivial and topological josephson junctions*, *Phys. Rev. Lett.* **125** (Sep, 2020) 116803.

[143] J. Schulenborg and K. Flensberg, *Absence of supercurrent sign reversal in a topological junction with a quantum dot*, *Phys. Rev. B* **101** (Jan, 2020) 014512.

[144] S. Tewari and J. D. Sau, *Topological invariants for spin-orbit coupled superconductor nanowires*, *Phys. Rev. Lett.* **109** (Oct, 2012) 150408.

[145] Y. Li, X. Chen, and M. P. A. Fisher, *Quantum zeno effect and the many-body entanglement transition*, *Phys. Rev. B* **98** (Nov, 2018) 205136.

[146] B. Skinner, J. Ruhman, and A. Nahum, *Measurement-induced phase transitions in the dynamics of entanglement*, *Phys. Rev. X* **9** (Jul, 2019) 031009.

[147] M. J. Gullans and D. A. Huse, *Dynamical purification phase transition induced by quantum measurements*, *Phys. Rev. X* **10** (Oct, 2020) 041020.

[148] L. Fidkowski, J. Haah, and M. B. Hastings, *How Dynamical Quantum Memories Forget*, *Quantum* **5** (Jan., 2021) 382.

[149] X. Cao, A. Tilloy, and A. D. Luca, *Entanglement in a fermion chain under continuous monitoring*, *SciPost Phys.* **7** (2019) 24.

[150] X. Turkeshi, R. Fazio, and M. Dalmonte, *Measurement-induced criticality in* $(2+1)$*-dimensional hybrid quantum circuits*, *Phys. Rev. B* **102** (Jul, 2020) 014315.

[151] A. Lavasani, Y. Alavirad, and M. Barkeshli, *Topological order and criticality in* $(2+1)$D *monitored random quantum circuits*, *Phys. Rev. Lett.* **127** (Dec, 2021) 235701.

[152] P. Sierant, M. Schirò, M. Lewenstein, and X. Turkeshi, *Measurement-induced phase transitions in* $(d+1)$*-dimensional stabilizer circuits*, *Phys. Rev. B* **106** (Dec, 2022) 214316.

[153] S. Vijay, *Measurement-driven phase transition within a volume-law entangled phase*, 2020.

[154] A. Nahum, S. Roy, B. Skinner, and J. Ruhman, *Measurement and entanglement phase transitions in all-to-all quantum circuits, on quantum trees, and in landau-ginsburg theory*, *PRX Quantum* **2** (Mar, 2021) 010352.

[155] T. Minato, K. Sugimoto, T. Kuwahara, and K. Saito, *Fate of measurement-induced phase transition in long-range interactions*, *Phys. Rev. Lett.* **128** (Jan, 2022) 010603.

[156] M. Block, Y. Bao, S. Choi, E. Altman, and N. Y. Yao, *Measurement-induced transition in long-range interacting quantum circuits*, *Phys. Rev. Lett.* **128** (Jan, 2022) 010604.

[157] S. Sahu, S.-K. Jian, G. Bentsen, and B. Swingle, *Entanglement phases in large-n hybrid brownian circuits with long-range couplings*, *Phys. Rev. B* **106** (Dec, 2022) 224305.

[158] S. Sharma, X. Turkeshi, R. Fazio, and M. Dalmonte, *Measurement-induced criticality in extended and long-range unitary circuits*, *SciPost Phys. Core* **5** (2022) 023.

[159] P. Zhang, C. Liu, S.-K. Jian, and X. Chen, *Universal Entanglement Transitions of Free Fermions with Long-range Non-unitary Dynamics*, *Quantum* **6** (May, 2022) 723.

[160] Q. Tang and W. Zhu, *Measurement-induced phase transition: A case study in the nonintegrable model by density-matrix renormalization group calculations*, *Phys. Rev. Research* **2** (Jan, 2020) 013022.

[161] O. Lunt and A. Pal, *Measurement-induced entanglement transitions in many-body localized systems*, *Phys. Rev. Res.* **2** (Oct, 2020) 043072.

[162] Y. Fuji and Y. Ashida, *Measurement-induced quantum criticality under continuous monitoring*, *Phys. Rev. B* **102** (Aug, 2020) 054302.

[163] E. V. H. Doggen, Y. Gefen, I. V. Gornyi, A. D. Mirlin, and D. G. Polyakov, *Generalized quantum measurements with matrix product states: Entanglement phase transition and clusterization*, *Phys. Rev. Res.* **4** (May, 2022) 023146.

[164] A. Altland, M. Buchhold, S. Diehl, and T. Micklitz, *Dynamics of measured many-body quantum chaotic systems*, *Phys. Rev. Res.* **4** (Jun, 2022) L022066.

[165] S. Choi, Y. Bao, X.-L. Qi, and E. Altman, *Quantum error correction in scrambling dynamics and measurement-induced phase transition*, *Phys. Rev. Lett.* **125** (Jul, 2020) 030505.

[166] Y. Li and M. P. A. Fisher, *Statistical mechanics of quantum error correcting codes*, *Phys. Rev. B* **103** (Mar, 2021) 104306.

[167] R. Fan, S. Vijay, A. Vishwanath, and Y.-Z. You, *Self-organized error correction in random unitary circuits with measurement*, *Phys. Rev. B* **103** (May, 2021) 174309.

[168] Y. Li, X. Chen, and M. P. A. Fisher, *Measurement-driven entanglement transition in hybrid quantum circuits*, *Phys. Rev. B* **100** (Oct, 2019) 134306.

[169] A. Zabalo, M. J. Gullans, J. H. Wilson, S. Gopalakrishnan, D. A. Huse, and J. H. Pixley, *Critical properties of the measurement-induced transition in random quantum circuits*, *Phys. Rev. B* **101** (Feb, 2020) 060301.

[170] Y. Li, X. Chen, A. W. W. Ludwig, and M. P. A. Fisher, *Conformal invariance and quantum nonlocality in critical hybrid circuits*, *Phys. Rev. B* **104** (Sep, 2021) 104305.

[171] A. Zabalo, M. J. Gullans, J. H. Wilson, R. Vasseur, A. W. W. Ludwig, S. Gopalakrishnan, D. A. Huse, and J. H. Pixley, *Operator scaling dimensions and multifractality at measurement-induced transitions*, *Phys. Rev. Lett.* **128** (Feb, 2022) 050602.

[172] X. Chen, Y. Li, M. P. A. Fisher, and A. Lucas, *Emergent conformal symmetry in nonunitary random dynamics of free fermions*, *Phys. Rev. Research* **2** (Jul, 2020) 033017.

[173] M. Buchhold, Y. Minoguchi, A. Altland, and S. Diehl, *Effective theory for the measurement-induced phase transition of dirac fermions*, *Phys. Rev. X* **11** (Oct, 2021) 041004.

[174] X. Turkeshi, A. Biella, R. Fazio, M. Dalmonte, and M. Schiró, *Measurement-induced entanglement transitions in the quantum ising chain: From infinite to zero clicks*, *Phys. Rev. B* **103** (Jun, 2021) 224210.

[175] M. Szyniszewski, O. Lunt, and A. Pal, *Disordered monitored free fermions*, 2022.

[176] M. Coppola, E. Tirrito, D. Karevski, and M. Collura, *Growth of entanglement entropy under local projective measurements*, *Phys. Rev. B* **105** (Mar, 2022) 094303.

[177] I. Poboiko, P. Ppperl, I. V. Gornyi, and A. D. Mirlin, *Theory of free fermions under random projective measurements*, 2023.

[178] O. Alberton, M. Buchhold, and S. Diehl, *Entanglement transition in a monitored free-fermion chain: From extended criticality to area law*, *Phys. Rev. Lett.* **126** (Apr, 2021) 170602.

[179] M. McGinley, S. Roy, and S. A. Parameswaran, *Absolutely stable spatiotemporal order in noisy quantum systems*, *Phys. Rev. Lett.* **129** (Aug, 2022) 090404.

[180] T. Iadecola, S. Ganeshan, J. H. Pixley, and J. H. Wilson, *Dynamical entanglement transition in the probabilistic control of chaos*, 2022.

[181] M. Buchhold, T. Mller, and S. Diehl, *Revealing measurement-induced phase transitions by pre-selection*, 2022.

[182] A. J. Friedman, O. Hart, and R. Nandkishore, *Measurement-induced phases of matter require adaptive dynamics*, 2022.

[183] V. Ravindranath, Y. Han, Z.-C. Yang, and X. Chen, *Entanglement steering in adaptive circuits with feedback*, 2022.

[184] N. O'Dea, A. Morningstar, S. Gopalakrishnan, and V. Khemani, *Entanglement and absorbing-state transitions in interactive quantum dynamics*, 2022.

[185] G. Martn-Vzquez, T. Tolppanen, and M. Silveri, *Diagnosing measurement-induced phase transitions without trajectory post-selection through predetermined measurements*, 2023.

[186] M. J. Gullans and D. A. Huse, *Scalable probes of measurement-induced criticality*, *Phys. Rev. Lett.* **125** (Aug, 2020) 070606.

[187] S. J. Garratt, Z. Weinstein, and E. Altman, *Measurements conspire nonlocally to restructure critical quantum states*, 2022.

[188] Y. Li, Y. Zou, P. Glorioso, E. Altman, and M. P. A. Fisher, *Cross entropy benchmark for measurement-induced phase transitions*, 2022.

[189] H. Dehghani, A. Lavasani, M. Hafezi, and M. J. Gullans, *Neural-network decoders for measurement induced phase transitions*, 2022.

[190] M. Ippoliti and V. Khemani, *Postselection-free entanglement dynamics via spacetime duality*, *Phys. Rev. Lett.* **126** (Feb, 2021) 060501.

[191] T.-C. Lu and T. Grover, *Spacetime duality between localization transitions and measurement-induced transitions*, *PRX Quantum* **2** (Oct, 2021) 040319.

[192] J. C. Napp, R. L. La Placa, A. M. Dalzell, F. G. S. L. Brandão, and A. W. Harrow, *Efficient classical simulation of random shallow 2d quantum circuits*, *Phys. Rev. X* **12** (Apr, 2022) 021021.

[193] M. Ippoliti, T. Rakovszky, and V. Khemani, *Fractal, logarithmic, and volume-law entangled nonthermal steady states via spacetime duality*, *Phys. Rev. X* **12** (Mar, 2022) 011045.

[194] R. Vasseur, A. C. Potter, Y.-Z. You, and A. W. W. Ludwig, *Entanglement transitions from holographic random tensor networks*, *Phys. Rev. B* **100** (Oct, 2019) 134203.

[195] Y. Bao, S. Choi, and E. Altman, *Theory of the phase transition in random unitary circuits with measurements*, *Phys. Rev. B* **101** (Mar, 2020) 104301.

[196] C.-M. Jian, Y.-Z. You, R. Vasseur, and A. W. W. Ludwig, *Measurement-induced criticality in random quantum circuits*, *Phys. Rev. B* **101** (Mar, 2020) 104302.

[197] Y. Li, S. Vijay, and M. P. Fisher, *Entanglement domain walls in monitored quantum circuits and the directed polymer in a random environment*, *PRX Quantum* **4** (Mar, 2023) 010331.

[198] J. Côté and S. Kourtis, *Entanglement phase transition with spin glass criticality*, *Phys. Rev. Lett.* **128** (Jun, 2022) 240601.

[199] Y. Li, R. Vasseur, M. P. A. Fisher, and A. W. W. Ludwig, *Statistical mechanics model for clifford random tensor networks and monitored quantum circuits*, 2021.

[200] S. Gopalakrishnan and M. J. Gullans, *Entanglement and purification transitions in non-hermitian quantum mechanics*, *Phys. Rev. Lett.* **126** (Apr, 2021) 170503.

[201] A. Biella and M. Schiró, *Many-Body Quantum Zeno Effect and Measurement-Induced Subradiance Transition*, *Quantum* **5** (Aug., 2021) 528.

[202] Y. L. Gal, X. Turkeshi, and M. Schir, *Volume-to-area law entanglement transition in a non-hermitian free fermionic chain*, 2023.

[203] S.-K. Jian, Z.-C. Yang, Z. Bi, and X. Chen, *Yang-lee edge singularity triggered entanglement transition*, *Phys. Rev. B* **104** (Oct, 2021) L161107.

[204] V. Ravindranath and X. Chen, *Robust π-modes and a bulk-boundary correspondence in non-unitary floquet models*, 2022.

[205] X. Turkeshi, M. Dalmonte, R. Fazio, and M. Schirò, *Entanglement transitions from stochastic resetting of non-hermitian quasiparticles*, *Phys. Rev. B* **105** (Jun, 2022) L241114.

[206] X. Turkeshi and M. Schiró, *Entanglement and correlation spreading in non-hermitian spin chains*, *Phys. Rev. B* **107** (Jan, 2023) L020403.

[207] M. Fava, L. Piroli, T. Swann, D. Bernard, and A. Nahum, *Nonlinear sigma models for monitored dynamics of free fermions*, 2023.

[208] C.-M. Jian, H. Shapourian, B. Bauer, and A. W. W. Ludwig, *Measurement-induced entanglement transitions in quantum circuits of non-interacting fermions: Born-rule versus forced measurements*, 2023.

[209] M. Szyniszewski, A. Romito, and H. Schomerus, *Entanglement transition from variable-strength weak measurements*, *Phys. Rev. B* **100** (Aug, 2019) 064204.

[210] M. Szyniszewski, A. Romito, and H. Schomerus, *Universality of entanglement transitions from stroboscopic to continuous measurements*, *Phys. Rev. Lett.* **125** (Nov, 2020) 210602.

[211] M. Ippoliti, M. J. Gullans, S. Gopalakrishnan, D. A. Huse, and V. Khemani, *Entanglement phase transitions in measurement-only dynamics*, *Phys. Rev. X* **11** (Feb, 2021) 011030.

[212] A. Lavasani, Y. Alavirad, and M. Barkeshli, *Measurement-induced topological entanglement transitions in symmetric random quantum circuits*, *Nature Physics* **17** (Mar, 2021) 342–347.

[213] S. Sang and T. H. Hsieh, *Measurement-protected quantum phases*, *Phys. Rev. Research* **3** (Jun, 2021) 023200.

[214] Y. Bao, S. Choi, and E. Altman, *Symmetry enriched phases of quantum circuits*, *Annals of Physics* **435** (2021) 168618. Special issue on Philip W. Anderson.

[215] T. Kalsi, A. Romito, and H. Schomerus, *Three-fold way of entanglement dynamics in monitored quantum circuits*, *Journal of Physics A: Mathematical and Theoretical* **55** (jun, 2022) 264009.

[216] U. Agrawal, A. Zabalo, K. Chen, J. H. Wilson, A. C. Potter, J. H. Pixley, S. Gopalakrishnan, and R. Vasseur, *Entanglement and charge-sharpening transitions in u(1) symmetric monitored quantum circuits*, *Phys. Rev. X* **12** (Oct, 2022) 041002.

[217] F. Barratt, U. Agrawal, S. Gopalakrishnan, D. A. Huse, R. Vasseur, and A. C. Potter, *Field theory of charge sharpening in symmetric monitored quantum circuits*, *Phys. Rev. Lett.* **129** (Sep, 2022) 120604.

[218] Q. Tang, X. Chen, and W. Zhu, *Quantum criticality in the nonunitary dynamics of* $(2+1)$*-dimensional free fermions*, *Phys. Rev. B* **103** (May, 2021) 174303.

[219] T. Müller, S. Diehl, and M. Buchhold, *Measurement-induced dark state phase transitions in long-ranged fermion systems*, *Phys. Rev. Lett.* **128** (Jan, 2022) 010605.

[220] X. Turkeshi, L. Piroli, and M. Schiró, *Enhanced entanglement negativity in boundary-driven monitored fermionic chains*, *Phys. Rev. B* **106** (Jul, 2022) 024304.

[221] G. Kells, D. Meidan, and A. Romito, *Topological transitions in weakly monitored free fermions*, *SciPost Phys.* **14** (2023) 031.

[222] C.-M. Jian, B. Bauer, A. Keselman, and A. W. W. Ludwig, *Criticality and entanglement in nonunitary quantum circuits and tensor networks of noninteracting fermions*, *Phys. Rev. B* **106** (Oct, 2022) 134206.

[223] T. Boorman, M. Szyniszewski, H. Schomerus, and A. Romito, *Diagnostics of entanglement dynamics in noisy and disordered spin chains via the measurement-induced steady-state entanglement transition*, *Phys. Rev. B* **105** (Apr, 2022) 144202.

[224] T. Botzung, S. Diehl, and M. Müller, *Engineered dissipation induced entanglement transition in quantum spin chains: From logarithmic growth to area law*, *Phys. Rev. B* **104** (Nov, 2021) 184422.

[225] Z.-C. Yang, Y. Li, M. P. A. Fisher, and X. Chen, *Entanglement phase transitions in random stabilizer tensor networks*, *Phys. Rev. B* **105** (Mar, 2022) 104306.

[226] A. Milekhin and F. K. Popov, *Measurement-induced phase transition in teleportation and wormholes*, 2023.

[227] S. Haldar and A. J. Brady, *A numerical study of measurement-induced phase transitions in the sachdev-ye-kitaev model*, 2023.

[228] S.-K. Jian, C. Liu, X. Chen, B. Swingle, and P. Zhang, *Measurement-induced phase transition in the monitored sachdev-ye-kitaev model*, *Phys. Rev. Lett.* **127** (Sep, 2021) 140601.

[229] Z. Weinstein, S. P. Kelly, J. Marino, and E. Altman, *Scrambling transition in a radiative random unitary circuit*, 2022.

[230] R. Wiersema, C. Zhou, J. F. Carrasquilla, and Y. B. Kim, *Measurement-induced entanglement phase transitions in variational quantum circuits*, 2021.

[231] J. Lopez-Piqueres, B. Ware, and R. Vasseur, *Mean-field entanglement transitions in random tree tensor networks*, *Phys. Rev. B* **102** (Aug, 2020) 064202.

[232] X. Feng, B. Skinner, and A. Nahum, *Measurement-induced phase transitions on dynamical quantum trees*, 2022.

[233] J. Iaconis, A. Lucas, and X. Chen, *Measurement-induced phase transitions in quantum automaton circuits*, *Phys. Rev. B* **102** (Dec, 2020) 224311.

[234] A. Chan, R. M. Nandkishore, M. Pretko, and G. Smith, *Unitary-projective entanglement dynamics*, *Phys. Rev. B* **99** (Jun, 2019) 224307.

[235] L. Piroli, Y. Li, R. Vasseur, and A. Nahum, *Triviality of quantum trajectories close to a directed percolation transition*, 2022.

[236] P. Sierant and X. Turkeshi, *Universal behavior beyond multifractality of wave functions at measurement-induced phase transitions*, *Phys. Rev. Lett.* **128** (Apr, 2022) 130605.

[237] S. Sang, Y. Li, T. Zhou, X. Chen, T. H. Hsieh, and M. P. Fisher, *Entanglement negativity at measurement-induced criticality*, *PRX Quantum* **2** (Jul, 2021) 030313.

[238] Z. Weinstein, Y. Bao, and E. Altman, *Measurement-induced power-law negativity in an open monitored quantum circuit*, *Phys. Rev. Lett.* **129** (Aug, 2022) 080501.

[239] G. S. Bentsen, S. Sahu, and B. Swingle, *Measurement-induced purification in large-n hybrid brownian circuits*, *Phys. Rev. B* **104** (Sep, 2021) 094304.

[240] X. Yu and X.-L. Qi, *Measurement-induced entanglement phase transition in random bilocal circuits*, 2022.

[241] A. Nahum and K. J. Wiese, *Renormalization group for measurement and entanglement phase transitions*, 2023.

[242] A. C. Potter and R. Vasseur, *Entanglement Dynamics in Hybrid Quantum Circuits*, pp. 211–249. Springer International Publishing, Cham, 2022.

[243] M. P. Fisher, V. Khemani, A. Nahum, and S. Vijay, *Random quantum circuits*, *Annual Review of Condensed Matter Physics* **14** (2023), no. 1 335–379, [https://doi.org/10.1146/annurev-conmatphys-031720-030658].

[244] C. Noel, P. Niroula, D. Zhu, A. Risinger, L. Egan, D. Biswas, M. Cetina, A. V. Gorshkov, M. J. Gullans, D. A. Huse, and C. Monroe, *Measurement-induced quantum phases realized in a trapped-ion quantum computer*, *Nature Physics* **18** (jun, 2022) 760–764.

[245] J. M. Koh, S.-N. Sun, M. Motta, and A. J. Minnich, *Experimental realization of a measurement-induced entanglement phase transition on a superconducting quantum processor*, 2022.

[246] J. C. Hoke, M. Ippoliti, D. Abanin, R. Acharya, M. Ansmann, F. Arute, K. Arya, A. Asfaw, J. Atalaya, J. C. Bardin, A. Bengtsson, G. Bortoli, A. Bourassa, J. Bovaird, L. Brill, M. Broughton, B. B. Buckley, D. A. Buell, T. Burger, B. Burkett, N. Bushnell, Z. Chen, B. Chiaro, D. Chik, C. Chou, J. Cogan, R. Collins, P. Conner, W. Courtney, A. L. Crook, B. Curtin, A. G. Dau, D. M. Debroy, A. D. T. Barba, S. Demura, A. D. Paolo, I. K. Drozdov, A. Dunsworth, D. Eppens, C. Erickson, L. Faoro, E. Farhi, R. Fatem, V. S. Ferreira, L. F. Burgos, E. Forati, A. G. Fowler, B. Foxen, W. Giang, C. Gidney, D. Gilboa, M. Giustina, R. Gosula, J. A. Gross, S. Habegger, M. C. Hamilton, M. Hansen,

M. P. Harrigan, S. D. Harrington, P. Heu, M. R. Hoffmann, S. Hong, T. Huang, A. Huff, W. J. Huggins, S. V. Isakov, J. Iveland, E. Jeffr, C. Jones, P. Juhas, D. Kafri, K. Kechedzhi, T. Khattar, M. Khezri, M. Kieferov, S. Kim, A. Kitaev, P. V. Klimov, A. R. Klots, A. N. Korotkov, F. Kostritsa, J. M. Kreikebaum, D. Landhuis, P. Laptev, K.-M. Lau, L. Laws, J. Lee, K. W. Lee, Y. D. Lensky, B. J. Lester, A. T. Lill, W. Liu, A. Locharla, F. D. Malone, O. Martin, J. R. McClean, T. McCourt, M. McEwen, K. C. Miao, A. Mieszala, S. Montazeri, A. Morvan, R. Movassagh, W. Mruczkiewicz, M. Neeley, C. Neill, A. Nersisyan, M. Newman, J. H. Ng, A. Nguyen, M. Nguyen, M. Y. Niu, T. E. O'Brien, S. Omonije, A. Opremcak, A. Petukhov, R. Potter, L. P. Pryadko, C. Quintana, C. Rocque, N. C. Rubin, N. S. D. Sank, K. Sankaragomathi, K. J. Satzinger, H. F. Schurkus, C. Schuster, M. J. Shearn, A. Shorter, N. Shutty, V. Shvarts, J. Skruzny, W. C. Smith, R. D. S. G. Sterling, D. Strain, M. Szalay, A. Torres, G. Vidal, B. Villalonga, C. V. Heidweiller, T. White, B. W. K. Woo, C. Xing, Z. J. Yao, P. Yeh, J. Yoo, G. Young, A. Zalcman, Y. Zhang, N. Zhu, N. Zobrist, H. Neven, R. Babbush, D. Bacon, S. Boixo, J. Hilton, E. Lucero, A. Megrant, J. Kelly, Y. Chen, V. Smelyanskiy, X. Mi, V. Khemani, and P. Roushan, *Quantum information phases in space-time: measurement-induced entanglement and teleportation on a noisy quantum processor*, 2023.

[247] L. Casparis, T. W. Larsen, M. S. Olsen, F. Kuemmeth, P. Krogstrup, J. Nygård, K. D. Petersson, and C. M. Marcus, *Gatemon Benchmarking and Two-Qubit Operations*, *Physical Review Letters* **116** (2016) 150505.

[248] R. H. Koch, D. P. Divincenzo, and J. Clarke, *Model for 1/f Flux Noise in SQUIDs and Qubits*, *Physical Review Letters* **98** (2007) 267003.

[249] F. Yoshihara, K. Harrabi, A. O. Niskanen, Y. Nakamura, and J. S. Tsai, *Decoherence of Flux Qubits due to 1/f Flux Noise*, *Physical Review Letters* **97** (2006) 167001.

[250] R. C. Bialczak, R. Mcdermott, M. Ansmann, M. Hofheinz, N. Katz, E. Lucero, M. Neeley, A. D. O'connell, H. Wang, A. N. Cleland, and J. M. Martinis, *1/f Flux Noise in Josephson Phase Qubits*, *Physical Review Letters* **99** (2007) 187006.

[251] B. van Heck, R. M. Lutchyn, and L. I. Glazman, *Conductance of a proximitized nanowire in the coulomb blockade regime*, *Phys. Rev. B* **93** (Jun, 2016) 235431.